Final Report
UM/THL-18-06

Compact Heat Exchanger Design and Testing for Advanced Reactors and Advanced Power Cycles

Award Identification Number:
The U.S. Department of Energy, DE-NE0000706

Period of Performance: 01/22/2014 to 12/31/2017

Principal Investigators
Xiaodong Sun, Mark Anderson, In Hun Kim, and Richard Christensen

Submitted by

Xiaoqin Zhang, Xiaodong Sun, and Richard Christensen
Thermal Hydraulics Laboratory
Nuclear Engineering Program
The Ohio State University
201 West 19th Avenue
Columbus, OH 43210

and

Ian Jantz and Mark Anderson
Department of Engineering Physics
University of Wisconsin, Madison
1500 Engineering Drive
Madison, WI 53706

Supported by

Nuclear Energy University Programs
The Department of Energy

THE OHIO STATE UNIVERSITY

WISCONSIN
UNIVERSITY OF WISCONSIN–MADISON

March 31, 2018

THE OHIO STATE UNIVERSITY
NUCLEAR ENGINEERING PROGRAM
THERMAL HYDRAULICS LABORATORY

UM/THL-18-06
NON-PROPRIETARY REPORT

Final Report

Compact Heat Exchanger Design and Testing for Advanced Reactors and Advanced Power Cycles

---

by

Xiaoqin Zhang, Xiaodong Sun, and Richard Christensen

The Ohio State University

and

Ian Jantz and Mark Anderson

University of Wisconsin, Madison

March 31, 2018

Prepared for

Nuclear Energy University Programs
The U.S. Department of Energy

Nuclear Engineering Program, The Ohio State University
201 West 19th Avenue, Columbus, OH 43210

ACKNOWLEDGEMENTS

This research was performed using funding received from the U.S. Department of Energy (DOE) Office of Nuclear Energy's Nuclear Energy University Programs.

EXECUTIVE SUMMARY

Goals, Objectives, and Approach

The goal of the proposed research is to demonstrate the thermal hydraulic performance of innovative surface geometries in compact heat exchangers used as intermediate heat exchangers (IHXs) and recuperators for the supercritical carbon dioxide (s-CO_2) Brayton cycle. Printed-circuit heat exchangers (PCHEs) are the primary compact heat exchangers of interest. The overall objectives are:

1. To develop optimized PCHE designs for different working fluid combinations including helium to s-CO_2, liquid salt to s-CO_2, sodium to s-CO_2, and liquid salt to helium;

2. To experimentally and numerically investigate thermal performance, thermal stress and failure mechanism of PCHEs under various transients; and

3. To study diffusion bonding techniques for elevated-temperature alloys and examine post-test material integrity of the PCHEs.

The project objectives were accomplished by defining and executing five different tasks corresponding to these specific objectives. The first task involved a thorough literature review and a selection of IHX candidates with different surface geometries as well as a summary of prototypic operational conditions. The second task involved optimization of PCHE design with numerical analyses of thermal-hydraulic performances and mechanical integrity. The subsequent task dealt with the development of testing facilities and engineering design of PCHE to be tested in s-CO_2 fluid conditions. The next task involved experimental investigation and validation of the thermal-hydraulic performances and thermal stress distribution of prototype PCHEs manufactured with particular surface geometries. The last task involved an investigation of diffusion bonding process and post-test destructive testing to validate mechanical design methods adopted in the design process. The experimental work utilized the two test facilities at The Ohio State University (OSU) including one existing High-Temperature Helium Test Facility (HTHF) and the newly developed s-CO_2 test loop (STL) facility and s-CO_2 test facility at University of Wisconsin – Madison (UW).

Accomplishments and Outcomes

The summary of these activities conducted and the resulting outcomes is as follows:

- A thorough literature review of available PCHE surface geometry designs with a summary of previous experimental work and proposed prototypic operational

conditions was carried out. Two specific advanced PCHE designs were emphasized: S-shaped fin channel and airfoil channel;

- Optimization methodologies based on the economic cost analysis were developed. An optimum sizing method was developed first to initiate preliminary selection of particular surface geometry for PCHE design. Correlations necessary for optimization process were also developed. A multi-objective genetic algorithm was adopted to optimize PCHE designs in terms of thermal, economic and mechanical analysis. The optimized design for different fluids were obtained and scaled-down for the fabrication of prototypic PCHE to be tested;
- Numerical simulation of PCHEs thermal-hydraulics were carried out. CFD (computational fluid dynamics) analysis was validated with available experimental data. The numerical results were used to develop optimized design of particular surface geometry;
- Numerical simulation of PCHEs mechanical integrity were also carried out. The stress distribution corresponding to mechanical loadings for different surface geometries were obtained, and the mechanical design methodologies in compliance with ASME standards were investigated and summarized. The mechanical integrity of PCHEs were confirmed with numerical results;
- The scaling analysis of PCHEs was completed, and the engineering design of PCHEs to be tested was finalized. The testing components were fabricated by domestic commercial vendors;
- S-CO_2 test facilities in both universities were designed and constructed. Experience of designing facilities and handling s-CO_2 was accumulated;
- Experiments were conducted and experimental results were obtained. The thermal-hydraulic and mechanical performance of PCHEs were validated at UW;
- Post-test inspection of a decommissioned PCHE was completed, and the maximum allowable working pressure was established based on testing results. The diffusion bonding parameters that affect the diffusion-bonds' mechanical strength were investigated.

Publications

Jentz, I., Marzouk, M.B., Anderson, M., and Sun, X., "System for Testing Thermal Shock in Printed Circuit Heat Exchangers," Transactions of the American Nuclear Society, Vol. 111, 2014 ANS Winter Meeting, November 9-13, 2014, Anaheim, CA, pp. 107-110. I. Jentz presented this summary at the conference.

Kim, I.H., Zhang, X, Sun, X, and Christensen, R.N., "Design Study and Cost Assessment of Straight, Zigzag, S-Shape, and OSF PCHEs for a FLiNaK – SCO2 Secondary Heat Exchanger in FHRs", Annals of Nuclear Energy, 94, pp. 129-137 (2016)

Zhang, X., Sun, X., Christensen, R.N. and Anderson, M., "Preliminary Structural Assessment of a Printed Circuit Heat Exchanger with S-shaped Fins," Proceedings of International Topical Meeting on Nuclear Reactor Thermal Hydraulics (NURETH-16), August 30 – September 4, 2015, Chicago, IL.

Zhang, X., Sun, X., and Christensen, R.N., "Design of an Advanced Intermediate Heat Exchanger for Supercritical CO2 Brayton Cycle," Proceedings of 2015 American Nuclear Society Winter Meeting and Nuclear Technology Expo, November 8012, 2015, Washington, DC.

Zhang, X., Sun, X., and Christensen, R.N., Anderson, M., and Carlson, M., "Optimization of S-Shaped Fin Channels in a Printed Circuit Heat Exchanger for Supercritical CO2 Test Loop", Proceedings of the 5th International Supercritical CO2 Power Cycles Symposium, March 29-31, 2016, San Antonio, TX.

Zhang, X., Sun, X., and Christensen, R.N., Anderson, M., and Carlson, M., "Multi-Objective Optimization of a PCHE-Type Intermediate Heat Exchanger using Genetic Algorithms", accepted by International Topical Meeting on Advances in Thermal Hydraulics 2016 (ATH 16), June 12-16, 2016, New Orleans, LA.

Zhang, X., Shi, S., Christensen, R.N. and Sun, X., "Review on Mechanical Design of Printed Circuit Heat Exchangers," International Conference on Nuclear Engineering (ICONE), July 2-6, 2017, Shanghai, China.

Zhang, X., Shi, S., Christensen, R.N. and Sun, X., Anderson, M. and Carlson, M., "Design and Test Plan of High-Temperature Supercritical CO2 Test Loop for Testing PCHE Type Heat Exchangers," International Topical Meeting on Nuclear Reactor Thermal Hydraulics (NURETH-17), September 3-8, 2017, Xi'an, China.

TABLE OF CONTENTS

LIST OF FIGURES

LIST OF TABLES

Introduction

The supercritical carbon dioxide (s-CO_2) Brayton cycle is one of the promising power conversion systems for advanced nuclear reactors, including the High-Temperature Gas-cooled Reactor (HTGR), the Sodium Fast Reactor (SFR), and Fluoride salt High-temperature Reactor (FHR). Coupling the s-CO2 Brayton cycle to the advanced nuclear reactors usually requires an intermediate heat exchanger (IHX) and recuperators. From the economic point of view, it is important to reduce the size and cost of the IHX/recuperators of the s-CO2 Brayton cycle, but their thermal hydraulic performances should not be deteriorated. An advanced heat exchanger, printed-circuit heat exchanger (PCHE), has been shown as a competitive candidate due to its extreme compactness and resistance in harsh conditions. This project mainly focused on demonstrating the thermal hydraulic performance of innovative surface geometries applicable in PCHEs. In the project, the design optimization of PCHEs of particular geometries as well as the mechanical integrity was accomplished in the first year. In the second year, numerical studies were continued and the experimental investigation was started after the completion of test facility design. In the third and extended year, thermal-hydraulic data and experimental results were obtained and the post-test inspection was completed on decommissioned PCHE.

A typical PCHE is fabricated of a number of substrate plates where surface passages are photo-chemically etched. The plates are diffusion-bonded to form a high mechanical-strength PCHE block. The overall performance as well as the total cost of a PCHE are strongly dependent upon the surface characteristics of the flow passages that are etched on plates, such as channel hydraulic diameter, channel angle and channel spacing. The available experimentally- and numerically-developed empirical correlations were used to develop new correlations that relate the Fanning factor and Nusselt number to the surface characteristic parameters. Four advanced flow channels, straight, zigzag, S-shaped fin and airfoil fin channels, were investigated in the design optimization process, using a correlation-based multi-objective evolutionary algorithm (MOEA). MOEAs are characterized by the capability in solving optimization problems with multiple conflicting objectives. An advanced MOEA, NSGA-II algorithm (Non-dominated Sorting Genetic Algorithms), was used to optimize PCHE design based on two objectives, i.e. the heat exchanger efficiency and the total cost. The optimized design has also been scaled-down to a practically engineered PCHE that was fabricated and planned to be tested in a helium-s-CO_2 test facility, in which an s-CO_2 test loop was designed and constructed to couple with an existing high-temperature helium test facility (HTHF).

Also of interest is the mechanical integrity of PCHE diffusion-bonded blocks with advanced channel geometries. The S-shaped and airfoil fin channels reduces pressure

drop effectively, however, at the cost of decreasing diffusion-bond interface area that is critical to the mechanical strength. ANSYS modeling and simulation has been conducted to numerically test the diffusion bond area. Both mechanical and thermal stress are numerically simulated. The 3-D printed test specimens for airfoil fin channels have been fabricated and tested in a pressurization rig. Pressurization experiments on stainless steel 316 test specimens were performed to examine the diffusion-bond strength and the integrity of PCHEs with advanced fin channels.

S-CO_2 test facilities were designed and constructed at both universities. The s-CO_2 test loop (STL) at the Ohio State University (OSU) was characterized with an operating pressure of 15 MPa and temperatures up to 650 °C. It was designed to couple with HTHF to provide prototypic testing conditions. The s-CO_2 test facility in University of Wisconsin – Madison (UW) was equipped with instrument to measure the pressure drop and heat transfer of PCHEs as well as the thermal strain distribution. The PCHE mechanical integrity was investigated. Some of the details of components in both experimental facilities are presented in the report.

The strength of diffusion-bonds of PCHEs are strongly dependent on several process parameters, which were investigated in the project. The post-test inspection revealed the importance of extra caution in diffusion-bonding process. It was found that the header attachment through welding could cause potential damage to the PCHE diffusion-bonded block, thus degrading the mechanical integrity.

The final report of this project is organized as follows: the first chapter presents the literature review, PCHE designs, design optimization methodologies and case studies, as well as the numerical analysis to assist design in terms of both thermal-hydraulic and mechanical performance. Chapter 2 describes the design of experimental test facilities including the components' selection, the construction of the facility and the engineering aspects of PCHEs to be tested. Experimental results are provided. Chapter 3 discusses the diffusion bonding parameters and presents the experimental inspection of PCHEs' mechanical integrity. The investigation method is presented as well.

1. PCHE Designs and Optimization

1.1 Literature Review of Available PCHE Physical Models and Experimental Data

1.1.1 Summary of available PCHEs' surface geometry performance and characteristics

For the PCHEs which are considered as promising candidates for the IHXs in advanced nuclear reactor systems, to date there are four outstanding types of flow channels available: straight channel, zigzag (wavy) channel, S-shaped fin and airfoil fin. The straight and zigzag channels are most often used by Heatric, the vender of PCHEs in the world. The S-shaped fin was developed in 2007 by Tokyo Institute of Technology (Tsuzuki et al., 2007) and the airfoil fin was developed in 2008 by POSTECH (Kim et al., 2008). Investigations for these two advanced surface fins have been carried out both numerically and experimentally in terms of thermal hydraulic performance in the PCHEs via preliminary parametric studies. For all surface geometries, the physical models for heat transfer and pressure drop performance have been developed, and an assessment based on a cost analysis has been conducted.

Straight and zigzag channels are of the continuous surface geometry type. These channel patterns are characterized by a uniform cross-section profile throughout the entire channel of a heat exchanger, usually featuring a semi-circular profile in typical applications. Several studies on these channels have been carried out both numerically and experimentally. The zigzag channels are more difficult to analyze numerically because the effects of certain geometric parameters, such as rounding at the channel bends, need to be considered. Experimental correlations have been developed, especially for zigzag channels, over a wide range of geometric parameters and thermal hydraulic characteristics. The test data and correlations on straight and zigzag channel PCHEs are obtained using either helium or s-CO2 as working fluid. Typical correlations are described in Table 1.

Table 1. Summary of typical thermal hydraulic correlations for four surface geometries

Surface Geometry	Schematic	Description	Correlation
Straight Channel	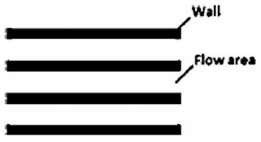	Semi-circular, laminar	$f \cdot \mathrm{Re} = 15.78$ $\mathrm{Nu} = 4.089$
		Semi-circular, turbulent	$\frac{1}{\sqrt{f}} = -2.0 \log\left(\frac{e/D}{3.7} + \frac{2.51}{\mathrm{Re}\sqrt{f}}\right)$ $Nu = 0.023\,\mathrm{Re}^{0.8}\,\mathrm{Pr}^{n}$

Zigzag Channel		Angle 45°, laminar, helium as test fluid	$f \cdot \mathrm{Re} = 15.78 + 0.62339\,\mathrm{Re}^{0.78214}$ $\mathrm{Nu} = 4.089 + 0.05988\,\mathrm{Re}^{0.66801}$
		Angle 52°, turbulent	$f = 0.1924\,\mathrm{Re}^{-0.091}$ $\mathrm{Nu} = 0.1696\,\mathrm{Re}^{0.629}\,\mathrm{Pr}^{0.317}$
S-shaped Fin	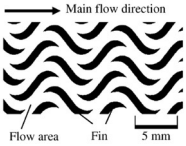	Fin angle 52°, turbulent	$f = 0.4545\,\mathrm{Re}^{-0.340}$ $\mathrm{Nu} = 0.1740\,\mathrm{Re}^{0.593}\,\mathrm{Pr}^{0.430}$
Airfoil Fin		n/a	n/a

Conventional zigzag channels may contribute to larger pressure drops due to the bends present in the flow path. These bends lead to swirl flows, reversed flows, and eddies around the bend corners that increase pressure drop. The sinusoidal curve flow channel with sharp bends was studied and demonstrated to decrease the pressure drop over the zigzag channel. However, the sinusoidal flow pattern causes stagnant flow areas around the bend, which restrains heat transfer. The offsetting arrangement of these sinusoidal curves improves heat transfer performance and results in the invention of the S-shaped fin. The S-shaped fin extends the ends of separated sinusoidal curves, becoming the shape's head and tail. The developing process is shown in the Figure 1. This new configuration of fins has been extensively compared with corresponding zigzag channels in experimental tests and shown to be superior in terms of pressure drop reduction, even though the heat transfer performance is slightly not as good. The effect of varying Prandtl number has been examined so that the thermal hydraulic correlations are developed based on both Reynolds and Prandtl number. Unfortunately, only turbulent flow data are available to date, therefore the correlation has been extended to transitional flow. Although turbulent flow assumptions loosely apply in the transitional flow regime, these correlations will still be used until new correlations for transition flow can be found for heat exchanger design. Typical correlations are summarized in Table 1, and the Nusselt number and Fanning factor as a function of the Reynolds number are shown in Figure 2.

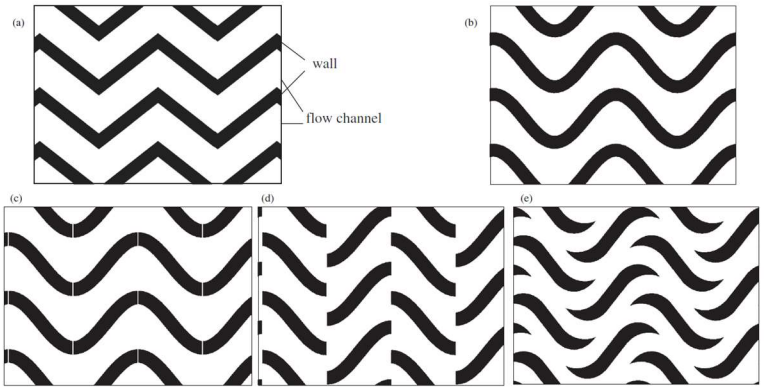

Figure 1. Developing process of the S-shaped fin (sinusoidal fin) surface geometry (Tsuzuki et al., 2009)

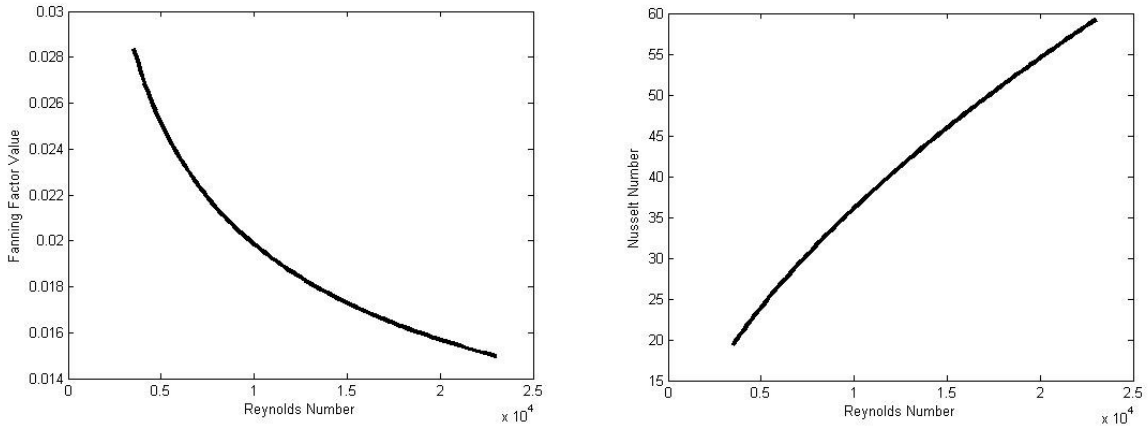

Figure 2. Fanning factor and Nusselt number against Reynolds number from the correlations for 52° S-shaped fin at turbulent flow region

A reference sinusoidal-fin model is identified from the literature. In principle, the S-shaped fin (or sinusoidal fin) is formed by shifting a sinusoidal curve in two opposite directions with the appropriate distance defined by the fin width. The sinusoidal curve is governed by a sine function that is defined by a fin length and a fin angle, which are the primary geometric parameters of the S-shaped fin. Note that with the fin angle below 45 degree, the shifting direction of the sinusoidal curve should be adjusted intentionally not perpendicular to the fin angle. In one of the models, the fin length, fin angle, fin width, neighboring fin gap and channel depth (fin height) are 4.8 mm, 52°, 0.8 mm, 2.7 mm, and 0.94 mm, respectively. Accordingly, the *x*- and *y*-direction pitches can be obtained through calculation, forming the unit cell model with four half S-shaped fins enclosed. The specification parameters of an S-shaped fin have been summarized in Table 2, and the detailed geometry characteristics are shown in Figure 3.

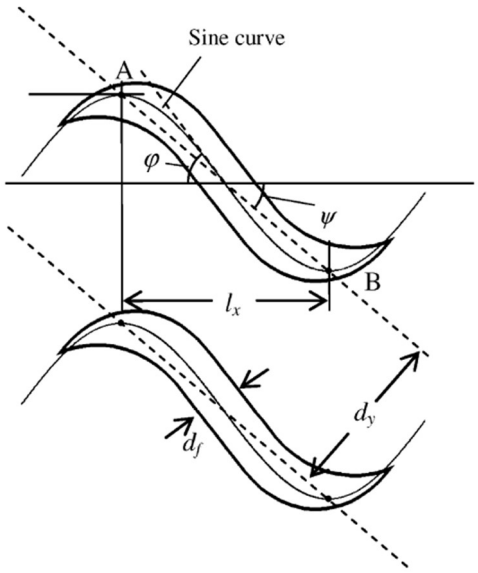

Figure 3. Detailed geometric characteristics of the S-shaped fin (Tsuzuki et al., 2007)

Table 2. Specification parameters of the reference model of S-shaped fin

Parameters	Values
Plate thickness, t_p, mm	1.5
Fin angle, φ, °	52
Fin length, l_f, mm	4.8
Fin width, d_f, mm	0.8
Fin gap, d_y, mm	2.7
Fin pitch in x-/y-direction, p_x/p_y, mm	7.565/3.428
Fin height, h, mm	0.94
Hydraulic diameter, D_h, mm	1.629
Free flow area in unit cell, A_c, mm^2	5.196
Heat transfer area in unit cell, A_s, mm^2	94.944

The airfoil PCHE features an islanded fin geometry different from other etched PCHE channel designs. The channels of the airfoil PCHE contain an array of offset airfoil shaped fins. The fins are patterned in alternating rows with the airfoils facing the direction of flow in the channel. In this fashion flow through the channel isn't constrained to a singular flow path, as in the typical straight and zig-zag channel designs. Flow is free to

pass through the entirety of the air foil array without constraint that is induced by the repeating channel walls of straight channel and zig-zag PCHE designs. Moving around each individual airfoil in the channel the fluid becomes well mixed and transfers heat as well as the standard zig-zag channel design without as much of a pressure drop (Carlson, 2012).

The channel pattern that is etched in an Airfoil PCHE is shown in Figure 4. The airfoils are described by the camber-less NACA airfoil equation, also shown in Figure 4. The pattern is described by the chord length of the airfoil, the thickness of the airfoil at its girth, the lateral pitch between airfoil columns (perpendicular to flow), and the axial pitch between airfoil rows (in the direction of flow). In sizing the array, chord length and axial pitch are set so that the most uniform hydraulic diameter is achieved, which occurs when the ratio of axial pitch to chord length (s/c) is 0.86 (Kruizenga, 2010). Values considered for the airfoil pattern are shown in Table 3. These values were chosen to be the same as those used in previous experimental analysis of Kruizenga and Carlson and result in a pattern that achieves 17.8% bond coverage of the etched PCHE plate. The etching process limits the depth of the air-foil fin channel to 1 mm, thus any increase in hydraulic diameter requires an increase in the pattern's spacing.

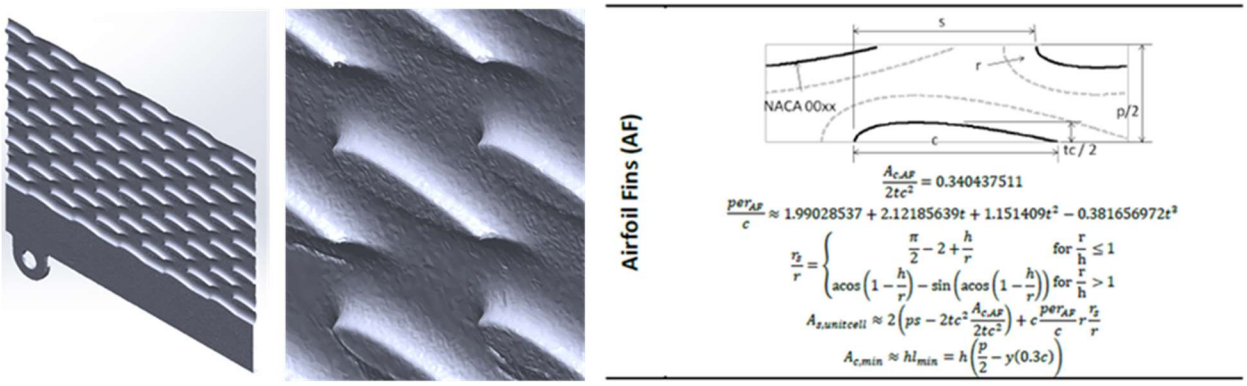

Figure 4: Optical scan of airfoil-fin channel (left), optical scan detail (center) camber-less NACA airfoil equation and airfoil-fin pattern (right).

Table 3: Airfoil Pattern Parameters

Description	Symbol	Unit	Design Value
Chord length	c	mm	8.1
Thickness	tc	mm	0.2
Axial pitch	s	mm	6.9
Lateral pitch	p	mm	7.3
Fillet radius	r	mm	0.95
Channel depth	d	mm	0.95

Hydraulic Diameter	D_h	mm	1.607

Most experimental and numerical studies on PCHEs have focused on Heatric's™ industry standard zig-zag channel (Carlson, 2012). The zig-zag channel consists of many turning micro channels, as shown in Figure 5. Bends in the channel vary from 65° to 80° to improve mixing of the s-CO_2 by breaking up the near wall boundary layer and enhancing heat transfer. Many subsequent bends lead to high pressure loss in zig-zag channel PCHEs. The Zig-zag geometry used at the University of Wisconsin is described in Table 4.

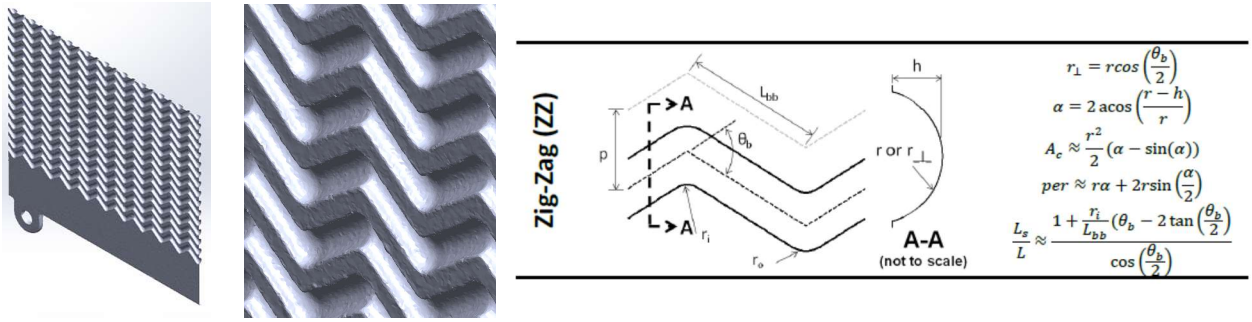

Figure 5: Optical scan of zig-zag channel (left), optical scan detail (center) zig-zag channel equations (right).

Table 4: Zig-zag Geometry Parameters

Description	Symbol	Unit	Design Value
Bend-to-bend length	L_{bb}	mm	4.724
Bend Angle	θ_b	deg	80
Inner bend radius	r_i	mm	0.583
Outer bend radius	r_o	mm	0.876
Lateral pitch	p	mm	3.277
Fillet radius	r	mm	0.95
Channel depth	d	mm	0.95
Hydraulic Diameter	D_h	mm	1.013

1.1.2 Summary of prototypic PCHE operating conditions

In this project the application of PCHEs in the s-CO_2 Brayton power conversion cycle for advanced nuclear reactor systems is emphasized. PCHE's will operate with different working fluids on either side of IHXs. Helium and liquid salt have been identified as two types of working fluids of interest. The helium-to-s-CO_2 IHXs are characterized by high temperature and high pressure, while the liquid salt-to- s-CO2 ones have a low salt-side

pressure but have potential corrosion issues. Most current s-CO_2 indirect Brayton cycle prototypic designs using helium or liquid salt as the primary-side fluid are based on typical 600-MW s-CO_2 direct cycles proposed by Dostal (Dostal, 2004). This direct s-CO_2 power conversion Brayton cycle is characterized by 550 to 650°C turbine inlet temperatures and 20 MPa operating pressures as well as a net plant efficiency varying from 43.9 to 47.8%. Particularly, this design contains recompression components and is referred as the s-CO_2 recompression cycle. Recompression values are described in Table 5.

The performance potential of helium cooled gas-cooled fast reactors (GFRs) coupled to an s-CO_2 power cycle has been studied for cost analysis and net plant efficiency optimization. The principal parameters of the core have been identified as: 600-MW thermal power, core inlet and outlet temperatures of 530 and 800 °C, respectively, core pressure of 7 MPa, and core mass flow rate of 388 kg/s. The key operating parameters of the helium-to-s-CO_2 IHX and recuperators are summarized in Table 6.

The lead alloy fast reactor has been chosen as a representative for the liquid-salt to s-CO_2 indirect Brayton cycle. This reference reactor is still based on the typical direct s-CO_2 Brayton cycle. The primary coolant conditions have been identified as: core thermal power, inlet and outlet temperatures, and total mass flow rates of 700-MW, 467 and 555 °C, and 54420 kg/s, respectively. It is demonstrated that the thermal efficiency is significantly improved by increasing the operating pressure on the s-CO_2 side. This optimization study leads to a reference design with a 20MPa operating pressure for an s-CO_2 power conversion loop, which is quite similar to the one in the direct cycle design. The operating conditions of the IHX are summarized in Table 7.

Table 5. Summary of the parameters for direct s-CO2 recompression Brayton cycle

Parameters	Design	
	Basic	Advanced
Cycle thermal power (MWth)	600	600
Thermal efficiency (%)	47.2	51.3
Net efficiency (%)	43.6	47.8
Compressor outlet pressure (MPa)	20	20
Pressure ratio	2.6	2.6
Turbine inlet temperature (°C)	550	650
Compressor inlet temperature (°C)	32	32
Cooling water inlet temperature (°C)	27	27
Total mass flow rate (kg/s)	3426	3027
Recompression fraction	0.41	0.41
Turbine efficiency (%)	94.2	94.2

Main compressor efficiency (%)	91.1	91.1
Recompression compressor efficiency (%)	90.5	90.5

Table 6. Summary of the operating conditions for helium-to-s-CO2 IHX/recuperators

HX type	Working fluid	Inlet temp. (°C)	Inlet pressure (MPa)	Outlet temp (°C)	Outlet pressure (MPa)
IHX	Helium	800.0	7	~502.0	/
	s-CO_2	488.8	19.922	650	19.792
Recuperator HT	Hot s-CO_2	534.3	8.039	165.8	7.878
	Cold s-CO_2	157.1	19.981	488.8	19.922
Recuperator LT	Hot s-CO_2	165.8	7.878	68.9	7.702
	Cold s-CO_2	61.1	20.0	157.1	19.981
Precooler	s-CO_2	68.9	7.702	32.0	7.692
	Water	27.0	0.1013	74.5	0.1013

Table 7. Summary of the operating conditions for lead alloy liquid salt-to-s-CO2 IHX

HX type	Working fluid	Inlet temp. (°C)	Inlet pressure (MPa)	Outlet temp (°C)	Outlet pressure (MPa)
IHX	Lead alloy	467.0	~0.5	555.0	~0.5
	s-CO_2	384.0	~20	530.0	~19.745

1.1.3 Summary of Experimental PCHE Work

The s-CO_2 PCHE design is based on past experimental work with s-CO2, PCHEs, and thermal stress analysis. The Ohio State University has had success fabricating diffusion-bonded PCHEs out of Alloy 617 for testing in their helium test facility (Mylavarapu, 2011), while the University of Wisconsin has experience with s-CO_2 heat transfer experiments (Kruizenga, 2010). Thermal stress experiments and analysis have also been performed for stainless steel PCHEs by France's CEA (Pra et al. 2008).

Helium Experiments at the Ohio State University

OSU (Mylavarapu, 2011) developed a high-temperature helium facility featuring two PCHEs, each diffusion-bonded out of 10 hot and 10 cold plates of Alloy 617. The plates were arranged in a counter flow configuration, featuring twelve 2 mm diameter semicircular channels per plate as shown in Figure 6.

Helium flow was varied from 85 to 390ºC /1.0 to 2.7 MPa on the cold side and 208 to 790ºC /1.0 to 2.7 MPa for the hot side, respectively, while the mass flow varied from 15 to 49 kg/h. The flow regime within the PCHE's straight channels extended from laminar to laminar-to-turbulent with Reynolds numbers of 950 to 4100 being realized on the cold side and 900 to 3900 on the hot side. Experimental values for the Fanning friction factor and Nusselt number were found to fit closely with circular pipe correlations, as shown in Figure 7.

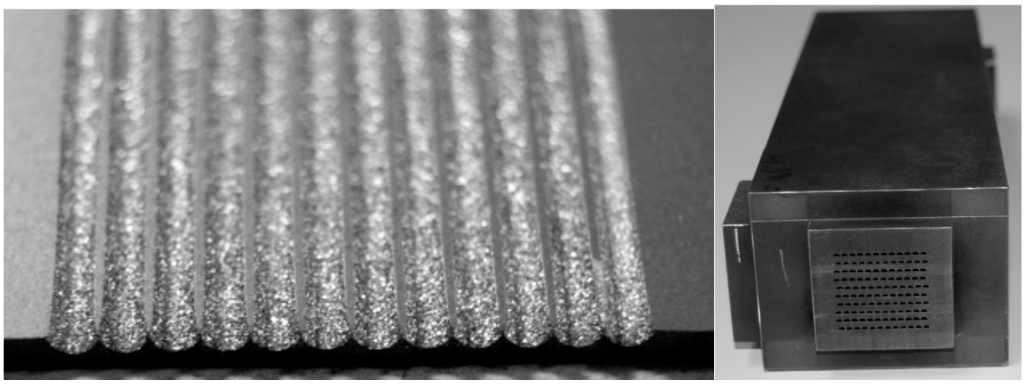

Figure 6. Ohio State's high temperature Helium PCHE was constructed with channels chemically etched into IN617 plate (left). The PCHE was diffusion-bonded out of 10 hot and 10 cold etched plates (right).

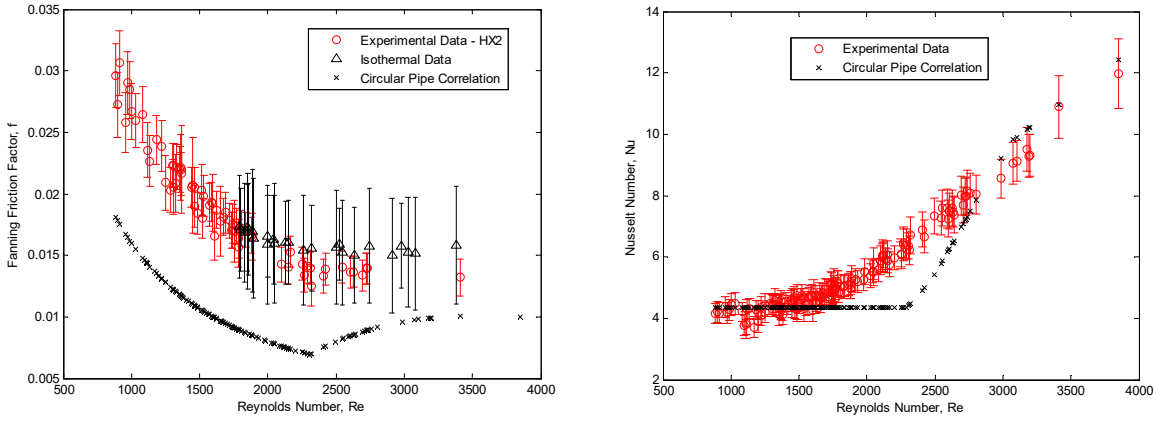

Figure 7. Performance of Ohio State's high temperature Helium PCHE. Experimental data for fanning friction factor (left) and Nusselt number (right) are compared with circular pipe correlations.

s-CO_2 Experiments at the University of Wisconsin

PCHE flow channel designs have been tested using s-CO_2 at the University of Wisconsin (Carlson, 2012). The system consisted of a single etched s-CO_2 flow channel. Heat flux across the channel walls was determined through measurements of the heat removed by

each of 20 cooling blocks that distributed the chilled water along both ends of the flow channel. Pressure differential was measured at the inlet and outlet of the channel.

A variety of flow channel geometries were used in an effort to increase heat transfer and reduce pressure losses. Channels investigated were two zigzag/wavy style channels and two patterned airfoil channels, as well as a traditional straight channel design. Zigzag channels tested featured 65° and 80° bends. Airfoil channels consisted of 4.0 mm and 8.1 mm long NACA0020 airfoils. Flow through all geometries covered a range of temperatures from approximately 25 to 100°C, pressures of 7.5 to 8.1 MPa, and mass fluxes of 326 to 762 kg/m^2-s. Channel geometries were compared on the basis of their Fanning friction factors and Nusselt numbers as shown in Figure 8.

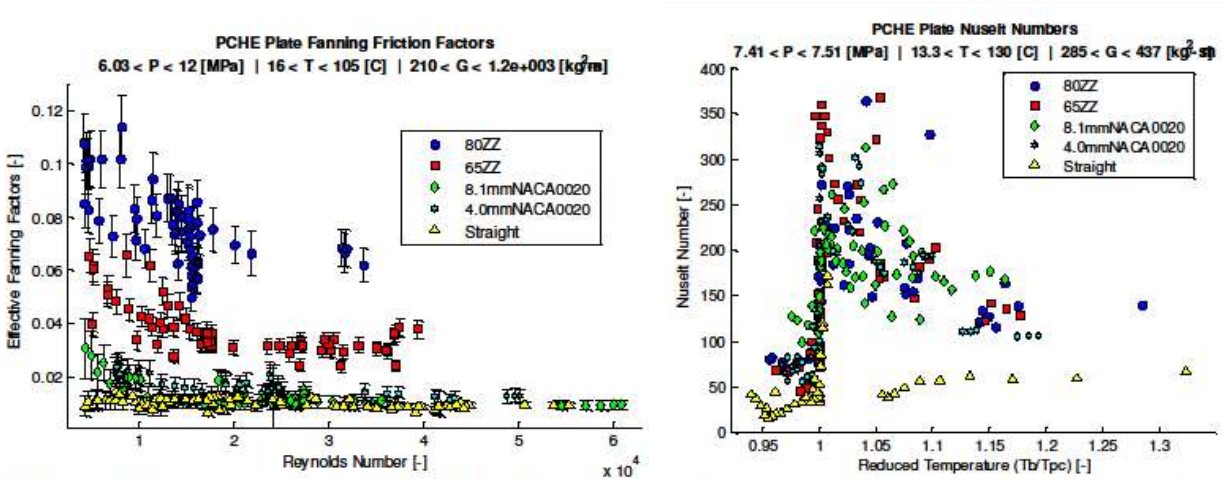

Figure 8. Performance of various flow channel geometries investigated at the University of Wisconsin. Fanning friction factors are compared for zigzag, airfoil, and straight channels (left). Nusselt numbers were investigated about the pseudo-critical point of s-CO_2 (right).

Thermal Stress Experiments

Some initial tests on thermal stress induced in PCHE's were conducted by Pra et al. (2008). In this study transient tests of a PCHE recuperator mock-up in an air test facility investigated its thermal and mechanical behavior at temperatures typical of a HTGR. Thermal shock tests were conducted by both rapidly raising and dropping PCHE temperature. Thermal shock was performed by raising the hot side inlet from 180 to 510°C in 120 seconds while cooling shock involved dropping the hot side inlet from 510 to 180°C in 5 seconds. Fatigue testing of the PCHE was achieved by alternating cold and hot shocks. The PCHE was loaded with 100 fatiguing cycles without noticeable failure.

Evaluation of stresses in the PCHE was provided by both direct measurement and through Finite Element analysis. Direct stress measurements were limited to five strain

gauges mounted on the exterior of the PCHE. These gauges recorded a peak inter plate stress of 375 MPa during fatigue testing. Using a finite element model, stresses internal to the PCHE were extrapolated from interior temperature measurements. The largest stress of 1024 MPa occurred during cold shock and was located between the zigzag channel section and outer metal wall near the hot inlet.

1.2 Design optimization of PCHEs for Helium-s-CO_2 IHX

1.2.1 Preliminary scoping of PCHE designs

A preliminary scoping study of helium-to-s-CO_2 IHX has been carried out, primarily focusing on the application of zigzag channels and S-shaped fin channels. The basic design methodology has been identified, as applied in the scoping of IHX using different combination of zigzag and S-shaped fin channels on hot and cold sides. A brief introduction to the design procedure is described as follows.

With available operating conditions of helium-to-s-CO_2 IHX from the previous literature review, the heat exchanger effectiveness ε, heat capacity ratio C^*, and corresponding number of heat transfer units NTU can be calculated,

$$\varepsilon = \frac{\dot{q}}{\dot{q}_{\max}} = \frac{\dot{q}}{C_{\min}\Delta T_{\max}} \tag{1.2.1}$$

$$C^* = \frac{C_{\min}}{C_{\max}} = \frac{(\dot{m}C_p)_{\min}}{(\dot{m}C_p)_{\max}} \tag{1.2.2}$$

$$\mathrm{NTU} = \frac{1}{1-C^*}\ln\left(\frac{1-C^*\varepsilon}{1-\varepsilon}\right) \tag{1.2.3}$$

where C_{min}, C_{max}, and ΔT_{max} are the minimum and maximum heat capacity, and the fluid inlet temperature difference, respectively. The primary procedure in this heat exchanger dimension scoping is to evaluate the core mass velocity or mass flux G, which is obtained as (Shah and Sekulic, 2003):

$$G = \left[\frac{2\rho_m}{\mathrm{Pr}^{2/3}}\cdot\frac{\Delta p}{\mathrm{NTU}}\cdot\left(\frac{j}{f}\right)\right]^{1/2} \tag{1.2.4}$$

This equation requires the knowledge of the ratio of the Colburn factor *j* and the fanning factor f. However, the ratio of j/f is a weak function of the Reynolds number, typically evaluated as the mean value of the entire range of possible Reynolds numbers in the

heat exchanger flow conditions. In this case, the evaluation of j/f based on laminar and turbulent flow correlations for zigzag channels and turbulent flow correlations for S-shaped fin channels has been carried out, of which the relations for turbulent flow of s-CO_2 side are shown in Figure 9. These evaluated values of j/f will be compared with the results from final scoping dimension. Additionally, the NTU of each side is evaluated with appropriate assumptions, considering the gas-to-gas countercurrent heat exchanger. The pressure drop in the equation is specified from design constraints, but due to the lack of relevant information, an assumption of specifying it to be 2% of the operating pressure has been made. This assumption is also needed to be validated with final scoping results.

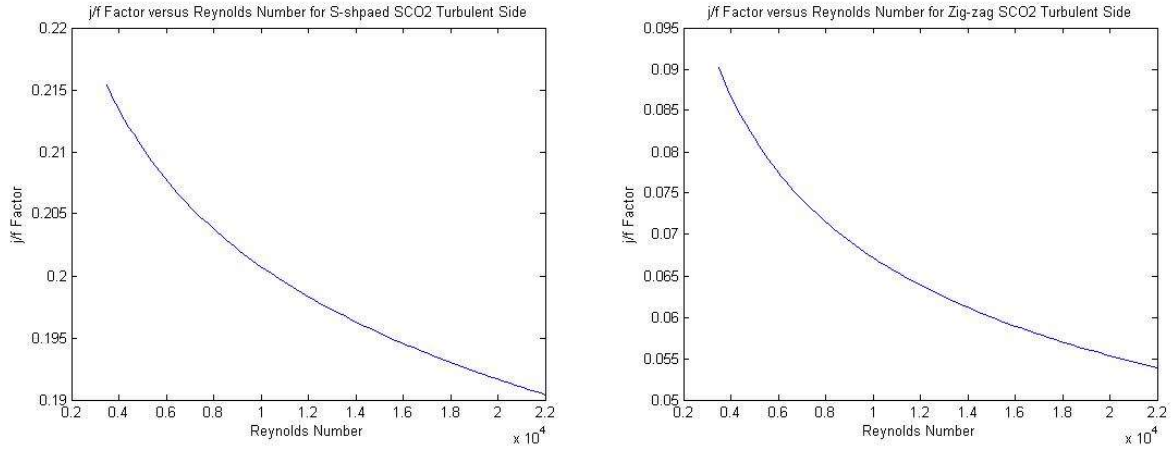

(a) (b)

Figure 9. j/f versus the Reynolds number for s-CO2 turbulent flow: (a) S-shaped fin channels and (b) zigzag channels

A Matlab code has been developed for the scoping study, since an iterative calculation is required. The heat exchanger length (either physical length in the case of S-shaped fins or flow channel length in the case of zigzag channels) can be computed based on the reference models' surface geometric characteristics. These reference models are essentially identical with the model for which correlations are developed. This is primarily because it has been shown that slight changes in surface geometry can yield appreciable differences in the correlations. This dependence of the choice of surface geometry on available experimental correlations may be overcome by using CFD simulations, which are however beyond the scope of the current design process. The calculated flow channel pressure drop based on the calculated heat exchanger length can be examined against the pressure drop design specification. In this process, the effect of variant properties of gas has been taken into account using property ratio method as shown in Eq. (1.2.5), where subscript cp means constant properties. The preliminary scoping results are summarized in Table 8. Note in the calculation of the heat exchanger active volume, the

assumption of a typical compact heat exchanger porosity 0.55 is made, which appears to be higher than the real situation because high pressure requirement at s-CO_2 side may lead to lower porosity value.

Table 8. Summary of preliminary scoping results for helium-to-s-CO2 IHX

#	Description	hot side Re	cold side Re	hot side pressure drop specified (kPa)	cold side pressure drop specified (kPa)	Hydraulic Diameter (mm)	hot side *j/f*	cold side *j/f*	HX active volume (m^3)	HX active core physical length (m)
1	zig 45 - zig 52	1458	28100	140	800	1.222	0.072	0.049	18.01	0.6169
2	ssh 52 - ssh 52	2440	65104	140	800	1.222	0.230	0.172	14.35	0.8214
3	zig 45 - ssh 52	1324	70295	140	800	1.222	0.073	0.171	18.05	0.7197
4	ssh 52 - zig 52	4968	22191	280	800	1.222	0.389	0.045	16.31	0.8494
5	zig 45 - zig 52	1475	19750	140	400	1.222	0.072	0.055	20.14	0.6059
6	ssh 52 - ssh 52	2498	43923	140	400	1.222	0.230	0.177	15.25	0.7918
7	zig 45 - ssh 52	1358	47567	140	400	1.222	0.073	0.176	18.29	0.6906
8	ssh 52 - zig 52	4768	15908	280	400	1.222	0.354	0.050	20.21	0.8243
9	zig 45 - zig 52	1217	15050	140	400	0.922	0.085	0.059	13.77	0.4375
10	ssh 52 - ssh 52	2716	31466	140	400	0.922	0.229	0.182	9.308	0.5934
11	zig 45 - ssh 52	1129	35121	140	400	0.922	0.086	0.180	12.15	0.4917
12	ssh 52 - zig 52	3643	12507	280	400	0.922	0.364	0.054	13.25	0.5587

$$\frac{Nu}{Nu_{cp}} = \left(\frac{T_w}{T_m}\right)^n, \frac{f}{f_{cp}} = \left(\frac{T_w}{T_m}\right)^m \tag{1.2.5}$$

In the scoping process, a stress analysis has been performed, mainly focusing on the zigzag semi-circular channels. Obviously, the major concerns about zigzag channels are centered on the *x*- and *y*-direction pitch (or the fin thickness and plate thickness). From literature review, it is suggested to use Eq. (1.2.6) for evaluation of the fin thickness t_f, i.e., the minimum distance between adjacent zigzag channels at any cross-section along the flow path:

$$t_f = \frac{1}{\left[\left(\sigma_D / \Delta p\right) + 1\right] N} = \frac{p_x}{\left(\sigma_D / \Delta p\right) + 1} \tag{1.2.6}$$

where σ_D, p_x and Δp are the stress, channel pitch and differential pressure between the hot and cold sides, respectively. Modifying this equation when that considering channel

pitch equals the sum of semi-circular channel diameter *d* and fin thickness, we can obtain following equation:

$$t_f = \left(\frac{\Delta p}{\sigma_D}\right) D \tag{1.2.7}$$

To determine the plate thickness t_p, a simplified approach that utilizes thick wall cylinder theory model is proposed. It is shown that the maximum stress occurs in the inner wall. Therefore, in this model we can simplify the original equation to:

$$\frac{r_o}{r_i} = \sqrt{\frac{p_i + \sigma_D}{\sigma_D + 2p_o - p_i}} \tag{1.2.8}$$

where r_o and r_i are the cylinder's inner and outer radii, respectively. For application to the plate thickness calculation, there are two models available to use Eq. (1.2.8). The first model treats the two vertical neighboring channels' curved and plain surface as the pressure boundaries and the mean wall thickness as the cylinder's wall thickness. The second model considers the plate thickness as the outer diameter of the thick walled cylinder, which appears to be more conservative than the first model. Preliminary calculation results show t_f and t_p to be 0.876 and 1.499 mm when 120% margin is considered.

1.2.2 Surface geometry selection based on cost assessment for s-CO_2 SHX

A PCHE surface geometry selection study based on a cost assessment, including initial capital cost and annual operating cost has been performed to determine the most cost-effective surface geometry using currently available heat transfer and pressure drop correlations before in-depth parametric studies on specific heat exchanger designs. From a literature review, it is shown that surface geometry with desired thermal hydraulic characteristics may not usually become the most promising candidate in the heat exchanger selection if the total cost issued as the selection criterion. For example, Yoon et al. (2014) performed a cost analysis for the PCHEs of four types of surface geometry for application in HTGRs and SFRs. It is claimed that at laminar operating conditions the zigzag channel type PCHE is the most cost-effective as a He-He IHX in HTGRs, whereas at turbulent operation condition the straight type PCHE keeps the lowest cost as a sodium-to-s-CO_2 IHX in SFRs. This result was out of expectation since conventionally the new surface designs (S-shaped and airfoil fins) are believed to be superior to zigzag or straight semi-circular channels because of their outstanding thermal hydraulic performance. Therefore, the study on cost-based surface geometry selection is

necessary. Currently a surface geometry selection based on cost assessment for s-CO_2 secondary heat exchanger (SHX) has been initiated, in which off-set strip fin (OSF) PCHE is also included. This can provide some insight in surface geometry selection for s-CO_2 IHX.

A 20-MW FLiNaK-s-CO_2 SHX in the Advanced High-Temperature Reactors has been identified as the main SHXs of interest for this study. The detailed operating conditions are summarized in Table 9. The candidate PCHEs of various kinds of surface geometries for both sides have been identified: straight, S-shape, OSF, and zigzag 52° channels for s-CO_2 side and straight, zigzag 15°, rectangle OSF 7.565 mm, and rectangle OSF 2.40 mm channels for FLiNaK side. Both single and double banking configurations of PCHE are taken into account. The model of each surface geometry is specifically designed considering mechanical stress requirement and corrosion margins. A FLiNaK Reynolds number-based cost-optimization procedure has been developed as shown in Figure 10.

Table 9. 20 MW SHX operating conditions (Sabharwall et al., 2011)

SHX	T_{in} (°C)	T_{out} (°C)	p (MPa)	Mass flow rate (kg/s)
FLiNaK	676.2	575.0	0.153	102.2
s-CO_2	494.0	651.2	20.8	102.2

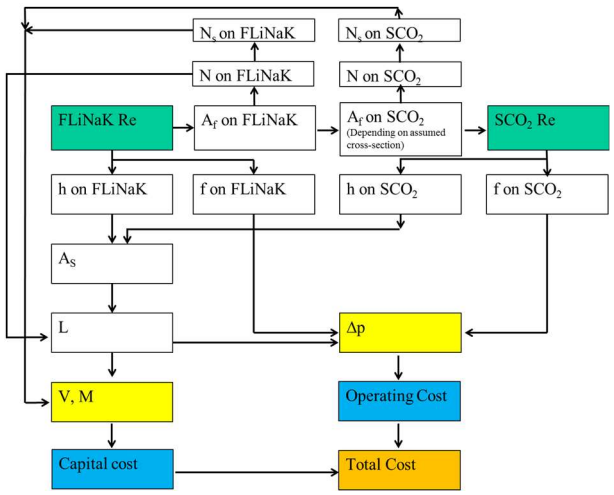

Figure 10. Iteration process to determine an optimized PCHE design based on varying Reynolds number at FLiNaK side

The cost assessment model used here refers to Kim and No (2012). According to their cost analysis model, the total cost C_t consists of the capital cost C_{cp} and operating cost C_o,

$$C_t = C_{cp} + C_o \tag{1.2.9}$$

where the capital cost has been simplified to only account for material cost excluding any other fabrication cost, labor cost, etc. The capital cost is proportional to the heat exchanger active core volume. The unit of the capital cost C_M ($) has to be identical with the unit of the operating cost ($/y). Therefore, the capital cost is converted to the payback cost assuming a 5% interest and a 30 year payback period. Note that C_M = 150 $/kg for Alloy 800 HT.

$$C_c = C_M M = C_M \rho_M V \tag{1.2.10}$$

$$C_{cp} = \frac{C_c r(1+IR)^n}{\left[(1+IR)^n - 1\right]} \tag{1.2.11}$$

In the operating cost estimation, the pumping power W_p calculated from Eq. (1.2.12) can be converted to the operating cost ($/y) by multiplying the electricity cost rate C_E ($/Wh) (in Eq. (1.2.13)), which is 0.0987 $/kWh (EIA, 2012), i = 1 is for FLiNaK side, and i = 2 is for the s-CO_2 side. This total cost estimation process is iterated with the FLiNaK Reynolds number varying from 100 to 600 to determine the optimized flow condition.

$$W_p = \Delta p \frac{\dot{m}}{\rho} \tag{1.2.12}$$

$$C_o = C_E \sum_{i=1}^{2} W_{pi} \tag{1.2.13}$$

The calculations show that with the single banking configuration, on the s-CO_2 side straight channels have the smallest Fanning factor followed by the S-shaped fin, OSF 7.565 mm, OSF 2.40 mm, and zigzag 52°. However, in terms of the Nusselt number, it is shown that zigzag 52° channels have the largest value, followed by the rest of them in the exactly opposite order for the Fanning factor. These results are shown in Figure 11 and Figure 16.

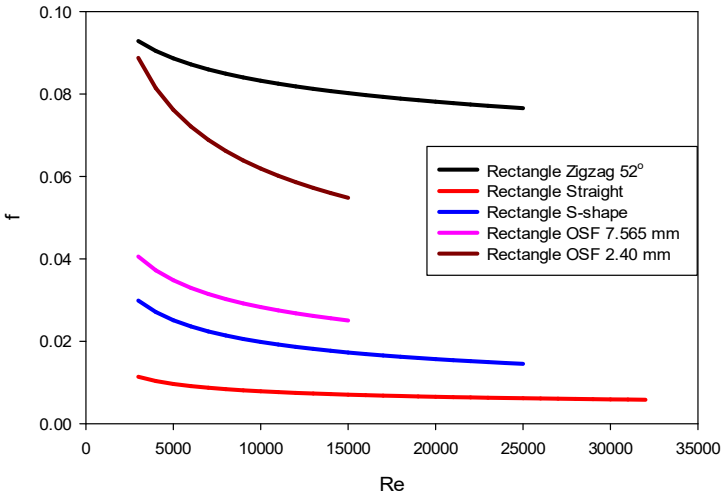

Figure 11. Fanning factor vs. Re for s-CO2 single banking configuration

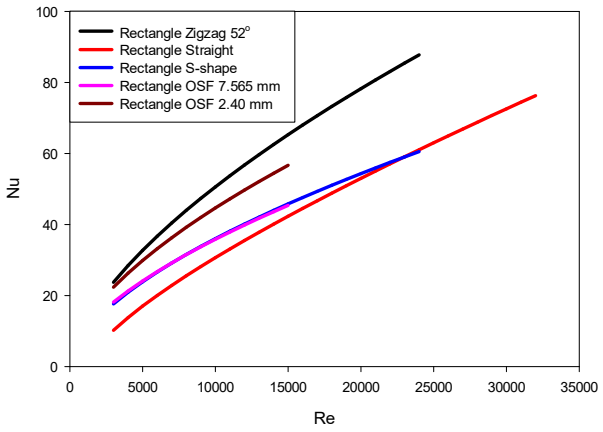

Figure 12. Nusselt number vs. Re for s-CO2 single banking configuration

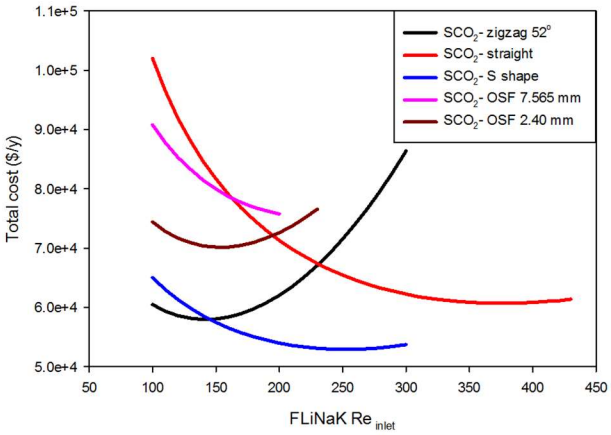

Figure 13. Total cost vs. Re for s-CO2 single banking configuration

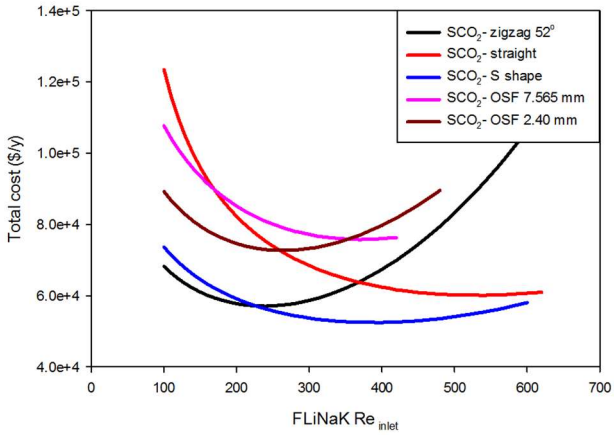

Figure 14. Total cost vs. Re for s-CO2 double banking configuration

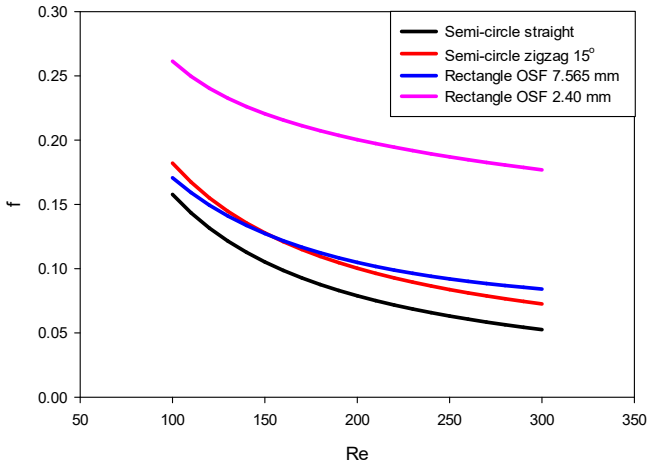

Figure 15. Fanning factor vs. Re for FLiNaK single banking configuration

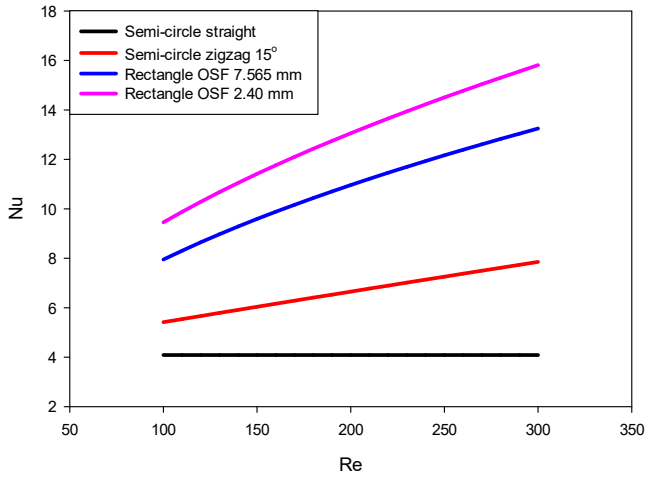

Figure 16. Nusselt number vs. Re for FLiNaK single banking configuration

The total cost analysis results show that in the s-CO_2 single banking configuration, the S-shaped fins yield the lowest total cost, followed by the zigzag 52° and straight channels options. Meanwhile, in the double banking configuration, the S-shaped fins also become the most cost effective option among others, with the second and third options being the same as those in the single banking configuration. The total cost comparison for different surface geometry options are presented in Figure 13 and Figure 14.

As to the FLiNaK side optimization, the calculation results show that the semi-circular straight channels have the smallest Fanning factor, with zigzag 15°, rectangular OSF 7.565 mm and rectangular OSF 2.40 mm in the increasing order of the value of Fanning factor. The Nusselt number, however, is the largest in the rectangular OSF 2.40 mm with the rest of them in the exact opposite order of the previous one. The calculation results are presented in Figures 14 and 15. In terms of the surface area per unit length for each type of the surface geometry, the OSF 2.40 mm surface is the most promising.

Based on above analysis, the OSF 2.40 mm surface for FLiNaK and the S-shaped fin surface for s-CO_2 have been proposed for 20 MW FLiNaK-s-CO_2 SHX in AHTRs. From the above cost analysis it can be concluded that S-shaped fins have the highest potential to effectively reduce the total cost of heat exchanger construction and operation in the applications involving s-CO_2 power conversion systems. This study can justify the preference towards the S-shaped fins in the cost-oriented heat exchanger design optimization, at least in the case of 20 MW FLiNaK-s-CO_2 SHX study.

1.2.3 Review of PCHE optimum sizing and economic assessment

Compact heat exchanger optimum sizing primarily based on cost analysis has attracted considerable attention in the community. Gezelius (2004) has addressed compact intermediate heat exchanger optimum design using Heatric-manufactured zigzag type PCHEs, where both the heat exchanger material cost and system cycle efficiency have been taken into account. Kim, et al., (2008b) have developed a simplified optimum sizing model for zigzag channel PCHEs from the economics point of view. Based on a capital and operating cost model, it has been shown that with reference geometric parameter input, such as the channel diameter, the capital cost increases with the flow area whereas the operating cost decreases exponentially with increasing the flow area. Figure 17shows how the cost changes with varying the flow area. It is observed that the total cost will increase dramatically when the flow area becomes smaller than the intersection point of the capital and operating cost curves. Thus the minimum allowable flow area point is defined to that intersection point. Additionally, it has been revealed that the reference PCHE design may require incredibly large aspect ratio (i.e., heat exchanger height versus length) with an optimum flow area that is determined based on the total cost curve. This fact indicates that almost 200 modules are needed and such a design induces serious thermal and mechanical problems, such as the thermal stress in the parallel modules configuration and manifolding difficulties. Therefore, the channel diameter was increased to achieve acceptable heat exchanger size with affordable additional total cost, and the recommended channel diameter for the IHX of a thermal duty at 600 MWt is below 5.0 mm. This finding implies that the channel diameter plays an important role in determining practical PCHE size. Nevertheless, this study is based on a few particular zigzag channel surface characteristics (only channel the diameter and the longitudinal pitch), and fails to discuss about the effect of channel angle, which greatly contributes to the thermal-hydraulic performance of micro-channels.

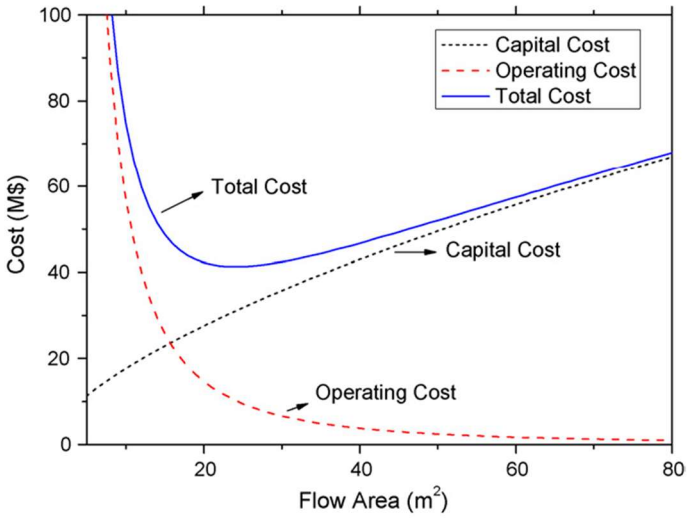

Figure 17. Optimum flow area for a reference IHX (Kim, 2008b)

To make assessment of the PCHE's cost for different geometries applied in both HTGRs (high-temperature gas-cooled reactors) and SFRs (sodium-cooled fast reactors), Yoon, et al., (2014) have investigated the relationship between the module number of PCHEs and total cost based on the similar cost model discussed earlier. Using reference PCHE surface geometric characteristics and heat exchanger dimensions, they obtained the optimized heat exchanger length and the least number of modules required to satisfy the specified heat transfer capacity. Based on that optimized heat exchanger size (that is, the optimized length), the relationship between the increasing number of modules and the corresponding total cost was established. The comparison among different geometries, including straight channel, zigzag channels with angle varying from 5° to 45° and airfoils has been made. It has been concluded that although airfoil channels exhibit better thermal performance, that is, higher overall heat transfer coefficient, for HTGRs' application they are not highly competitive compared with the zigzag channels in terms of the total cost at a particular module number. A similar trend was observed in the SFR case. It was then recommended that the zigzag PCHEs are the most proper heat exchanger type for helium-helium IHXs in HTGRs, which is typically operated in laminar conditions while the straight PCHEs are the most preferred for sodium-s-CO_2 IHXs in SFRs, which is typically operated in turbulent conditions. This conclusion is mainly concerned with the assessment of different geometries (including different angles of zigzag channels) of PCHE micro-channels (in fact, due to lack of correlations for S-shaped fin channels, this type of surface geometry is excluded) in terms of the total cost. It has for the first time provided a view of the economic competitiveness of all of existing surface geometries. However, the paper fails to address the effect of some other surface characteristic

parameters, for instance, the hydraulic diameter and zigzag longitudinal pitch, etc., on the economics assessment of different surface geometries.

Both of the studies mentioned above have involved the modeling of cost analysis, the discussion of some geometric parameters and heat exchanger sizing aspect. As to the sizing aspect, the flow area is corresponding to the required module number. Given a heat exchanger sizing problem with prescribed operating conditions, surface characteristics, the heat exchanger dimension (assumed to be determined by flow area A_c and heat exchanger physical length L) and corresponding total cost are closely related. Therefore, in the design optimization, with the full knowledge of correlations for heat transfer coefficient and pressure drop, we can then define the surface characteristic parameters as design variables and the total cost as objective function. After defining the design space, we can obtain the optimized design points by adopting genetic algorithm. The genetic algorithm is a search heuristic in computer science that is inspired by natural selection. This algorithm can expedite the searching of optimized points for non-linear problem, in this case, the relatively smaller total cost. However, in practice we are concerned with not only the total cost of a heat exchanger, but also the thermal-hydraulic aspect, such as heat exchanger effectiveness. Therefore, an improved approach to attain multi-objective optimization might be introduced for the current research purpose.

Sanaye et al. (2009) and Lee et al. (2013) are those among others who employ multi-objective optimization method in the field of heat exchanger design. Sanaye et al. established a correlation-based cost analysis model for plate-fin heat exchanger design optimization considering thermal effectiveness of heat exchanger simultaneously. The plate-fin heat exchanger correlations of the Colburn factor j and Fanning factor f contain surface geometric parameters, which are considered to be the design variables. This essentially facilitates the process of optimization since the objective functions can be directly modeled with the design variables. In other words, an explicit mathematical function can be modeled as the objective function. Their cost model is slightly different from the one used, but the principal concept is quite similar, i.e., the total cost consisting of the capital and operating costs. The specific function developed is not necessarily applied to the PCHE design, but the ε-NTU method that was introduced in their study was used in current research. In the algorithm development, in order to obtain Pareto-optimal points (or unbiased optimal points), a fast and elitist non-dominated sorting genetic-algorithm (NSGA-II) is applied to get the maximum effectiveness and minimum total cost. The solutions are clustered as a Pareto-optimal front, which consists of all design points that non-dominating in terms of two objective functions. With regard to how to select design points as final optimization results, a sensitivity study was proposed.

Moreover, Lee et al. (2013) have adopted a multi-objective optimization method using the genetic algorithm to deal with a double-faced type PCHE of zigzag channels. The reference zigzag type PCHE was based on Ishizuka experiment (2005). The objective functions were chosen to be the effectiveness and non-dimensional pressure drop while design variables were A/D_h, L/D_h and B/D_h of which the definitions are shown in Figure 18. These three design variables sufficiently describe the zigzag type channel surface geometric characteristics. However, whether to take the corner roundness into account is questionable. There were no physical or correlation-based modeling involved in the optimization. Instead, several engineering techniques, as follows, were adopted to establish the objective function and design space for the design variables. Firstly, 20 design points were generated using LHS (Latin hypercube sampling). Next, the corresponding evaluation of objective functions' values were then obtained by constructed mathematical functions, which are based on RANS analysis (Reynolds-Averaged Navier-Stokes analysis) validated by CFD simulations for reference cases. Based on these 20 design points, a RSA (response surface approximation) model is used to construct a pool of surrogate design points, which constitute the design space for later genetic algorithm calculation. Again NSGA-II method is used to obtain the Pareto-optimal solutions. The two branches of multi-objective functions compete with each other, thus the Pareto-optimal front shown in Figure 19 resemble a concave curve. Finally, K-means clustering is used to group the global Pareto-optimal solutions to user-defined clusters. The procedures of this optimization involve a lot of mathematical and statistical techniques to reduce either experimental or numerical efforts. However, the RANS is not able to directly give mathematical functions for the total cost, which is the primary interest in our PCHE design optimization. The uncertainty, especially as to the fidelity of the surrogate design points, is necessary to measure and control.

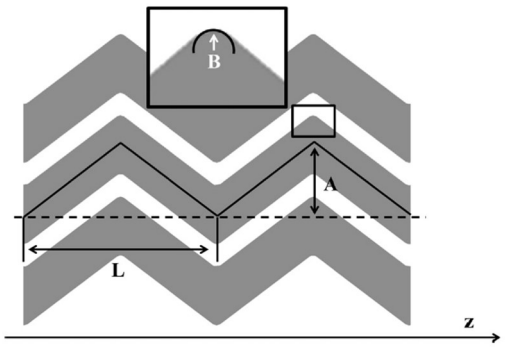

Figure 18. Definition of zigzag channel surface geometric parameters (Lee et al. 2013)

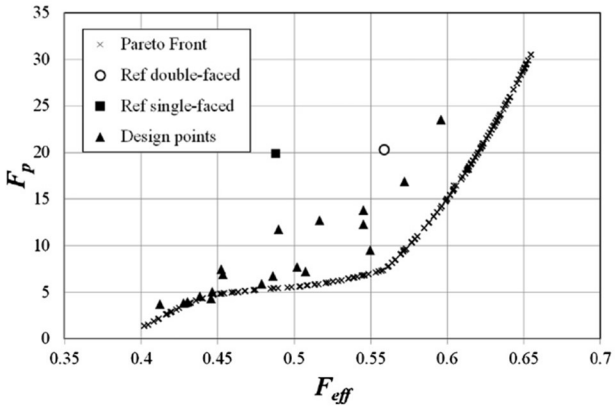

Figure 19. Objective function values corresponding to Pareto-optimal front and reference cases (Lee et al., 2013)

Kim et al. (2012) have developed Nusselt and Fanning factor correlations parametrically depending upon the zigzag channel angles, hydraulic diameter and longitudinal pitch numerically for zigzag type PCHEs in helium application. Based on these available correlations that are developed numerically, it is possible to develop new correlations containing these surface geometric parameters. In addition, it is straightforward to develop a cost analysis model based on the correlations. In addition, the effectiveness versus total annual cost being objective functions is reasonable. Therefore, the optimization design for the zigzag channels can be completed with a few CFD simulations required. With respect to S-shaped fin PCHE design optimization, it is recommended to follow Lee's approach to first set up surrogate data mathematically and then to use CFD analysis for validation.

1.2.4 PCHE IHX design optimization methodology

Correlations Development

Kim et al. (2012) have developed correlations for predicting the Fanning friction factor and Nusselt number for zigzag type PCHEs. These correlations (referred to numerically-developed or original correlations) are in the form as shown below

$$f \cdot \mathrm{Re} = 15.78 + a \cdot \mathrm{Re}^{b} \tag{1.2.14}$$

$$\mathrm{Nu} = 4.089 + c \cdot \mathrm{Re}^{d} \tag{1.2.15}$$

The parameters *a,b,c,d* in these correlations are dependent upon the surface characteristics of zigzag channels. In their study, three primary surface characteristic parameters have been identified, i.e. the zigzag channel angle ϕ, hydraulic diameter d_h and longitudinal pitch p_l. Figure 20 has defined these geometric parameters. Correlations

have been developed numerically based on each combination of nine angles, two hydraulic diameters and two pitches. Some of them have been listed in Table 10. The selected angles vary from 5° to 45°. The hydraulic diameters of 0.922 and 1.222 mm as well as the pitch of 12.3 and 24.6 mm have also been selected.

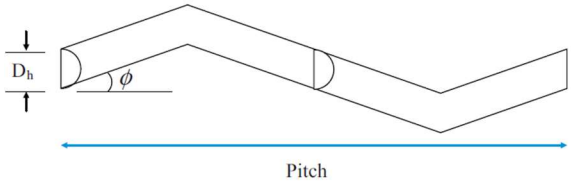

Figure 20. The geometry of a zigzag channel

Table 10. The parameters in the newly-developed and original correlations for 6 cases

Case #		a	b	c	d	d_h/mm	angle/°	pitch/mm
1	Original	0.29342	0.78118	n/a	n/a	0.922	35	24.6
	New	0.3022	0.7832	n/a	n/a			
2	Original	0.46869	0.78205	n/a	n/a	1.222	40	24.6
	New	0.4430	0.7803	n/a	n/a			
3	Original	0.19392	0.82838	n/a	n/a	0.922	25	12.3
	New	0.1850	0.8284	n/a	n/a			
4	Original	n/a	n/a	0.01877	0.78945	0.922	30	24.6
	New	n/a	n/a	0.0185	0.7876			
5	Original	n/a	n/a	0.06368	0.68516	0.922	45	12.3
	New	n/a	n/a	0.0669	0.6882			
6	Original	n/a	n/a	0.02182	0.77285	1.222	25	24.6
	New	n/a	n/a	0.0249	0.7680			

The numerically-developed correlations indicate increased Fanning factor and Nusselt number compared with plain straight channel. In general, the pressure drop increases dramatically with the large angle of a zigzag channel. Especially for the zigzag channel of the 45° angle, the Fanning factor is almost 100 times to the one in a straight channel. This probably results from the absence of the rounding of the channel bends in the CFD models that were used to develop correlations. In real life the rounding of the channel bends will be formed by chemical etching on the plates either on purpose or unintentionally. From the summarization of previous studies on pipe-bends effect on pressure drop, it has confirmed that these bends will significantly reduce the form loss of the bends. These trends suggest the consideration of channel rounding effect in PCHE designs rather than only relying on the by-product rounding of etching in fabrications

(Carlson, 2012). Therefore, the extremely large Fanning factors in large-channel-angle cases can be explained by the numerical modelling of CFD simulations during correlation development. This fact may potentially affect the IHX design optimization result. However, due to the limited correlations available for the design optimization, these numerically-developed correlations were still be used in this study.

Since the parameters in the original correlations highly depend upon surface characteristic parameters, it is necessary to develop new correlations (referred to newly-developed or predicted correlations) that are directly correlated with the surface characteristic parameters. In the development of new geometry-based correlations, it was found that it was fairly difficult to correlate angles below 25°. Thus the angles to be correlated were reduced to those above 25°. This would also affect the optimization result because unnecessary constraints would be imposed on the searching space, then further affecting the population of feasible solutions to be considered in optimization. Additionally, correlations with only two hydraulic diameters and two pitches are not sufficient to develop correlations that can be generally used. This also restricts the applicability of newly-developed correlations, and it is risky to extend the range of the parameters in the correlations.

Although there are several restrictions for the new developed correlations, they are still better tools in optimizing the IHX design than to compare different designs parametrically. In the predicted correlations a new non-dimensional parameter was introduced, defined as

$$\gamma = \frac{p_l}{2D_h} \tag{1.2.16}$$

The predicted correlations for four original parameters are shown as follows

$$a = A_1 \gamma^{-0.3} \ln(1.0312 - 0.0314 \sec\phi) \tag{1.2.17}$$

$$\begin{cases} B_1 = -0.0061\gamma^2 + 0.171\gamma - 0.8134 \\ B_2 = 0.0041\gamma^2 - 0.1325\gamma + 0.5855 \\ b = \left[B_1 \left(\sec\phi - 1 \right)^2 + B_2 \left(\sec\phi - 1 \right) + 1.181 \right]^{\frac{\cos\phi}{0.0569\gamma}} \end{cases} \tag{1.2.18}$$

$$\begin{cases} C_1 = -0.013\gamma^2 + 0.4395\gamma - 4.817 \\ c = 0.02 \exp\left\{ 2.02 - C_1 \left(\sec\phi - 1.6717 \right) \right\} - 0.0002\gamma^{2.2} \end{cases} \tag{1.2.19}$$

$$\begin{cases} D_1 = 0.0071\gamma^2 - 0.0915\gamma + 0.8157 \\ d = \gamma^{-0.2}\left[0.7918 - D_2\left(\sin\phi - 1.1179\right)\right] \end{cases} \tag{1.2.20}$$

To validate weather these newly-developed correlations are capable of predicting Fanning factor and Nusselt number accurately compared with original ones, 6 cases have been studied, listed in Table 10. Figure 21 through Figure 32 have compared both of the correlations against Reynolds number and shown the deviation of new correlation from original ones. It can be observed that except case #6 the prediction of new correlations falls within ±5% deviation of those of original correlations. Even for the last case, the prediction falls within ±10% deviation. In some sense, for Nusselt number the deviation around ±10% is still acceptable.

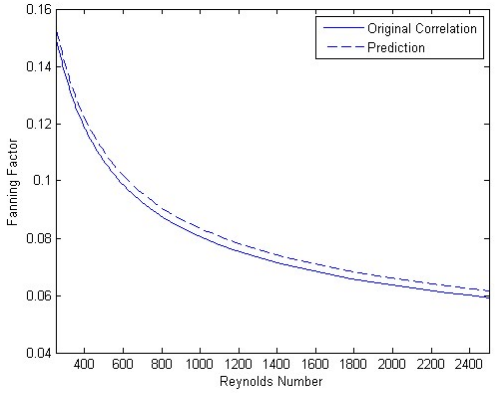

Figure 21. The comparison of the original and newly-developed correlations for Fanning factor versus Reynolds number in Case #1

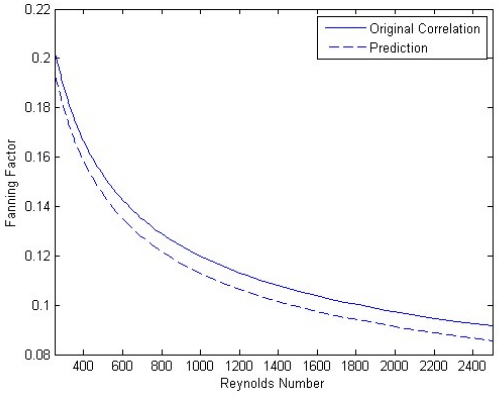

Figure 22. The deviation of the newly-developed correlation for Fanning factor from the original one in Case #2

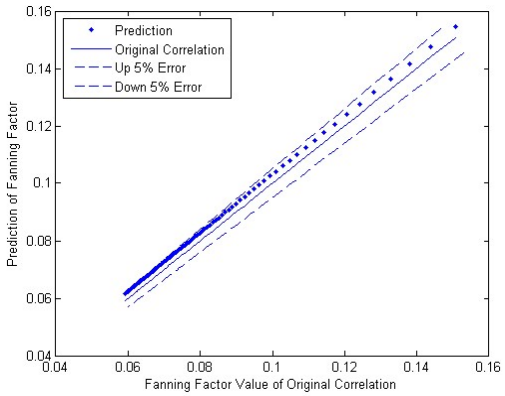

Figure 23. The deviation of the newly-developed correlation for Fanning factor from the original one in Case #1

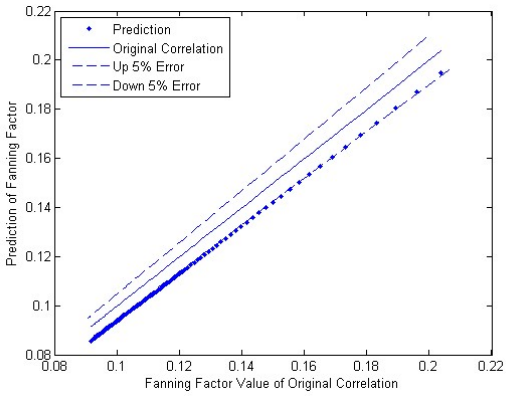

Figure 24. The comparison of the original and newly-developed correlations for Fanning factor versus Reynolds number in Case #2

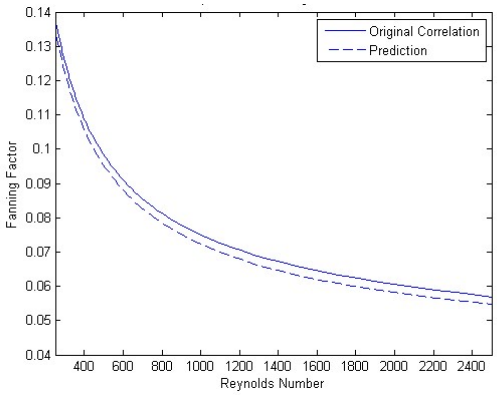

Figure 25. The comparison of the original and newly-developed correlations for Nusselt number versus Reynolds number in Case #3

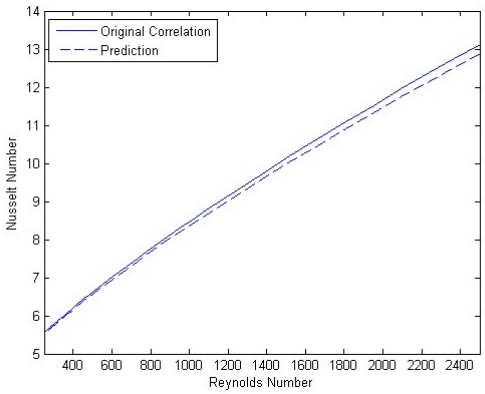

Figure 26. The comparison of the original and newly-developed correlations for Nusselt number versus Reynolds number in Case #4

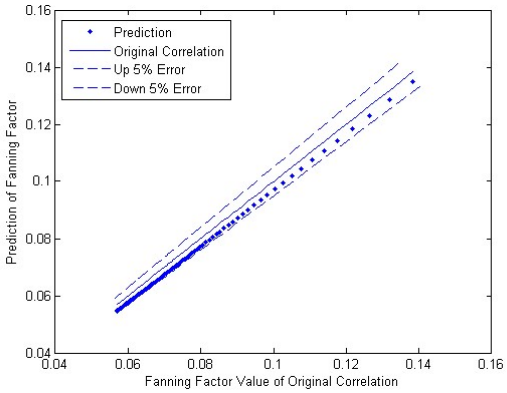

Figure 27. The deviation of the newly-developed correlation for Fanning factor from the original one in Case #3

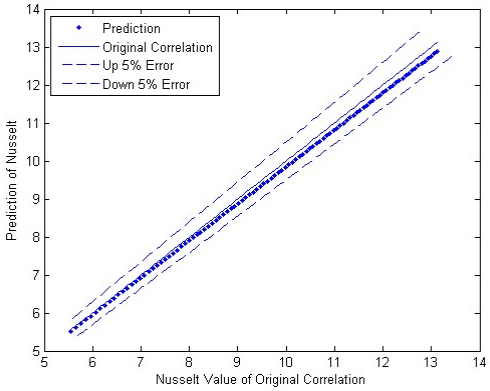

Figure 28. The deviation of the newly-developed correlation for Fanning factor from the original one in Case #4

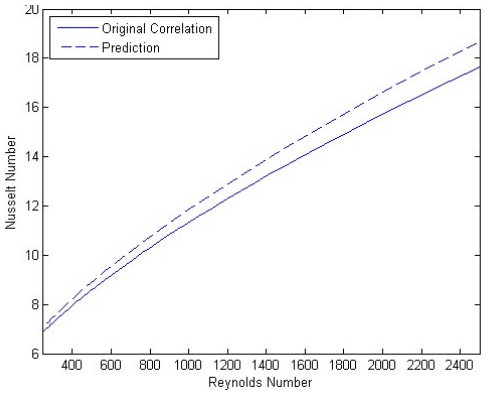

Figure 29. The comparison of the original and newly-developed correlations for Nusselt number versus Reynolds number in Case #5

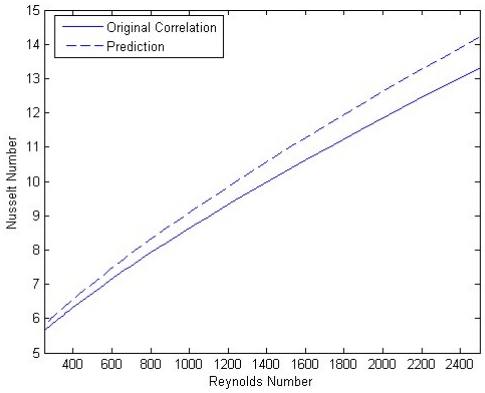

Figure 30. The comparison of the original and newly-developed correlations for Nusselt number versus Reynolds number in Case #6

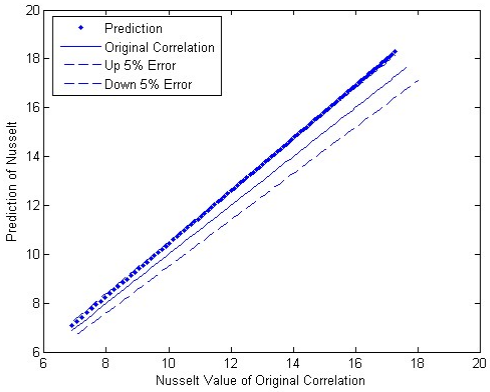

Figure 31. The deviation of the newly-developed correlation for Fanning factor from the original one in Case #5

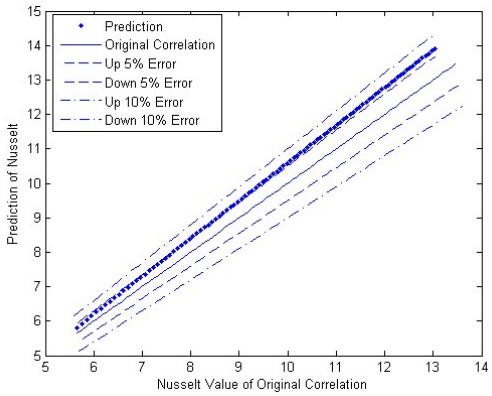

Figure 32. The deviation of the newly-developed correlation for Fanning factor from the original one in Case #6

The application of Genetic Algorithm in the multi-objective optimization

Generally, for multi-objective optimization problems, the objectives are usually conflicting, preventing simultaneous optimization of each objective. For real engineering problems, the minimization of cost and maximization of performance are some of the realistic but also difficult optimization objectives. In the PCHE IHX design optimization, the total cost, which consists of the capital cost on material investment and the operating cost, and the thermal performance of a heat exchanger has been identified as two objectives to be optimized. These two objectives have been studied in some of the compact heat exchanger design problems (e.g. Sanaye, et al., 2009 and Lee, et al., 2013) and were found in trade-off relationships. This justifies that the IHX design can be optimized using Multi-objective Optimization Evolutionary Algorithms (MOEA), which are characterized by the capability in solving optimization problems with multiple conflicting objectives.

One of the Evolutionary Algorithms (EA) is the Genetic Algorithm (GA). GA is a search meta-heuristic that mimics the process of natural selection. GA is widely used for optimization and search problems, especially powerful when dealing with a large population of feasible solution. Deb (2002) developed a fast and elitist non-dominated sorting genetic algorithm (NSGA-II) for multi-objective optimization problems. Traditionally, the multi-objective problem is converted to a single-objective problem by combining the individual objective functions into a single composite one. The single-objective optimization can be achieved by methods such as weighted sum method, but those methods highly depend on the correct selections of the weighting functions, which are actually very difficult to determine accurately. On the other hand, NSGA-II is capable of searching optimal solutions without introducing any subjective functions or parameters. Here only two-objective optimization problems are considered. Since two objectives are conflicting with each other, some of the optimal solutions may not be better than others

in terms of both objective functions. That is to say, these optimal solutions will not dominate each other. In fact, these optimal solutions form a non-dominated set called Pareto-optimal set. In the Pareto-optimal set, all solutions are non-dominated with respect to each other. In a two-objective optimization problem where both objectives are preferred to be minimized, a Pareto-optimal set is a somewhat convex front of all solutions on the graph (sometimes it can be of concave shape). NSGA-II is capable of searching a global Pareto-optimal front that contains well-distributed optimal solutions. In the IHX design optimization problem, the total cost and IHX thermal effectiveness were selected as objective functions. Therefore, the goal of the design optimization was converted to be the searching of a Pareto-optimal front of a cost-versus-100%-minus-effectiveness problem. Note that the heat exchanger effectiveness is to be maximized, thus 100%-minus-effectiveness was selected as the objective function instead such that the optimization problem becomes the one of minimize-minimize type.

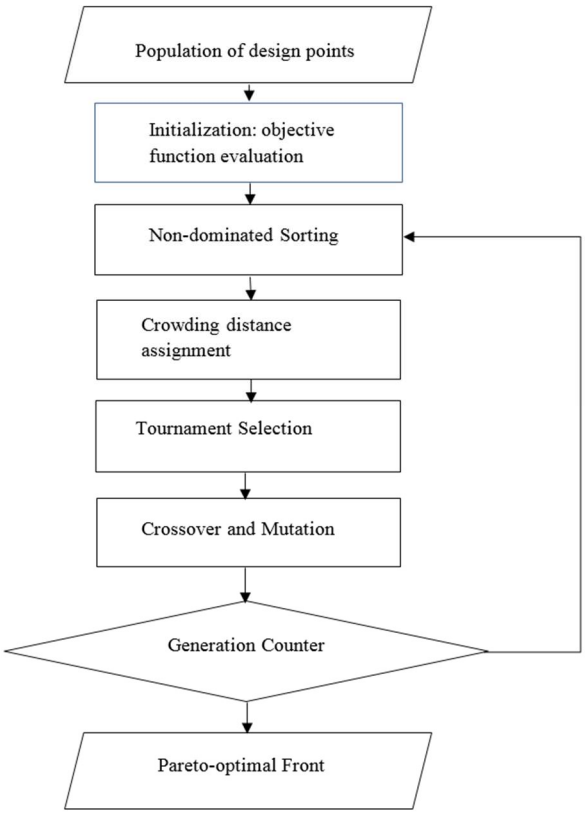

Figure 33. The flowchart of the NSGA-II code

A Matlab code was developed to perform NSGA-II. A flowchart graph in Figure 33 has shown the structure of the NSGA-II code. This code can search and obtain a well-distributed global Pareto-optimal front in a reasonable amount of computational time. Note that only two objective functions can be input simultaneously. There are three major

parameters to be used throughout the entire code calculation, the population size, the binary-coded chromosome size and the generation number. In the code each individual solution in the searching space is referred to a chromosome in the GA, which is usually binary-coded. The population size is given to define the number of chromosome solutions. The chromosome size is given to define the number of digits that are used to represent the real parameters and the generation number is given to define the number of calculation the code will conduct to find optimized results. Regarding the structure of the NSGA-II code, it primarily consists of three modules. The first is the non-dominated sorting module. It assigns a ranking number to each member of the population set in one particular generation based on the evaluated value of two objective functions. The ranking number is associated with the non-dominated front that each member belongs to. The non-dominated front with the lowest rank is first to be sorted out. The non-dominated front with the second lowest rank is to be sorted out afterwards, and so on. The rank of each front serves as a fitness number used in one of the next modules called reproduction module. It is obvious that all of members in the first front are the 'desired' solutions because they dominate, or, in other words, are better than, all of members in the rest of the fronts. Therefore, this front can be treated as a local Pareto front. The second module is the crowding distance assignment module. This module provides a niched-distance measure that is used in the reproduction module. The main purpose is to maintain the diversity of solutions in the next generation. Basically, it estimates half of the perimeter of the maximum hypercube that can be allowed around a solution without including any other solution in the same non-dominated front inside the hypercube. Obviously, a large crowding distance indicates that the solution is less crowded. The third module is the reproduction module, which employs constrained crowded tournament selection, uniform crossover and point-wise mutation. Firstly, in tournament selection two solutions are selected randomly for comparison. Then the solution with low rank will win, or the one with larger crowding distance will win if the ranks are identical. This ensures that local Pareto-optimal solutions will survive to reproduce their genes to the next generation, and these solutions will be finely spread out as well. Moreover, the crossover and mutation is based on binary-coded chromosome of each solution.

A simple commonly-used test problem was used to verify the NSGA-II code. The most studied single-variable test problem is Schaffer's two-objective problem (Dev, 2001) as described below

$$\begin{cases} Minimize: f_1(x) = x^2; \\ Minimize: f_2(x) = (x-2)^2; \\ -A \le x \le A. \end{cases} \tag{1.2.21}$$

The Pareto-optimal solution is known as $0 \le x^* \le 2$, and the Pareto-optimal set is a convex set:

$$f_2^* = \left(\sqrt{f_1^*} - 2\right)^2 \tag{1.2.22}$$

which is in the range of $0 \le f_1^* \le 4$. Figure 34 shows the Pareto-optimal front of the test problem. In the test, A is selected to be 10, and the population size, binary-coded chromosome size and generation are set up as 200, 13 and 200, respectively. Figure 35 and Figure 36 shows the initial population of solutions and the obtained Pareto-optimal front. The corresponding clustered solutions are also marked in the graph. These solutions are clustered using a clustering technique similar to the one used in the Strength Pareto Evolutionary Algorithm (Zitzler, 1999). It is observed that the solutions quickly converge to the global Pareto-optimal front, but the solutions are spread out after a number of generations. This is primarily due to the relatively small crossover pick-up parameter, which will results in more generations required to generate other non-dominated solutions that are less crowded. After all, the well-distributed clustered solutions imply that not only the crowdedness of solutions is reduced but also the clustering technique is appropriate. Overall, the performance of the constructed NSGA-II code satisfies the requirement, and it is verified to be used in IHX design optimization problem.

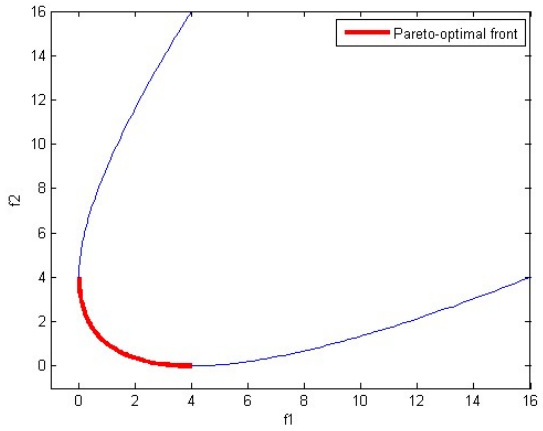

Figure 34. The Pareto-optimal front in the single-variable test problem

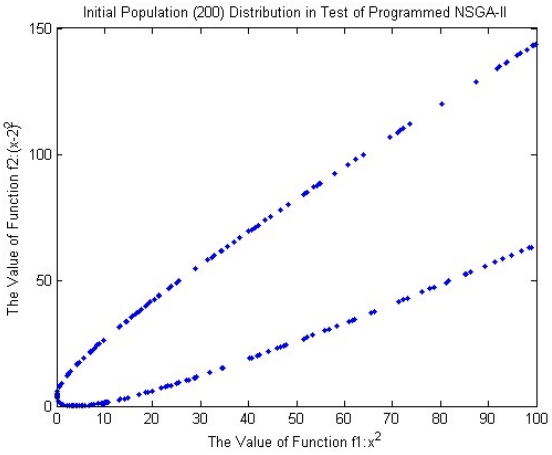

Figure 35. The distribution of the initial population of solutions

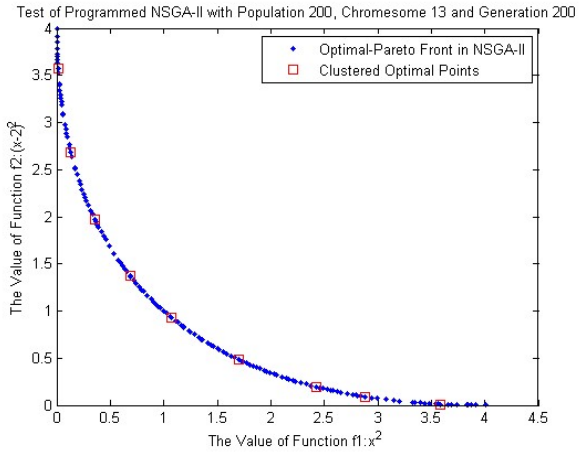

Figure 36. The obtained Pareto-optimal front and the clustered solutions

IHX design optimization with high-angle zigzag channels

For the IHX design optimization, the operating conditions, heat exchanger surface geometry, objective functions and design variable were first determined. As discussed in section 1.1.2, the prototypic operating conditions for helium-to-s-CO_2 IHX have been summarized. However, the mass flow rate of the helium-to-s-CO_2 IHX is not provided. This parameter is calculated based on the given operating conditions. The other parameters are slightly modified to maintain the nominal thermal duty as 600 MWth, which are listed in the Table 11. With respect to the heat exchanger surface geometry selection, it was suggested that S-shaped fin channel should be selected for s-CO_2 side because of the reduced Fanning factor and maintained heat transfer coefficient. The specific parameters are listed in the Table 12 as compared with the original ones since slight changes have been made.

Table 11. The operating conditions for the helium-to-s-CO2 IHX rating calculation with 600 MWth thermal duties

Working Fluids	Inlet Temperature (C°)	Mass Flow Rate (kg/s)	Operating Pressure (MPa)
Helium	800	388	7
s-CO_2	488.8	2991	20

Table 12. Comparison of the dimensions between the reference numerical and experimental models

Items	Numerical model	Experimental model
Plate thickness, mm	1.500	1.500
Fin height, mm	0.940	0.940
Longitudinal pitch, mm	7.565	7.565
Lateral pitch, mm	3.426	3.426
Neighboring fin gap, mm	2.656	2.700
Hydraulic diameter, mm	1.130	1.090
Fin angle, °	52	52
Free flow area, mm^2	1.652	n/a
Heat transfer surface, mm^2	58.892	n/a
Ratio of longitudinal pitch to arc length	0.751	n/a

As to helium side, the zigzag channel is defined by the channel angle ϕ, hydraulic diameter d_h and longitudinal pitch p_l, which have been incorporated into the newly-developed correlations. These three surface geometric parameters are also used as design variables to be input in the optimization process as they are expected to control the total cost and the thermal effectiveness simultaneously in a trade-off manner. Note that in fact the channel diameter D is used as the design variable instead of the hydraulic diameter just for convenience. The heat exchanger design process has been divided into a series of rating problems because in the Pareto-optimal front searching process, the surface geometric parameters are treated as known variables. In that case, the purpose of the rating is to calculate the total heat transfer rate to satisfy the required thermal duty. To achieve a heat exchanger design that satisfies the specified nominal thermal duty, the required heat transfer area must be determined, which can be calculated according to the module number *M* and the heat exchanger physical length L. The current possible size of a single PCHE module to fabricate is 600 mm × 3000 mm × 1000 mm ($W \times H \times L$) as mentioned in Yoon, et al., (2014). Therefore, the frontal size of a single module is determined as 600 mm × 3000 mm. It is more reasonable to treat the physical length *L* as one of the design variable since a smaller module number is preferred to reduce the initial material investment. Thus the physical length L becomes the fourth design variable and the module number will be adjusted to satisfy the thermal duty in the rating process.

The number of channels at both sides in one single module is determined by calculating the plate thickness and lateral channel pitch. With the knowledge of the heat exchanger width and lateral channel pitch, the number of channels one single plate can accommodate is then determined. The number of plates can also be easily calculated with the determined plate thickness. The plate thickness at zigzag channel is evaluated based on the simplified stress analysis as described in section 1.2.1. The second conservative approach is adopted without any extra margin considered since this approach can ensure sufficient margin already.

The objective functions were defined to be the total cost and the thermal effectiveness as discussed before:

$$f_1 = C_t = C_{cp} + C_o, \tag{1.2.23}$$

$$f_2 = \left[1 - \left(1 - \varepsilon\right)\right] \times 100\% = \left[1 - \left(1 - \frac{1 - \exp\left[-NTU(1 - C^*)\right]}{1 - C^* \exp\left[-NTU(1 - C^*)\right]}\right)\right] \times 100\% \tag{1.2.24}$$

The economic model is described in section 1.2.2, and the definition of variables shown in the second objective is available in section 1.2.1. Note that the heat exchanger effectiveness formula is essentially the one of the counter-flow heat exchanger. The design variables and their design space (searching space) are listed in Table 13. The design space for the first three design variables are primarily restricted by the application range of newly-developed correlations. The design space for the last one is mainly limited by the feasible aspect ratio, as discussed in section 1.2.3. In order to provide sufficient feasible solutions for optimization, the aspect ratio (heat exchanger height versus length) is set to be no larger than 10. In addition, the design points number shown in the Table 11 is actually determined by the size of the binary-coded variable “chromosome”. It can be adjusted to satisfy the required precision of a design variable in the design space. The design points number may also affect the population size.

Table 13. The design space of the design variables (d is the corresponding zigzag channel diameter)

Design Variables	Lower Limit	Upper Limit	Design Points Number
D_h / D	0.922 mm/1.5 mm	1.222 mm/ 2.0 mm	2^3
ϕ	25°	45°	2^5
p_l	10.0 mm	25.0 mm	2^8
L	0.300 m	1.000 m	2^7

Optimization results and discussion

First, the solutions of the entire searching space have been visualized in the Figure 37. The population size is up to 10,000, which is sufficient to display the solution distribution. It is observed that the entire cost-versus-100%-minus-effectiveness space forms a convex shape, which implies that the convergence to the global Pareto-optimal front will not be computationally difficult. However, a large number of solutions are located at “high-cost” region, indicating the inherent feature of this optimization problem, that is, most of the solutions may not be economically feasible. Second, no constraint is introduced in the optimization process. It is expected that with such large Fanning factor for zigzag channel of angle above 35°, the annual cost will be extremely large, then affecting the Pareto-optimal solutions distribution. Figure 38shows the optimization results, and it is consistent with the previous guess. Most of the clustered solutions lie in the “high-cost” region, and these solution corresponds to 45° channel angle. Although these solutions can ensure high effectiveness (larger than 99.9%), which is actually achieved by increasing the physical length, the annual total cost is extremely high and unacceptable (larger than 50 M$/year). More detailed information is listed in Table 14.

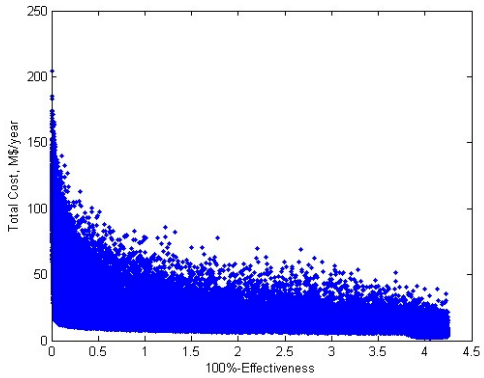

Figure 37. Visualization of the entire searching space of unconstrained solutions, simulated with population size 10,000

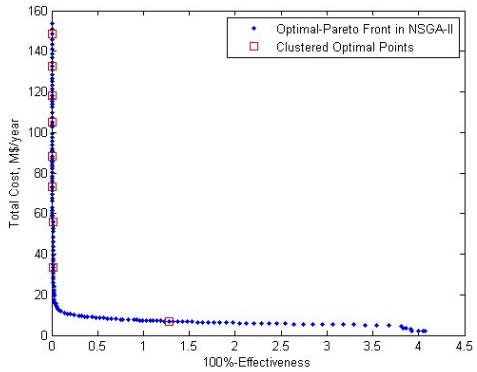

Figure 38. The Pareto-optimal front and clustered solutions for unconstrained optimization

Table 14. The Pareto-optimal clustered solutions

Unconstrained Optimization							
Cluster Number	D (mm)	ϕ (°)	p_l (mm)	L (m)	100-Effectiveness (%)	Effectiveness (%)	Total cost (M$/year)
1	1.643	45	10.1	1	0.0039	99.996	148.4
2	1.643	45	10.5	1	0.0043	99.996	132.5
3	1.643	45	11.0	1	0.0047	99.995	118.3
4	1.643	45	11.6	1	0.0052	99.995	104.8
5	1.643	45	12.6	1	0.0062	99.994	88.0
6	1.643	45	14.2	1	0.0075	99.992	73.4
7	1.643	45	18.6	1	0.0107	99.989	55.7
8	1.643	25	10.5	1	0.0140	99.986	33.6
9	2.000	25	25.0	0.559	1.279	98.721	6.9
Constrained Optimization							
1	2.000	25	25.0	0.934	0.113	99.887	11.5
2	2.000	25	25.0	0.851	0.193	99.807	10.5
3	2.000	25	25.0	0.763	0.341	99.659	9.4
4	2.000	25	25.0	0.675	0.603	99.397	8.3
5	2.000	25	25.0	0.587	1.069	98.931	7.2
6	2.000	25	25.0	0.498	1.903	98.097	6.2
7	2.000	25	25.0	0.421	3.174	96.826	5.2
8	2.000	25.6	25.0	0.377	3.809	96.191	4.2
9	2.000	25	21.0	0.322	3.920	96.080	2.6

Since unconstrained optimization yields undesired results, the constrained NSGA-II code is then introduced. The constraint is determined as the total cost being below 12 M$/year. The population size and generation number are adjusted such that the clustered solutions are computationally stable. The selected constrained optimization results are listed in Table 12. In this case, the population size is 250, with the generation number being 400. The Pareto-optimal front is shown in Figure 39.

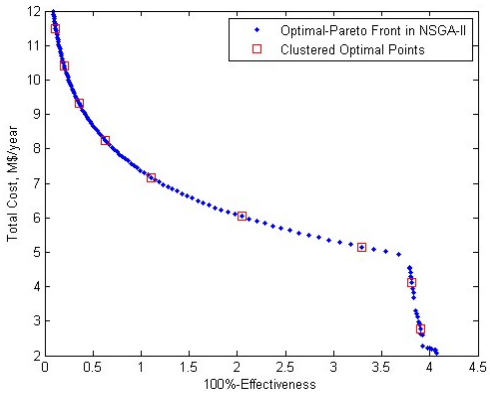

Figure 39. The Pareto-optimal front and clustered solutions for constrained optimization

Obviously, the Pareto-optimal front for the constrained optimization results is the lower part of the unconstrained Pareto-optimal front. It is observed that most of the results show preference to the channel diameter 2.0 mm, angle 25° and pitch 25 mm, then it can be concluded that it is actually not necessary to optimize the surface geometric parameters anymore based on the correlations used in the optimization. This is mainly due to the unrealistic large Fanning factor the correlations have predicted in the optimization. The newly-developed correlations do not display large deviation from the original ones. Thus, they are acceptable in terms of the accuracy of the prediction. The original correlations by Kim, et al. 2012 might overestimate the Fanning factor, especially for channel angles beyond 35°. In fact, most of the Pareto-optimal solutions that are ruled out due to the total cost constraint are those with angle 45°. This can be explained by the overestimated Fanning factor as well as the increased physical length. On one hand, the extremely large Fanning factor leads to the domination of the operating cost in the total cost. The operating cost of those solutions is dramatically larger than the associated capital cost, usually over 100 times, which implies the capital cost is essentially negligible. In that case, the reduction of the physical length, which in general leads to the reduction of the heat exchanger material investment, will not affect the total cost. Therefore, the solutions with large channel angles are not possible to exist in the lower Pareto-optimal front. On the other, the physical length is indirectly related to the thermal effectiveness. The increased physical length can improve the effectiveness, but increases the operating cost simultaneously. It seems to be natural since the total cost and effectiveness are conflicting as discussed before, but the total cost increases much quickly. That's why most of Pareto-optimal solutions with large angles lie in the "high-cost" region, which is eventually eliminated in the constrained optimization. Nevertheless, it is still unclear how surface geometric parameters affect the global Pareto-optimal front since the correlations overestimate the Fanning factor.

Although the IHX design optimization results indicate that it has essentially become a physical-length optimization problem, the results are still useful to determine the optimal solution for one particular design that has been currently demonstrated better than other designs in terms of both objectives. This particular design, named as design A, is characterized by the channel diameter, angle and pitch being 2.0 mm, 20° and 25.0 mm, respectively. It is observed that there are two zones in the Pareto-optimal front, separated by a point between the second and third rightmost solution point. It is confirmed that solutions with a small physical length are likely to lie in the lower zone whereas solutions with a large physical length are distributed in the upper zone. The check of the entire searching space of the physical length for the design A has shown that the most of the solutions with the physical length larger than approximately 0.4 m essentially lie on the Pareto-optimal front, that is, the solutions inherently form a Pareto-optimal front controlled by the physical length. However, the solutions with the physical length smaller than 0.4 m do not necessarily lie on the Pareto-optimal front. This phenomenon can be explained by the relative role of the capital cost in the total cost. In the lower zone where solutions are characterized by relatively small physical length, the capital cost is comparable with the operating cost, accounting for a large percentage of the total cost. As the physical length increases, the total cost increases rapidly whereas the effectiveness is not as sensitive as the total cost. Therefore, a balance between the capital cost and the operating cost versus the effectiveness is critical, which forms the Pareto-optimal front. Regarding the upper zone, it is found that the capital cost gradually become negligible compared with the dramatically increased pressure drop. Thus, the physical length controls the total cost and the effectiveness simultaneously. It is recommended to avoid such a zone when the extremely large pressure drop is unacceptable in the IHX design. From an economic point of view, it is necessary to sacrifice the effectiveness to keep the total cost as low as possible.

From the above analysis, it can be concluded that for a particular IHX design with specified surface geometries and heat exchanger dimensions including frontal size, the physical length should be as small as possible unless the pressure drop is maintained low somehow. According to this guideline, cluster #9 in the constrained optimization is selected as one of the IHX designs. As far as the effectiveness is concerned, the cluster #6 is also selected because the effectiveness is increased with relatively small increase in cost and the absolute total cost. The detailed information corresponding to these two selected solutions is listed in the Table 15.

Table 15. The detailed information of two selected design solutions

Items	Units	Cluster #9	Cluster #6
Module Number	n/a	15	10

H.T.C.(heat transfer coefficient) at helium side	kW/m^2-C°	1.423	1.764
H.T.C. at s-CO_2 side	kW/m^2-C°	1.588	1.968
NTU	n/a	5.46	6.98
Effectiveness	%	96.08	98.09
Reynolds number at helium side	n/a	1,634	2,455
Reynolds number at s-CO_2side	n/a	19,489	29,189
Total mass of IHX material	Mg	72.7	74.9
Pressure drop at helium side	kPa	26.6	73.3
Pressure drop at s-CO_2 side	kPa	32.0	97.2
Pumping power at helium side	MW	2.86	7.85
Pumping power at s-CO_2 side	MW	0.79	2.40
Capital cost	M$/year	0.64	0.66
Operating cost	M$/year	1.95	5.49

An alternative design based on GA optimization

As discussed above, it is found that the correlations that are developed numerically highly overestimate the Fanning factor, thus affecting the decision-making of the final design selection. Since several experimentally-developed correlations for particular zigzag channel PCHEs are available, an alternative design has been identified. The physical length serves as the only one design variable with the design space being [0.3, 1.0] m. The surface geometric information is listed in the Table 16.

Table 16. The surface geometric parameters of the 15° angle zigzag channel

Items	Values
Plate thickness, mm	1.48
Pitch, mm	24.6
Lateral pitch, mm	2.62
Channel diameter, mm	1.51
Hydraulic diameter, mm	0.922
Channel angle, °	15

The available correlations are shown as follows (Kim, et al., 2013)

$$f \cdot \mathrm{Re} = 15.78 + 0.0557\,\mathrm{Re}^{0.82}, 0 < \mathrm{Re} < 3000 \quad (1.2.25)$$

$$\mathrm{Nu} = 4.089 + 0.00497\,\mathrm{Re}^{0.95}\,\mathrm{Pr}^{0.55}, 0 < \mathrm{Re} < 3000, 0.66 < \mathrm{Pr} < 13.41 \quad (1.2.26)$$

Because both 15° and 25° zigzag channels are characterized by relatively small Fanning factor, the single-variable optimization result was expected to be similar to the previous one. Figure 40 shows the optimization result. Compared with the initial population of 5000 solutions shown in Figure 41, it is obvious that most of the solutions inherently form a Pareto-optimal front. Only a few solutions in the lower zone need to be searched for the Pareto-optimal front. According the previous guideline, the first and fourth rightmost solutions are selected. The detailed information is listed in the Table 17.

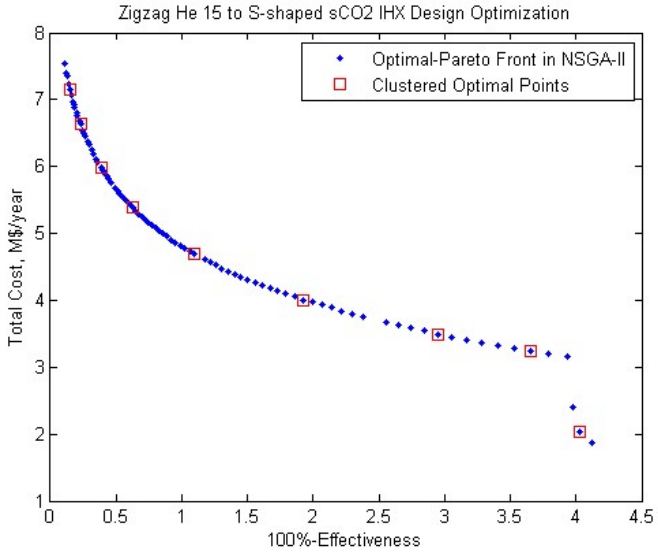

Figure 40. The Pareto-optimal front and clustered solutions for the alternative IHX design

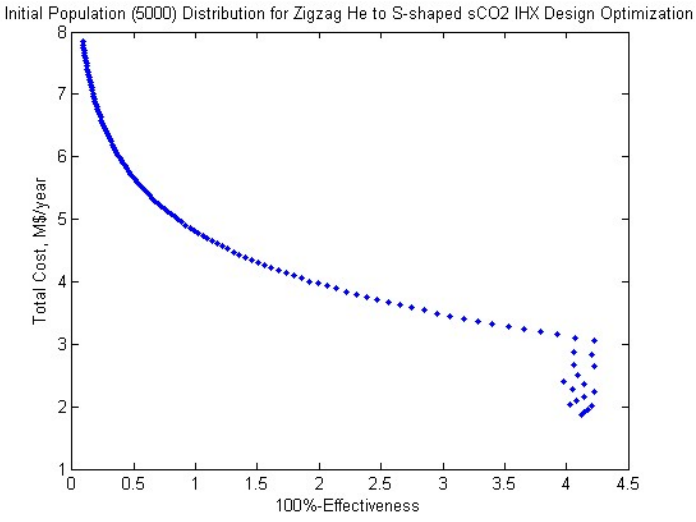

Figure 41. The distribution of solutions of a population size 5000

Table 17. The detailed information of two selected design solutions in the alternative IHX design

Items	Units	Cluster #9	Cluster #6
Module Number	n/a	22	140
H.T.C. at helium side	kW/m^2-C°	1.659	2.123
H.T.C. at s-CO_2 side	kW/m^2-C°	1.121	1.434
NTU	n/a	5.41	6.96
Effectiveness	%	95.97	98.08
Reynolds number at helium side	n/a	1,806	2,843
Reynolds number at s-CO_2side	n/a	13,895	21,803
Total mass of IHX material	Mg	106.6	107.3
Pressure drop at helium side	kPa	14.9	39.2
Pressure drop at s-CO_2 side	kPa	18.2	61.2
Pumping power at helium side	MW	1.60	4.19
Pumping power at s-CO_2 side	MW	0.45	1.51
Capital cost	M$/year	0.94	0.95
Operating cost	M$/year	1.10	3.06

Correlation Development of Low-angle Zigzag Channels

It has been found that the correlations numerically developed by Kim et al. (2012) highly overestimate the Fanning factors of zigzag channels with angles beyond 30°. The optimization results have indicated that the low-angle channels are more competitive since the pressure drop reduction outweighs other factors in the optimization and low-angle channels exhibit low pressure drop loss. In addition to the hydraulic advantages of low-angle channels, in fact the numerically-developed correlations' prediction of Fanning factors for low-angle channels is much reliable compared with the one for high-angle channels. It is reasonable to focus on low-angle zigzag channels in the PCHE design optimization. Hence there is need to develop new correlations for low-angle channels using similar procedures and methods that are employed in developing the ones for high-angle channels. The dimensionless parameters used in the low-angle channel correlations are the same as those used before, and the angle range is determined to be from 5 to 25 degrees. Note that the extremely low-angle channels are more like straight channels instead of conventional zigzag channels. Any channels with angles below 5° will be treated as straight channels. The low-angle correlations for four original parameters are shown as follows:

$$\begin{cases} A_1 = 0.336\gamma^{0.2} + 11.034\gamma - 41.326 \\ a = \left[\gamma^{-2}\left(A_1\left(\sin^{0.78}\phi - 0.1024\right) + 0.2174\right)\right]^{\frac{1}{0.5}} \end{cases} \tag{1.2.27}$$

$$\begin{cases} B_1 = 4.0439\times10^{-4}\gamma^3 - 0.01\gamma^2 + 0.0865\gamma - 0.2967 \\ B_2 = 0.0066\gamma - 0.1785 \\ B_3 = 8.7254\times10^{-4}\gamma^3 - 0.0246\gamma^2 + 0.2314\gamma - 0.7362 \\ B_4 = -0.027 \\ b_{ref} = B_1 e^{B_2\phi}\sin\left(\frac{6}{5}\phi^2 - 12\phi - 170^\circ\right) + B_3 e^{B_4\phi} + 1 \\ t_b = \frac{1}{\sec\phi - 1} \\ T_b = -2.52\times10^{-6}t_b^2 + 0.0014t_b + 1.059 \\ b = \left(\gamma^{-0.08}T_b b_{ref}\right)^2 \end{cases} \tag{1.2.28}$$

$$\begin{cases} C_1 = -0.0154\gamma^2 + 0.3751\gamma - 1.418 \\ C_2 = 0.0422\gamma^2 - 0.7793\gamma + 4.1222 \\ C_3 = -0.0132\gamma^2 + 0.4033\gamma - 1.6034 \\ t_c = \sin^{0.9}\phi \\ c_{ref} = 0.08\sin\left(C_1\left(7.58\pi t_c + 3.48\pi\right)t_c + C_2\pi\right) + C_3 \\ c = \left[\gamma^{-1.8}\left(20.9742t_c - 0.8812\right)c_{ref}\right]^{\frac{1}{0.5}} \end{cases} \tag{1.2.29}$$

$$\begin{cases} D_1 = 0.1788\gamma - 1.8296 \\ D_2 = -0.0011\gamma + 0.8502 \\ D_3 = 0.01\gamma + 0.8999 \\ t_d = \tan^{0.11}\phi \\ d_{ref} = 0.0418t_d^2 - 0.3936t_d + 1.5501 \\ d = \left[\gamma^{-0.1}\left(D_1\left(t_d - D_2\right)^2 + D_3\right)d_{ref}\right]^{\frac{1}{0.11}} \end{cases} \tag{1.2.30}$$

Table 18 shows the comparison of the original parameters and the predicted values by new correlations. As is observed, some of relative errors reach approximately 27%, which implies that the case studies must be carried out to justify the newly-developed correlations' application.

Table 18. The comparison of the original and predicted parameter values

	Original		Prediction		Ralative Error		Original		Prediction		Ralative Error	
Degree	a	b	a	b	a	b	c	d	c	d	c	d
Angle	Dh = 0.922 mm, pitch = 24.6 mm											
5	0.0019	1.1187	0.00200	1.13652	5.1%	1.6%	0.00036	1.18213	0.00034	1.17904	4.2%	0.3%
10	0.01775	0.90795	0.02059	0.91165	16.0%	0.4%	0.00220	0.99841	0.00226	0.99652	2.7%	0.2%
15	0.06455	0.81021	0.05302	0.82668	17.9%	2.0%	0.00544	0.91361	0.00567	0.91280	4.2%	0.1%
20	0.08918	0.8136	0.09551	0.82042	7.1%	0.8%	0.00894	0.86708	0.00837	0.86231	6.3%	0.6%
25	0.1442	0.79529	0.14546	0.78833	0.9%	0.9%	0.01321	0.82738	0.01374	0.82774	4.0%	0.0%
Angle	Dh = 0.922 mm, pitch = 12.3 mm											
5	0.00366	1.07165	0.00296	1.08446	19.0%	1.2%	0.00061	1.13917	0.00057	1.13585	6.4%	0.3%
10	0.02536	0.91728	0.02792	0.92077	10.1%	0.4%	0.00251	1.01844	0.00260	1.01808	3.5%	0.0%
15	0.0696	0.85362	0.07077	0.86479	1.7%	1.3%	0.00607	0.93106	0.00540	0.92774	11.0%	0.4%
20	0.12817	0.83085	0.12663	0.82833	1.2%	0.3%	0.01180	0.85964	0.01085	0.85388	8.1%	0.7%
25	0.19392	0.82838	0.19214	0.82704	0.9%	0.2%	0.02165	0.79051	0.02249	0.79038	3.9%	0.0%
Angle	Dh = 1.222 mm, pitch = 24.6 mm											
5	0.0034	1.0502	0.00250	1.05540	26.6%	0.5%	0.00071	1.10341	0.00067	1.10755	6.2%	0.4%
10	0.02342	0.8863	0.02519	0.88648	7.5%	0.0%	0.00314	0.96567	0.00320	0.96014	1.8%	0.6%
15	0.06677	0.81258	0.06461	0.82872	3.2%	2.0%	0.00830	0.86054	0.00837	0.87597	0.9%	1.8%
20	0.12748	0.78479	0.11619	0.79315	8.9%	1.1%	0.01703	0.79007	0.01779	0.81640	4.5%	3.3%
25	0.17458	0.79345	0.17679	0.78947	1.3%	0.5%	0.02182	0.77285	0.02250	0.76955	3.1%	0.4%

Table 19 shows the detailed information of the selected cases with large deviation of the predicted parameter values, and the comparison result of the Fanning factors and Nusselt numbers are shown in Figure 42 through Figure 53. Through the case studies, we can conclude that the large deviation would not strongly affect Fanning factors. However, relatively, the Nusselt numbers deviation from the original is quite large. Fortunately, these deviations are controlled within ±10%, which is still acceptable in application of these correlations to the optimization process. Therefore, the newly-developed correlations' application has been justified.

Table 19. The parameters in the newly-developed and original correlations for 6 cases

Case #		a	b	c	d	d_h/mm	angle/°	pitch/mm
1	Original	0.06455	0.81021	n/a	n/a	0.922	15	24.6
	New	0.05302	0.82668	n/a	n/a			
2	Original	0.00366	1.07165	n/a	n/a	0.922	5	12.3
	New	0.00296	1.08446	n/a	n/a			
3	Original	0.0034	1.0502	n/a	n/a	1.222	5	24.6
	New	0.0025	1.0554	n/a	n/a			
4	Original	n/a	n/a	0.00894	0.86708	0.922	20	24.6
	New	n/a	n/a	0.00837	0.86231			
5	Original	n/a	n/a	0.00607	0.93106	0.922	15	12.3
	New	n/a	n/a	0.00540	0.92774			
6	Original	n/a	n/a	0.00071	1.10341	1.222	5	24.6
	New	n/a	n/a	0.00067	1.10755			

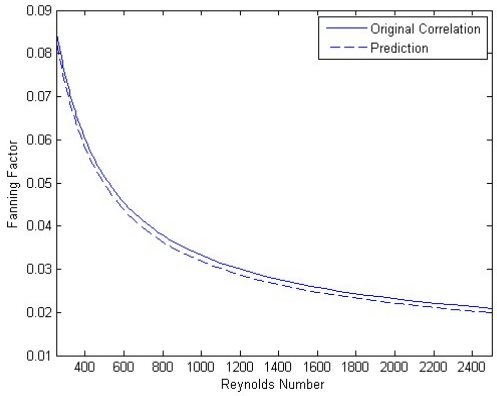

Figure 42. The comparison of the original and newly-developed correlations for Fanning factor versus Reynolds number in Case #1

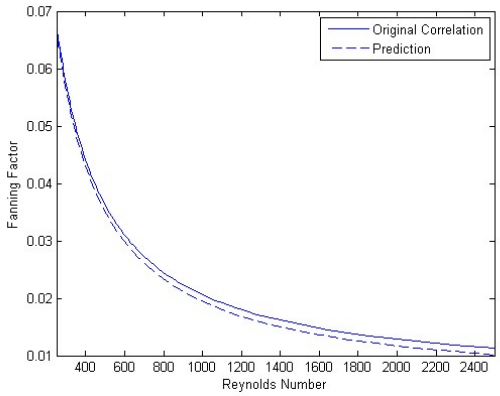

Figure 43. The comparison of the original and newly-developed correlations for Fanning factor versus Reynolds number in Case #2

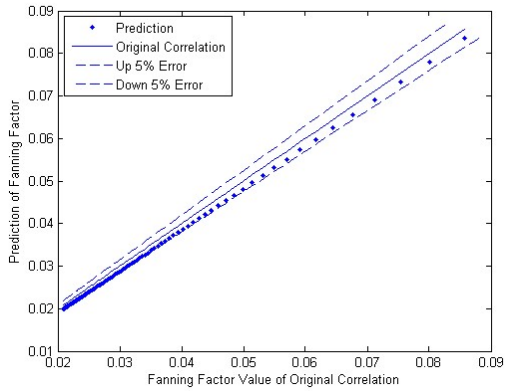

Figure 44. The deviation of the newly-developed correlation for Fanning factor from the original one in Case #1

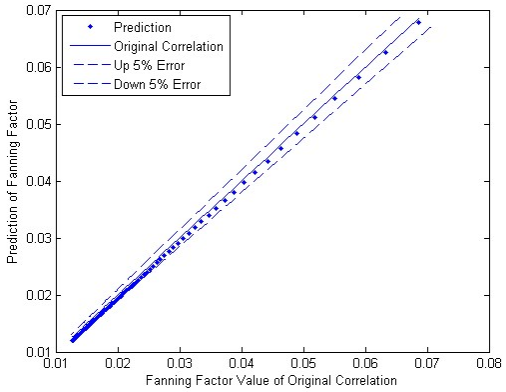

Figure 45. The deviation of the newly-developed correlation for Fanning factor from the original one in Case #2

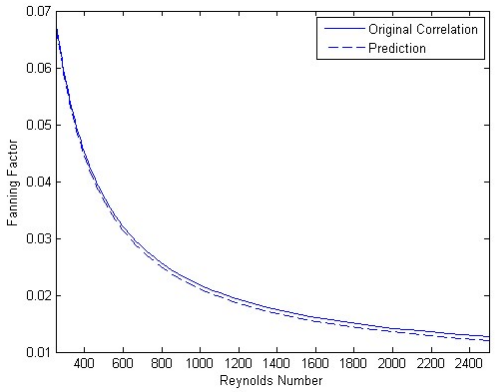

Figure 46. The comparison of the original and newly-developed correlations for Fanning factor versus Reynolds number in Case #3

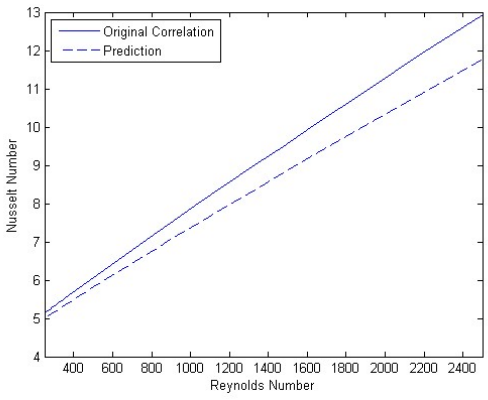

Figure 47. The comparison of the original and newly-developed correlations for Fanning factor versus Reynolds number in Case #4

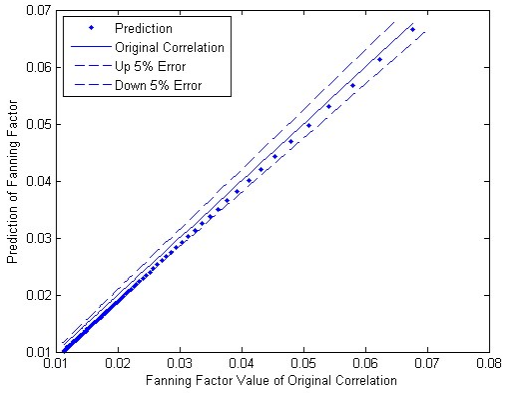

Figure 48. The deviation of the newly-developed correlation for Fanning factor from the original one in Case #3

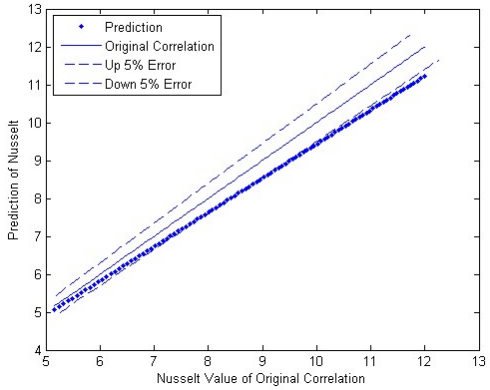

Figure 49. The deviation of the newly-developed correlation for Fanning factor from the original one in Case #4

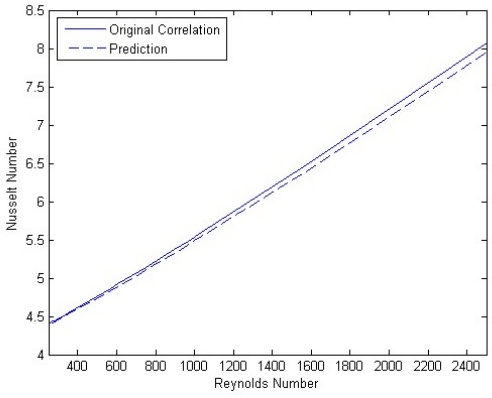

Figure 50. The comparison of the original and newly-developed correlations for Fanning factor versus Reynolds number in Case #5

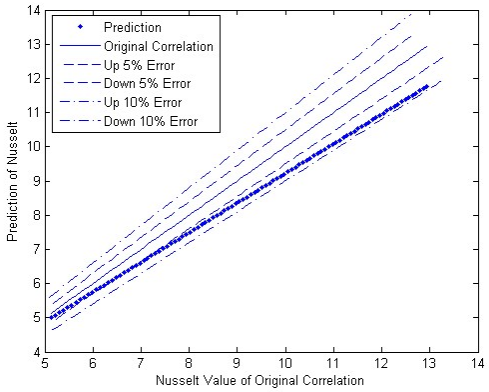

Figure 51. The comparison of the original and newly-developed correlations for Fanning factor versus Reynolds number in Case #6

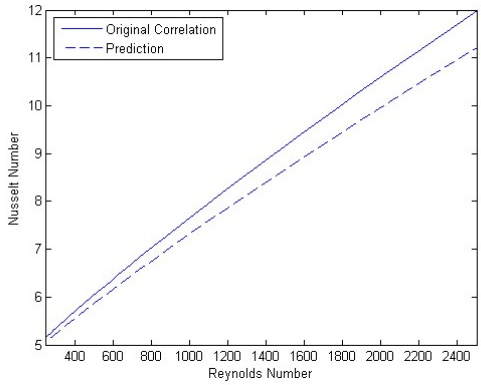

Figure 52. The deviation of the newly-developed correlation for Fanning factor from the original one in Case #5

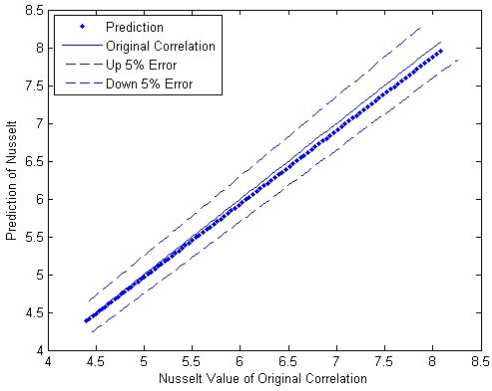

Figure 53. The deviation of the newly-developed correlation for Fanning factor from the original one in Case #6

IHX design optimization with low-angle zigzag channels

Using the low-angle newly-developed correlations, we need not concern about the issue of overestimated Fanning factors since the small angle at the channel bends would not induce large pressure drop. Figure 54 and Figure 55 shows the design points' population of the entire searching space and optimized results from that population, respectively. The physical length of the heat exchanger is constrained within 0.3-0.5 m. This is because, as observed from Figure 56 with physical length from 0.2-0.7 m, most of design points with large physical length contribute to the high-cost region where the high effectiveness is also achieved. Obviously, the high-cost region is certainly unfeasible from economic point of view. Thus, the larger length may not be considered as optimized designs. Figure 57 shows the optimized results after imposed with 6.44 M$ as the constrained condition on the total cost. The clustered design points from the optimal-Pareto front are listed in Table 20. The total cost of all clustered design points fall within 2 to 6 M$, which is reasonable as the heat transfer capacity is considerably large.

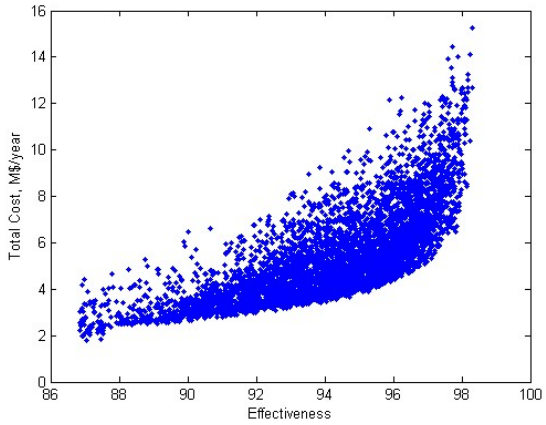

Figure 54. Visualization of the entire searching space of unconstrained solutions with physical length in the range of 0.3-0.5 m, simulated with population size 5,000

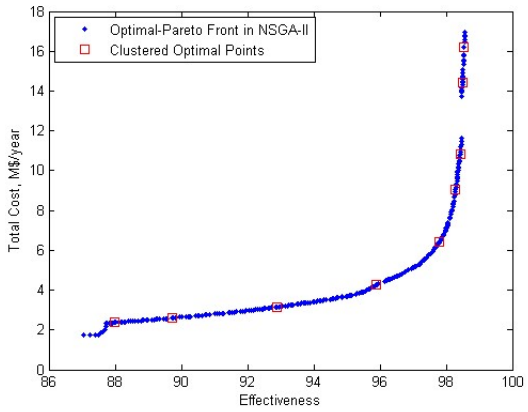

Figure 55. The Pareto-optimal front and clustered solutions for unconstrained optimization

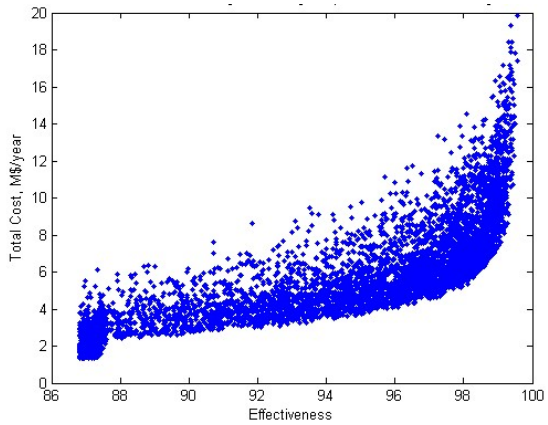

Figure 56. Visualization of the entire searching space of unconstrained solutions with physical length in the range of 0.3-0.5 m, simulated with population size 5,000

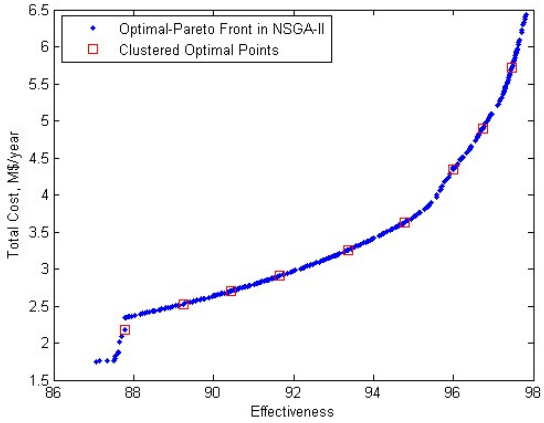

Figure 57. The Pareto-optimal front and clustered solutions with 6.44 M$ as constrained condition for the optimization

Table 20. The Pareto-optimal clustered solutions for the optimal-Pareto front of the channel diameter 1.5-2.0 mm

Unconstrained Optimization						
Cluster Number	D (mm)	ϕ (°)	p_l (mm)	L (m)	Effectiveness (%)	Total cost (M$/year)
1	1.79	5.0	21.89	0.325	89.98	2.37
2	1.73	5.0	21.69	0.349	89.72	2.60
3	1.73	5.0	22.76	0.429	92.90	3.16
4	1.69	5.32	16.46	0.498	95.87	4.26
5	1.73	18.65	20.73	0.500	97.79	6.44
6	1.69	21.83	16.37	0.500	98.29	9.03
7	1.67	23.73	15.21	0.500	98.43	10.81
8	1.50	23.10	13.85	0.500	98.49	14.41
9	1.50	24.37	12.98	0.500	98.54	16.22

Constrained Optimization						
1	1.92	5.0	12.49	0.365	87.78	2.17
2	1.79	5.0	22.18	0.349	89.25	2.53
3	1.79	5.0	21.60	0.371	90.43	2.70
4	1.79	5.0	22.47	0.402	91.64	2.90
5	1.79	5.0	22.57	0.453	93.38	3.26
6	1.79	5.0	21.60	0.500	94.77	3.63
7	1.69	5.63	17.63	0.500	95.99	4.34
8	1.73	7.54	15.88	0.500	96.74	4.90
9	1.69	16.11	23.44	0.500	97.46	5.71

One of the tasks in the design optimization is to find an optimized channel diameter since the original channel diameters fail to cover a broad range of possible designs. As mentioned, the newly-developed correlations are based on four surface characteristic parameters. That is to say, these correlations are strongly surface-geometry dependent. The original correlations have specified the applied range of each geometric parameter. Therefore, any attempts to extend the applied range of geometric parameters will result in misrepresentation of the thermos-hydraulic performances of particular zigzag channel configuration. Fortunately, the newly-developed correlations are characterized by dimensionless number γ, which indicates that the similarity rule could apply to the extension of the applied range of parameters. It is reasonable to assume that the similar channel configuration with the channel diameter and longitudinal pitch enlarged or shortened by the same factor exhibits similar thermo-hydraulic performances at the same time. Figure 58 shows the process of increasing or decreasing the channel diameter with constant ratio of other geometric parameters. Hence, the increased channel diameter range from 1.5 to 4.0 mm can be studied to finalize the optimized PCHE design.

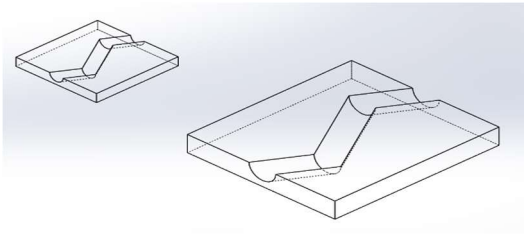

Figure 58. The process of changing the size of the zigzag channel

Figure 59 through Figure 61 have shown a series of optimal-Pareto fronts for different channel diameter ranges. It has been found that smaller channel diameters lead to larger total cost at the same heat exchanger effectiveness, while larger channel diameters become more economically appealing. This is mostly due to the pressure drop reduction

with increasing channel diameter, which is related to the operating cost reduction. However, it is also observed that the optimized channel configuration does not always favor the designs with the large diameter. For instance, regarding 90% and 95% of heat exchanger effectiveness, the channel diameter around 2.8 mm is predominantly cost-effective. Table 21 shows the comparison of optimized results of different channel diameter ranges. It is obvious that the optimized channel diameter falls within the range of 2.5 to 3.0 mm. Using this approach, the optimized channel diameter can be determined, and the optimized value of other parameters can be finalized accordingly.

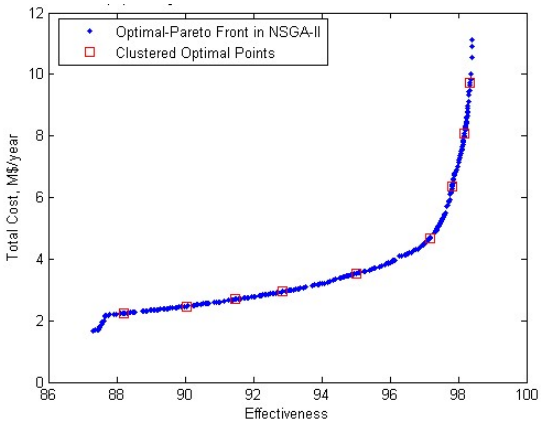

Figure 59. The Pareto-optimal front and clustered solutions for unconstrained optimization, with diameter in the range of 1.65-2.2 mm

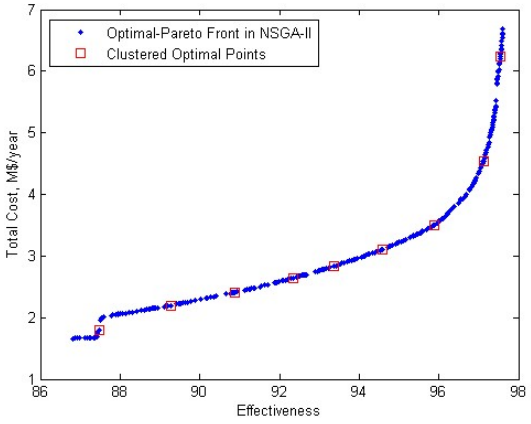

Figure 60. The Pareto-optimal front and clustered solutions for unconstrained optimization, with diameter in the range of 2.25-3.0 mm

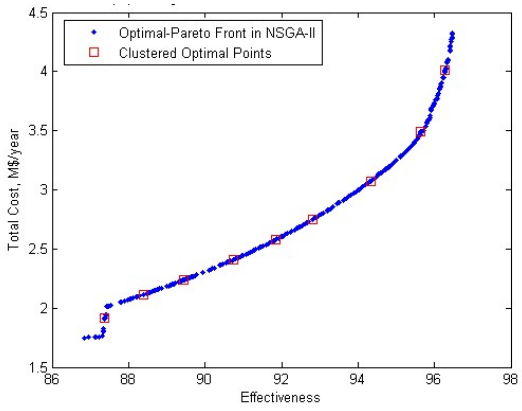

Figure 61. The Pareto-optimal front and clustered solutions for unconstrained optimization, with diameter in the range of 3.0-4.0 mm

Table 21. The comparison of the optimized results for different channel diameter range

Diameter Range	Item	Units	Clustered Optimal Results								
			#1	#2	#3	#4	#5	#6	#7	#8	#9
1.65-2.2 mm	Channel diameter	mm	2.08	2.08	2.08	2.08	2.08	2.09	2.07	1.68	1.68
	Channel angle	°	5.00	5.00	5.00	5.00	7.86	18.65	22.78	20.87	22.78
	Pitch	mm	23.86	24.08	24.08	24.18	24.50	25.14	19.82	17.68	15.98
	Length	m	0.352	0.390	0.424	0.465	0.497	0.500	0.500	0.500	0.500
	Total cost	M$/year	2.24	2.47	2.69	2.94	3.54	4.67	6.35	8.09	9.74
	Effectiveness	%	88.21	90.05	91.48	92.87	95.02	97.16	97.83	98.19	98.35
2.25-3.0mm	Channel diameter	mm	2.33	2.77	2.77	2.77	2.77	2.77	2.77	2.40	2.25
	Channel angle	°	5.32	18.33	18.33	18.33	18.65	18.33	21.51	22.46	24.68
	Pitch	mm	34.14	34.29	34.14	34.58	33.99	34.58	28.33	23.24	19.90
	Length	m	0.317	0.308	0.341	0.385	0.429	0.495	0.500	0.500	0.500
	Total cost	M$/year	1.78	2.13	2.35	2.65	2.98	3.40	3.92	4.91	6.61
	Effectiveness	%	87.43	88.49	90.36	92.28	93.94	95.54	96.52	97.29	97.55
2.625-3.5 mm	Channel diameter	mm	2.63	2.78	2.78	2.78	2.78	2.78	2.78	2.78	2.79
	Channel angle	°	7.86	18.33	18.33	18.65	18.33	18.65	18.33	19.92	22.78
	Pitch	mm	32.54	34.24	34.92	33.90	34.07	34.92	34.58	32.37	26.78
	Length	m	0.325	0.305	0.331	0.355	0.388	0.423	0.469	0.498	0.500
	Total cost	M$/year	1.86	2.10	2.28	2.47	2.68	2.91	3.22	3.58	4.16
	Effectiveness	%	87.39	88.29	89.75	91.15	92.45	93.63	94.91	95.99	96.69
3.0-4.0 mm	Channel diameter	mm	3.00	3.24	3.24	3.24	3.24	3.24	3.24	3.24	3.00
	Channel angle	°	20.87	19.60	19.92	19.92	19.92	19.92	19.92	21.83	23.10
	Pitch	mm	42.23	36.80	36.80	36.03	35.83	36.80	36.61	32.93	28.28
	Length	m	0.302	0.322	0.339	0.363	0.388	0.417	0.465	0.497	0.500
	Total cost	M$/year	1.91	2.12	2.24	2.41	2.58	2.75	3.07	3.49	4.01
	Effectiveness	%	87.37	88.40	89.45	90.73	91.84	92.80	94.32	95.65	96.28

Since no specific criteria available to guide the selection of the PCHE optimized designs, the design point with 90% and 95% of effectiveness will be selected. The detailed information of these two final designs are listed in the Table 19. Regarding the actual

configuration of the heat exchanger complex, there are 20 individual modules and each module consists of 5 blocks, i.e. 100 blocks in total. Each block is 0.6x0.6 in width and height, as shown in the Figure 62. The diagram of PCHE configurations does not take into account the manifold design and supporting structure issues. From the information shown in the Table 22, each block consists of 21,996 zigzag channels and 26,988 S-shaped fin channels. Each block is capable of transfer heat load of 6.57 and 6.22 MW for the cases of 95% and 90% effectiveness, respectively. These two designs will be used as the reference design basis for the following test PCHE design.

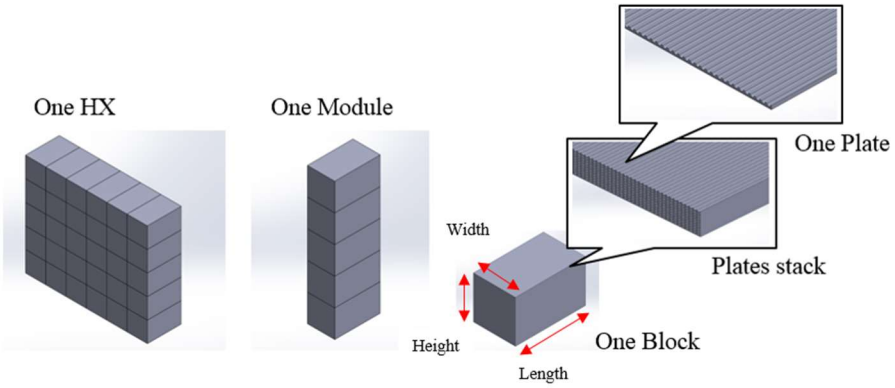

Figure 62. Schematic of PCHEs configuration

Table 22. The figuration of PCHE heat exchanger blocks.

Category		Number	Item	Units	95%	90%
SPECIFIED PARAMETERS	General	1	Nominal thermal duty	MW	600	600
	Primary side	2	Mass flow rate	kg/s	428	428
		3	Pressure	MPa	7	7
		4	Inlet temperature	°C	800	800
	Secondary side	5	Mass flow rate	kg/s	2991	2991
		6	Pressure	MPa	20	20
		7	Inlet temperature	°C	488.8	488.8
THERMO-HYDRAULIC DATA	Primary side	8	Outlet temperature	°C	504.4	519.8
		9	Reynolds number	n/a	2372	2358
		10	Pressure drop	kPa	14.66	10.47
		11	Heat transfer coefficient	kW/m^2-°C	2.70	2.69
		12	Heat transfer area	m^2	8076	5754
		13	Surface area density	m^2/m^3	485	484
		14	Pumping power	MW	1.74	1.25
	Secondary side	15	Outlet temperature	°C	665.1	656.0
		16	Reynolds number	n/a	19828	19897
		17	Pressure drop	kPa	48.20	34.17
		19	Heat transfer coefficient	kW/m^2-°C	3.08	3.07
		20	Heat transfer area	m^2	9713	6933

		21	Surface area density	m^2/m^3	584	584
		22	Pumping power	MW	1.20	0.85
GEOMETRIC PARAMETERS	General	23	Heat exchanger core volume	m^3	16.64	11.88
		24	Heat exchanger mass	kg	139.1	99.3
		25	Number of modules	n/a	20	20
		26	Frontal area	m^2	36	36
		27	Number of plates per block	n/a	312	312
		28	Heat exchanger physical length	m	0.46	0.33
	Primary side	29	Channel diameter	mm	2.92	2.92
		30	Hydraulic diameter	mm	1.78	1.78
		31	Channel angle	°	19.29	18.97
		32	Longitudinal pitch	mm	34.41	34.24
		33	Transverse pitch	mm	4.18	4.18
		34	Plate thickness	mm	2.33	2.33
		35	Number of channels per plates	n/a	141	141
		36	Free flow area	m^2	7.35	7.35
	Secondary side	37	Hydraulic diameter	mm	1.13	1.13
		38	Fin angle	°	52	52
		39	Longitudinal pitch	mm	7.57	7.57
		40	Transverse pitch	mm	3.43	3.43
		41	Plate thickness	mm	1.5	1.5
		42	Number of channels per plates	n/a	173	173
		43	Free flow area	m^2	4.46	4.46
AUXILIARY DATA		44	Heat exchanger capacity	MW	656.6	622.3
		45	Overall H.T.C. at primary side	kW/m^2-°C	1.47	1.47
		46	Overall H.T.C.at secondary side	kW/m^2-°C	1.22	1.22
		47	Total surface density	m^2/m^3	1069	1068
		48	Specific performance	MW/m^3	39.46	52.40
		49	Material cost	M$/year	1.23	0.88
		50	Operating cost	M$/year	1.58	1.13
		51	Total cost	M$/year	3.42	2.44
		52	Effectiveness	%	95.00	90.04

1.3 Perform Numerical Modeling of Thermal-hydraulics of PCHEs

1.3.1 CFD Optimization of Airfoil Channels

Computational Fluid Dynamic (CFD) methods are being used to find the optimum spacing of airfoil-fins in the airfoil-fin channel design. The model being developed is the first to fully model the geometry of the chemically etched airfoil-fin channels used in s-CO2 PCHEs. Optimization focuses on the three performance parameters of heat-transfer, pressure drop, and mechanical integrity of the channel. The optimal design will maximize

heat-transfer and minimize pressure drop while maintaining sufficient strength of the overall PCHE piece.

Other studies have looked at spacing optimization but have failed to model the full topology of the etched airfoil-fin channel. These studies have identified optimum spacing configurations for simplified airfoil-fin channel geometries. These have assumed that the channel and airfoils are perfectly rectangular and have maintained the sharp features of the "as drawn" channel. This isn't an accurate representation of the airfoil-fin channel as residual features from the etching process are considerably large relative to the size of the microchannel. Optical measurement of airfoil-fin channel geometries has shown 25% differences between the expected and actual etched geometries. The difference is primarily in the filleting of airfoil features and the rounding of the airfoil tail. This can be seen in Figure 63 where the airfoil shape is significantly filleted and the airfoil-tail rounded.

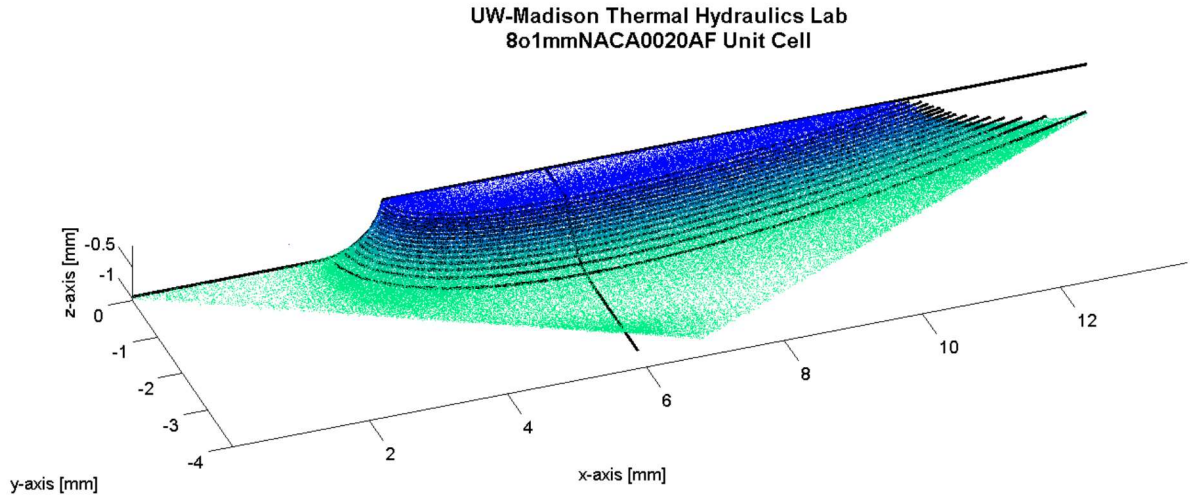

Figure 63. Optical topology measurements of an etched NACA0020 airfoil-fin.

The geometry model used in the CFD analysis is built off of optical measurements of actual etched airfoil-fin channels. The extent of filleting and trimming of the airfoil tail were determined from point clouds of t optical scan data. Figure 63 shows the as designed geometry of the airfoil-fin channel compared to the optically measured etched geometry. Filleting of the airfoil was found to be 1.09 mm and the trimming of the airfoil tail found to be 0.3 mm. In large etched parts these aren't significant; however in microchannels they drastically change the geometry, as channel depths and hydraulic diameters are on the order of 1 mm. This measured filleting and tail-trim were applied to the CFD model geometry.

Table 23. Designed and measured geometry of the 8.1mm NACA0020 airfoil-fin channel

Description	Symbol	Unit	Design	Measured	Uncertainty
Chord Length	c	mm	8.1	7.801	0.05
Thickness / Chord Length	t	-	0.2	0.205	0.05
Fillet Radius	r	mm	0	1.091	0.05
Channel Depth	h	mm	0.95	0.774	0.05
Axial Pitch	s	mm	6.9	6.933	0.025
Lateral Pitch	p	mm	7.3	7.296	0.025
Number of Rows	Nr	-	72	72	-
Airfoils per Row	Naf	-	3	3	-
Hydraulic Diameter ($4V_f/A_s$)	d_{hyd}	mm	1.447	1.337	0.0834
Cross-Sectional Area	-	mm^2	16.19	13.23	1.247
Unit-Cell Surface Area	-	mm^2	101.8	90.89	3.906

An array of spacing sample points were chosen for investigation in the CFD model. The axial and lateral spacing of 8.1mm NACA0020 airfoil-fins are varied and are expressed as dimensionless spacing parameters which compare the spacing to the airfoil shape as follows:

$$\zeta_h = \frac{axial\ pitch}{chord\ length} = \frac{s}{8.1\ mm} \tag{1.3.1}$$

$$\zeta_v = \frac{lateral\ pitch}{chord\ thickness} = \frac{s}{1.62\ mm} \tag{1.3.2}$$

One hundred sample points were chosen across 10 lines of constant aspect of ζ_v and ζ_h. Sample points and their corresponding hydraulic diameter distribution, as well as bond coverage, are shown in Figure 64. The sample points are shown as black dots and color coded maps are given for the hydraulic diameter in the left figure and for the airfoil-fin bond coverage in the right figure. One of the aspect lines contains the prototypic spacing configuration used in previous experimental analysis of the airfoil-fin channels. This prototypic spacing is given in Table 23and evaluates to ζ_v=2.253 and $\zeta_h = 0.451$.

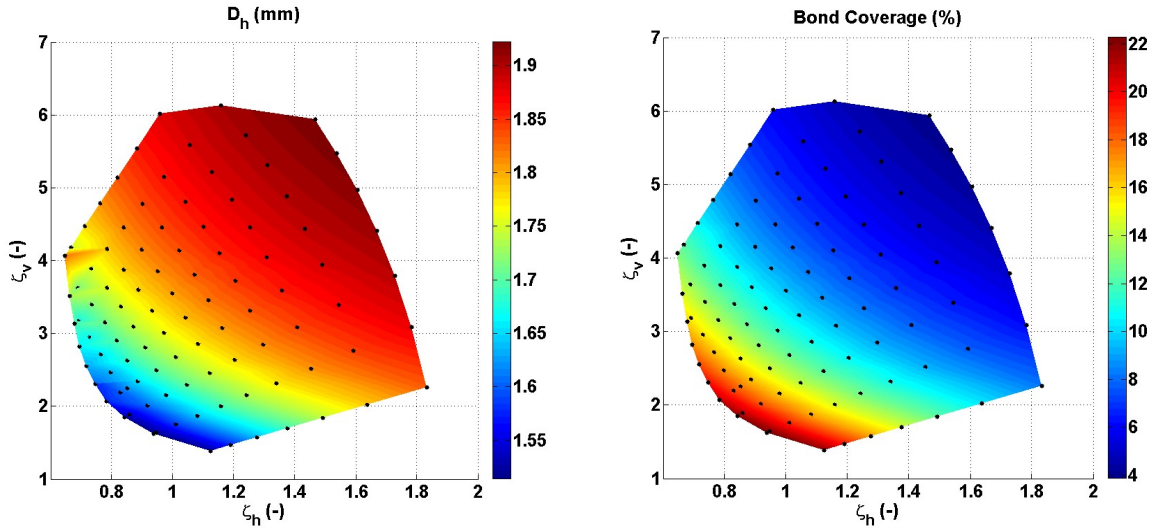

Figure 64. Model simulation results

The CFD model is currently being run to determine to performance of CO2 at various pressures and temperatures flowing through a model channel reflecting each of the 100 spacing sample points. Heat-transfer, pressure drop, and mechanical integrity data at each sample point will be used to create a performance map and determine the optimal spacing configuration.

1.3.2 CFD Validation of straight channel PCHEs

Straight channel modelling

Mylavarpu (2011) had tested two straight channel recuperator PCHEs using HTHF with high temperature and pressure helium, and generated a great number of data for both isothermal and thermal experiments. Although Figley (2009) has investigated the numerical simulations of straight channels, the results have not been validated against the later available experimental results. In addition, the conclusion drawn from the previous numerical analyses showed contradictory with the experimental data in terms of the critical Reynolds number where turbulent and transitional flow starts to occur. Therefore, it is necessary to simulate the straight channels using experimental data to validate numerical models and further apply them to investigate IHXs' thermal hydraulics.

Figure 65 shows the configuration of the straight channel PCHEs tested in HTHF. It should be noted that the Z-type channel at hot side makes it difficult to model in CFD analysis since it is not periodic in one of the two directions anymore. This may certainly increase computational time if the actual configurations are modelled. To simplify the problems, it is assumed that both sides are straight channels across the length of the heat exchanger such that it becomes a pure conjugate heat transfer problem. The model in

the CFD analysis is shown in Figure 66. The simulation is carried out using ANSYS Fluent 16.0.

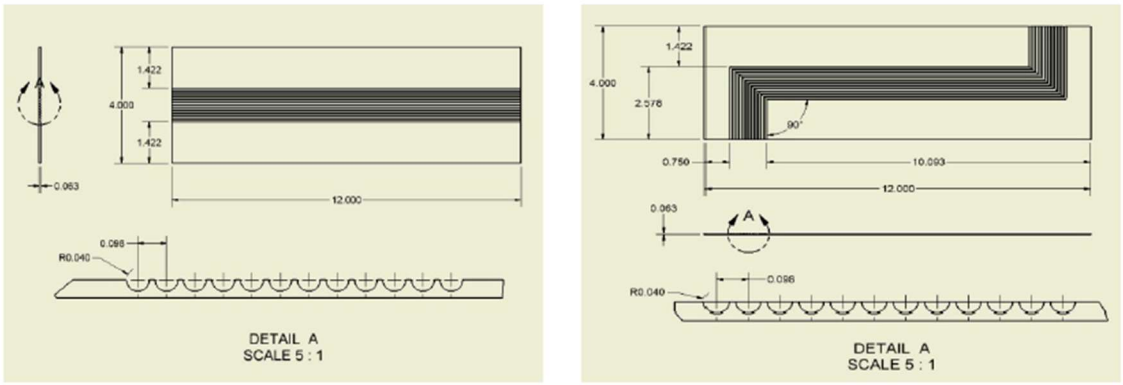

Figure 65. The configuration of recuperator PCHEs tested in HTHF

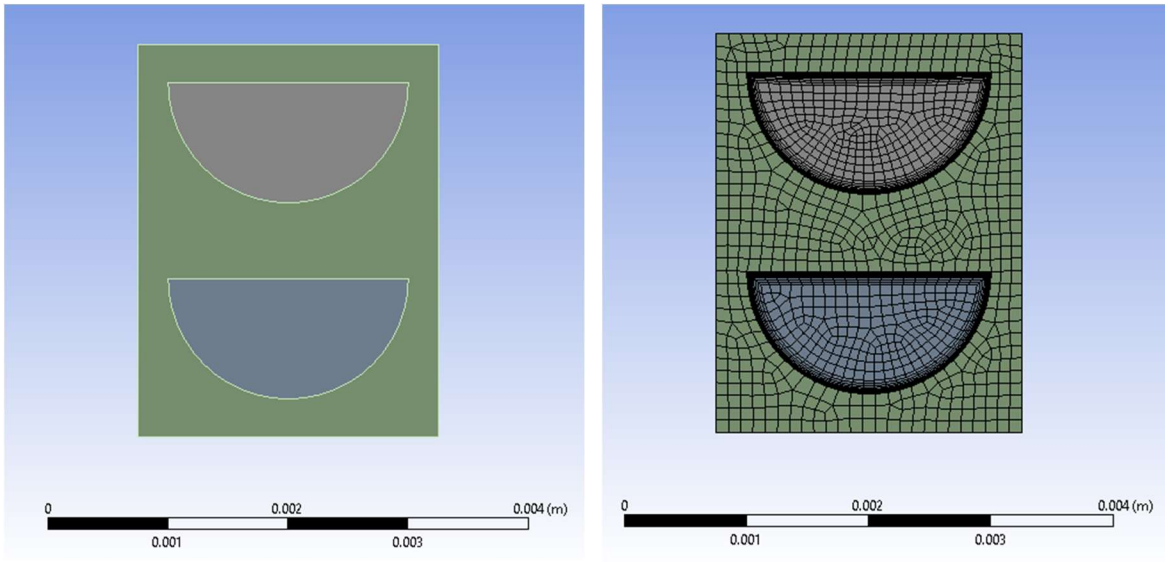

(a) (b)

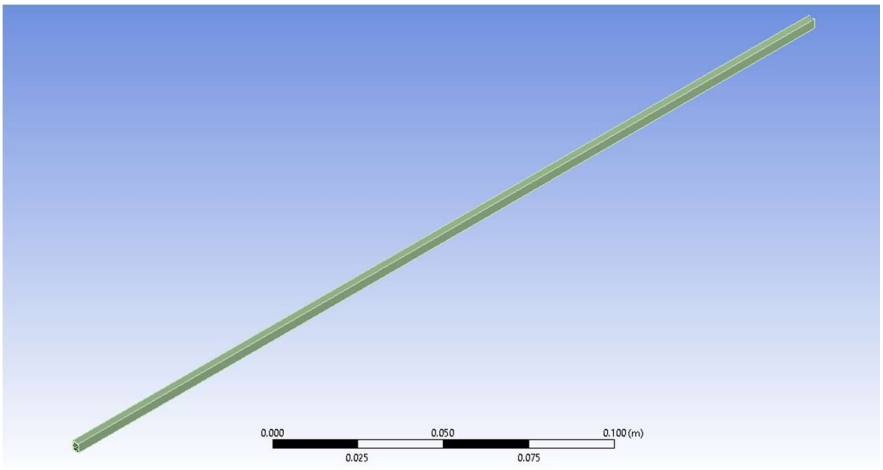

(c)

Figure 66. Modeling of straight channels in CFD: (a) Front view; (b) Mesh of channels; (c) entire model

For helium recuperator PCHEs, in general the flow falls in laminar or transitional-turbulent flow regime. The available experimental data have a wide range of Reynolds number from 1000 to 4000. Because of completely different mechanisms of laminar and turbulent flows in terms of fluid dynamics and heat transfer, in the numerical analysis these situations should be simulated separately using suitable models. The critical Reynolds number needs to be determined through multiple simulations at the transition regime validated with experimental data.

The meshing scheme can be represented by Figure 66(b). Since the entire model is a sweepable body featured by the frontal surface, a sweep method is applied to mesh the whole model. This structured mesh may save the computational cost. However, generally it may yield very large aspect ratio due to the nature of the model. In the laminar flow simulation, the inflation layers in the fluid interior close to the wall will not necessarily have a great impact on the calculation of wall shear stress, but for the turbulent flow, this may require the wall y+ value typically smaller than 1. In fact, in some of the models such as the standard k-ω model, the wall distance of the first cell adjacent to the wall should be sufficiently small such that the low-Reynolds number viscous flow can be captured by turbulence model. 3000 divisions are provided to mesh the sweep direction in fluid and 1500 in solid. 0.1 mm element size for the frontal surface is applied to both fluid and solid interior. The mesh-independence study has been investigated to ensure the accuracy of the simulation results.

Two sets of experimental data were used and input into ANSYS Fluent. Both of them are isobaric data at around 2 MPa and 2.5 MPa. The former set of data involves low and

middle range of Reynolds number while the later one involves high range of Reynolds number. The thermo-physical properties can be modelled using polynomials in terms of temperatures. The input polynomials are in the form as follows:

$$\psi\left(T\right) = a + bT + cT^2 + \ldots + fT^5 \tag{1.3.3}$$

The coefficients in the functions can be found in Table 24.

Table 24. Coefficients for the temperature functions of thermos-physical properties

Pressure	Properties	a	b	c	d	e	f
2 MPa	ρ (kg/m)	8.8910	-3.3619×10^{-2}	6.6172×10^{-5}	-7.1460×10^{-8}	4.0174×10^{-11}	-9.1972×10^{-15}
	μ $(Pa*s)$	4.3865×10^{-6}	6.1134×10^{-8}	-3.8207×10^{-11}	3.0748×10^{-14}	-1.5081×10^{-17}	3.1985×10^{-21}
	k $(W/m\text{-}K)$	3.2343×10^{-2}	4.9519×10^{-4}	-3.2997×10^{-7}	2.6742×10^{-10}	-1.3091×10^{-13}	2.7623×10^{-17}
	C_p $(J/kg\text{-}K)$	5192					
2.5 MPa	ρ (kg/m)	1.0976×10^{1}	-3.9956×10^{-2}	7.1917×10^{-5}	-6.3891×10^{-8}	2.2408×10^{-11}	n/a
	μ $(Pa*s)$	4.5175×10^{-6}	6.0023×10^{-8}	-3.3874×10^{-11}	2.2179×10^{-14}	-6.7173×10^{-18}	n/a
	k $(W/m\text{-}K)$	3.3726×10^{-2}	4.8499×10^{-4}	-2.9040×10^{-7}	1.9053×10^{-10}	-5.7328×10^{-14}	n/a
	C_p $(J/kg\text{-}K)$	5191					

The boundary conditions for inlets are set to be mass-flow-rate inlets with constant uniform flow rate normal to the surface. The outlets are set to be pressure-outlets, determined by the experimental data. It should be noted that the outlet pressure is essentially the measured absolute pressure at the outlets in the experiments. The pressure drop at the outlet header and other locations, etc. are neglected. Other surfaces are set to be adiabatic.

Data reduction method

One of the tasks in modeling PCHEs using CFD analysis is to extract thermal-hydraulic information including Fanning factor and Nusselt number from the numerical results. One of the indicators for CFD validation is to compare these two parameters with experimental data. However, it is necessary to select and clarify the data reduction method, which can be derived as follows.

Since we are interested in the pressure drop, according to the definition of local Fanning factor, we have

$$\left(\frac{dp}{dz}\right)_{local} = \frac{4f'_{local}}{D_h} \cdot \frac{\dot{m}^2}{2\rho_{local}A_c^2} = \frac{2\dot{m}^2}{D_h A_c^2} \cdot \left(\frac{f'}{\rho}\right)_{local} \tag{1.3.4}$$

By integrating the term above along the flow path, we could obtain that

$$\Delta p = \int \left(\frac{dp}{dz}\right) dz = \int \frac{2\dot{m}^2}{D_h A_c^2} \cdot \left(\frac{f'}{\rho}\right) dz = \frac{2\dot{m}^2 \Delta z}{D_h A_c^2} \cdot \sum_j^N \frac{f_j'}{\rho_j} = \frac{2\dot{m}^2 l}{D_h A_c^2} \cdot \frac{1}{N} \sum_j^N \frac{f_j'}{\rho_j} \tag{1.3.5}$$

In order to have a formulation in the form of below

$$\Delta p = \frac{2\dot{m}^2 l}{D_h A_c^2} \cdot \frac{\overline{f}'}{\overline{\rho}} \tag{1.3.6}$$

we can define that

$$\overline{f}' = \overline{\rho} \cdot \frac{1}{N} \sum_j^N \frac{f_j'}{\rho_j} \tag{1.3.7}$$

which can be used for the data reduction of Fanning factor. Then in the simulation results of ANSYS Fluent, one can rewrite the equation with:

$$\overline{f}' = \overline{\rho} \cdot \frac{1}{N} \sum_j^N \frac{f_j'}{\rho_j} = \overline{\rho} \cdot \frac{1}{N} \sum_j^N \Delta p_j \frac{D_h A_c^2}{2\dot{m}^2 \Delta z} \tag{1.3.8}$$

where Δp_j is calculated by measuring the pressure drop at each cell of different locations of interest in a pre-defined order. For heat exchangers, the density should be evaluated at the mean temperatures of inlet and outlet temperatures. Similarly, as to the heat transfer coefficient-related data reduction, since we are interested in the heat transfer rate in heat exchangers, then it is obtained that:

$$\dot{Q} = \int \left(\frac{d\dot{Q}}{dz}\right) dz = \int h P_{wet} \left(T_b - T_w\right) dz = \sum_j^N h_j P_{wet} \left(T_{b,j} - T_{w,j}\right) \Delta z \tag{1.3.9}$$

Here let's assume the heat transfer is from the fluid to the solid, which does not lose generality. In order to have a formulation in the form of below

$$\dot{Q} = \overline{h} A_s \left(\overline{T}_b - \overline{T}_w\right) \tag{1.3.10}$$

we can then define that:

$$\bar{h} = \frac{1}{\left(\bar{T}_b - \bar{T}_w\right)} \cdot \frac{1}{N} \sum_j^N h_j \left(T_{b,j} - T_{w,j}\right) = \frac{1}{\left(\bar{T}_b - \bar{T}_w\right)} \cdot \frac{1}{N} \sum_j^N \frac{\dot{m} \Delta i_j}{P_{wet} \Delta z} \tag{1.3.11}$$

where it is true that

$$h_j \left(T_{b,j} - T_{w,j}\right) P_{wet} \Delta z = \dot{m} \Delta i_j \tag{1.3.12}$$

In the simulation results of ANSYS Fluent, one can obtain enthalpy difference by the formulation below:

$$\Delta i_j = i_j \left(p_{sys}, T_j\right) - i_{j-1} \left(p_{sys}, T_{j-1}\right) \tag{1.3.13}$$

where T_j is measured at the cross-section of the flow channel at different locations of interest. However, usually the thermal-hydraulic related parameters are presented by Nusselt number. Hence we can rewrite the heat transfer coefficient into Nusselt number as shown below:

$$\mathrm{Nu} = \frac{\bar{h} D_h}{\bar{k}} = \frac{D_h}{\bar{k}\left(\bar{T}_b - \bar{T}_w\right)} \cdot \frac{1}{N} \sum_j^N \frac{\dot{m} \Delta i_j}{P_{wet} \Delta z} \tag{1.3.14}$$

Note that the data reduction method is only applicable to the Fanning factor and Nusselt number that are used to evaluate the entire performance of heat exchanger, since all of the thermo-physical properties are evaluated at the mean temperatures based on inlet and outlet temperatures. Although the averaged Fanning factor and Nusselt number can also be used for local analysis, it is not suggested to be used for s-CO_2 application since the thermo-physical properties vary largely.

Laminar flow data

Using the data reduction method above, we can extract detailed information from the simulation results to obtain corresponding Fanning factor and Nusselt number. In order to compare with the experimental results using the identical method employed in the Mylavarapu's dissertation (Mylavarapu, 2011), the definition of the Fanning factor and Nusselt number are slightly changed, as follows:

$$\bar{f}' = \frac{1}{N} \sum_j^N f_j' = \frac{1}{N} \sum_j^N \Delta p_j \frac{\rho_j D_h A_c^2}{2 \dot{m}^2 \Delta z} \tag{1.3.15}$$

$$\mathrm{Nu} = \frac{1}{N}\sum_{j}^{N}\mathrm{Nu}_{j} = \frac{1}{N}\sum_{j}^{N}\frac{D_h \dot{m}\Delta i_j}{P_{wet}k_j\left(T_{b,j} - T_{w,j}\right)\Delta z} \tag{1.3.16}$$

Figure 67 to Figure 69 shows the numerical results obtained through the formulation above compared with the experimental data. From the plots, there are two distinct lines for Fanning factor that results from the extra pressure drop in the experimental settings. One of the recuperator PCHE had relatively large additional pressure drop due to the configurations of PCHE, as explained in the dissertation. As a result, the high Fanning factor obtained from these data are not accurate and will be neglected. Therefore, it is observed that the numerically-obtained Fanning factor follows the trend of experimental data and fit very well.

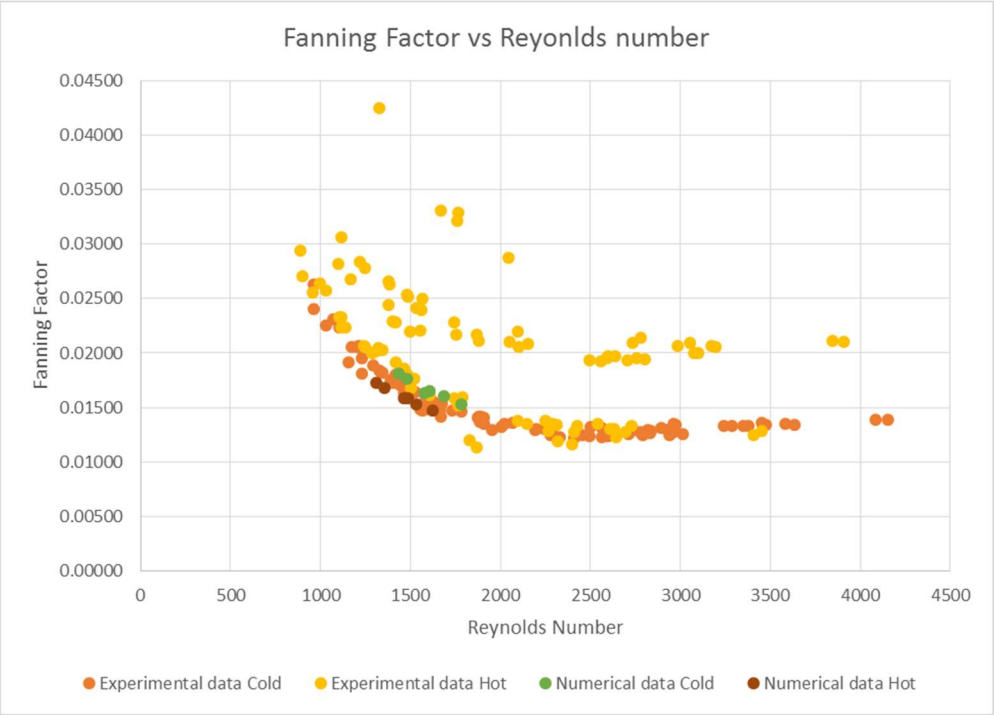

Figure 67. Fanning factor versus Reynolds number of both experimental and numerical results

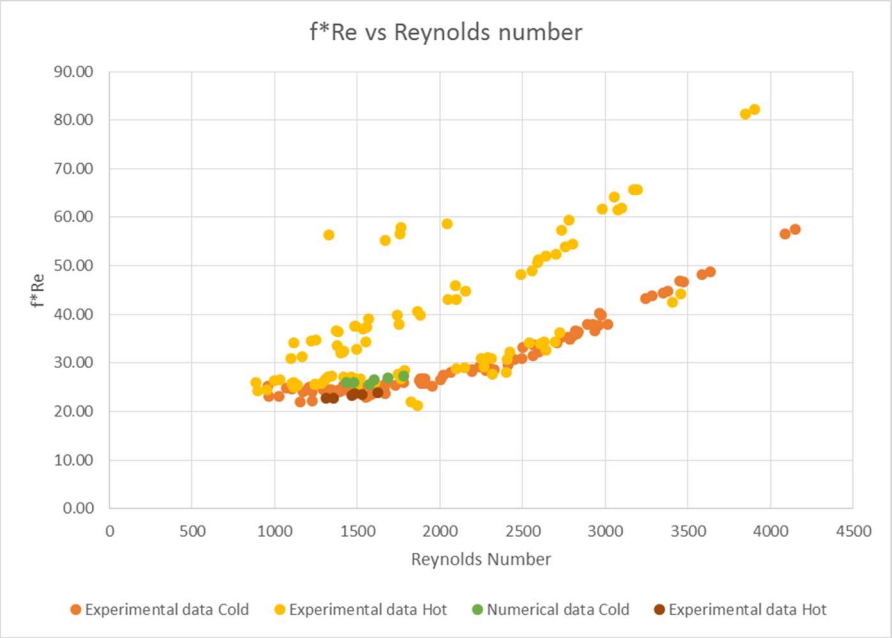

Figure 68.fRe versus Reynolds number of both experimental and numerical results

Similarly, since the heat transfer results fall within the range of experimental data, it can be concluded that the laminar flow model for Nusselt number is valid in the numerical simulation. The next step is to simulate the turbulent-transitional flow of helium in straight channels to compare with the experimental data.

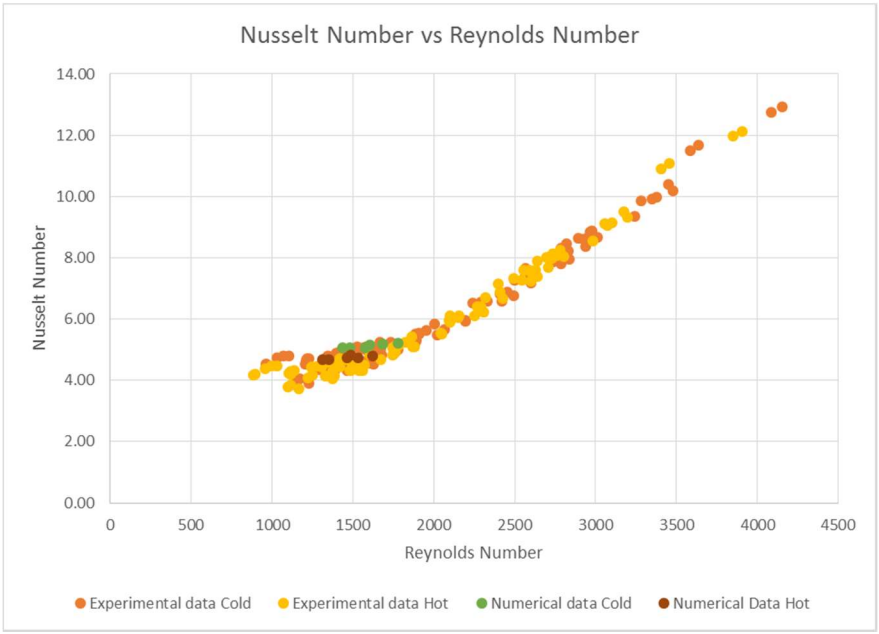

Figure 69. Nusselt number versus Reynolds number of both experimental and numerical results

1.3.3 CFD Optimization of S-shaped Fins

Review of Geometrical Characteristics of S-Shaped Fins

The reference S-shaped fin channels are designed based on the S-shaped-fin PCHE that was tested in TIT (Tokyo Institute of Technology). The detailed information of the geometrical parameters can be found in Figure 3 and Table 2.

The equation-based curves that constitutively form the shape of the S-shaped fins are defined by the fin length l_f, fin angle φ, and fin width d_f. The periodically-staggered pattern is determined by the logitudinal pitch p_x and the transverse pitch p_y. The sinusoidal curve can be expressed by

$$y = \xi \sin(\omega x) \tag{1.3.17}$$

The relationships between the geometrical parameters and ξ, ω are defined as

$$\xi = \frac{1}{2} l_f \sin\psi \tag{1.3.18}$$

$$\omega = \frac{\pi}{l_f \cos\psi} \tag{1.3.19}$$

where the pitch angle ψ can be obtained from:

$$\frac{\pi}{2}\tan\psi = \tan\varphi. \tag{1.3.20}$$

The S-shaped fin can be formed by shifting the sinusoidal curve along a direction vector (*a, b*), which can be computed by

$$a = \frac{d_f \cos\beta}{2\cos\left(\frac{\pi}{2} - \varphi - \beta\right)}, \tag{1.3.21}$$

$$b = \frac{d_f \sin\beta}{2\cos\left(\frac{\pi}{2} - \varphi - \beta\right)}, \tag{1.3.22}$$

where β is the direction vector angle with respect to the *x*-axis. It is a user-defined parameter that controls the arc length of the fin tips. Different values of β result in a different shape of S-shaped fins, which also affects the thermal-hydraulic characteristics. Generally, a large direction vector angle leads to a long arc of the fin tip. For some S-shaped fins' shapes with small fin length and fin angle, β needs to be sufficiently small such that a sinusoidal fin shape can be formed.

The transverse pitch p_y is dependent on the fin gap g_p, which is further dependent upon the fin height H_f (also referred to as the channel depth) and the fin width d_f due to the mechanical strength requirement. In the mechanical analysis, two neighboring S-shaped fins are assumed to be treated as two ridges for a typical zigzag channel. It is recommended to use the Eq. (1.5.21) for a simplified mechanical analysis to determine the zigzag channel's ridge thickness $d_{f,zz}$:

$$d_{f,zz} = \left(\frac{\Delta p}{\sigma_D}\right) g_p, \tag{1.3.23}$$

where Δp and σ_D are the pressure differential between plates and the maximum allowable stress of the plate base material, respectively. Therefore, we can use the same equation to determine the fin gap g_p:

$$g_p = \left(\frac{\sigma_D}{\Delta p}\right) d_{f,ss}. \tag{1.3.24}$$

The neighboring fin distance d_y can then be obtained as follows:

$$d_y = d_f + g_p. \tag{1.3.25}$$

Therefore, we can calculate p_x and p_y by

$$p_x = 2l_f \cos\psi, \tag{1.3.26}$$

$$p_y = d_y \big/ \cos\psi. \tag{1.3.27}$$

As the etching process usually creates a semi-circular cross-sectional profile, it is reasonable to assume that the fin height is only half of the fin gap, i.e.,

$$H_f = \frac{1}{2} g_p. \tag{1.3.28}$$

Therefore, we can conclude that the geometrical characteristics of the S-shaped fin channels can be defined by the fin angle, fin length, fin height and fin width. The latter two parameters are actually dictated by the required mechanical strength. As analyzed in a previous study, the reference S-shaped fin model was simulated with prescribed mechanical loading, showing reliable structural integrity under a pressure differential up to 15 MPa. Accordingly, the fin height and fin width will be identical to those in the reference model.

It is noted that the tips' roundness and the arc length of guide wings in the S-shaped fin channels also play an important role in the thermal-hydraulic performances. However, the roundness radius is difficult to be controlled in the current etching technique, since the S-shaped fins' width is in the length scale of 1 mm. The tips may be completely etched away in some cases. In this study, the roundness radius is recommended to be 0.1 mm. Regarding the arc length, it is essentially dictated by the direction vector angle, and in some particular S-shaped fin designs with extremely small fin angle and small fin length, it is even impossible to form the S-shaped fin by shifting the sinusoidal curves. For a simplified analysis, the direction vector angle is defined to be 10° and the effect of the arc length will not be considered.

Numerical Simulation

Numerical studies were carried out to investigate the thermal-hydraulics of the various designs of S-shaped fin channels. Due to the periodic nature of S-shaped fin channels, a computational model consisting of two rows of fins that are periodic in both *x*- and *y*-direction, as shown in Figure 70, is selected to reduce the computational cost in CFD simulations. There are 13 plus 2 halves of solid fins in the conjugate heat transfer model. Three plates sandwich both hot and cold fluid flow domains. The boundary conditions are all set to be periodic except the inlets and outlets as well as the front and rear adiabatic walls. Therefore, the computational domain can simulate an infinitely large core without any wall effects. The actual dimensions of the computation model are specified by the particular study case.

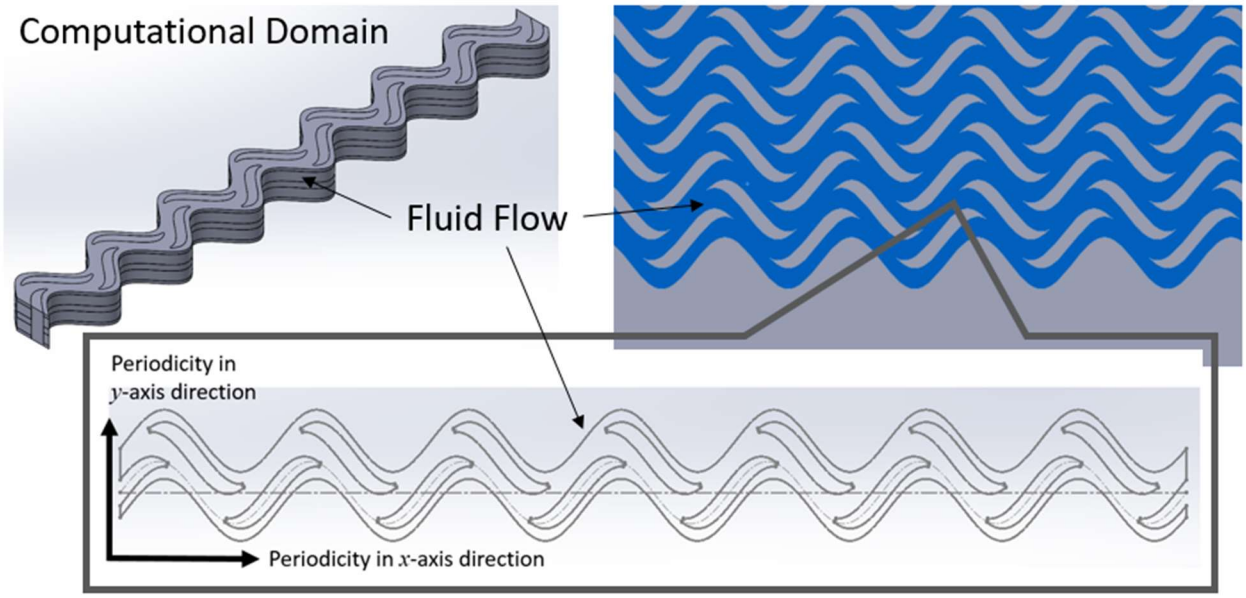

Figure 70. The Periodicity of the Computational Domain.

Besides the CFD simulation of the reference model, 9 cases were also simulated, which were selected by Latin hypercube sampling in terms of two design variables, i.e., the fin angle and fin length. Figure 71 shows the surface geometry of S-shaped fin channels in the 9 cases. The detailed information is listed in Table 25. In these models, the fin height and fin width were specified to be 0.94 mm and 0.8 mm, respectively. The direction vector angle is chosen to be 10°, as explained in the previous section. The distribution of the samplings is also shown in Figure 71. It should be noted that the cases with extremely small fin angle and fin length often result in difficulties in CAD modeling. Consequently, the sampling space is defined to be 10 - 60° for the fin angle and 4 - 16 mm for the fin length.

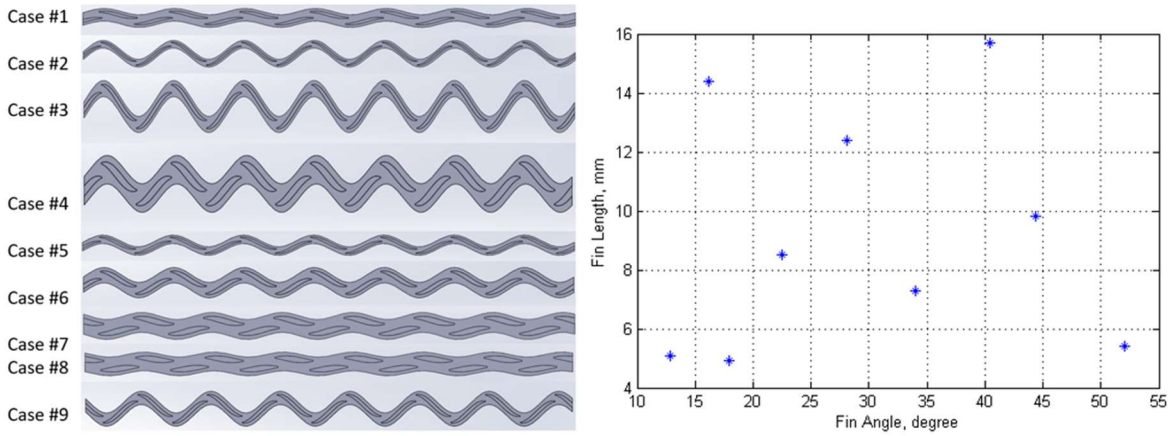

Figure 71. The S-shaped Fin Simulation Model of 9 Cases and the Distribution in the Design Space.

Table 25. Geometrical Parameters of 9 Cases of S-shaped Fin Design

Case	ϕ	l_f	ψ	ξ	ω	a	b	p_x	p_y
Units	degree	mm	degree	mm	mm-1	mm	mm	mm	mm
1	16.17	14.45	10.46	1.311	0.221	1.34	0.24	28.36	5.04
2	40.43	15.74	28.48	3.750	0.227	0.51	0.09	27.62	3.05
3	22.50	8.50	14.78	1.084	0.382	0.73	0.13	16.44	2.77
4	51.97	5.45	39.15	1.719	0.743	0.45	0.08	8.45	3.45
5	28.15	12.38	18.82	1.995	0.268	0.64	0.11	23.46	2.83
6	34.02	7.26	23.26	1.432	0.471	0.57	0.10	13.33	2.92
7	17.86	4.92	11.60	0.494	0.652	0.84	0.15	9.63	2.74
8	12.87	5.13	8.28	0.369	0.619	1.46	0.13	10.15	2.70
9	44.37	9.84	31.93	2.600	0.376	0.48	0.09	16.70	3.16

Tsuzuki et al. (2009) performed a parametric study on the shape of the S-shaped fins using 3D-CFD simulation. Three turbulence models in the Fluent code were used to compare with the experimental results. It was recommended to use k-ε RNG model due to the relatively more accurate heat transfer calculations than other k-ε models. In the current studies, both k-ε and k-ω turbulence models were used in the CFD simulation using ANSYS-Fluent. It was found that k-ω models were difficult to obtain converged results while the simulation of k-ε models was able to converge with the relaxation factor reduced. One of the possible reasons for that phenomenon can be the inappropriate uniform pressure outlet boundary conditions. The velocity field at the middle cross-sections of the S-shaped fins is not uniform due to the presence of neighboring fins, thus creating pressure gradients at those cross-sections. Therefore, it is possible that some turbulence models will fail because of the uniform outlet pressure boundary condition specified in the simulation. As to the k- ε models, the results showed that there was no obvious difference between k-ε RNG and k-ε Realizable model. Eventually, we chose the k-ε Realizable model for more stable convergence.

Four meshing schemes were tested for mesh independence study in the reference model, as listed in Table 26. All parts in the computational model use sweep meshing method to reduce the overall number of element. Since the fluid flow contacts the solid fin walls as well as the top and bottom plate walls, the cells adjacent to the solid fin walls are inflated with 10 layers while the cells close to the top and bottom walls are biased meshed in sweeping direction, as shown in Figure 72. The Meshing Scheme for Both Fluid and Solid Computational Domain.. It was found that the difference in the heat transfer performances between the medium-fine and fine meshing schemes is negligible while the difference of the pressure drops is less than 1%. Therefore, the medium-fine mesh is chosen.

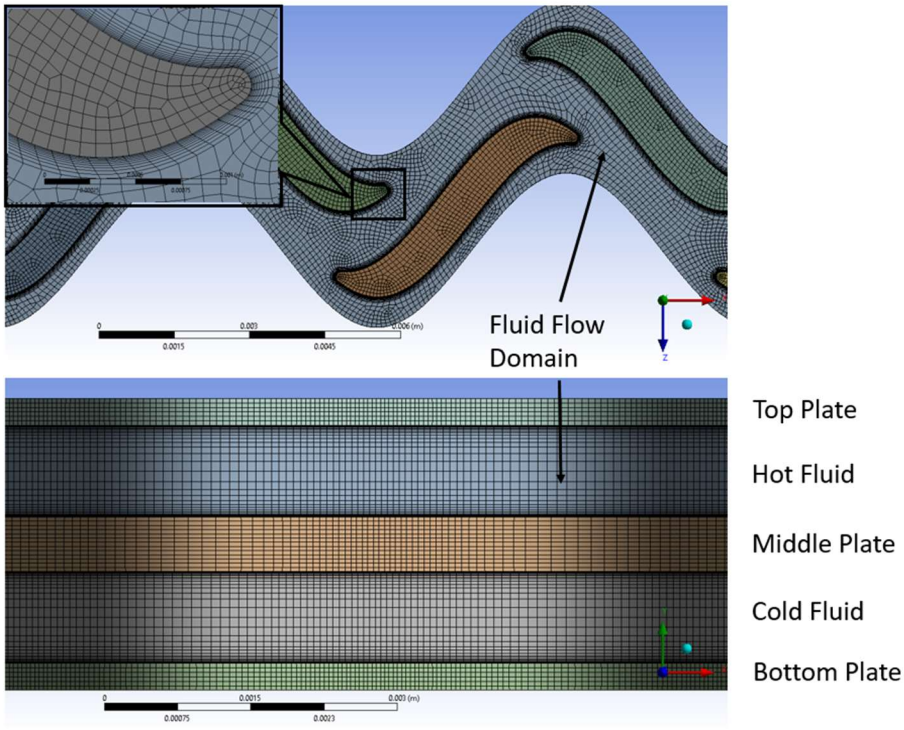

Figure 72. The Meshing Scheme for Both Fluid and Solid Computational Domain.

Table 26. Mesh Independence Study

Description	Mesh Elements in Fluid Flow Domain	Pressure Drop (kPa)	Relative Deviation
Coarse	1,568,330	82.385	5.68%
Medium	2,697,300	79.747	2.30%
Medium-Fine	4,856,300	78.352	0.51%
Fine	6,253,150	77.956	0.00%

For the simulations of 9 cases, polynomial functions of the s-CO_2 thermo-physical properties were used for the temperature range of 150 to 700°C and the system pressure of 15 MPa. The data were retrieved from the NIST Webbook (National Institute of Standards and Technology). The base material was selected to be alloy 617, the same as the one used in the prototypic PCHE.

A pressure drop factor, defined as the pressure drop per unit length, can be used to analyze the pressure drop characteristics, which is defined as follows:

$$\delta P = \frac{P_1 - P_2}{L_{12}}. \tag{1.3.29}$$

This pressure drop factor does not currently involve Reynolds number dependence. All of the simulations assume a fixed Reynolds number of typical 20,000. Therefore, the mass flow rate is accordingly adjusted. The subscript 1 and 2 denote the selected locations of the area-averaged gauge pressure. The global heat transfer coefficient is calculated as

$$h = \left| \frac{Q}{A_s(T_w - T_b)} \right|. \tag{1.3.30}$$

Because of the complexity of the S-shaped fin's geometry, it is difficult to obtain an averaged local heat transfer coefficient. Therefore, the temperature difference between the wall and the bulk fluid is defined to be half of the logarithmic mean temperature difference (LMTD). The simulation results of 9 cases are listed in Table 27.

Table 27. Simulation Results of 9 Cases of S-shaped Fin Designs.

Case	$T_{c,in}$	$T_{h,in}$	$T_{c,out}$	$T_{h,out}$	P_1-P_2	δP	h
Unit	K	K	K	K	kPa	kPa/mm	W/m2-K
1	675	875	804.4	747	6.21	0.044	3245.0
2	675	875	821.7	729.7	15.62	0.113	3638.2
3	675	875	793.1	758.7	8.16	0.099	4067.5
4	675	875	787.9	764.7	13.22	0.313	4384.8
5	675	875	810.7	740.8	11.89	0.101	3922.4
6	675	875	791.8	759.9	8.26	0.124	3321.8
7	675	875	767.5	784.2	5.58	0.116	4379.4
8	675	875	766.3	785.5	5.03	0.103	4085.5
9	675	875	805.7	745.9	11.74	0.141	3842.7

Shape Optimization of the S-shaped Fin Channels

Based on the simulation results, it is possible to perform a shape optimization of the S-shaped fin channels for the application to the reference PCHE. As discussed beforehand, the design variables are the fin angle and fin length, as these two factors are critical to the thermal-hydraulic performances of the S-shaped fin channels. The design space is identical to the sampling space. The objective functions are selected to the test PCHE thermal effectiveness and the pressure drop across the core. Regarding the thermal modeling of the test PCHE, various design models of the S-shaped fin channels are used in the evaluation of the two objective functions, where the pressure drop and heat transfer coefficient are calculated using a surrogate model. It is noted that since there is no Reynolds number dependence in the developed surrogate model. For the reference

PCHE, the number of S-shaped fin channels and the core length of the heat exchanger are pre-defined. A second order RSM (Response Surface Methodology) surrogate model is developed based on the simulation results, which can be expressed by:

$$y = \beta_0 + \sum_{j=1}^{k} \beta_j x_j + \sum_{j=1}^{k} \beta_{jj} x_j^2 + \sum \sum_{i<j=2}^{k} \beta_{ij} x_i x_j \tag{1.3.31}$$

where x, y and β are the design variables, dependent variables, and RSM coefficients, respectively. The calculated coefficients are listed in Table 39. Note that since the heat transfer area and hydraulic diameter of S-shaped fin channels are difficult to be calculated directly from the geometrical parameters, the corresponding surrogate models for the hydraulic diameter and heat transfer area are also developed as well, as listed in Table 28. Figure 73 and Figure 74 show the thermal-hydraulic dependence on the fin angle and fin length using the surrogate model.

Table 28. Coefficients of RSM Surrogate Model.

Description	Heat transfer area	Hydraulic diameter	Pressure drop per unit length	heat transfer coefficient
symbol	A_s	D_h	δP	h
β_0	6.511	1.170	1.391×10^{-1}	5.084×10^{3}
β_1	-6.175×10^{-2}	4.824×10^{-3}	9.751×10^{-3}	-1.033×10^{3}
β_2	-2.802×10^{-1}	6.114×10^{-2}	-5.948×10^{-2}	4.682×10^{2}
β_3	7.527×10^{-2}	5.921×10^{-5}	1.369×10^{-2}	1.932×10^{2}
β_4	9.338×10^{-2}	-1.263×10^{-2}	4.306×10^{-2}	7.636×10
β_5	-5.417×10^{-2}	1.121×10^{-3}	-4.154×10^{-2}	-2.064×10^{2}

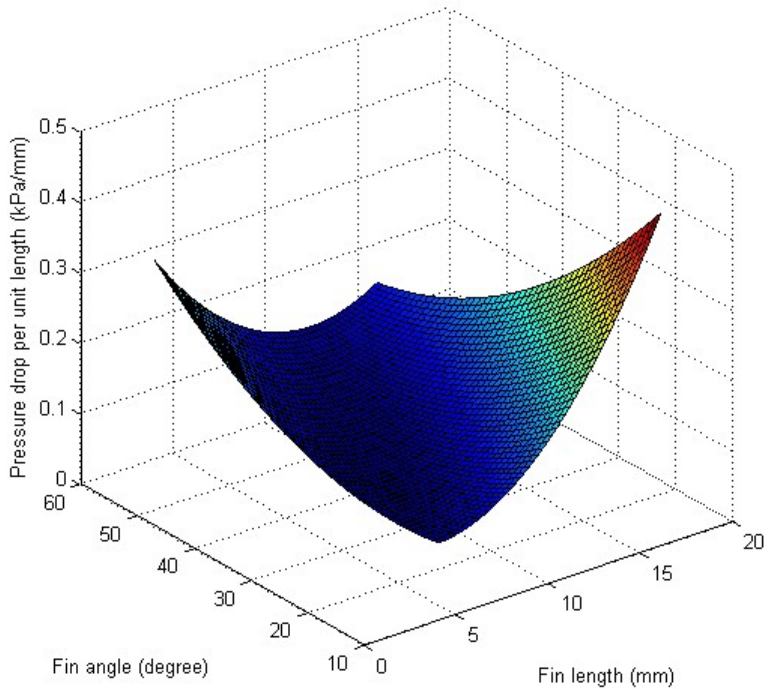

Figure 73. The Pressure Drop Dependence based on the Surrogate Model

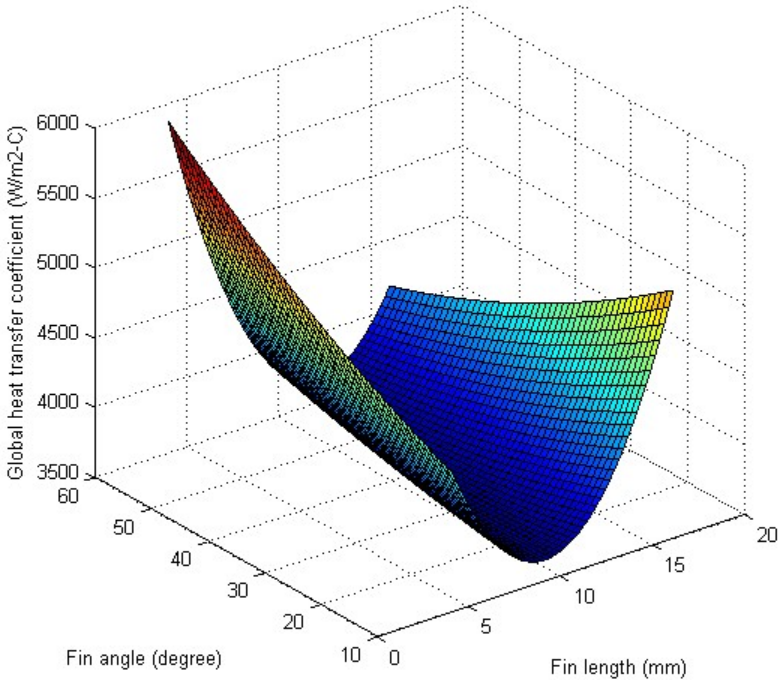

Figure 74. The Heat Transfer Coefficient Dependence based on the Surrogate Model

With respect to the pressure drop across the heat exchanger core, it can be calculated through the pressure drop factor and the heat exchanger core length. Regarding the heat exchanger thermal effectiveness, a counter-flow ε-NTU method is adopted. With the

assumption of a simple slab heat conduction model between the hot and cold sides using the mean plate thickness t_o, the overall heat transfer coefficient U can be calculated by:

$$\frac{1}{U_h A_{s,h}} = \frac{1}{U_c A_{s,c}} = \frac{1}{h_h A_{s,h}} + \frac{t_w}{k_w A_{s,w}} + \frac{1}{h_c A_{s,c}} \tag{1.3.32}$$

Like the optimization of zig-zag channel PCHEs,, NSGA-II, one of popular genetic algorithms, is used in the shape optimization. The in-house NSGA-II code was was used to optimize the shape of S-shaped fins in terms of the evaluation of both the heat exchanger core pressure drop and thermal effectiveness.

Figure 75 shows the entire solution space with 5,000 sampled S-shaped fin designs. It can be observed from the distribution of the solutions that generally the heat exchanger core pressure drop increases as the heat exchanger thermal effectiveness increases. This is consistent with the expectation that the minimization of the pressure drop and the maximization of the heat transfer performance are usually conflicting with each other. Figure 75 also shows the Pareto-optimal solutions using the NSGA-II algorithm and the corresponding clustered solutions, which are listed in Table 29. Figure 76 shows the distribution of the fin angle and the fin length for all of the Pareto-optimal solutions. It indicates that the optimized designs can be divided into two groups: the low-angle-fin group and the high-angle-fin group. In the low-angle-fin group, the small-angle S-shaped fins are able to reduce the pressure drop since small angles streamline the flow and mitigate the flow stagnation that is usually found at the tips of fins. Long fins are also favorable in pressure drop reduction since the flow can be stabilized through long fin channels. However, the thermal effectiveness is decreased for long fins because the thermal boundary layer is developed through long fin channels and the heat transfer becomes worse. For S-shaped fins with a fin angle of 10°, a long fin body creates a long fin tip that separates the flow along the fin body, (e.g. a S-shaped fin design with 10° fin angle and 12.88 mm fin length, as shown in Figure 77, which increases the pressure drop and enhance the heat transfer simultaneously. In the high-angle-fin group, most of the S-shaped fin designs are the ones with the fin angle of 60°. Short fins are favorable in terms of the thermal effectiveness. However, the pressure drop increases as the fin length decreases. Therefore, we recommend the S-shaped fin channel with 11.6° fin angle and 6.08 mm fin length for the low pressure-drop applications and the one with 60° fin angle and 9.95 mm fin length for the medium-pressure-drop and high-thermal-effectiveness applications.

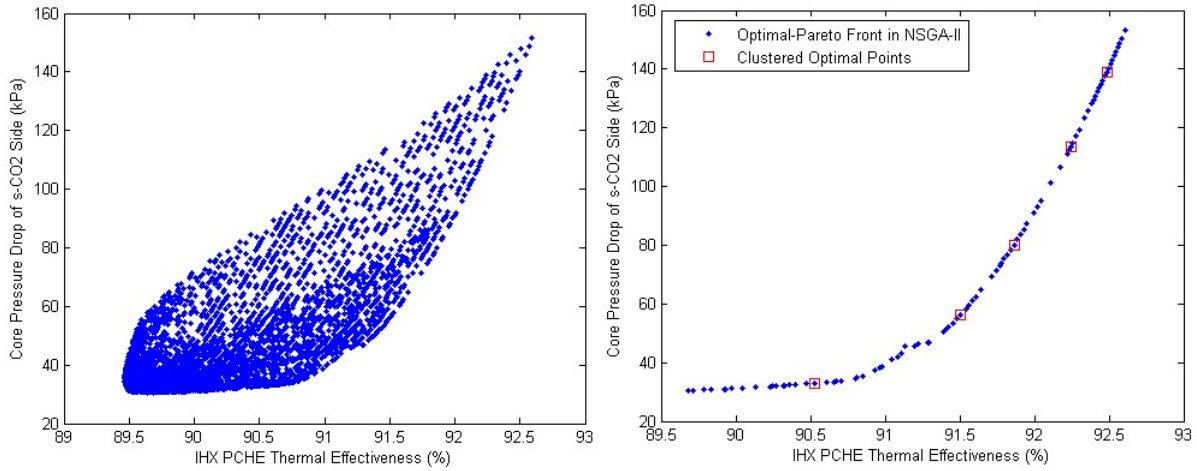

Figure 75. 1.5.14. The Population of 5,000 Solutions in the Design Space (left) and the Optimization Results using NSGA-II and the Clustered Results (right)

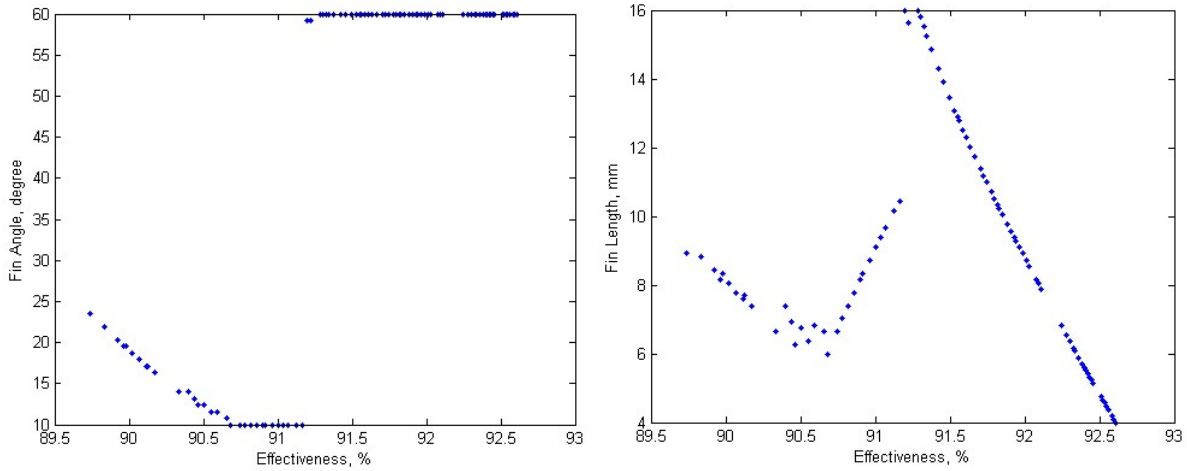

Figure 76. The Optimization Results using NSGA-II and the Clustered Results

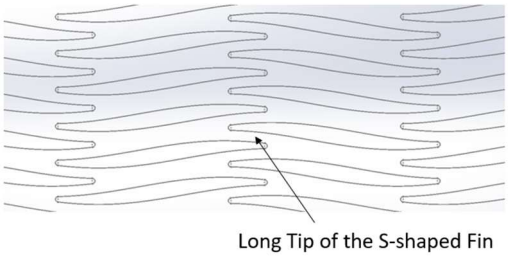

Figure 77. The Schematic of the S-shaped Fin with 10° Fin Angle and 12.88 mm Fin Length

Table 29. Design Parameters of 5 Clustered Solutions from Optimization.

Item	Symbol	Units	#1	#2	#3	#4	#5
Fin angle	φ	degree	11.6	60.0	60.0	60.0	60.0

Fin length	l_f	mm	6.08	13.35	9.95	6.83	4.94
HX capacity	Q	kW	13.46	13.60	13.66	13.71	13.75
Cold side mass flow rate	q_m	kg/s	0.067	0.084	0.085	0.087	0.089
Cold side inlet temperature	$T_{c,in}$	°C	418.8	418.8	418.8	418.8	418.8
Cold side outlet temperature	$T_{c,out}$	°C	591.6	593.5	594.2	594.9	595.3
Reynolds number	Re	n/a	20000	20000	20000	20000	20000
HX core cold side pressure drop	Δp	kPa	33.04	56.28	80.17	113.46	138.94
Cold side heat transfer coefficient	h	kW/m^2-°C	4.538	4.329	4.611	4.931	5.154
Overall heat transfer area	A_s	m^2	0.122	0.154	0.156	0.160	0.163
HX thermal effectiveness	ε	%	90.53	91.51	91.86	92.24	92.48
Number of heat transfer units	NTU	n/a	4.00	4.25	4.35	4.45	4.53

1.4 Perform Numerical Modeling of Thermo-mechanical Stress of PCHEs

1.4.1 Qualitatively static stress numerical analysis on S-shape fins

Conventional zigzag type PCHEs are capable of withstanding higher pressure with adjusting transversal pitch and plate thickness, which can be analyzed by hand calculations. Additionally, many years of accumulated experience in industry has made safety recommendations on the mechanical integrity, especially for the zigzag channels. In contrast, as an advanced PCHE surface, it is questionable whether the S-shape fin can withstand harsh operating conditions, such as the pressure differential up to 13 MPa in helium-s-CO_2 IHXs. Although the S-shaped fin channels evolved from the conventional zigzag channels by transforming into sinusoidal curve and then offset the configuration, the stress distribution is not similar to the one of zigzag type PCHEs anymore. Furthermore, like the shape of airfoil fins, the S-shaped fins possess sharp edges at the tips of fins, which are certainly expected to experience fairly large stress concentration. This mechanical concern might not be as serious as thought because in reality the chemical etching may, to some degree, round the tips such that severe stress concentration will be mitigated. Nevertheless, these spots will still experience relatively large stress either in static or transient situations. Other concerns might be related to the diffusion bonding area along the edge of the S-shape fins connecting the upper plate, as shown in the sectional view of the model in Figure 78. Therefore, it is necessary to perform stress analysis using commercial 3-dimensional simulation tool, in this case, ANSYS

Workbench to measure the thermo-mechanical stress and to assure the mechanical integrity of the S-shaped fin PCHEs.

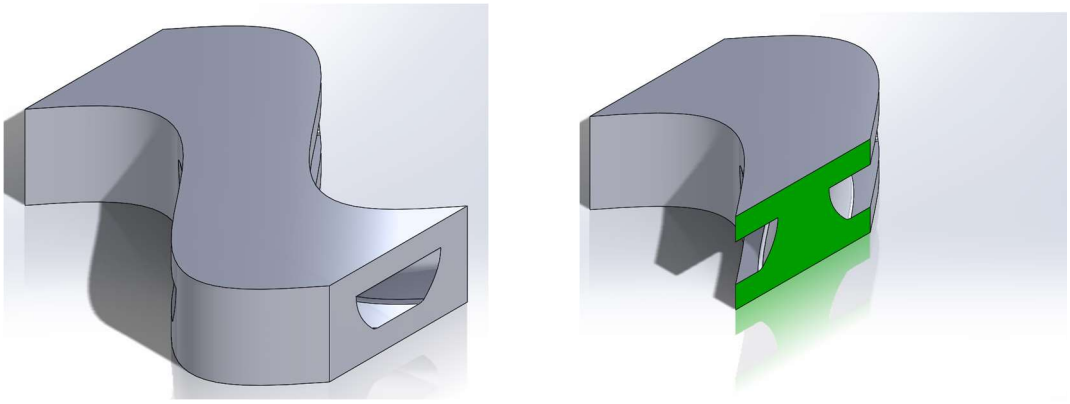

Figure 78. Isometric view and sectional view of the single-fin unit cell model

The reference model is basically based on the S-shape fin type PCHEs tested by Ngo, et al. (2007). The sinusoidal curve functions are governed by the parameters given in the literature, but the S-shaped fin's dimensions according to the curve functions in the numerical model deviate from the recorded values in the Ngo's experiments. In order to get simulations in accordance with the experimental data when this numerical model is analyzed in CFD studies, the final actual dimensions are adjusted to be identical with those in Ngo's experimental tests. The details of the model dimension are listed inTable 2.

In the mechanical analysis, several unit cell models are created to address inherent modeling challenges in the S-shape fins. The reference model has more compactness in the transversal direction such that it is impossible to create a unit cell model like the one shown in Figure 78. The S-shape fin unit cell model is linearly periodically symmetric in either direction, therefore there are two different models available shown in Figure 79, which can, theoretically, model the stress distribution identically. However, in the current capability of ANSYS, it is difficult to model two-direction linear periodic symmetry. This implies that at least in one direction, the boundary conditions other than the linear periodic symmetry will be applied, which will certainly affect the simulation results. This type of difficulty imposed by S-shape fin's inherent features may require other approaches to reduce the effect of different boundary conditions. In this case, multiple-fin models are created to address the problem. Figure 80shows three models used in the numerical analysis. It is noteworthy that these models are modeled with fillet of which dimension is based on the one measured in the airfoil fin PCHEs fabricated by UW.

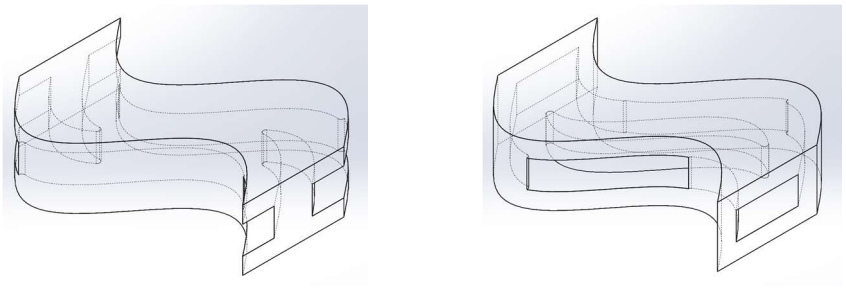

Figure 79. Two proposed unit cell models that can simulate identical cases

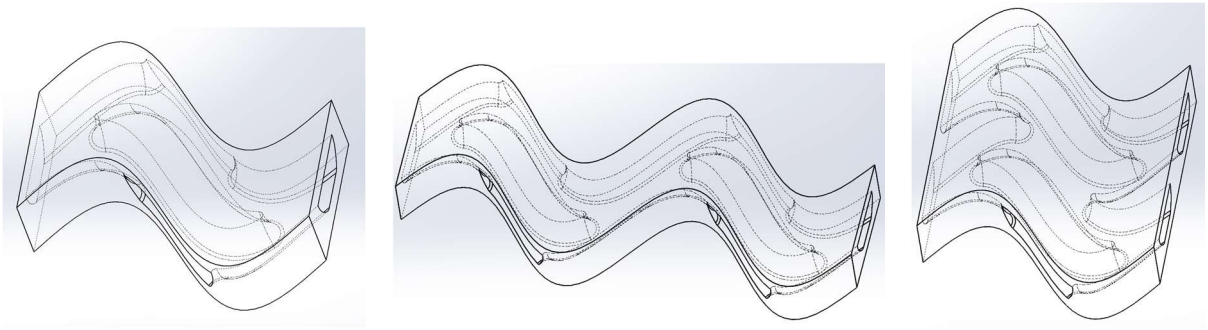

(1) Single-fin unit cell model; (2) Longitudinal multiple-fin model; (3) Transversal multiple-fin model

Figure 80. 3-D S-shaped fin models used in mechanical analysis

The meshing utilizes global medium mesh sizing with advanced function turned on. Body of influence is used to refine the mesh around the diffusion bonding area, with the mesh size in the range of 0.07 to 0.03 mm. The statistic information of elements has been listed in Table 28.

Table 30. Statistic information of cases studied

Model	Mesh Size	Number of Elements	Max. Stress (MPa)
Single-fin #1	0.05 mm/0.07 mm	164,922	131.75
Single-fin #2	0.02 mm/0.05 mm	1,295,579	137.46
Multiple-fin #3	0.05 mm/0.07 mm	317,373	129.17
Multiple-fin #4	0.03 mm/0.05 mm	1,071,008	135.52
Multiple-fin #5	0.05 mm/0.07 mm	303,874	129.33
Multiple-fin #6	0.03 mm/0.05 mm	1,050,929	144.43

The original analysis results show that the diffusion bonding areas of the S-shape fin experience stress beyond the yield strength of the material of the plates that is currently set up as stainless steel 316. This indicates that it is necessary to invoke non-linear analysis for these specific problems. The material strain-stress curve information is

obtained from the ASME code with multiple linearity fitting provided by UW-Madison. Considering a 13-MPa pressure differential between the hot and cold sides, hot helium and cold s-CO_2 in this case, a uniform force load of 336 N is imposed at the top of the model. Because the simulation always fails with the linear periodic symmetry as the boundary conditions, the frictionless support boundary conditions have to be then introduced to the model, which somehow distorts the simulation result, especially for the unit cell model. As shown in Figure 81, the maximum stress concentration occurs at the longitudinal side boundary surface. The deflection is automatically scaled shown in the figure. This cannot be explained as a real-life stress situation since no severe stress concentration is observed right in the middle cross-section of the single S-shape fin in the model, which is centrosymmetric with side boundary surface. This fact verifies the previous statement that the frictionless support boundary conditions largely distort the simulations, which can be explained as the result of absence of loads supposed to be added somewhere at the quarterly fins around the unit cell models corners.

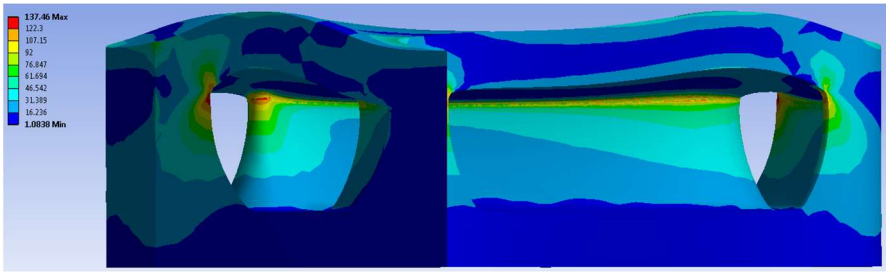

(1) Stress distribution (max. stress 137.46 MPa);

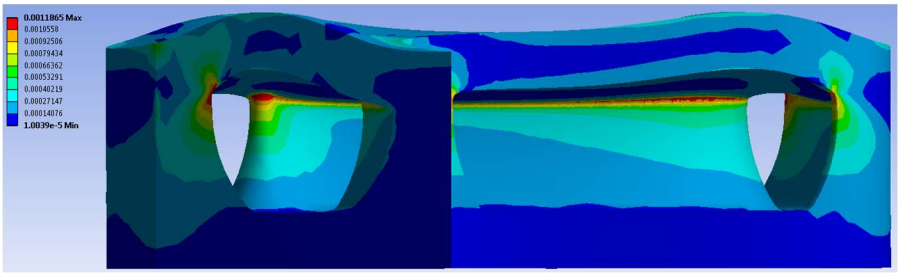

(2) Strain distribution (max. strain 1.1865%)

Figure 81. Stress and strain distributions in the single-fin model #2 (right side view)

These quarterly fins, as expected, may be supported in reality by other quarterly fins in the near-by unit cell models, which, however, fails to be reflected in the current simulations. Figure 82 has shown the configuration of S-shaped fins on a typical plate. There are several strategies proposed to reduce the effect the boundary conditions may have on simulation results. One of them is to model multiple fins of which some portions of the fins are far away from the boundary conditions. Figure 83 have shown a series of

comparison of single-fin and multiple-fin models. It is obvious that the stress distribution is more realistic. However, the CPU time that the simulation costs has increased dramatically. In addition, the maximum stresses detected at the fin tips in both models are still not matched up. Nonetheless, some conclusions can be drawn from the preliminary qualitative analyses of both simulations.

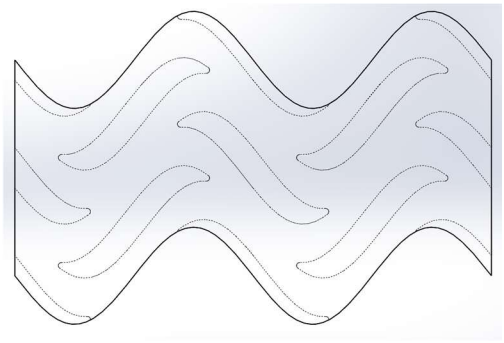

Figure 82. Stress and strain distributions in the single-fin model #2 (right side view)

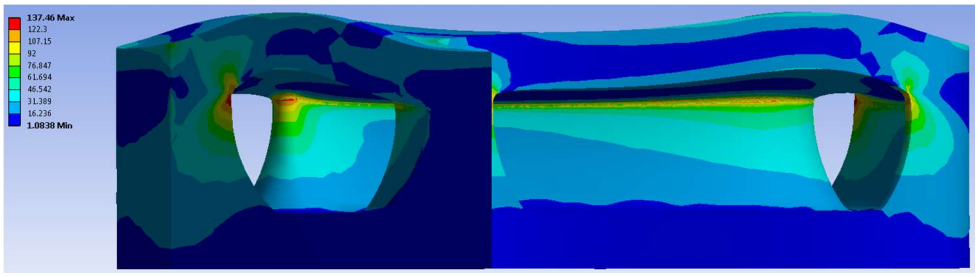

(a.1) Right view of the stress distribution of the single-fin model case #2

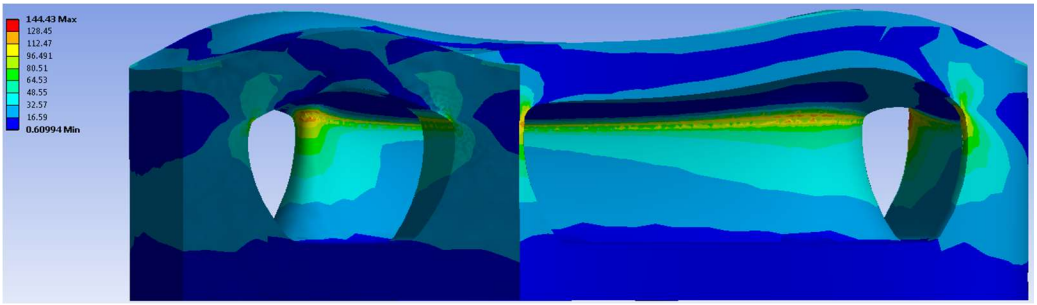

(a.2) Right sectional view of the stress distribution of the multiple-fin model case #6

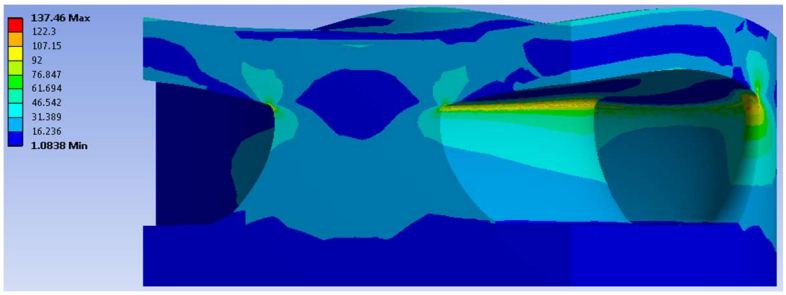

(b.1) Right sectional view of the stress distribution of the single-fin model case #2

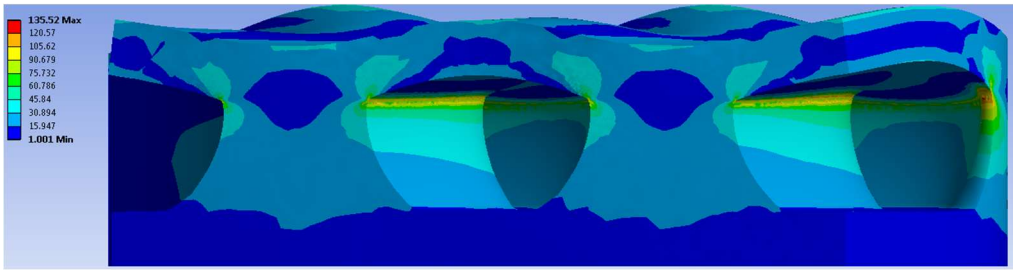

(b.2) Right sectional view of the stress distribution of the multiple-fin model case #3

Figure 83. Comparison of the stress distribution between the single-fin and multiple-fin models

Firstly, the stress concentration spots observed in the single-fin model simulations disappear when we observe longitudinal-multiple-fin model at the sectional view, which verifies that the frictionless support boundary conditions may affect simulation result, as discussed above. Second, from the second pair of comparison, we can observe that in the multiple-fin model, the stress along the edge of fin and upper plate is mitigated, which is possibly due to the frictionless support boundary conditions at sinusoidal curve side surfaces. Furthermore, it is observed that the stresses at the tip of the fin in the multiple-fin model are mitigated compared with those in the single-fin model. Therefore, we can conclude the single-fin model is more conservative than the real situations, considering harsh boundary conditions. With regard to high stress location, it is observed that high stresses occur at both the fin tip and diffusion bonding edge, where the sinusoidal curve bends at the peaks. In Figure 83, it can be observed that the bends at the peaks are less supported by neighboring fins than other portions of the curve. The second location of high stresses is probably due to the configuration of the fins on the plate. From Figure 94, it can be observed that the peak portion of the upper and bottom sinusoidal curves that shape the fin are least mechanically supported by the neighboring fins, which lead to higher stresses along those diffusion bonding areas.

Finally, the maximum stress shown in the simulation results is around 130 MPa, no matter where it occurs, at unrealistic spots or the fin tips. And the average stress along the diffusion bonding area is around 100 MPa. The tensile yield strength is 117 MPa at the

temperature where the simulations are run. This indicates that the percentage of elements that would be yielded need to be examined to determine whether the fins will fail in the situation of 13 MPa pressure differential. This may be further investigated in the future research work.

1.4.2 Quantitative static stress numerical analysis on S-shape fins

In this stress assessment, ANSYS-Mechanical has been used to model the stress distribution. A rectangular-shape model with no fillets was chosen for the reference simulation model. The fillets of the S-shaped fin that connect the fin body and the bottom plate, as shown in the Figure 84(a), are formed due to the nature of the photo-chemical etching. These fillets that are essentially the by-products of the etching process are beneficial because of its potential mitigation of stress concentration at the bottom plate, as is discussed in the later section. Hence, the stress analysis should focus on the stress distribution at the diffusion-bonded areas that connect the fin body and the upper plate. It is noted that in the no-fillet model a 0.1 mm roundness of tips of the fin is included.

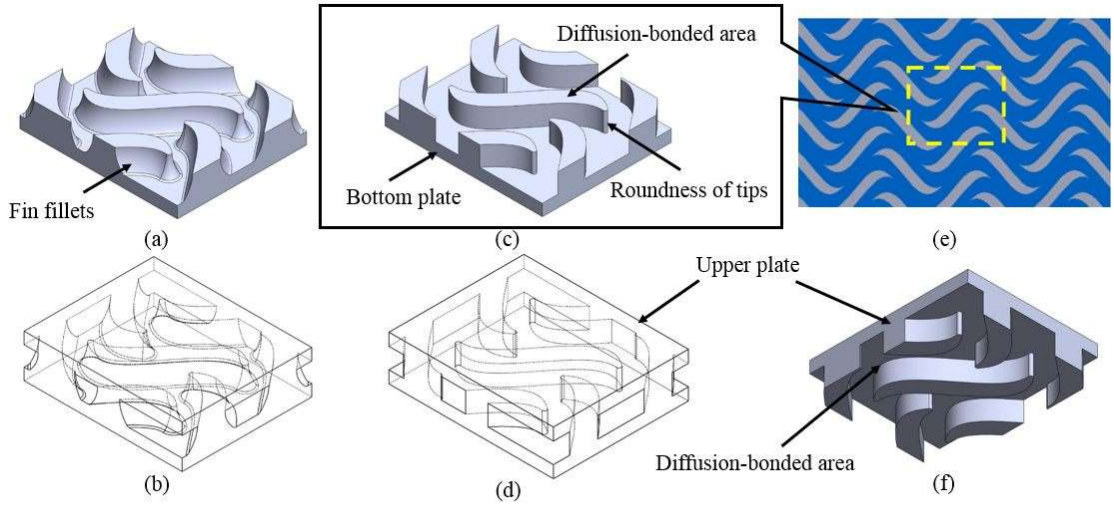

Figure 84. (a) The Actual Chemically-etched S-shaped Fin Channel Model with Fillets; (b) The Fillet Model with an Upper Plate; (c) The No-fillet Rectangular Model; (d) The Reference Model; (e) The Configuration of the Rectangular Model in the Etched Plate; (f) The Diffusion-bonded Areas at the Upper Plate in the Reference Model.

The reference model includes an entire S-shaped fin as well as four half-fins. As is observed from an individual S-shaped fin, the diffusion-bonded areas may experience large stresses. Especially, the tips at the head and tail of fins are expected to have excessive stress concentration and local plastic deformation. Therefore, these areas

should be carefully addressed in the process of meshing. In the reference simulation model, the diffusion-bonded areas are meshed with element size 0.100 mm, while the tips of the fin are meshed with element size 0.015 mm, and the rest of the model is meshed with the maximum element size 0.520 mm, as shown in Figure 85. Since the local plasticity is expected to occur at the tips of fins, the non-linear mode of the solver is activated. Therefore, a non-linear plastic simulation has been carried out as opposed to a linear elastic simulation for the S-shaped fin model to address local excessive stress concentration at tips of fins.

The constant pressure load is imposed on both surfaces of the upper plate, with 20 MPa on the lower surface and 7 MPa on the other. With the assumption that the middle cross-section of an entire fin is structurally the least weak location, four sides of the reference model were set to be fixed supports as boundary conditions. The bottom plate surface was also set to be fixed support. Because the non-linear behavior of the simulation is expected, the force convergence and Newton-Raphson residuals options are activated to monitor the iterative computation process. Since in the preliminary study only stresses induced by mechanical loading were investigated, no thermal stresses are considered in the setup.

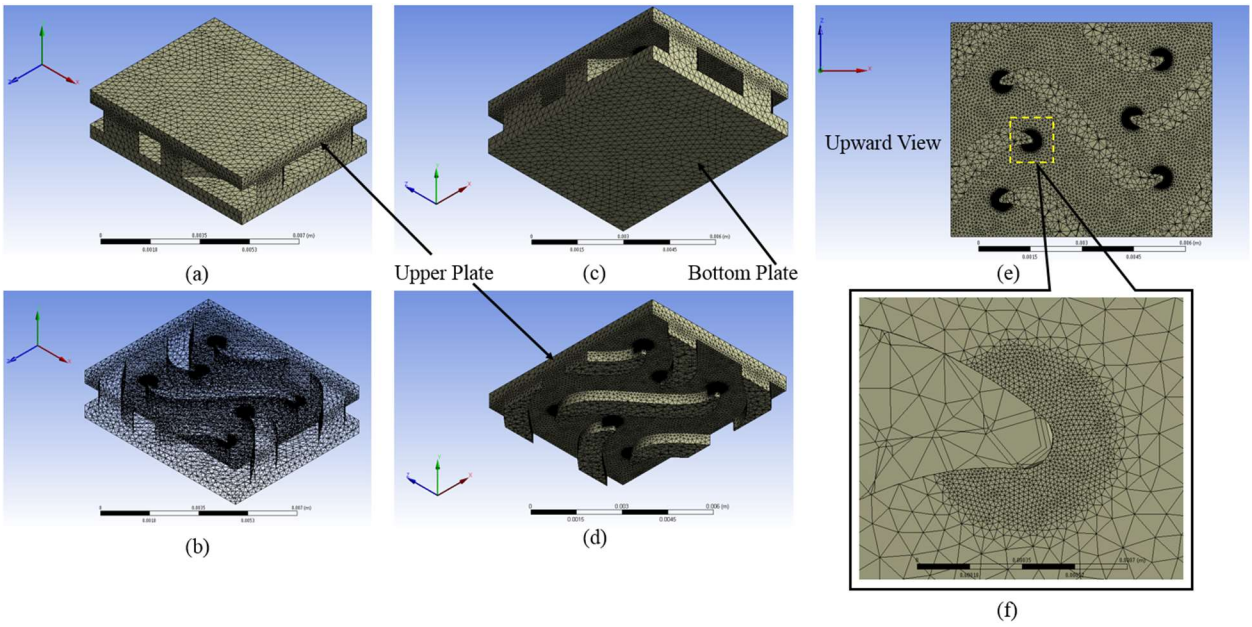

Figure 85. The Meshing Scheme for the Reference Simulation Model: (a) Downward Isometric View; (b) Mesh Formation; (c) Upward Isometric View; (d) Upward Isometric View without Bottom Plate; (e) Upward View from the Bottom; (f) Close View of Meshing at a Tip of the fin.

The visualized stress intensity distribution results indicate that the most severe deformation occurs at the tips of fins, with the maximum stress intensity reaching 146.4

MPa. Figure 86 shows the stress field and the mesh scheme near the tips of fins. Note that the PCHE construction material's yield strength is 116 MPa at temperature 550 °C. This indicates that a portion of the fin has yielded. Figure 87 shows five slices of planes of stress distribution at different locations of the fin. Note that plane P0 is essentially the lower surface of the upper plate in the model. It implies that the tips of fins have enormous stresses, whereas the diffusion-bonded areas along the perimeter of the fin do not experience extreme stress concentration. By checking the nodal stress intensity information of these planes, it is determined that the portion of the fin that yield accounts for less than 1% of the total elements in each plane, as listed in Table 31. The elements in the entire model that undergo plastic deformation accounts for approximately 2.14%. In addition, the local stress of elements in each sliced plane was also analyzed, as listed in Table 31. The elements with local stress beyond 101 MPa accounts for 3.16% of the entire model, including the elements that yield.

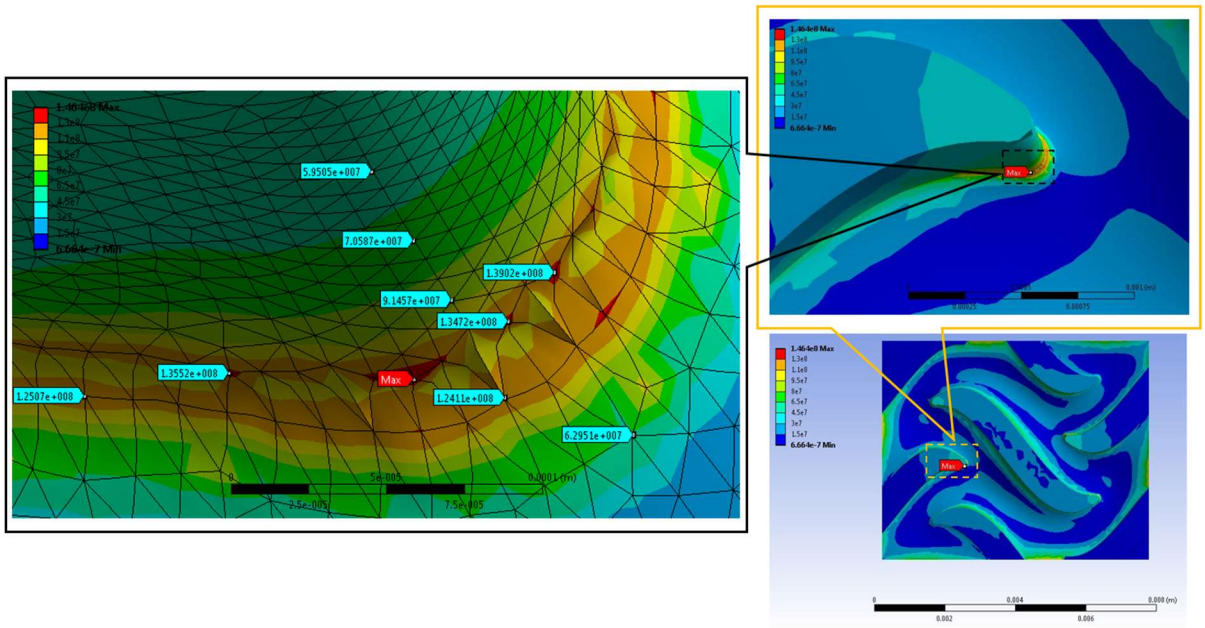

Figure 86. The Stress Intensity Distribution of the Reference Model at one of the Tips of Fins, Maximum Stress Intensity 146.4 MPa, with Element Number = 595,395.

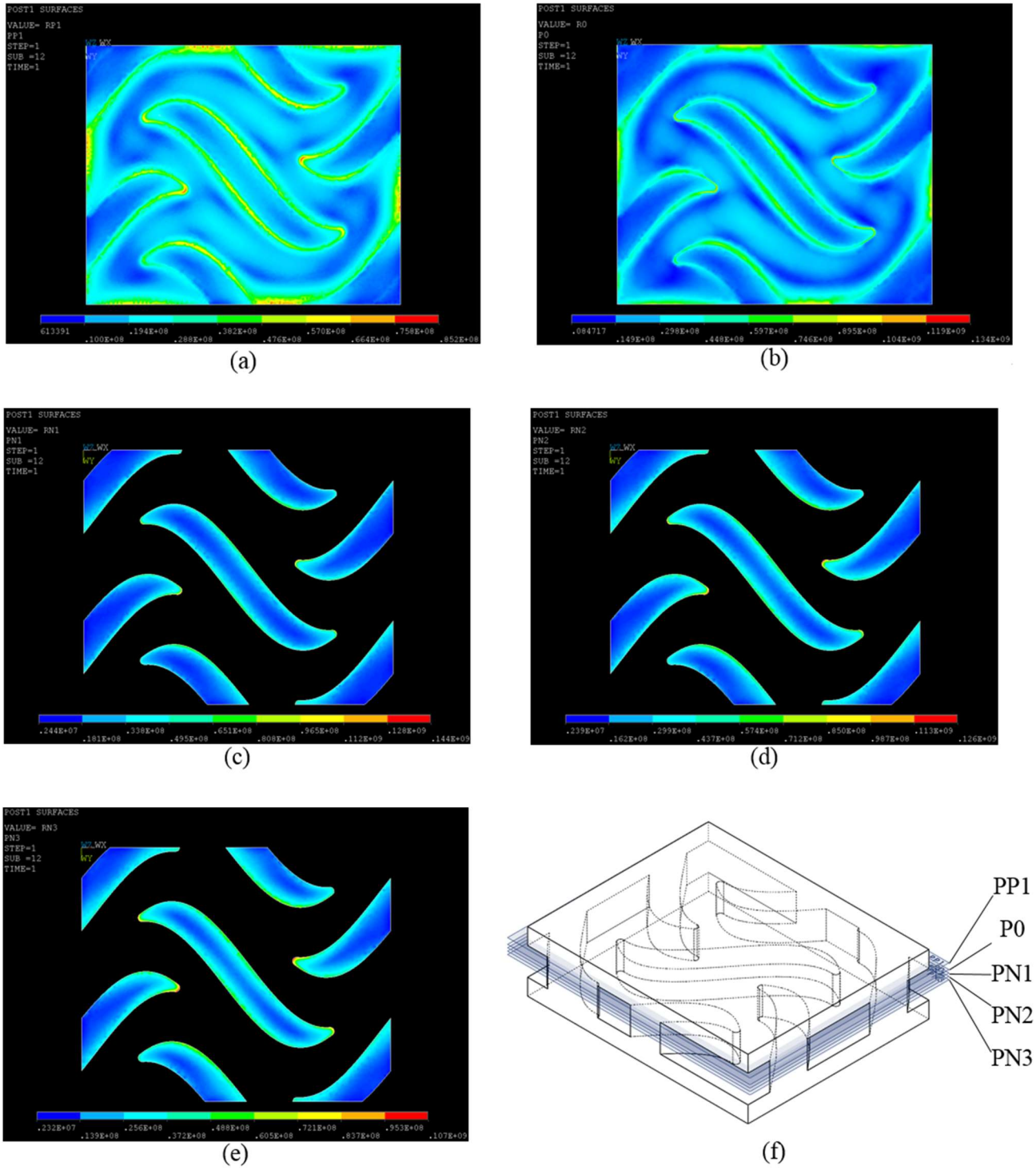

Figure 87. Sliced Planes of Stress Intensity Distribution of the Reference Simulation Model

Table 31. Information of the sliced planes of stress distribution of the reference simulation

Plane Surface	Offset distance relative to Plane P0, mm	Maximum stress intensity, MPa	Yielding, %	Local Stress > 101 MPa, %
PP1	+0.0437	85.2	0	0
P0	0	134.3	0.320	0.782
PN1	-0.0092	143.5	0.923	1.845
PN2	-0.0196	126.3	0.517	2.114
PN3	-0.0319	107.0	0	0.323

Based on the reference model, a series of sensitivity studies have been carried out. There are several issues concerning the accurate simulation of the stress. Firstly, it is necessary to find an appropriate meshing scheme for accurate simulation. The meshing refinement needs to be balanced with the computational cost. Furthermore, the reference simulation model needs to be compared with a large-scale models to verify whether the effect of the boundary conditions on the local stress concentration simulation is negligible or not. In this case, a larger rectangular-shape model containing multiple fins has been simulated. Besides, due to the geometric periodicity of the S-shaped fin configuration, it is proposed to study whether a fin-scale simulation is feasible. The performed sensitivity studies may provide some insights on stress simulations for complex surface geometries in compact heat exchangers.

Table 32 has summarized the mesh-sensitivity study results for various meshing schemes. As is mentioned before, the mesh sizing for the diffusion-bonded areas and the tips of the fin should be different. The indicator of reasonable meshing scheme is the convergence of the maximum stress intensity. Regarding the tips of fins, the results show that the meshing scheme of case 5 with the 0.015 mm element sizing is the most appropriate because the maximum stress intensity changes little while the element number of the case 6 with 0.01 mm element sizing almost doubles. This indicates the maximum stress intensity converges with mesh sizing 0.015 mm at tips of fins. The same approach can be used to select the most suitable meshing scheme for diffusion-bonded areas. Therefore, case 5 has been selected for the reference simulation model, as discussed in the previous section.

Table 32. Information for different meshing schemes

Case	Type of model	Mesh sizing at diffusion-bonded areas, mm	Mesh sizing at tips of fins, mm	Element number	Maximum stress intensities, MPa
1	Single-fin	0.10	0.05	161,742	107.4
2	Single-fin	0.10	0.03	245,127	123.8

3	Single-fin	0.10	0.025	382,557	133.4
4	Single-fin	0.10	0.02	391,874	133.8
5	Single-fin	0.10	0.015	595,395	146.4
6	Single-fin	0.10	0.01	1,385,467	149.6
7	Single-fin	0.08	0.025	418,177	138.9
8	Single-fin	0.08	0.015	702,232	147.0
9	Single-fin	0.07	0.025	455,047	138.7
10	Single-fin	0.06	0.015	888,674	145.5
11	Multiple-fin	0.08	0.025	1,019,119	131.6
12	Multiple-fin	0.10	0.015	1,742,121	149.5

The comparison of the reference simulation model with the large-scale model has been made. The major concern about the reference model is that it is uncertain whether stress fields near the tips and the diffusion-bonded areas of fins are affected by the assumed fixed support boundary conditions at four sides of the model. During the stress analysis of the large-scale model, it is assumed that the S-shaped fin at the center of the large-scale model will be the least affected by the specified boundary conditions, since it is relatively far away from them. Quantitatively, the effect of the boundary conditions on the tips of the fin can be evaluated by comparing the maximum stress intensity near the tips. The information of case 5 and 12 from Table 30 shows an agreement on the maximum stress intensity for two models. It should be noted that there is still lack of effective tools to compare the stress distribution of two models from quantitative point of view because of the complicated surface geometry of S-shaped fins. An alternative way for the comparison is to analyze the yielded portion of the entire model. It is found that there has been 2.83% of elements in the large-scale model that yield, while only 2.14% of the reference model yield. Additionally, 4.04% of elements in the large-scale model have local stress beyond 101 MPa, whereas in the reference model it is 3.16%. This can be explained by observing the stress field near the tips of the fin shown in Figure 88. It can be found that in the reference simulation model the stress field at the bottom surface of the upper plate near the tip of the fin is distorted compared with the similar location in the large-scale model. This implies that the stress field in the reference model is affected by specified boundary conditions in the simulation, especially when it comes to the portion of elements at tips of the S-shaped fin that have large local stresses. However, with little deviation of the maximum stress intensity and distortion of the stress filed at certain locations, the reference model is still capable of simulating the stress filed of S-shaped fins in the preliminary stress analysis, considering the extremely saved computational cost.

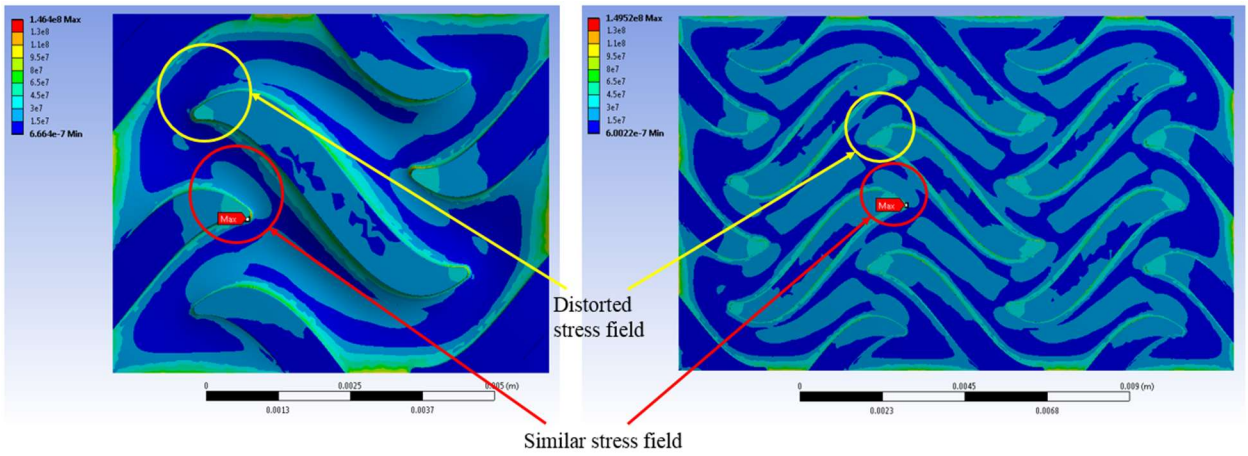

Figure 88. The Comparison of Global Stress Intensity Distribution between the Reference Model (Left) and the Multiple-fin Large-scale Model (Right).

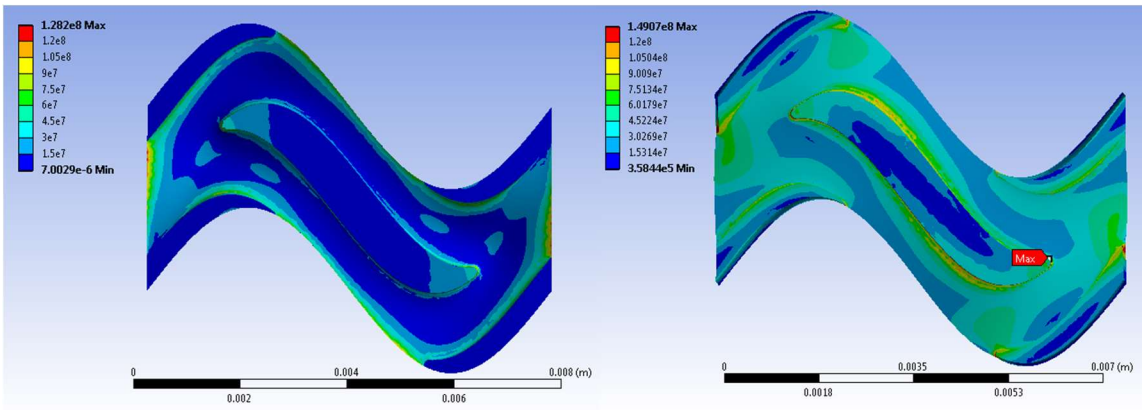

Figure 89. The Stress Intensity Distribution of the Fin-scale Model with Fixed Support (Left) and Free Support (Right) Boundary Conditions

A fin-scale model is also established to be simulated for stress analysis. Figure 89 shows the simulation results for different boundary conditions imposed on the sides of the model. The fin-scale model was originally proposed for the stress assessment due to its small scale to save computational cost. Theoretically, this model can be imposed with linear periodic symmetry to address the inherent periodicity of S-shaped fins. Unfortunately, the non-linear simulation always failed with linear periodic boundary condition at either direction. With alternative boundary conditions, such as fixed support and free support, the results shows that the stress fields are distorted largely and thus are strongly affected by boundary conditions compared with the reference model. Therefore, it is no longer suitable for S-shaped fin stress analysis.

Using ASME standards, it is possible to evaluate the structural integrity of S-shaped fin PCHEs with the obtained stress simulation results. In the ASME BPVC section III, specific

rules are described for construction of nuclear facility components. As is also discussed in Lee et al, these rules are applicable to PCHEs, where channels are treated as pressure-containing vessels. Considering the Design loading and Level A service loadings, we can compare the local stress levels obtained from the simulation results with specified design criteria in ASME code. For design limit, the general membrane stress intensity, derived from Pm, shall not exceed S0, the maximum allowable stress intensity:

$$P_m \leq S_0 \tag{1.4.1}$$

and the combined primary membrane stress plus bending stress intensity, shall not exceed 1.5 S_0:

$$\left(P_L + P_b\right) \leq 1.5 S_0 \tag{1.4.2}$$

where P_L and P_b are the local primary-membrane stress and the bending stress, respectively. For service limits of Level A service loadings, the general primary membrane stress intensity P_m, shall not exceed S_{mt}:

$$P_m \leq S_{mt} \tag{1.4.3}$$

where the S_{mt} values are the lower of two stress intensity values, S_m, which is the lowest stress intensity value at a given temperature among the time-independent strength quantities, and S_t, which is a temperature and time-dependent stress intensity limit. The combined primary membrane plus bending stress intensities for Level A service loadings, shall satisfy the following limits with:

$$P_L + P_b \leq K S_m \tag{1.4.4}$$

$$P_L + P_b \,/\, K_t \leq S_t \tag{1.4.5}$$

The factor K_t accounts for the reduction in extreme fiber bending stress due to the effect of creep, given by:

$$K_t = \left(K + 1\right) / 2 \tag{1.4.6}$$

The factor K is the section factor for the cross section being considered. For conservative estimation, it is assumed that K is set to be 1. The specified stress intensities limits are listed in Table 33. Then it is possible to use local stress (P_L+P_b) for stress assessment in compliance with the rules specified above.

Table 33. The specified stress intensities limits in ASME BPVC (ASME, 2015)

Temp., ºC	S_0, MPa	S_{mt}, 10^5 hr, MPa	S_{mt}, 3×10^5 hr, MPa	S_t, 10^5 hr, MPa	S_t, 3×10^5 hr, MPa
500	107	106	106	131	125
525	101	105	105	118	108
550	88	101	87	101	87
575	77	79	67	79	67

First of all, according to the design limit (2), the maximum allowable local stress is 132 MPa. Only 1.38% of total elements in the reference model fail to satisfy this criteria, and all of them occur at tips of S-shaped fins. Secondly, according to the service time limit, except 3.16% of total elements beyond 101 MPa, 105 hours of service time is allowed for S-shaped fin PCHEs, which is approximately 11.5 years. This implies that the S-shaped fin body can easily satisfy the design limit and service limit, with only small portion of the fin at fin tips being possible to limit the design and reduce service time. Therefore, the mechanical integrity concerning the S-shaped fin bodies and diffusion-bonded areas can be maintained in compliance with ASME standards.

As is mentioned before, the reference model is different from the S-shaped fins in the real situation. Thus, it is still challenging to state that the simulation can represent the real stress situation of S-shaped fins. One of major concerns is the difference between the selected simulation model and the real S-shaped fin channels. Firstly, as shown in Figure 84(e), the reference simulation model does not include any fillets that connect the fin body to the bottom plate. As is known, in the photo-chemical etching technique, as the etchant attacks the exposed plate surface area to form desired channels, a characteristic roundness will occur with rounded interior corners, also known as fillets in S-shaped fin channels. These fillets can mediate the stress concentration that could occur at bottom plates. Hence, the current simulation results tend to be conservative in the absence of fillets. Furthermore, the roundness of tips of the S-shaped fins in the reference model is set to be 0.1 mm according to the actual shape obtained by etching in TIT experiment. Figure 91 shows the particular round effect of the etching process of S-shaped fins that has been investigated before. However, the dimension of the tips' roundness varies because it is strongly dependent upon the manufacturing conditions. It is still unclear how the roundness dimension may affect the mitigation of stress concentration at tips of fins. Moreover, the diffusion-bonded areas that connect the fin body with the upper plate have sharp 90º angle in the reference model, as shown in Figure 90(c). However, this is not necessarily the case since in reality the diffusion-bonding process leads to physical roundness at the sharp tips. Using elastic model for simulation, such sharp tips at the diffusion-bonded areas may result in diverging stresses. The similar situation for zigzag

channel tips has been discussed in the literature. Fortunately, in this study the plasticity of SS 316 at sharp tips have been well captured in the simulation. The plastic deformation, or the yielding of some portion of the fin tips, accommodates the excessive strain energy that caused by the sharp tips. In other words, the current simulation is more conservative than that in real situation where sharp tips are unintentionally rounded during diffusion-bonding. Therefore, the actual stress situation of the manufactured S-shaped fins may be less harsh than the simulated models thanks to the nature of the chemical etching and diffusion bonding technique.

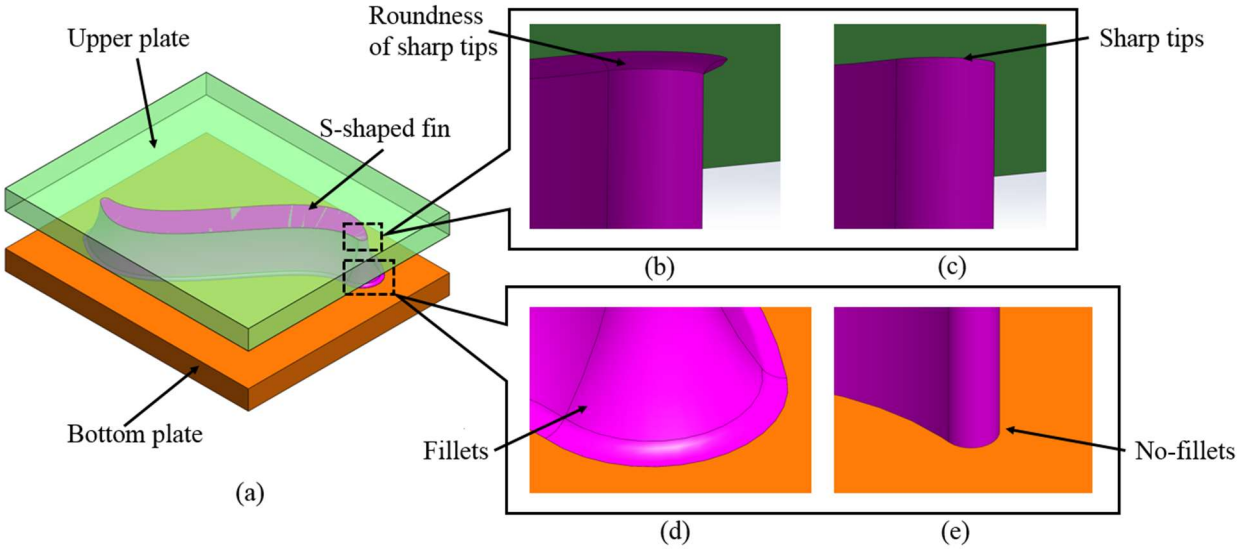

Figure 90. Surface Geometrical Difference between the Actual S-shaped Fin and Reference Model (a) Actual S-shaped Fin; (b) Roundness of Sharp Tips; (c) Sharp Tips in the Reference Model; (d) Fillets at the Bottom Plate; (e) Reference Model with No Fillets.

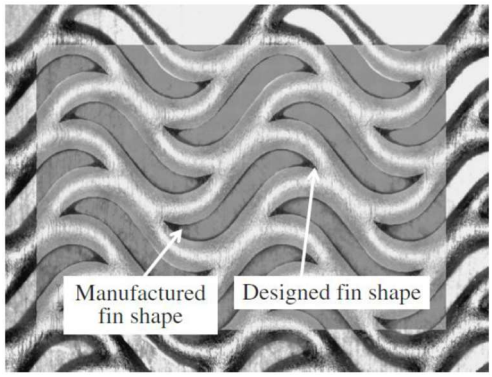

Figure 91. A Plane View of the S-shaped Fin PCHE Surface and the Rounding Effect in Manufacturing Process.

The stress distribution of S-shaped fin channels is inherently difficult to be analytically modeled. Accordingly, the unique geometry and high-pressure application of the S-

shaped fins make it particularly challenging to be referenced to the existing codes such as ASME code. The ASME BPVC section VIII Division 2 describes the design procedures and criteria for the design of pressure equipment based on design-by-rules methodologies. The diffusion-bonded PCHE channels are generally considered to be pressure-containing vessels. It is possible to follow relevant rules in the BPVC for the mechanical design of straight or zigzag semi-circular channels for intermediate-pressure applications. Unfortunately, when it comes to S-shaped fins and high-pressure applications, the design-by-rules methods are no longer suitable due to the complexity of channel configurations and the elastic-plastic behavior of the material under high pressure. An alternative tool recommended by BPVC is the design-by-analysis method. Although it seems to be powerful tool for the mechanical design of the S-shaped fin channels, it requires the stress linearization and classification of the numerical results based on an accurate modeling to satisfy the design criteria. Particularly, concerning S-shaped fin channels, this task will be arduous and challenging. The numerical simulation of stress analysis for S-shaped fin channels in this paper is a preliminary step in the design-by-analysis method in compliance to BPVC code, and further studies are needed in the future.

It should be noted that the reference temperature 550 ºC does not reflect the highest temperature that some spots of the prototypic PCHE may experience according to the operating conditions, and thermal stresses are not considered in the current stress analysis. These factors may further limit the design and service time. It is also possible that the working fluid s-CO2 is likely to affect the actual life time of PCHEs. It is then suggested that either should the base structural material of PCHEs change to alloys with higher mechanical strength such as Alloy 617, or the design should be modified and optimized to assure structural integrity and extend service time at prototypic operating conditions.

1.4.3 Static Stress Analysis of Airfoil PCHE

The airfoil PCHE features a unique islanded fin geometry that is uniquely different from other etched PCHE channel designs. The channels of the airfoil PCHE contain an array of offset airfoil shaped fins. The fins are patterned in alternating rows with the airfoils facing the direction of flow in the channel. In this fashion flow through the channel isn't constrained to a singular flow path, as in the typical straight and zig-zag channel designs. Flow is free to pass through the entirety of the air foil array without constraint that is induced by the repeating channel walls of straight channel and zig-zag PCHE designs. Moving around each individual airfoil in the channel the fluid becomes well mixed and transfers heat as well as the standard zig-zag channel design without as much of a pressure drop (ASME, 2015).

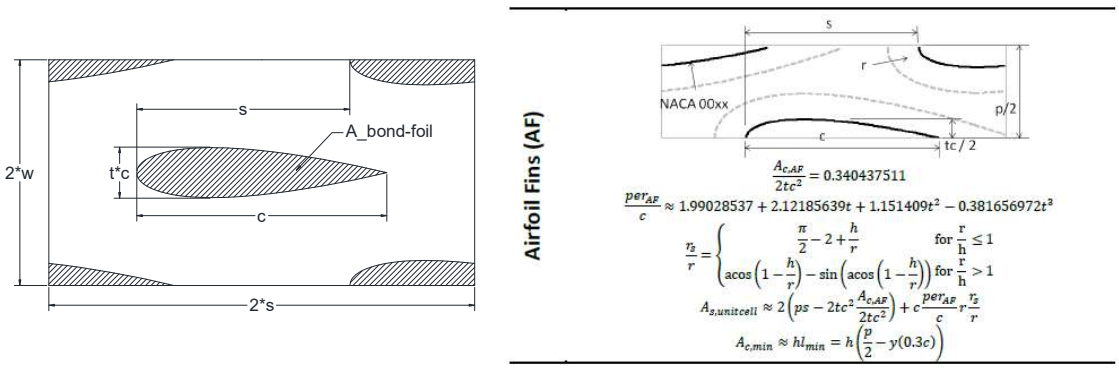

Figure 92. (left) rubbing of airfoil channel. (right) camber-less NACA airfoil equation and airfoil pattern

The pattern considered is shown in Figure 92. The airfoils are described by the camber-less NACA airfoil equation, also shown in Figure 92. The pattern is described by the chord length of the airfoil, the thickness of the airfoil at its girth, the lateral pitch between airfoil columns (perpendicular to flow), and the axial pitch between airfoil rows (in the direction of flow). In sizing the array, chord length and axial pitch are set so that the most uniform hydraulic diameter is achieved, which occurs when the ratio of axial pitch to chord length (s/c) is 0.86. Values chosen for the considered airfoil pattern being considered are shown in Table 34. These values were chosen to be the same as those used in previous experimental analysis of Kruizenga and Carlson and result in a pattern that achieves 17.8% coverage of the etched PCHE plate.

Table 34. Airfoil Pattern Parameters

Airfoil Unit Cell Geometry			
Description	**Symbol**	**Unit**	**Design**
chord length	c	mm	8.1
thickness/chord length	t	-	0.2
channel depth	d	mm	0.95
axial pitch	s	mm	6.9
lateral pitch	w	mm	3.65
unit cell area	A_cell	mm^2	100.74
bondable area of single airfoil	A_bond-foil	mm^2	8.93
percent of area bondable	Bond_%	%	17.85

Mechanically the airfoil PCHE presents a unique problem in the evaluation of its strength. Unlike standard PCHE designs which all use some form of continuous walled micro-channels, the airfoil design has discontinuous support in the PCHE section. This creates unique stress distributions in the section that are 3 dimensional in their distribution, and must be modeled and understood as such. This is a great deal more complexity than is

present in the stress distributions of standard continuous micro-channels, which are generally 2 dimensional. Additional complexity results from the consideration of the entirety of a heat exchanger, including supporting exterior walls and manifolding structures.

Modeling of mechanical stress in the airfoil PCHE considers the complexities of geometry, material, and stress models used. Models were developed starting from the simplest geometries with the most basic material properties and stress model assumptions. With simple model results the modeling effort complexity was increased and continues to be increased. Geometries, materials, and stress models are discussed briefly before discussion of particular modeling cases.

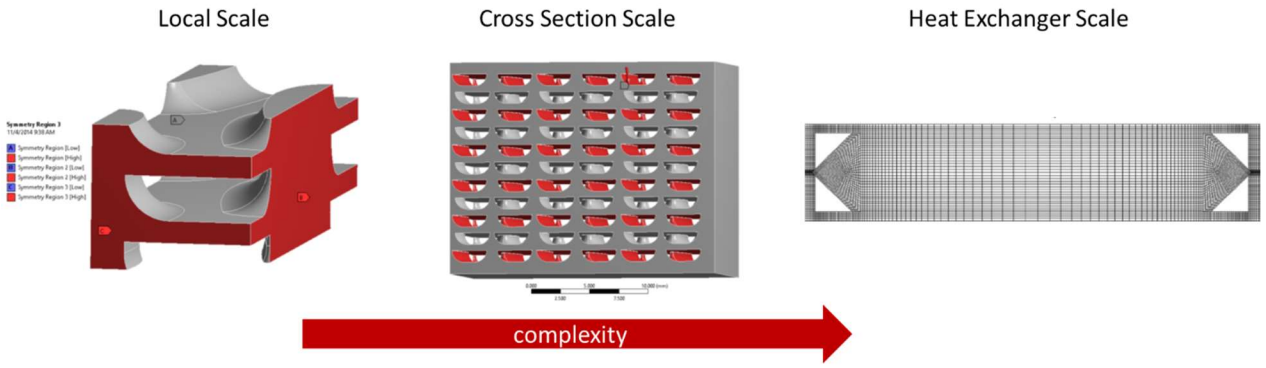

Figure 93. Geometry scales of the model effort with the local scale being the simplest model and the full heat exchanger scale being the most difficult to model

Geometrically of the airfoil PCHE structure is split between three different scales, the local scale, the cross section scale, and the full heat exchanger scale. Illustrations of the three scales are shown in Figure 93. The local scale is geometry immediately surrounding the airfoil channel and can be generally modeled as repeating unit cell which is inherent to the interior of the overall heat exchanger. The cross section scale encompasses geometries of the heat exchanger cross section including walls and surrounding support structures. As such, the cross section scale is considerably more complex than the local scale. The full heat exchanger scale looks at the entirety of the heat exchanger including manifolding. It is the most complex and is often simplified with porous media properties drawn from the local and cross sectional scales.

The materials modeled are those that will be experimentally tested, they are 316 stainless steel and Accura 60 (a plastic resin). These were chosen as test sections can be made of both materials. The diffusion bonding of 316 stainless steel is readily achievable at vendors such as Vacuum Process Engineering and Refrac. 316 is also substantially

cheaper than nickel alloys being considered for PCHE systems. Accura 60 is a resign that is printable through Stereolithography (SLA), which is cheaper and quicker to manufacture than diffusion bonding. Most modeling uses 316 stainless steel as the PCHE material, Accura 60 is only used for models of Accura 60 pressurization tests. Choice in the material modeled drives the choice of stress model that is used. Modeling of the ductile 316 stainless steel can be carried out to the full extent its plasticity, while a model of the brittle Accura 60 is simply elastic.

Stress models are split between three degrees of increasing complexity, the elastic model, the plastic model, and the creep model. The elastic model is a simple linear stress-strain model with Young's Modulus of Elasticity as the slope of the stress-strain curve. It is only valid up to the yield stress, at which point the plastic model must be used. The plastic model assumes the true stress-strain curve above the yield point is known. It is valid for any static model, if time is to be considered the creep model is used. The creep model is the most complex and must be built out of a set of plastic stress-strain models each from different length creep tests. Figure 94 depicts the stress-strain relations used in each model. The stress models available depend on the quality of material data available. A wealth of stress-strain data is available for 316 stainless steel, while properties beyond Young's Moduls and ultimate tensile strength are not known for Accura 60.

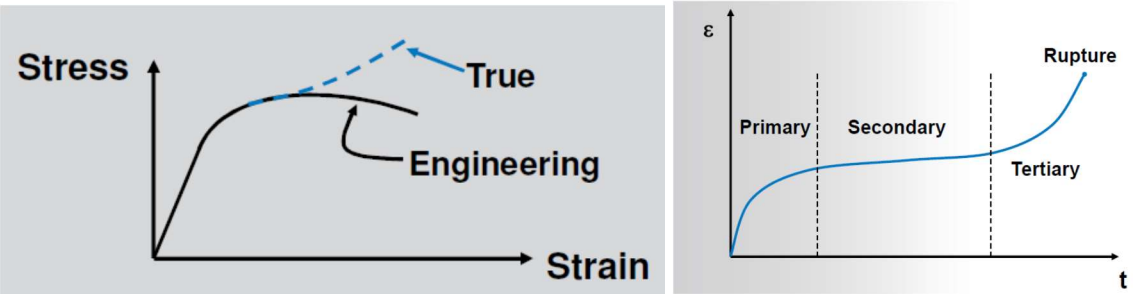

Figure 94. Stress models used in the ANSYS solver, (left) linear elastic model and its extension into the plastic model, (right) full creep model

ANSYS Mechanical and ANSYS Mechanical APDL were used in the finite element analysis (FEA) of the airfoil PCHE system. In all models the geometry of interest is transformed into a mesh of hexagonal elements which is used by the ANSYS solver. The ANSYS solver is an iterative force based solver. From the geometry and loading conditions, the forces on each element are resolved. With the forces set for each element of the geometric mesh, strain is varied and the process repeated until a solution emerges.

The ANSYS solver can handle all three stress models and calculates strain in order of model complexity, from elastic, through plastic, to creep, as shown in Eq. 1.4.7.

$$\dot{\varepsilon} = \dot{\varepsilon}_{el} + \dot{\varepsilon}_{pl} + \dot{\varepsilon}_{cr} \tag{1.4.7}$$

Plastic and elastic properties of 316 stainless steel were obtained from the AMSE Boiler and Pressure Vessel Code (BPVC). Data was extracted from stress-strain charts in the BPVC's main pressure vessel section (section III division I). The charts show experimental stress-strain data at 15 high temperature from 427 °C to 816 °C with creep tests of up to 34 years. Chart data was simplified to a 9 data point fit for each temperatures elastic stress-strain curve. Since BPVC data is only given for 15 discrete temperatures, data for intermediate temperatures was interpolated. The BPVC stress-strain for 316 stainless steel at 538 °C and its 9 point interpolation to 550 °C is shown in Figure 95.

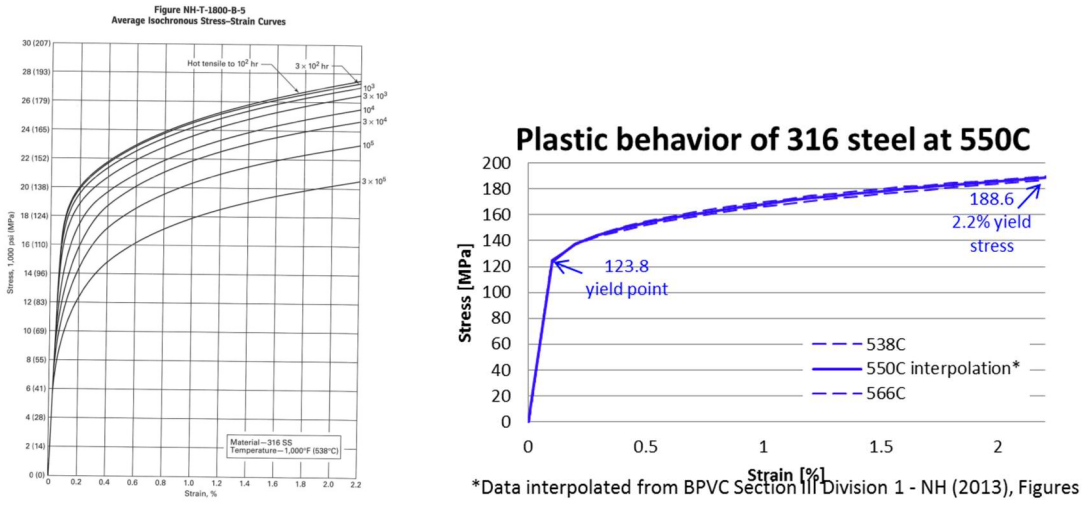

Figure 95. Stress-strain chart for 316 stainless steel

Elastic models were the first developed because of their simplicity and usefulness in determining qualitative mechanical properties. This model is good at identifying stress concentration of the geometry and the effect of boundary conditions and supporting walls in a section. The results of the elastic models were useful in furthering of 316 stainless steel models and in predicting the onset of brittle failure in SLA printed specimens.

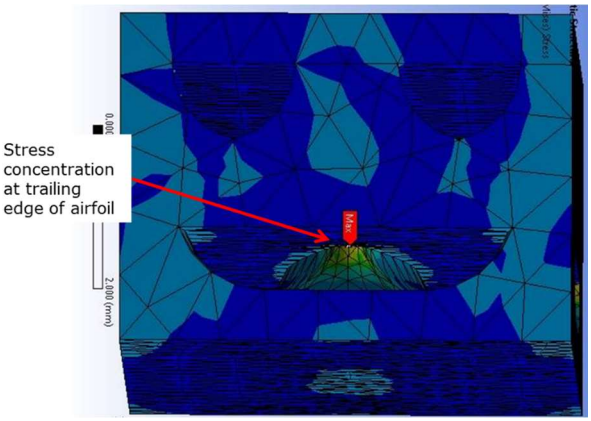

Figure 96. tail side stress concentration on a local scale model

Local scale elastic modeling highlighted the head and tail of the airfoil-fin as the area of concern for airfoil PCHE systems. The local scale is enforced by applying symmetry conditions to the six faces of the unit cell. In these models 20 MPa of pressurization in the airfoil channel created stress concentrations in excess of the yield point of 316 stainless steel (123.8 MPa at 550 C). Figure 96 shows the location of the tail side stress concentration in an elastic model. Here the lower airfoil channel is pressurized while the upper straight channels are not pressurized. Large curvature at the head and tail combine with the diffusion bond interface to create a high localized concentration of stress. This stress concentration is influenced by the geometry of the air foil section. Increasing the coverage of airfoils in the section by decreasing the lateral spacing between airfoil columns brings the stress concentration down by distributing the 20 MPa within the channel over more tightly packed airfoils. Decreasing the curvature at the tail of the airfoil by rounding its profile also decreases the stress concentration, as the geometric concentration is more spread out. This can be seen in the plot of results shown in Figure 97. Here the maximum stress, the concentration, is compared to the airfoil coverage for various tail rounding. The embedded picture shows the four rounding profiles, with more rounding creating less curvature at the airfoil tail.

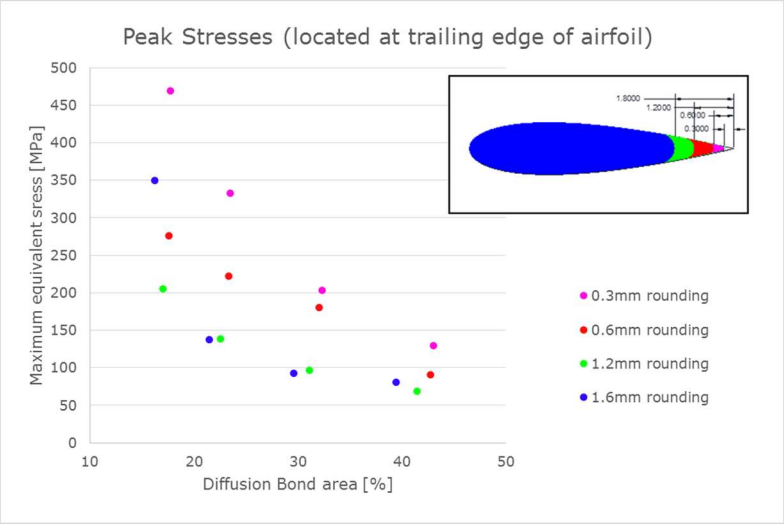

Figure 97. Plot of local elastic model results for stress concentration at the airfoil tail for various channel coverage and founding of the airfoil tail

Cross section scale elastic modeling was used to show the effect of wall structures in the PCHE cross section and to determine the onset of brittle failure in an SLA printed part. Since stress concentrations at the tail of the airfoil-fin were identified in previous models, they could be used to evaluate the variation of stress states in a cross sectional sample. The cross section of concern consists of 11 stacks of airfoil plates surrounded by exterior walls, shown in Figure 98. The plates are 12 airfoil columns wide and feature the airfoil pattern shown in Figure 93. Symmetry is used at the center of the cross section, the left face of Figure 100 being the centerline and symmetry of the cross section while the right face is the surrounding wall. In the model the cross section is pressured to 1 MPa at every other plate and the stress concentration is evaluated at each airfoil tail. A plot of the airfoil tail stresses over the cross section is shown in Figure 99 with circular points representing the location of each airfoil tail. The airfoil tails next to the PCHE wall, on the right side of the model, see the least stress as they are substantially supported by the adjacent wall. This support diminishes quickly when moving away from the wall. It was found that all but the airfoils nearest the wall see the impact of the wall's support and are stressed similarly. Higher stresses occurred in the pressurized channels than those without pressurization. This inter-channel stress difference can be seen in the horizontal striation in Figure 101.

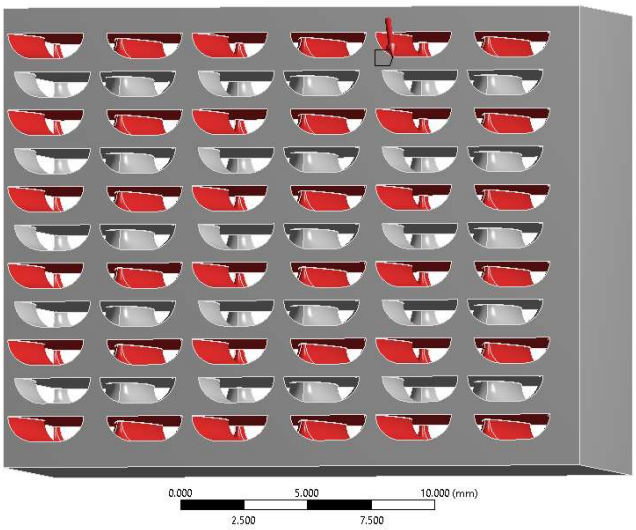

Figure 98. Elastic cross-section model featuring 11 stacked airfoil channels and supporting PCHE walls. Red channels are pressured. Symmetry about left face is used to get a full cross section.

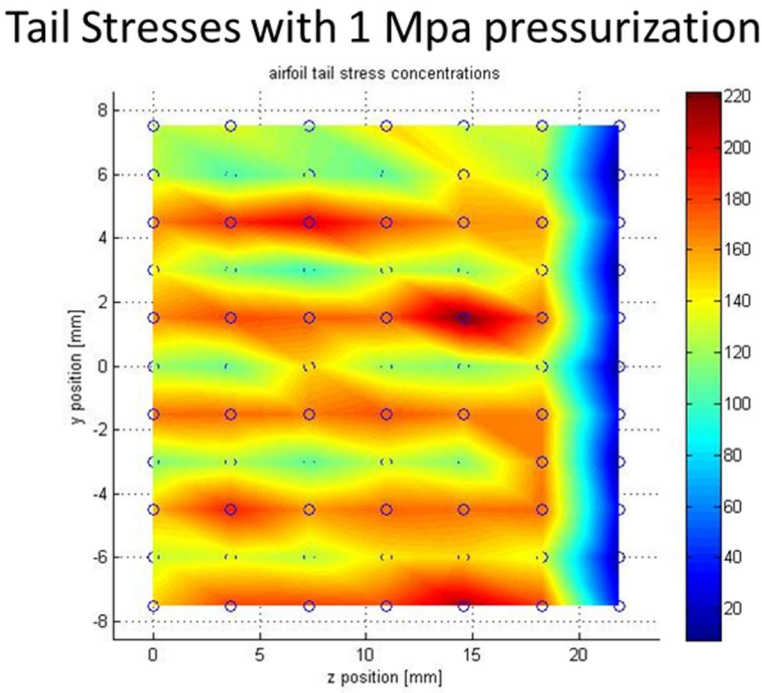

Figure 99. Airfoil tail stress results for the elastic cross section model. Airfoils near wall have lower stress due to wall support. Pressurized channels have highest stresses.

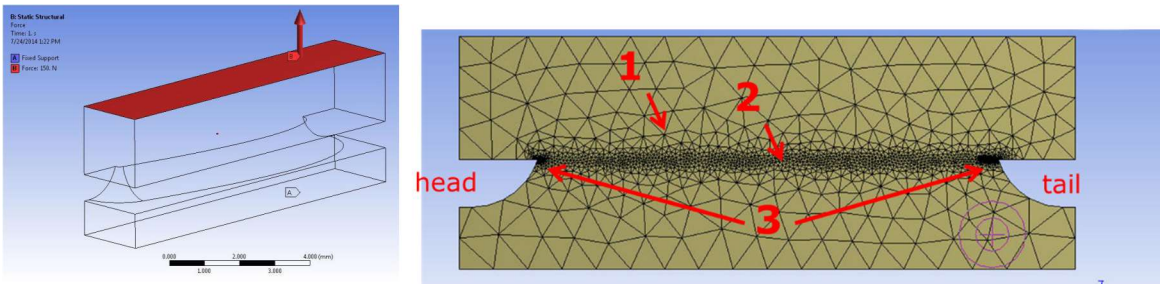

Figure 100. Plastic model of airfoil in tension. (left) tensile loading, (right) refinement of the model mesh with course mesh in channel was (1) refined mesh at the diffusion bond interface (2) and further refinement at the head and tail (3)

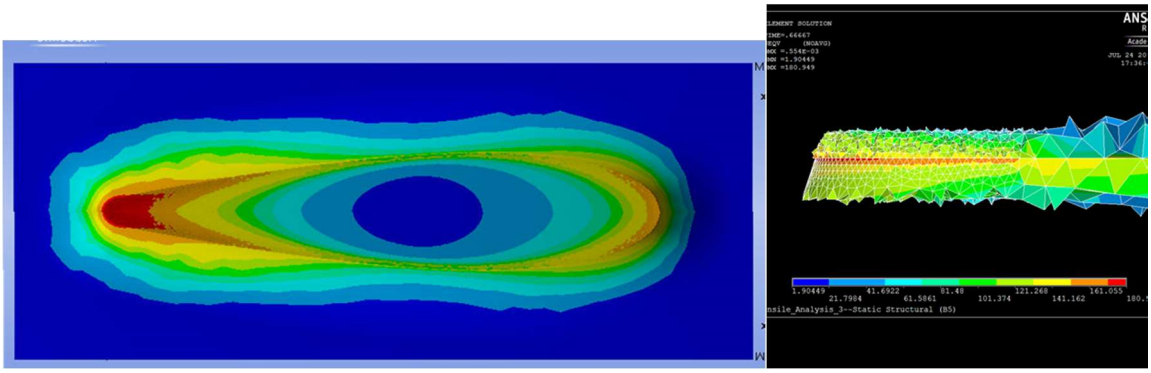

Figure 101. Propagation of yielding at the diffusion bond interface. (left) yielding propagates from head and tail of airfoil diffusion bond, (right) close up of yielding at the tail diffusion bond

These cross section results are useful in predicting the onset of brittle failure in the identical SLA printed piece. Made out of Accura 60, the SLA printed section has an ultimate tensile strength of 58 MPa. The 1 MPa pressurization model results shown in Fig. 112 have a maximum stress of 222 MPa. Since the model and material are elastic, this result can be linearly extrapolated to find that a 262 MPa pressurization would yield the 58 MPa ultimate tensile strength of the part. Thus brittle failure of the SLA printed part is expected to begin at a pressurization of 262 MPa.

Plastic models where initiated on the local scale to investigate to propagation of the tail stress concentration beyond the yield point. In PCHEs constructed of 316 stainless steel or other ductile metal the stress concentration seen in elastic models should yield away to some extent. As the stress concentration passes the yield point, the material should strain away. This should alter the geometry to an extent and allow the stress to spread out within the yielding section. Yielding is allowable to some extent, as small features that contain stress concentrations make up a miniscule portion of the overall supporting

structure. The airfoil PCHE structure should be able to withstand pressurization far above that which initiates the onset of yielding.

A local plastic model was developed to investigate the propagation of yielding in a singular airfoil-fin. The model is shown in Figure 100 and consists of a single air-foil fin under a tensile load. Tensile loading is the primary form of loading in the pressurized airfoil PCHE system. The model contains a geometric mesh with refinement of the mesh size at the diffusion bond interface and further refinement at the head and tail of the airfoil fin. The area of interest with respect to yielding is the diffusion bond interface, as it is the weakest part in the PCHE assembly and also the area of highest stress.

Solving the plastic airfoil-fin tensile model for various tensile loads shows the propagation of yielding in the airfoil. Figure 102 shows the distribution of stress along the diffusion bond interface with the areas of highest stress (in red) propagating through yielding from the head and tail of the airfoil. A 0.2mm thin area around the diffusion bond was analyzed to determine the extent of yielding. The percent of diffusion bond yielded was taken as the percent of this thin volume that was in excess of the 316 stainless steel yield stress of 123.8 MPa at 550 C. The airfoil can hold loads up to 1200 N at 550 C with the diffusion bond yielding no more than 20%. A plot of yielding with tensile load and a plot of yielding as a function of airfoil coverage at 20 MPa pressurization can be seen in Figure 102.

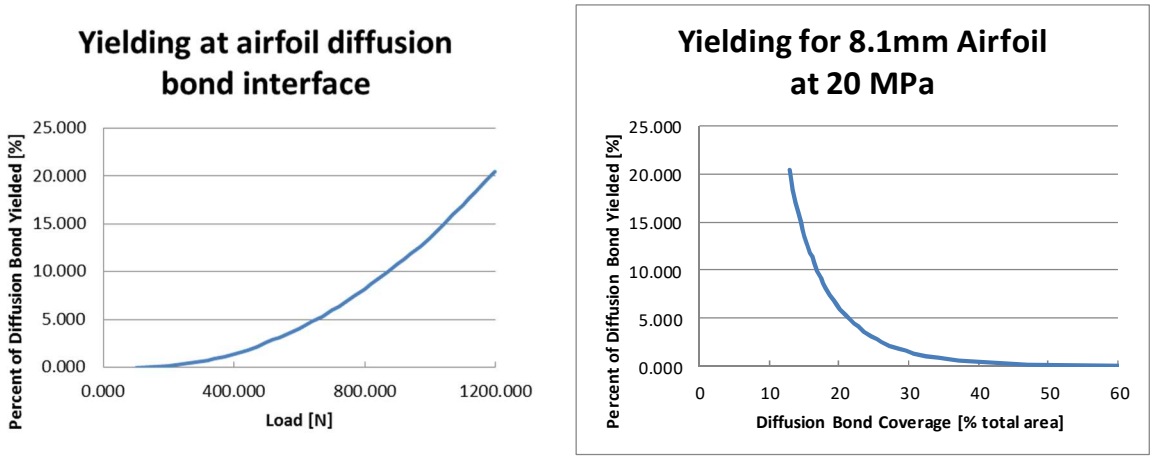

Figure 102. Percent yield of the diffusion bond interface, (left) in terms of load on a single airfoil, (right) in terms of airfoil bond coverage with pressurization of 20 MPa

1.4.4 FEA Methods of ASME BPVC Compliance

The American Society of Mechanical Engineering's (ASME) Boiler and Pressure Vessel Code (BPVC) requirements can be met through the mechanical finite element analysis (FEA) methods. These methods have been used to investigate the mechanical integrity of the airfoil-fin channeled PCHE. Compliance with ASME BPVC guidelines when

constructing and analysis FEA models can be used to meet BPVC requirements for micro-channel PCHE's.

A review of ASME BPVC Section VIII Division 2 Part 5 was performed to establish methods for addressing its design by analysis requirements, particularly those for protection against plastic collapse, preotection against local failure, and protection against failure from cyclic loading. In particular the loading conditions and models needed to meet ASME standards were established. The airfoil-fin PCHE can be readily code qualified when pressurization and thermal loads are used. Static FEA models can be a simpler elastic stress analysis or a more complex, but less conservative, plastic deformation model. Transient fatigue FEA models are only require for loads that produce cyclic stress, such thermal loads that occur during heating and cooling of the power cycle.

1.5 Mechanical Design Methods Review

In the early discussion about the mechanical design methods for PCHEs (Dostal et al. 2004 and Hesselgreaves 2001), most of efforts were focused on a simplified stress analysis model for straight and zigzag channels, which is based on the thick walled cylinder theory. However, this method is generally not conservative. Additionally, Southall et al. (2008) presented a mechanical design method that complies ASME codes. Both methods are introduced as follows.

1.5.1 Surface Geometrical Characteristics of Zigzag or Straight Channel

In general, zigzag channels are characterized by a cross-sectional profile. As stated before, the cross-sectional profile of the zigzag channel is assumed to be semi-circular. The norminal channel diameter D is equal to the transverse channel width, which is different from the true channel width *w*, as shown in Figure 103. The channel depth h_c is equal to the half of the channel diameter.

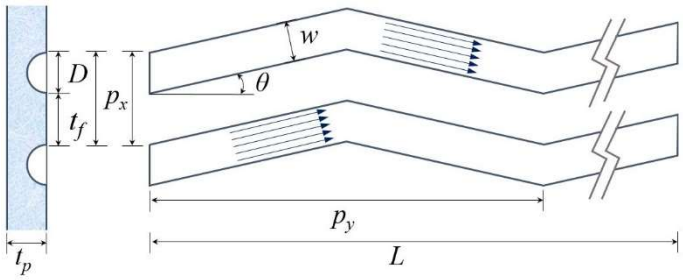

Figure 103 Schematic of zigzag channel (or straight channel) surface characteristics (Zhang et al. 2015b)

The relationships of the ridge thickness t_f and the plate thickness t_p can be determined by a simplified mechanical stress analysis that is discussed later. From Figure 103 it is obvious that the transverse channel pitch p_x is equal to the sum of t_f and D. These parameters are of interest in mechanical design.

For straight channels, it shares similar cross-sectional geometrical characteristic except that the flow passage is straight instead of zigzag pattern, hence the discussion about zigzag channels does not lose generalization.

It should be noted that the surface geometry seems to significantly depend on particular etching and diffusion-bonding process. This is concluded from observing the cross-sectional profile of flow channels in the heat exchanger core fabricated by different vendors. For instance, in literature it is reported that the cross-sectional profile is not necessarily semi-circular. In fact, it is rather circular segments with a channel depth only about 70% of the profile radius according to the experimental measurement (Carlson, 2012). Such measurement was also conducted at OSU (Wegman, 2016). This discrepancy from what researcher conventionally conceived of could be probably attributed to several factors including the difference of etching techniques provided by vendors, etc. In addition, it is also worth mentioning that the cross-sectional profile does change after diffusion bonding as the top plate crushes the ridges between channels. The corner tip radius at the diffusion-bonded interface of the ridge between channels varies with individual fabricated heat exchanger. Figure 6 shows the micrographic image of a Heatric PCHE plate cross-section, which indicates the smooth roundness of the bottom of channel and the adjacent rough area, i.e. the corner tip radius. The rough region is probably due to compression during diffusion bonding, according to Southall et al. (2009). Unfortunately, the dimension of that radius is not reported. For simplicity, in the later analyses, it is still assumed to have semi-circular profile for zigzag channels.

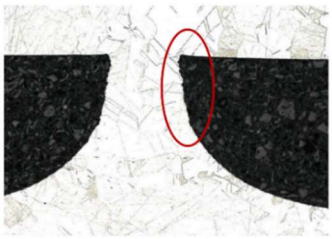

Figure 104 A micro-scale image of zigzag channels with smooth roundness at the bottom and adjacent rougher area (Sourthall et al. 2009)

1.5.2 Simplified Mechanical Design Method

In general, the flow channels that are etched on metal plates are considered as pressure-containing vessels. In the case of zigzag channels, due to the semi-circular cross-

sectional profile, they can be modeled as either circular or rectangular channels in simplified stress analysis. Obviously, the major concerns about zigzag channels are centered on the transverse pitch p_x and the plate thickness t_p. Hesselgreaves (2001) suggests to use following formula for evaluation of the fin thickness, i.e., for the zigzag channels, the ridge thickness t_f is

$$t_f = \frac{p_x}{\left(S/\Delta P\right)+1}, \tag{1.5.1}$$

where S and ΔP are the maximum allowable stress and pressure differential between hot and cold fluid, respectively. It should be noted that the actual ridge thickness is the minimum distance between neighboring channels at any cross-section along the flow path, rather than the nominal ridge thickness as shown in Figure 103. Since we have

$$p_x = D + t_f, \tag{1.5.2}$$

the ridge thickness t_f can be simply obtained by

$$t_f \geq \left(\frac{\Delta P}{S}\right) D, \tag{1.5.3}$$

To determine the plate thickness t_p, a simplified approach that utilizes the thick walled cylinder theory model is proposed. It is shown that the maximum stress occurs in the inner wall. Therefore, in this model we can simplify the original equation to the following formula (Mylavarapu, 2011):

$$\frac{r_o}{r_i} \geq \sqrt{\frac{P_i + S}{S + 2P_o - P_i}}, \tag{1.5.4}$$

where r_i, r_o, P_i and P_o are the cylinder's inner, outer radius and internal, external gage pressure, respectively. This formula is valid only if the internal pressure is greater than the external pressure. For the opposite situation, the formula should be modified as follows (Zhang, 2016):

$$\frac{r_o}{r_i} \geq \sqrt{\frac{S - P_i}{S - 2P_o + P_i}}. \tag{1.5.5}$$

For the application to the plate thickness calculation, the inner and outer radius used in the formula need to be identified. A common method is to treat two vertical neighboring channels' interior surfaces as the pressure boundaries, and therefore the outer diameter

of the cylinder is equal to the plate thickness. As to the inner diameter, usually it is equal to the channel diameter. Then we can be obtain the formula for calculating the plate thickness:

$$t_p \geq D\sqrt{\frac{S-P_i}{S-2P_o+P_i}}. \tag{1.5.6}$$

This simplified mechanical design method is effective and useful for a quick hand-calculation design. It can be used in the iterative heat exchanger design process along with thermal design and economic analysis, etc. However, it is also not conservative, and does not involve any other design information of an entire metal plate such as the side margin which is essentially the distance between the outmost channel and the edge of plate. Furthermore, this method is particularly applicable to straight and zigzag channel which are characterized by semi-circular cross-section. Therefore, a more sophisticated method is required for detailed mechanical design.

1.5.3 Mechanical Design Method Based on ASME Codes

The design requirement of diffusion-bonded microchannel heat exchangers were outlined in Code Case 2621-1 in 2009, and the design method was provided by Heatric in compliance in Section VIII Division 1. It is in detail described in reference Le Pierres et al. (2011). It is an analytical approach based on a conservative model where the semi-circular channel configurations are treated as stayed plates on a flat plate, as shown in Figure 105. It is essentially a simplified model originating from the design requirements for non-circular vessels with rectangular cross-section supported by stayed plates in ASME codes (2011). The stayed plate thickness d_f and the thin wall thickness t_w, are identified as two critical thickness of interest in the stress analysis of rectangular pressure vessels. Note that d_f actually corresponds to the ridge thickness t_f in zigzag or straight channels.

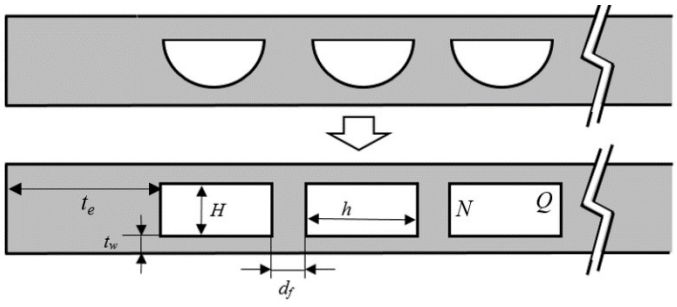

Figure 105 Schematic of the conversion of channels to rectangular vessel with stayed plates. (Zhang, 2016)

The design criteria include (1) the membrane stress in the stayed plate $S_m{}^S$ shall not exceed the design stress; (2) the membrane stress in the long side of vessel $S_m{}^L$ shall not exceed the design stress and (3) the total stress $S_t{}^L$, which is the sum of the membrane and bending stress $S_b{}^L$ in the long side of vessel, shall not exceed 1.5 times of the design stress. Explicitly, they can be expressed as follows:

$$S_m^S \le SE, \tag{1.5.7}$$

$$S_m^L \le SE, \tag{1.5.8}$$

$$S_t^L = S_m^L + S_b^L \le 1.5SE, \tag{1.5.9}$$

where S and E are the maximum allowable stress intensity and joint factor, respectively. It is recommended that E be 0.7 for diffusion-bonded block (Le Pierres et al. 2011). This assumption is probably because the individual bond cannot be inspected in reality. The stress values can be computed through the following equations:

$$S_m^S = \frac{Ph}{d_f}, \tag{1.5.10a}$$

$$S_m^L = \frac{PH}{2t_w}, S_b^L = \frac{Ph^2c}{12I}, \tag{1.5.10b, c}$$

where P, h, H, c and I are the design pressure, the cross-sectional gap along the long and short side, the distance from the neutral axis to the inside surface and moment of inertia of a strip thickness, respectively. c and I can be computed by:

$$I = \frac{t_w^3}{12}, c = \frac{t_w}{2}. \tag{1.5.11a, b}$$

The same model can also be used to design the side margin thickness t_e. The design criteria include (1) the membrane stress at the edge $S_m{}^E$ shall not exceed the design stress; (2) the total stress $S_t{}^N$, which is the sum of the membrane stress $S_m{}^E$ and the bending stress $S_b{}^N$ at the location of N (the middle of the short side); (3) the total stress $S_t{}^Q$, which is the sum of the membrane stress $S_m{}^E$ and the bending stress $S_b{}^Q$ at the location of Q (the corner) shall not exceed 1.5 times of the design stress. Explicitly, they can be expressed as follows:

$$S_m^E \le SE, \tag{1.5.12}$$

$$S_m^E + S_b^N \le 1.5SE, \tag{1.5.13}$$

$$S_m^E + S_b^Q \le 1.5SE. \tag{1.5.14}$$

These stress values can be computed through following equations:

$$S_m^E = \frac{Ph}{2t_e}, \tag{1.5.15a}$$

$$S_b^N = \left(\frac{Pc}{24I}\right)\left(2h^2 - 3H^2\right), S_b^Q = \frac{Ph^2}{12I}, \tag{1.5.15b, c}$$

where c and I can be computed by:

$$I = \frac{t_e^3}{12}, c = \frac{t_e}{2}. \tag{1.5.16a, b}$$

The mechanical design methods above are generally appropriate for straight and zigzag channels, but questionable in applicability to islanded fin channels. It could be used as a starting point for structural assessment, but it would be too conservative in estimation. Therefore, an alternative method is required for complex surface geometries.

1.5.4 Alternative Mechanical Design Method

The mechanical design method based on the model of rectangular vessels with stayed plates is so-called Design-by-Rule method in ASME codes. When it comes to a complex geometry, such as S-shaped fin and airfoil channel, or high-pressure applications, the Design-by-Rule methods are no longer suitable due to the complexity of channel configurations and the elastic-plastic behavior of the material under high pressure. From preliminary numerical simulation of the stress distribution, it reveals that the excessive stress concentration occurs at corner tips of the flow channels (Zhang et al, 2015a). Hence, the Design-by-Rule requirement can be used as a starting point for the structural evaluation of complex geometry, and for a more accurate analysis, an alternative approach in ASME codes called the Design-by-Analysis method is recommended. The method requirements are organized based on the failure modes including the protection against plastic collapse. There are three available analysis methods for this failure mode:

(a) Elastic Stress Analysis Method – Stresses are computed using an elastic analysis, classified into categories, and limited to allowable values that have been conservatively established such that a plastic collapse will not occur.

(b) Limit-Load Method – A calculation is performed to determine a lower bound to the limit load of a component. The allowable load on the component is established by applying design factors to the limit load such that the onset of gross plastic deformations (plastic collapse) will not occur.

(c) Elastic-Plastic Stress Analysis Method – A collapse load is derived from an elastic-plastic analysis considering both the applied loading and deformation characteristics of the component. The allowable load on the component is established by applying design factors to the plastic collapse load.

For the elastic-stress-analysis method, it requires the stress linearization and classification of the numerical results based on an accurate modeling to satisfy the design criteria. Section VIII Division 2 lists the procedures of the stress categorization assessment. This is extremely challenging when it comes to complex geometry as the three-dimensional stress categorization significantly relies on personal knowledge and judgement.

For the limit-load method and elastic-plastic-stress-analysis method, the process of stress classification is not required. The procedure of the assessment is similar in both method. First a numerical model of the component including all relevant geometry characteristics should be developed. Such model should accurately represent all the geometry, boundary conditions and applied loads. Secondly, all applicable load cases should be defined. In this case, it is the internal pressure imposed on the surface of channels, as the flow channels are viewed as pressure-containing vessels. Lastly, an appropriate plastic model should be used. The acceptance criteria is that the plastic collapse load is taken as the load which causes overall structural instability (or plastic collapse). In other words, the load is taken when the simulation cannot converge after small increment of load is applied.

The primary difference between these later two methods is the particular model adopted. For the limit-load method, an elastic-perfectly-plastic (EPP) material model with small displacement theory is used in the analysis. The yield strength defining the plastic limit is equal to $1.5S$. For the elastic-plastic-stress-analysis method, a true stress-strain curve model that includes temperature dependent hardening behavior might be used. When using this material model, the hardening behavior is included up to the true ultimate stress and perfect plasticity behavior (i.e. the slope of the stress-strain curves is zero) beyond

this limit. It is worth noting that such material non-linearity in simulation is computationally very expensive.

1.5.5 Case study of S-shaped fin channel PCHE

In order to test the applicability of Design-by-Analysis methods for complex geometry and compare the design failure criteria for other mechanical design methods discussed above, a case study of S-shaped fin channel was carried out. As an example, the S-shaped fin channel PCHE is tested for mechanical integrity numerically. The accurate CAD modelling of such complex geometry is challenging. However, the outline of S-shaped fins can be model using a sinusoidal curve expressed in a mathematical function, which could be found in literatures (Zhang et al. 2016). Besides, the original plate design of the PCHE prototype is too large to do any direct numerical simulation on personal computers. Only a small portion of the metal plate is used in the numerical analysis. Figure 9 shows the CAD model and the computational domain.

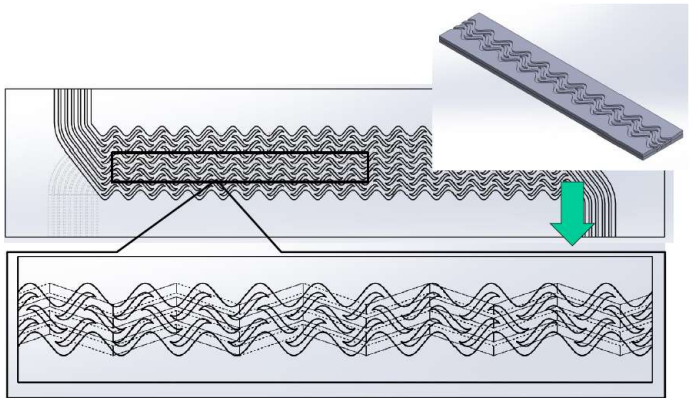

Figure 106 Computational domain for numerical analysis based on the original plate design

Mechanical Assessment Based on Design-by-Analysis Method

It is necessary to simulate the temperature conditions for the stress analysis since the material strength is reduced dramatically at high temperatures around 600 ºC. The temperature distribution of the computational domain could be obtained from CFD analysis. The temperature mapping along with mechanical loading gives an accurate stress distribution. In order to obtain the result with relatively low computational cost, several techniques can be adopted to achieve similar goal without sacrificing simulation accuracy. Such simulation was performed using ANSYS Workbench.

Since the channel array in the heat exchanger core matrix is periodically configured in vertical and lateral direction, therefore it is reasonable to model a pair of metal sheets with different surface geometry with only a few channels involved, as shown in Figure

107. In addition, the temperature distribution information obtained from the CFD calculation can be transferred to individual 1/6 slice-cut section of the original CFD computational domain for structural calculation. This can significantly reduce the computational cost, as the mesh for structural calculation must be very fine. Each section can then be analyzed individually. Finally, the mechanical loading can be further simplified to a fixed value instead of transferring the internal pressure information from the CFD calculation to the structural analysis that changes along the flow direction. This can certainly save more computational efforts.

With the basic setting of 13 MPa pressure difference in the temperature range of 480 ºC to 730 ºC (the internal pressure in zigzag and S-shaped fin channels are 2 MPa and 15 MPa, respectively) and EPP model for alloy 617, the simulation results indicate that the maximum stress occurs at the corner tip of the semi-circular channel, which is 236.5 MPa. The largest deformation occurs at the location where the two channels (zigzag and S-shaped fin channel) are aligned, as is shown in Figure 107. This indicates that the weakest spot is the place where the upper and lower channel are perfectly aligned with no additional structural support from the ridge walls.

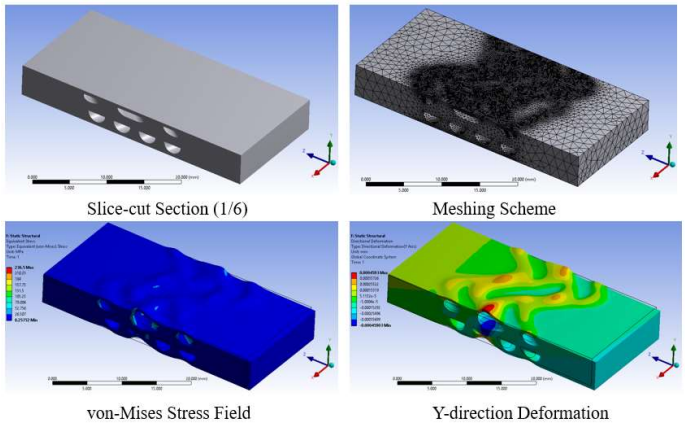

Figure 107 Meshing and simulation results of one of the six slice-cut sections

The calculation using the Design-by-Analysis method is also performed. The internal pressure loading for the zigzag channel is fixed to be 2 MPa, but the one for the S-shaped fin channel is progressively increased until the plastic instability happens. Figure 108 shows the recorded mechanical loading in S-shaped fin channel vs. the maximum total strain obtained from the simulation. The plateau region indicates plastic instability in the simulation due to the plastic collapse of the model under around 75 MPa. When the internal pressure loading is close to the plastic collapse load, the total equivalent strain changes drastically with small increment of the pressure loading. (Note that at the high loadings the maximum total equivalent strain increases with a magnitude of 10^0 mm/mm).

Therefore, the limit load can be determined to be approximately 50 MPa, with a safety factor of 1.5 taken into account, which is recommended by BPVC VIII-2 appendix 3.

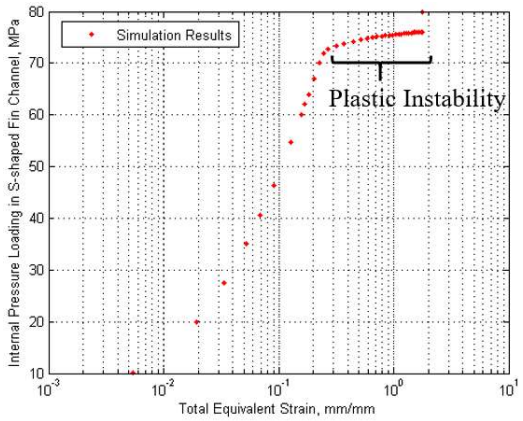

Figure 108 The loading pressure vs. the maximum total strain

Figure 109 shows the yielded portions in the model, which is displayed by the capped isosurface. The yielded volume is defined as the elements with equivalent stress (von-Mises stress) greater than the yield stress, which is taken as the one at temperature of 600 ºC. It clearly shows that the yielding occurs at the edges of bonding interfaces. Note that at the pressure loading around 15 MPa, the yielded volume is barely visible.

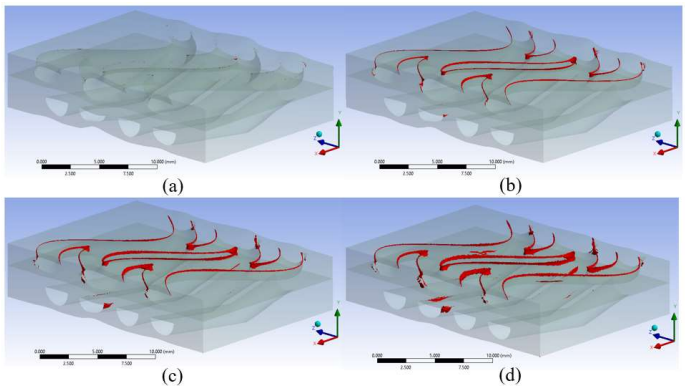

Figure 109 Yielded portions under pressure loading in the numerical model. The internal pressure in the S-shaped fin channel is (a) 30 MPa; (b) 45 MPa; (c) 60 MPa; (d) 70 MPa.

Thermal stress is also another concern as the temperature changes drastically across the heat exchanger core. The complex configuration of hot and cold channels in PCHE results in highly complicated temperature distribution. A direct approach to simulate the thermal stress and strain is to run a conjugate heat transfer simulation essentially representing a small portion of IHX, and then couple finite element analysis with the temperature results to simulate thermal strains. Figure 110 shows the thermal strain and stress distribution of

the computational domain. It can observed that the thermal strain can be neglected as the volume of elements that yield is very small.

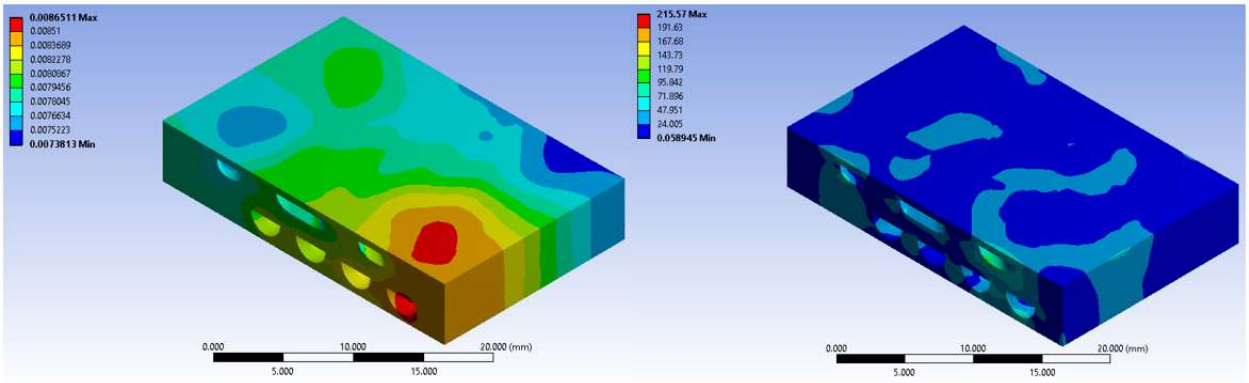

Figure 110. Thermal Strain (Left) and Thermal Stress (Right) Distribution

Comparison with Design-by-Rule Method

According to the ASME codes for the rectangular vessels with stayed plates, the S-shaped fin design fails the criteria with the basic internal pressure loading in S-shaped fin channels (15 MPa). It is required that either the wall thickness t_w is increased from 0.711 mm to at least 0.915 mm or the lateral pitch p_y is decreased from 7.434 mm to 6.221 mm or smaller. However, from the mechanical analysis based on the Design-by-Analysis method, this is certainly a conservative estimation. This is probably due to the fact that generally the Design-by-Rule method does not allow plastic deformation to occur. However, the Design-by-Analysis does not necessarily forbid plasticity, as long as the plastic zones are small enough to avoid the whole structural collapse. Therefore, it indicates that the current ASME codes do not apply to complex PCHE surface geometry, or it will generate highly conservative evaluation results, and the Design-by-Analysis method is recommended.

1.6 Design optimization of PCHEs for liquid-salt-s-CO_2 IHX

1.6.1 Molten salt-s-CO_2 IHX optimum sizing

s-CO_2 Brayton power cycle is one of the power cycles selected for AHTR (Advanced High-Temperature Reactor) that is characterized with using molten fluoride salt as the primary coolant. The design of IHX that couples the primary loop using molten salt and the secondary loop using s-CO_2 is particularly important. Therefore, for liquid-salt-s-CO_2 IHX design, the molten salt is selected as liquid salt

Surface geometry selection

As there are still limited reliable empirical correlations to predict s-CO_2 side thermal-hydraulics, the selection of s-CO_2 side PCHE channel surface geometry was made between 52º S-shaped fin and 52º Zigzag channel. From Table 35 we can see a summarized list of available correlations obtained experimentally. For the other two channels, since the heat transfer correlation is not in the form of Nusselt number, it is then not considered in the optimum sizing study. A geometrical similarity ratio is applied in the variation of surface geometry design. It is justified by the fact that the thermal-hydraulic performances for particular channel is maintained as long as the geometry is similar and operating Reynolds and Nusselt numbers are the same. The detailed surface geometry information is listed in Table 36.

Table 35. The available PCHE surface geometry designs for s-CO_2 application and the empirical correlations obtained from the experimental testing

Surface geometry description	Applicable range	Effective Fanning factor	Nusselt number (or heat transfer coefficient)	Source
52º S-shaped fin	$3\times10^3<Re<2\times10^4$	$f=0.4545Re^{-0.340}$	$Nu=0.1740Re^{0.593}Pr^{0.430}$	Ngo et al. (2007)
52º Zigzag channel	$3\times10^3<Re<2\times10^4$	$f=0.1924Re^{-0.091}$	$Nu=0.1696Re^{0.629}Pr^{0.317}$	Ngo et al. (2007)
32.5º Zigzag channel	$2.4\times10^3<Re<6\times10^3$	$4f=0.1798-5.608\times10^{-6}Re$	$h=2.52Re^{0.681}$	Nikitin et al. (2006)
40º Zigzag channel	$5\times10^3<Re<1.3\times10^4$	$4f=0.3727-6.180\times10^{-6}Re$	$h=5.49Re^{0.625}$	Nikitin et al. (2006)

Table 36. The available PCHE surface geometry designs for s-CO_2 application and the empirical correlations obtained from the experimental testing (Carlson, 2012)

Description	Units	52º S-shaped fin	52º Zigzag channel	32.5º Zigzag	40º Zigzag
Channel depth	mm	0.94	0.94	0.90	0.90
Profile radius	mm	Est. ~1.334	0.831	0.801	0.689
Hydraulic diameter	mm	1.09	1.09	1.15	1.15
Unit flow area	mm^2	1.23	1.23	1.166	1.032
Pitch	mm	3.426	3.426	2.97	3.25
Angle	º	52º	52º	32.5º	40º

Surface area per unit flow length	mm^2/mm	5.353	4.004	4.554	4.612
Plate thickness	mm	1.5	1.5	1.63	1.63

For the molten salt side, the straight circular channel is selected. This is because 1) for molten salt flow at relatively low Reynolds number, the clogging issue may arise. Straight circular channel can reduce the clogging effect; 2) the corrosion at the molten salt side might be aggressive at high temperature. Circular channels reduce the contact area, thus reduce the corrosion effect to some extent; 3) molten salts have relatively large thermal conductivity (as shown in Table 37), thus the heat transfer enhancement through surface geometry optimization is not priority.

Table 37. Selected molten salts' thermal properties (Sohal et al. 2010)

Molten Salt	Wt. %	Melting point (ºC)	Density (kg/m^3)	Specific heat capacity (J/kg-ºC)	Viscosity (Pa-s)	Thermal Conductivity (W/m-ºC)	Prandtl No.
FLiNak	29-12-59	454	2020	1882.8	0.0029	0.92	5.938
KCl-$MgCl_2$	62-38	435	1664	1158.97	0.0014	0.40	4.0

The recommended correlation for molten salts' heat transfer is the Gnielinski correlation, which has 10% deviation in prediction (Yoder, 2014):

$$\mathrm{Nu} = \frac{(f/2)(\mathrm{Re}-1000)\,\mathrm{Pr}}{1+12.7(f/2)^{1/2}(\mathrm{Pr}^{2/3}-1)} \tag{1.6.1}$$

The f is the friction factor developed by Filonenko:

$$f = \left(1.58\ln(\mathrm{Re})-3.28\right)^{-2} \tag{1.6.2}$$

The correlations are recommended for use for $2300<Re<1\times10^6$ and $0.5<Pr<2000$. For laminar flow, the following correlations are used:

$$\begin{aligned} &\mathrm{Nu} = 4.3636, \\ &f = \frac{16}{\mathrm{Re}}. \end{aligned} \tag{1.6.3}$$

Thermal and structural design

Since there is no particular design for molten salt cooled reactors coupled with s-CO_2 Brayton cycle, the lead alloy-s-CO_2 design is applied. The mass flow rate is therefore scaled down to 4335 kg/s for FLiNaK. The operating conditions can be reference to Table 7. Since the operating temperature is not extremely high, stainless steel 316 is selected as the base material.

The thermal design can be reference to the one used in the helium-to-s-CO_2 design in section 1.2. For the structural stress analysis, since the operating pressure of the molten salt side is close to atmospheric pressure, the ridge thickness and plate thickness according to the simple stress analysis method are very small. To maintain the channel design consistency, 50% of the circular channel diameter is required as the ridge thickness; the plate thickness is determined by stress analysis at the s-CO_2 side, which is around 20 MPa. For the reference S-shaped fin channel design, the plate thickness is too small to withstand the design pressure of 20 MPa. Therefore, the plate thickness should be increased in compliance with ASME standards. A conservative estimation is applied in the calculation.

The most challenging location is the long side of the channel (the width) which requires the total stress that consists of the membrane stress of the ridge and bending stress not exceed 1.5 times of the design stress. For SS 316, the maximum allowable stress at the worst temperature is 110 MPa. Using Eq. (1.5.7) through (1.5.11), we can obtain

$$20\mathrm{MPa} \times \left(\frac{H}{2t_w} + \frac{h^2}{2t_w^2} \right) \le 110\mathrm{MPa} \ . \tag{1.6.4}$$

Since H/h is 0.94/1.9 = 0.5, and $h = 1.734D_h$, we can then obtain

$$t_w = 0.562D_h \tag{1.6.5}$$

A double banking configuration for both sides is considered, as shown in Figure 111.

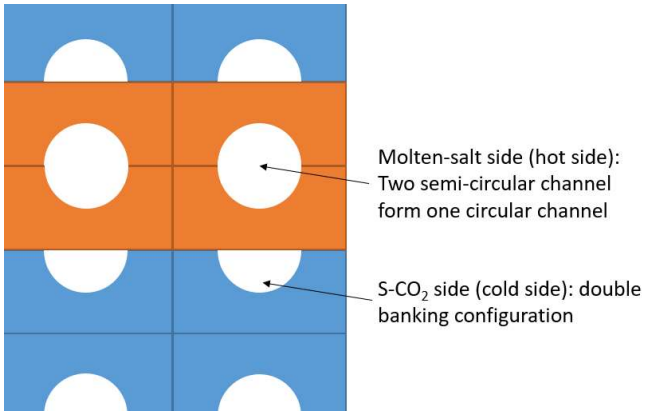

Figure 111. Double banking configuration of s-CO_2 side channels with molten salt side circular straight channel

Design optimization

There are three variables for the design optimization: the molten salt side channel diameter, the s-CO_2 surface geometry similarity ratio, which controls the relative size of the S-shaped fin channel, and the physical length of the heat exchanger. Since none of them is related to the change of surface geometry, the optimization is only for optimum sizing for the IHX. A parametric study is carried out to determine the design space for the three variables. Figure 112 through Figure 114 show the dependence of the pressure drop, heat transfer coefficient (HTC), the total cost and the heat exchanger thermal effectiveness based on the calculation. It can be concluded that the increase of the molten salt side straight channel diameter generally lowers the pressure drop and heat transfer coefficient on both primary and secondary sides. However, since the molten salt side channel becomes bigger, it requires more frontal area, which reduces the s-CO_2 side frontal area. This results in the increase of required number of modules, and thus increases the total required pumping power. Therefore, as can be seen from Figure 112, the operating cost is significantly increased for the molten salt side channel diameter being 5 mm, whereas the thermal effectiveness is almost the same. Similar trend can be found when increasing the size of S-shaped fin channel. As to increasing the physical length, in general, both the pressure drop and heat transfer coefficient increase. However, in the comparison of the total cost vs. thermal effectiveness, small enhancement in the thermal effectiveness requires huge increase in operating cost. An optimum heat exchanger size can be achieved through optimization.

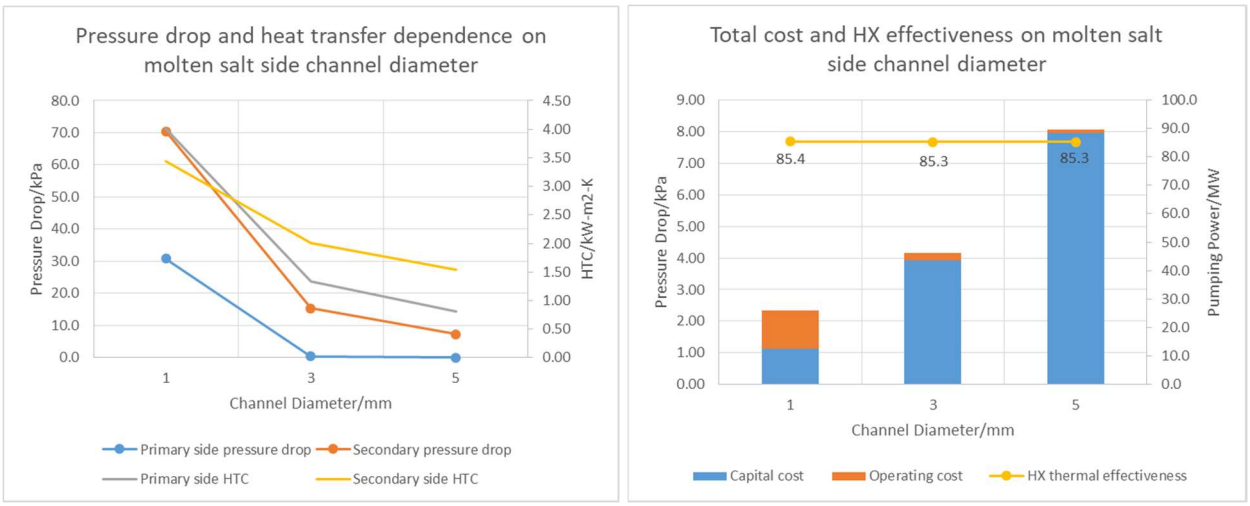

Figure 112. The parametric study on the effect of the molten salt side channel diameter

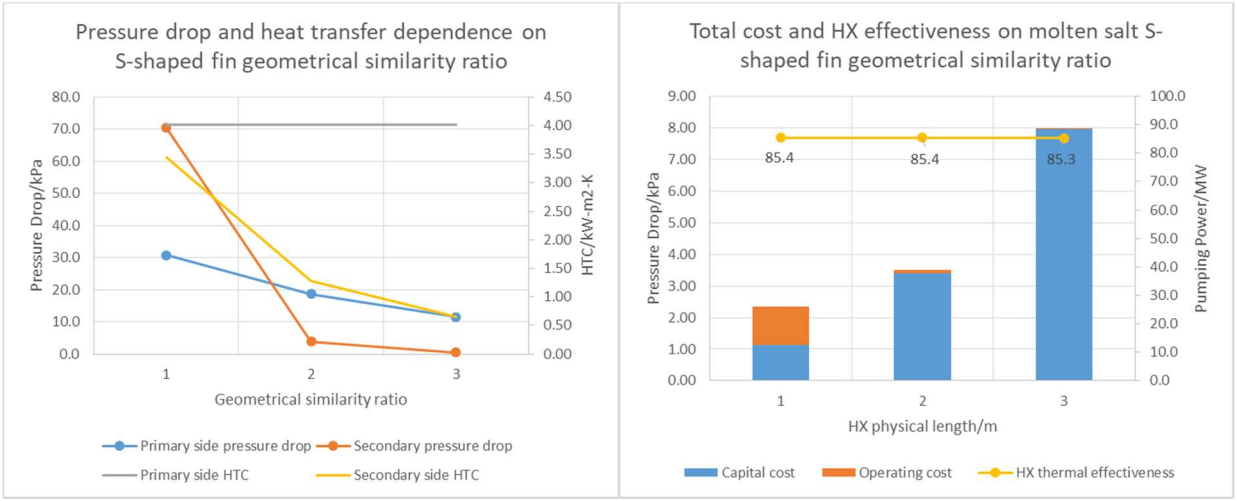

Figure 113. The parametric study on the effect of the s-CO_2 side geometric similarity

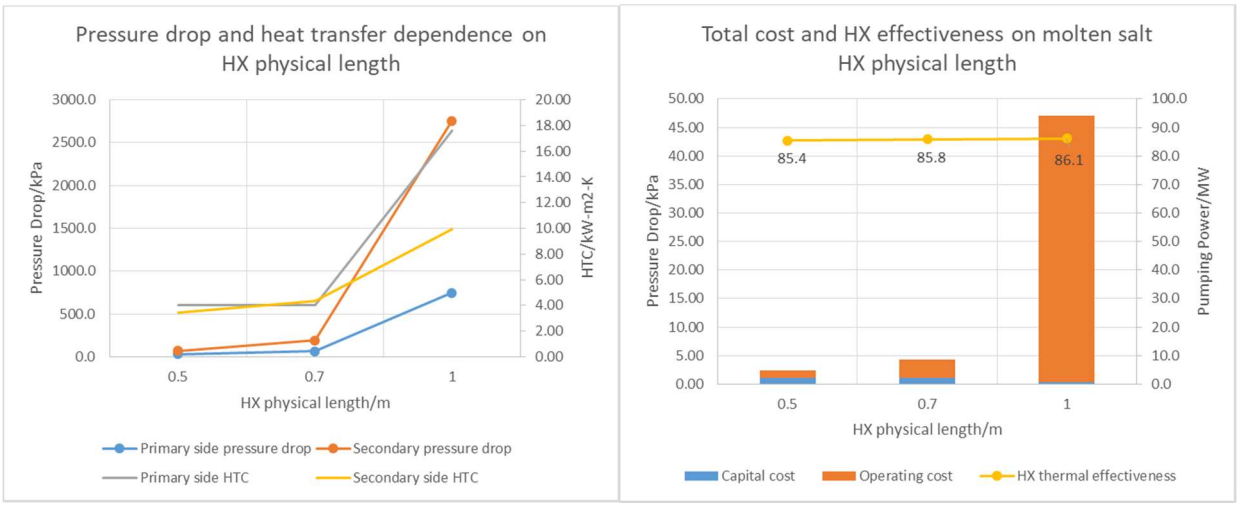

Figure 114. The parametric study on the effect of the physical length of heat exchanger

The optimization results is shown in Figure 115. It indicates that the optimum designs have fairly similar thermal effectiveness whereas the total cost varies largely. It is recommended to use design #1 listed in Table 38.

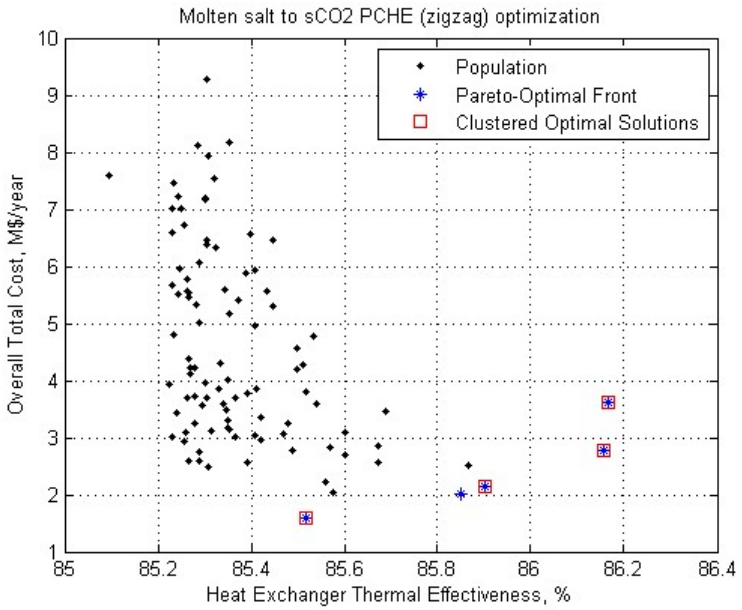

Figure 115. Optimization results for molten salt-s-CO_2 IHX using S-shaped fin channel

Table 38. Detailed optimization results for molten salt-s-CO_2 IHX using S-shaped fin channel

Category		Number	Item	Units	#1	#2	#3	#4
INPUT		1	Molten salt channel diameter	mm	1	1	1	1.29
		2	Channel angle	°	0	0	0	0
		3	Geometrical similarity ratio	n/a	1	1.000	1.286	1
		4	Length	m	0.300	0.471	0.700	0.700
SPECIFIED PARAMETERS	General	5	Thermal duty	MW	700	700	700	700
	Primary side	6	Mass flow rate	kg/s	4335	4335	4335	4335
		7	Pressure	MPa	0.1	0.1	0.1	0.1
		8	Inlet temperature	C	555	555	555	555
	Secondary side	9	Mass flow rate	kg/s	3910	3910	3910	3910
		10	Pressure	MPa	20	20	20	20
		11	Inlet temperature	C	384	384	384	384
OUTPUT	Primary side	12	Outlet temperature	C	468.9	468.6	468.3	468.3
		13	Reynolds number	n/a	231	416	602	548
		14	Pressure drop	kPa	9.2	26.1	56.1	24.1
		15	Heat transfer coefficient	kW/m2-C	4.01	4.01	4.01	3.12

		16	Heat transfer area	m2	7770	6783	6954	7633
		17	Surface area density	m2/m3	399.7	399.7	324.6	378.6
		18	Pumping power	MW	0.020	0.056	0.120	0.0516
	Secondary side	19	Outlet temperature	C	530.2	530.9	531.3	531.3
		20	Reynolds number	n/a	13820	24876	36061	32815
		21	Pressure drop	kPa	13.4	55.7	72.1	131.1
		22	Heat transfer coefficient	kW/m2-C	2.28	3.24	3.14	3.81
		23	Heat transfer area	m2	13007	11355	11631	12782
		24	Surface area density	m2/m3	669.1	669.1	543.0	634.0
		25	Pumping power	MW	0.368	1.533	1.984	3.606
GEOMETRIC PARAMETERS	General	26	Heat exchanger core volume	m3	19.4	17.0	21.4	20.2
		27	Heat exchanger mass	Mg	154	135	170	160
		28	Number of modules	n/a	36	20	17	16
		29	Frontal area	m2	32.4	28.3	35.7	33.6
		30	Number of plates per block	n/a	458	458	372	434
		31	Heat exchanger physical length	m	0.300	0.471	0.700	0.700
	Primary side	32	Channel diameter	mm	1.000	1.000	1.000	1.286
		33	Hydraulic diameter	mm	1.000	1.000	1.000	1.286
		34	Channel angle	°	0	0	0	0
		35	Transverse pitch	mm	1.500	1.500	1.500	1.929
		36	Plate thickness	mm	1.11	1.11	1.29	1.26
		37	Number of channels per plates	n/a	400	400	400	311
		38	Flow area	m2	6.5	3.6	2.5	3.5
	Secondary side	39	sCO2 side geometrical similarity ratio	n/a	1	1.000	1.285714	1
		40	Hydraulic diameter	mm	1.09	1.090	1.401429	1.09
		41	Fin angle	°	52	52	52	52
		42	Longitudinal pitch	mm	7.565	7.565	9.726	7.565
		43	Transverse pitch	mm	3.426	3.426	4.405	3.426
		44	Plate thickness	mm	1.500	1.500	1.929	1.500
		45	Number of channels per plates	n/a	175	175	136	175
		46	Flow area	m2	8.87	4.93	4.37	3.74
AUXILIARY DATA		47	Heat exchanger capacity	MW	702	706	708	708
		48	Overall H.T.C. at primary side	kW/m2-C	1.85	2.16	2.13	1.94
		49	Overall H.T.C at secondary side	kW/m2-C	1.11	1.29	1.27	1.16
		50	Total surface density	m2/m3	1069	1069	868	1013

	51	Specific performance	MW/m3	36.1	41.6	33.0	35.1
	52	NTU	n/a	3.00	3.05	3.09	3.09
	53	Material cost	M$/year	1.36	1.19	1.50	1.41
	54	Operating cost	M$/year	0.23	0.96	1.27	2.21
	55	Percentage of material to operating cost	%	582.6	124.0	118.2	64.0
	56	Total pumping power	MW	0.39	1.59	2.10	3.66
	57	Percentage of pumping power to thermal duty	%	0.055	0.225	0.297	0.517
	58	Total cost	M$/year	1.60	2.15	2.77	3.62
	59	Effectiveness	%	85.5	85.9	86.2	86.2
	60	LMTD	C	48.8	48.2	47.7	47.7

Figure 116 shows the optimized result for using zigzag channel on the s-CO_2 side. It demonstrates similar trend to the S-shaped fin channel. However, when comparing the design with lowest cost obtained from optimization, we can see that zigzag channel design is inferior because of much higher total cost with the similar thermal effectiveness. Such comparison is shown in Table 39.

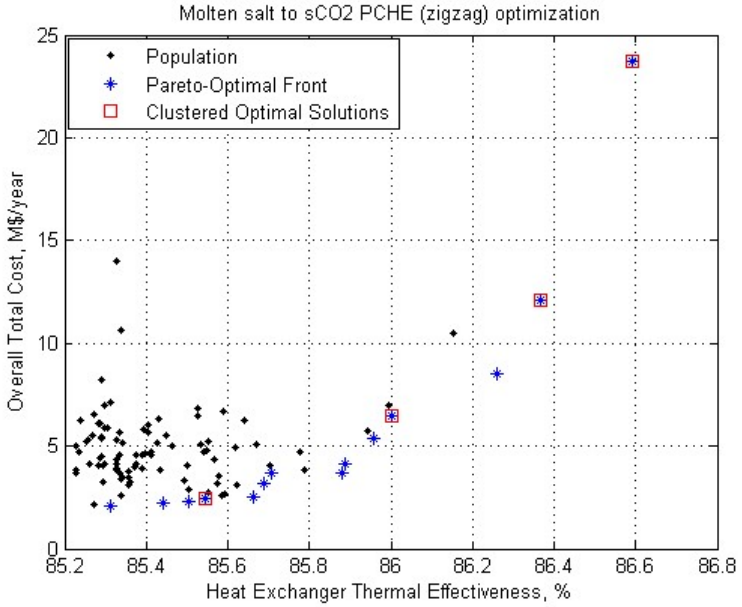

Figure 116. Optimization results for molten salt-s-CO_2 IHX using zigzag channel

Table 39. Optimization results comparison for molten salt-s-CO_2 IHX using s-CO_2 and zigzag channel

Category	Number	Item	Units	S-shaped fin	zigzag
INPUT	1	Molten salt channel diameter	mm	1	1.286

		2	Channel angle	°	0	0
		3	Geometrical similarity ratio	n/a	1	1.571
		4	Length	m	0.300	0.529
SPECIFIED PARAMETERS	General	5	Thermal duty	MW	700	700
	Primary side	6	Mass flow rate	kg/s	4335	4335
		7	Pressure	Mpa	0.1	0.1
		8	Inlet temperature	C	555	555
	Secondary side	9	Mass flow rate	kg/s	3910	3910
		10	Pressure	MPa	20	20
		11	Inlet temperature	C	384	384
OUTPUT	Primary side	12	Outlet temperature	C	468.9	468.7
		13	Reynolds number	n/a	231	382
		14	Pressure drop	kPa	9.2	12.7
		15	Heat transfer coefficient	kW/m2-C	4.01	3.12
		16	Heat transfer area	m2	7770	8272
		17	Surface area density	m2/m3	399.7	263.5
		18	Pumping power	MW	0.020	0.027
	Secondary side	19	Outlet temperature	C	530.2	530.6
		20	Reynolds number	n/a	13820	22939
		21	Pressure drop	kPa	13.4	72.6
		22	Heat transfer coefficient	kW/m2-C	2.28	2.84
		23	Heat transfer area	m2	13007	13806
		24	Surface area density	m2/m3	669.1	439.7
		25	Pumping power	MW	0.368	1.997
GEOMETRIC PARAMETERS	General	26	Heat exchanger core volume	m3	19.4	31.4
		27	Heat exchanger mass	Mg	154	249
		28	Number of modules	n/a	36	33
		29	Frontal area	m2	32.4	52.3
		30	Number of plates per block	n/a	458	302
		31	Heat exchanger physical length	m	0.300	0.529
	Primary side	32	Channel diameter	mm	1.000	1.286
		33	Hydraulic diameter	mm	1.000	1.286
		34	Channel angle	°	0	0
		35	Transverse pitch	mm	1.500	1.929
		36	Plate thickness	mm	1.11	1.61
		37	Number of channels per plates	n/a	400	311
		38	Flow area	m2	6.5	5.0

	Secondary side	39	sCO2 side geometrical similarity ratio	n/a	1	1.571
		40	Hydraulic diameter	mm	1.09	1.713
		41	Fin angle/channel angle	°	52	52
		42	Longitudinal pitch	mm	7.565	11.888
		43	Transverse pitch	mm	3.426	5.384
		44	Plate thickness	mm	1.500	2.357
		45	Number of channels per plates	n/a	175	111
		46	Flow area	m2	8.87	8.40
AUXILIARY DATA		47	Heat exchanger capacity	MW	702	704
		48	Overall H.T.C. at primary side	kW/m2-C	1.85	1.76
		49	Overall H.T.C at secondary side	kW/m2-C	1.11	1.05
		50	Total surface density	m2/m3	1069	703
		51	Specific performance	MW/m3	36.1	22.4
		52	NTU	n/a	3.00	3.02
		53	Material cost	M$/year	1.36	2.20
		54	Operating cost	M$/year	0.23	1.22
		55	Percentage of material to operating cost	%	582.6	180.1
		56	Total pumping power	MW	0.39	2.02
		57	Percentage of pumping power to thermal duty	%	0.055	0.288
		58	Total cost	M$/year	1.60	3.42
		59	Effectiveness	%	85.5	85.7
		60	LMTD	C	48.8	48.5

2. Experimental Investigation of PCHE Thermal and Structural Performance

2.1 Design of the Experimental Facility and Test PCHE in OSU

2.1.1 Conceptual design of the experimental facility

Existing High-Temperature Helium test Facility (HTHF)

The helium-s-CO_2 PCHE was fabricated and planned to be tested in a coupled test system, which consists of the existing HTHF and an s-CO_2 test loop that is designed. Figure 62 shows the layout of the HTHF. The HTHF was originally constructed to conduct thermal-hydraulic testing for two helium straight-channel PCHE recuperators at temperatures and pressures up to 800 °C and 3 MPa, respectively. The HTHF consists of a pre- and main-radiant heater, a gas booster, a cooling system, essential piping, valves, various instruments, and two PCHEs that are made of Alloy 617. The pre-heater and main-heater are essentially the same with a maximum heating capacity approximately 23 kW. The gas booster installed in the HTHF is a single-stage double-acting air-drive booster. An inline air-drive pressure regulator valve was installed at downstream of the booster to mitigate the flow oscillation induced by the reciprocation of the booster pistons during operation. A blind flange was reserved for future use of the facility. In the helium-s-CO_2 test loop, the hot helium flow from the blind flange, i.e. flange No.14, as shown in the Figure 117, to the PCHE to be tested (called “test PCHE” thereafter) and back to the HTHF through flange No.17.

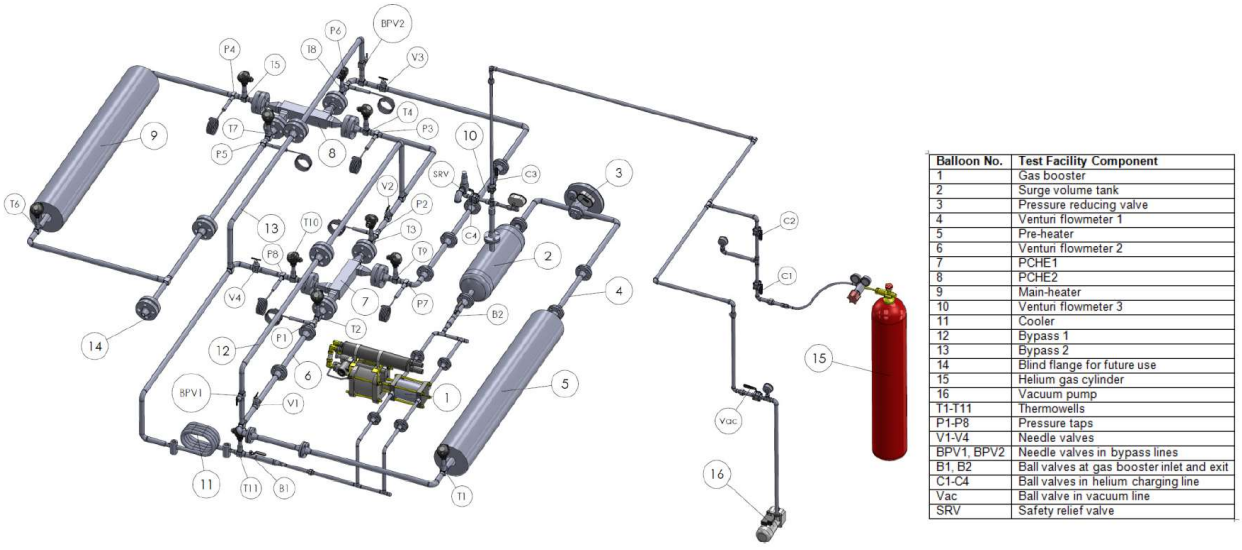

Balloon No.	Test Facility Component
1	Gas booster
2	Surge volume tank
3	Pressure reducing valve
4	Venturi flowmeter 1
5	Pre-heater
6	Venturi flowmeter 2
7	PCHE1
8	PCHE2
9	Main-heater
10	Venturi flowmeter 3
11	Cooler
12	Bypass 1
13	Bypass 2
14	Blind flange for future use
15	Helium gas cylinder
16	Vacuum pump
T1-T11	Thermowells
P1-P8	Pressure taps
V1-V4	Needle valves
BPV1, BPV2	Needle valves in bypass lines
B1, B2	Ball valves at gas booster inlet and exit
C1-C4	Ball valves in helium charging line
Vac	Ball valve in vacuum line
SRV	Safety relief valve

Figure 117. The layout of the high-temperature helium test facility (HTHF)

The major concern about coupling the existing HTHF with the s-CO_2 test loop for experiments is that the helium flow is required to reach up to 800 °C and 7 MPa in the

prototypic PCHE design, while the existing HTHF was designed to withstand up to 800°C and 3 MPa. This actually calls for a scaling analysis to scale down the system pressure in the prototypic design such that the test PCHE can satisfy the operating conditions on the helium side. Furthermore, the heating power supply of HTHF is also likely to constrain the actual size of the test PCHE. As mentioned in the previous section, in the prototypic design, for instance, the heat load of one particular block of the 95%-effectiveness PCHE is approximately 6.57 MW, whereas the maximum heating power supplied by HTHF is theoretically only 46 kW. In fact, the maximum heat load that can be supplied to the test PCHE is much less than 46 kW. Therefore, the test PCHE is much smaller than one block of the optimized PCHE design.

Conceptual design of the s-CO_2 Test Loop (STL)

The STL was under designed and was constructed. The conceptual design layout is shown in Figure 118. The loop consists of the test PCHE, an s-CO_2 recuperator, an s-CO_2 pre-heater, a gear pump, a Coriolis type flowmeter, a cooling system, an s-CO_2 supply system, an accumulator, an exhaust valve, flanges, piping, valves and instrumentation. It was designed to operate up to 650 °C and 16 MPa. In the STL, the s-CO_2 supply system discharges the CO_2 from the gas cylinders to the loop. The CO_2 is then compressed by the gear pump and flows to the pre-heater and the recuperator. The pre-heater and the recuperator heat up the flow to the desired inlet temperature of the test PCHE. The purpose to install a recuperator instead of using the pre-heater to directly raise the CO_2 temperature is that the required heating power is relatively huge, otherwise the size of the heater is too large to be accommodated in the laboratory. Additionally, the recuperator can mitigate the cooling burden of the cooling system and harsh operating conditions of the piping where the gear pump and flowmeter are located. The accumulator is to absorb thermal expansion and/or flow oscillation of s-CO_2 during transients such as start-up heating of the loop. There is also a by-pass line at the recuperator, of which the main purpose is to control the flow rates going through the recuperator during the operation. The heat transfer and pressure drop data of the recuperator at different flow rates is helpful to determine the PCHE thermo-hydraulic performances. Also, the s-CO_2 flow at higher temperatures is expected to have larger volumetric flow rate than the flow at lower temperatures. Therefore, it is necessary to control the flow rate at the hot-leg inlet of the recuperator.

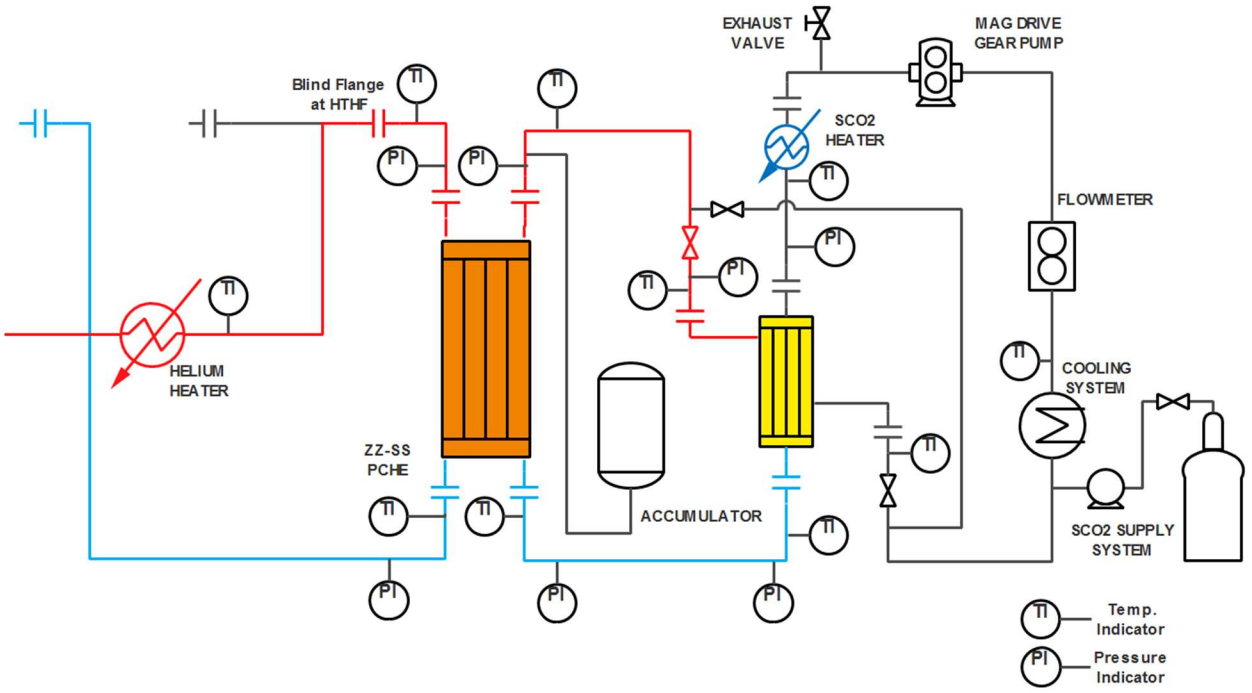

Figure 118. The schematic of the STL

The hotest piping of the entire system was made of Alloy 800H since it is capable of withstanding high pressures and temperatures and is economically feasible. The test PCHE was made of Alloy 617, while the s-CO_2 recuperator was made of Stainless Steel 316. The pipe size and thickness was designed based on ASME codes.

As stated in the ASME B31.3 (ASME code for Process Piping), the required thickness of straight sections of a pipe is suggested in accordance with Eq. (2.1.1)

$$t_m = t + c \tag{2.1.1}$$

The minimum thickness for the pipe selected should not be less than t_m, which is the minimum required thickness including mechanical, corrosion and erosion allowance. t is the pressure design thickness as calculated in Eq. (2.1.2). c is the sum of mechanical allowances. Eq. (2.1.2) presents the determination of the pipe thickness under an internal pressure,

$$t = \frac{PD}{2(SE + PY)} \tag{2.1.2.a}$$

$$t = \frac{P(d + 2c)}{2[SE - P(1 - Y)]} \tag{2.1.2.b}$$

where $P, D, S, E, Y,$ *d* are internal design gage pressure, outer diameter of pipe, maximum allowable stress according to varying temperatures, quality factor, coefficient from either the table listed in ASME B31.3 or additional expression based on the relation of the thickness, and inner pipe diameter, respectively. It is noteworthy that P and S should be in the same unit of either MPa or psi; E is typically equal to 1 for seamless pipes; Y is a coefficient to account for the non-linear reduction in allowable stress at design temperature above 482 °C; and *d* is the inner diameter of the pipe, which should be the maximum value allowable under the purchase specification in the pressure design calculation. The values are valid for $t < D/6$, and interpolation for intermediate temperatures is advised. For $t \geqslant D/6$, Y is calculated by the expression (2.1.3)

$$Y = \frac{d + 2c}{D + d + 2c} \tag{2.1.3}$$

where c is usually taken as 1 mm. For the pressure rating calculations, Eq. (1.2.2) can be modified to the form shown below

$$P = \frac{2tSE}{D - 2tY} \tag{2.1.4.a}$$

$$P = \frac{2tSE}{d + 2c + 2t(1 - Y)} \tag{2.1.4.b}$$

It is required that the internal pressure design thickness for straight pipe not be less than the one calculated from Eq. (2.1.2). Therefore, the internal gage pressure should not be greater than that calculated from Eq. (2.1.4). If it is assumed that *d* is calculated based on the expression (2.1.5),

$$d = D - 2t_m = D - 2(t + c) \tag{2.1.5}$$

According to the above specified methods, the pipe size can be determined. Considering that the maximum thickness of nominal pipe size (NPS) 1'' available for alloy 800H pipe is SCH 160, the maximum operating temperature is set to be 650 °C (with 50 °C temperature margin for the PCHE outlet temperature on the s-CO_2 side). In that case, the thickness is 6.350 mm. Using this value, we can obtain that the minimum thickness to withstand pressure 16 MPa is 4.676 mm, which is less than the practical thickness. Therefore, NPS 1'' SCH 160 Alloy 800H pipe can satisfy the temperature-pressure rating up to 650 °C and 16 MPa, with a large margin against the nominal operating conditions.

The nominal operating pressure and temperature of the system is restricted to the availability of major components as well as fittings. Since high system pressure may impose great challenges on the fittings and lead to potential leakage, the temperature-pressure rating of fittings must be satisfied. This is related to not only the s-CO_2 loop but also the helium loop. According to ASME B16.5 using Alloy 800 as material, class 2500 flange can satisfy the requirement at temperature 600 °C and 17.85 MPa, while class 2500 flange can withstand up to 725 °C and 3.36 MPa, as listed in Table 40. It should be noticed that the class 1500 flange can withstand 2.01 MPa at 725 °C, which is the same type of flange used as the blind flange in HTHF. Accordingly, the class 1500 must be used, and the temperature and pressure margin at the inlet of the helium side in the test PCHE can be very small. Due to the maximum pressure at helium side that available flanges can withstand being only around 2 MPa, it is then determined that the nominal operation pressure and temperature is 2 MPa with 730 °C for helium and 15 MPa with 595 °C for s-CO_2.

Table 40. Temperature-pressure rating of Alloy 800 flanges

Temperature., °C	Pressure, bar	
	Class 1500	Class 2500
575	119.7	199.5
600	107.0	178.5
625	91.2	117.7
725	20.1	33.6
750	15.1	25.2

With regard to the pre-heater, there are three types of electric heaters that are suitable for the STL, namely, cartridge heaters, circulation heaters, and radiant heaters. Cartridge heaters, which have relatively high power density, are capable of supplying sufficient heating power in a small space. Considering the working fluid as gas, the design with a coiled tube, as demonstrated by Figure 119(a), which is surrounded by cartridge heaters contained in a canister, was considered because it can increase the heat transfer area and thus improve the heat transfer efficiency. In addition, it does not occupy large space as the available facility construction area is limited. As to the circulation heaters, they are often used in industry to heat flowing fluids, such as water, process water, oil, gases, steam and corrosive solutions. A fluid flows directly over the heating elements inside the circulation heater to get heated up. The size of a circulation heater depends on the required heating power. The last type of heaters is the radiant heater, which was actually used and installed in the HTHF to heat up helium. The heating elements are embedded in thermal insulation and heat up the pipe that is located at the center of heating modules by thermal radiation. Usually, the radiant heaters require multiple heating modules as

shown in Figure 119(c), hence the heating modules that wraps the pipe can be very long. Since radiant heaters provide flexibility in choosing the total required power for heating, it was selected to be the heating elements of choice installed on the STL. The number and size of heating modules are dependent on the required heating capacity as well as the construction limits in practical situations.

(a) (b) (c)

Figure 119. (a) Cartridge heater design with coiled tube in the UW-Madison's s-CO2 loop; (b) Circulation heater basic construction; (c) Radiant heater that is used in OSU HTHF

A magnetic drive gear pump was considered to be installed in the STL. The main concern is to effectively eliminate the leakage issue at such a high pressure. However, as the operating system pressure can reach up to 15 MPa, the available off-shelf magnetic drive gear pumps are very limited. Additionally, a Coriolis type flowmeter is being acquired.

2.1.2 Design of mobile experimental platform (MEP) for the STL

The STL was designed to be coupled with the HTHF helium facility and DRACS molten-salt facility. However, the sites of two existing facilities are located in different buildings. Therefore it calls for a mobile experimental platform (MEP) to accommodate all major components of STL and provide mobility to move STL from one site to another. Some challenges and limits are imposed on the design of MEP by practical situations at the buildings. First, the spatial room available for STL is very limited. The test PCHE couples HTHF with STL at the blind flange marked as 14 in Figure 120. Thus the length of MEP is restricted to less than 10 ft. (approximately 3 m). Additionally, the width must be less than 32 in. (0.8 m) because of the limited width of the doors. Since the width of MEP is specified, the design must be compact and two levels of MEP is required. On the upper level is the heating section of STL. There are double radiant heaters wrapped around the pipes to supply the required heating capacity. The heated pipes are 7 ft. long (2.1 m) with four hinged hangers used to support the pipes. One end of the heating section connects the test PCHE inlet and the other connects the lower level. The lower level consists of a magnetically sealed gear pump, a flowmeter and a cooling system with two tube-in-tube

heat exchangers as coolers. The lower level connects the outlet of PCHE, the upper level and the gas supply system. Grayloc connectors are currently planned to be used for connections between major components at the lower level. A 3-D modeling of MEP is shown in Figure 120.

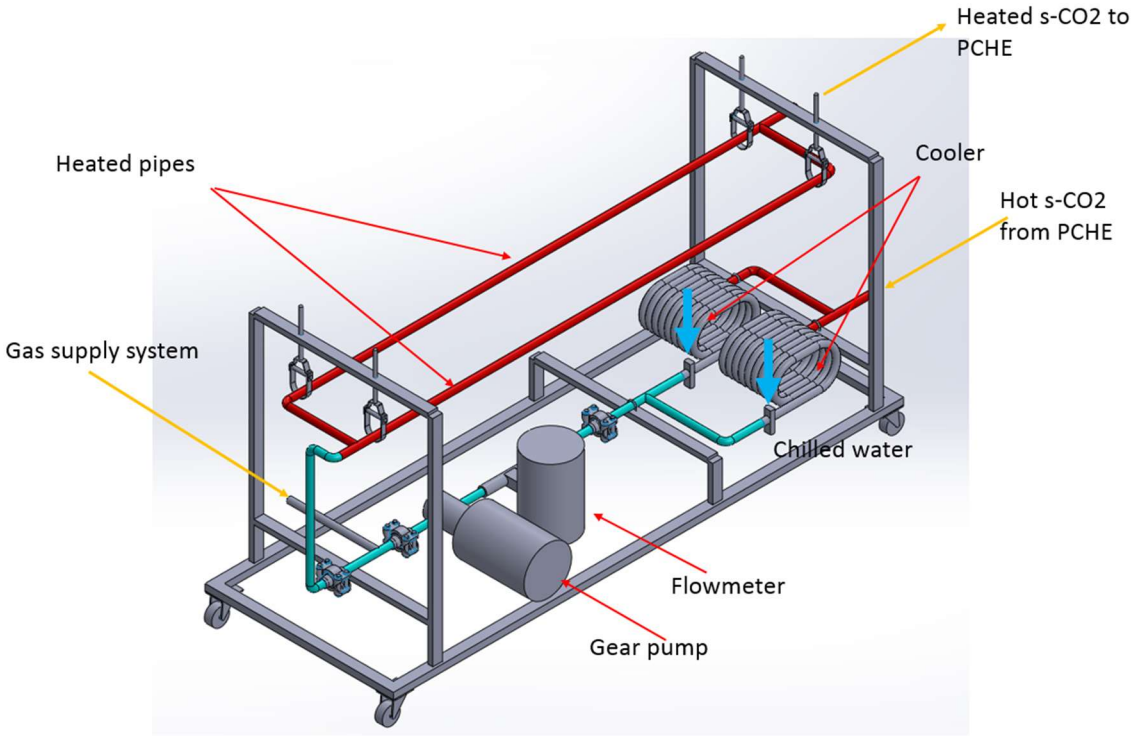

Figure 120. Configuration of MEP in the conceptual design

The gas supply system consists of a supercritical fluid filling pump (or compressor), a vacuum pump and a gas cylinder. The filling pump can provide the discharging of carbon dioxide into the STL to specified system pressure. The nominal pressure in the system is 15 MPa. The filling pump can also control and adjust the system pressure. Therefore, there is no need to install an accumulator or a regulator valve. The gas supply system, except the gas cylinder, can also be installed on PEM. The PI&D drawing is shown in Figure 121.

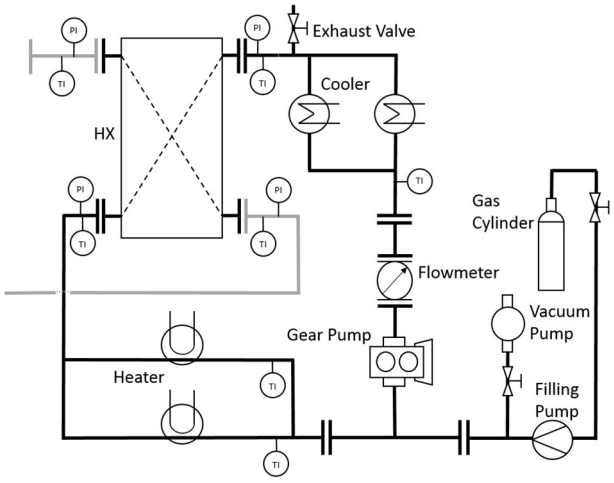

Figure 121. PI&D drawing of the STL system in the conceptual design

Update of design of the STL

One of the major concerns in design of the STL is the availability of the commercial pumps or compressors for supercritical fluid at high pressure. It is strongly suggested by the vendors that the s-CO_2 pump should operate at SG (specific gravity) larger than 0.5. This requirement indicates that the temperature at the pump must be lower than 60 ºC, otherwise it is very difficult to find a suitable pump. Another constraint is the high pressure of the system. Most of the commercially available pumps are not able to withstand high pressure up to 150 MPa (2176 psi), therefore it is extremely difficult to find suitable pumps and the previous design of the STL must be adjusted. The limits of available pumps dictate the heating and cooling power required for the entire system. Without recuperation, nearly 40 kW heating power is required even the s-CO_2 flow rate has been reduced significantly. This may enormously increase the budget for the construction of the STL, and auxiliary cost associated with the support and maintenance to the facility will increase. Hence, it is necessary to have a recuperator for the STL, and due to the nature of high system pressure, PCHE was again chosen to be as the recuperator. The updated PI&D drawing for the STL system as well as the test PCHE coupled with HTHF is shown in Figure 122.

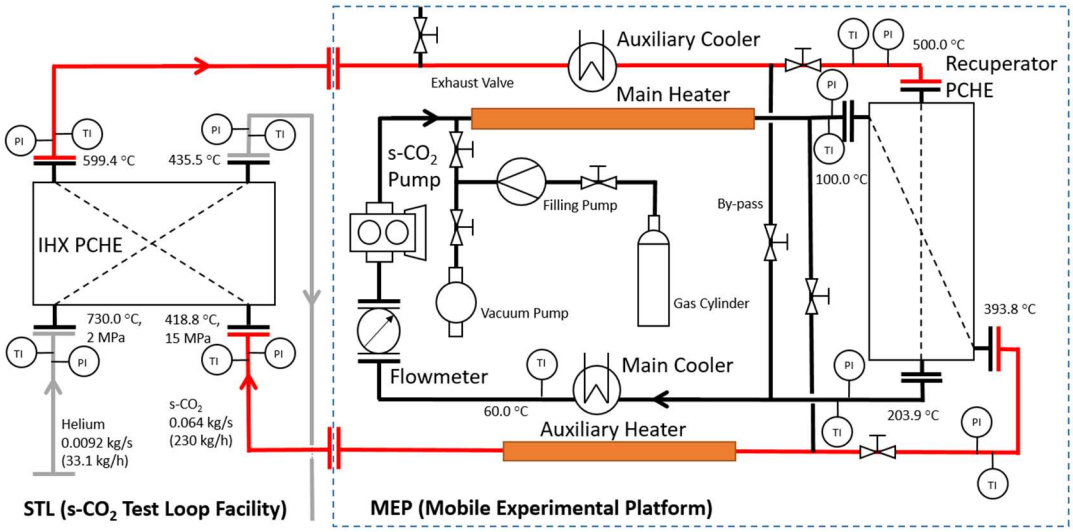

Figure 122. PI&D drawing of the modified design of STL

Figure 123 shows the 3-D modeling of the MEP. Since the space in the laboratory to accommodate additional experimental systems is extremely limited, the MEP has to be designed in a very compact way. Moreover, the heating elements to use in the MEP are ceramic fiber radiant heaters, which will occupy most of the space due to the nature of this type of heaters. Radiant heaters could be infinitely added to increase the heating power. Another advantage of them is that they don't intrude in the pipes and require extra component to install in the loop system. However, one of the disadvantages is that they need to occupy relatively large area of piping that will be heated up. This drawback affects the design of the MEP significantly. As can be seen in the right figure of Figure 123, both the main and auxiliary heaters are humongous compared with the MEP itself. The heaters' specification is listed in Table 41.

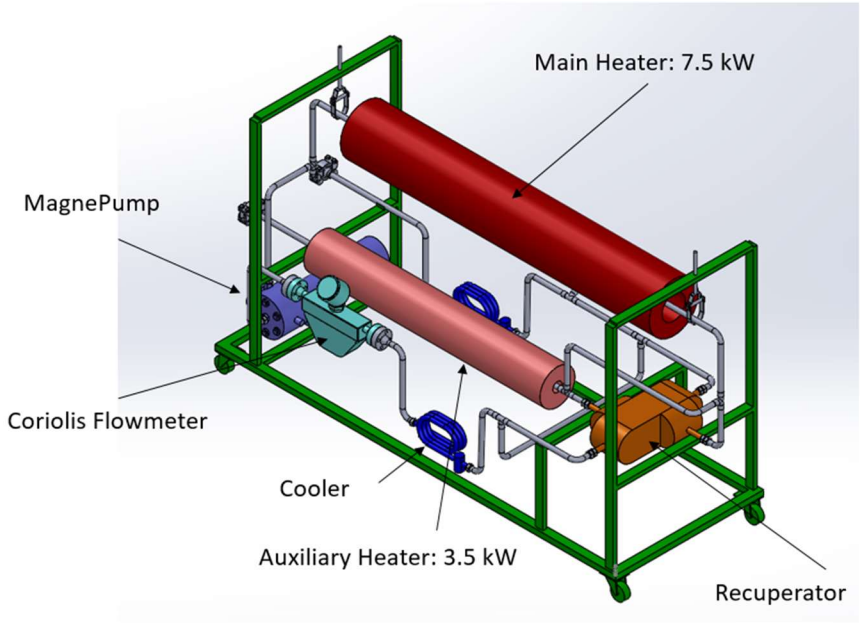

(a)

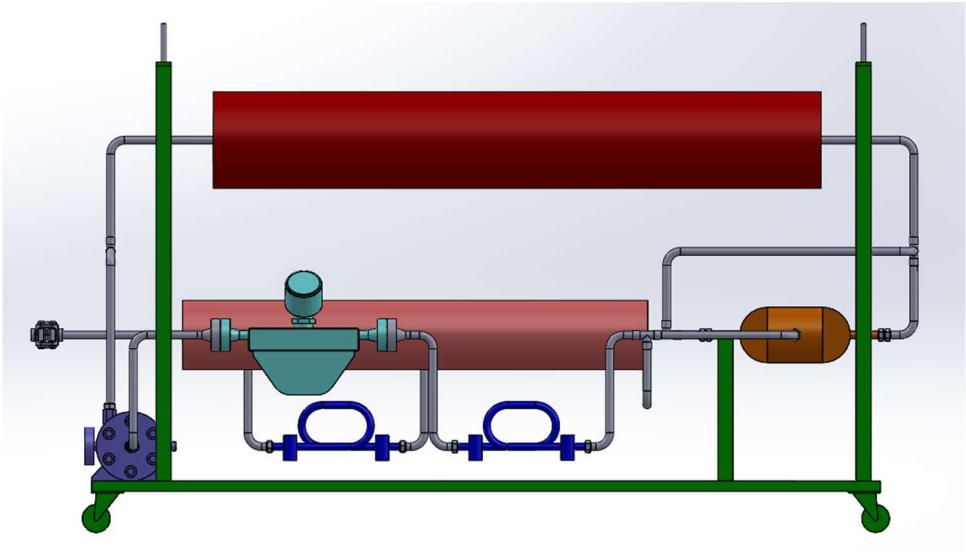

(b)

Figure 123. The isometric view (a) and the front view (b) of the 3D modeling of the MEP

Other major components are two coolers installed on the MEP. The auxiliary cooler will cool down the s-CO_2 flow before entering the recuperator primarily because the piping fitting at that section provided by Swagelok cannot withstand temperature above 600°C. The main cooler will cool down the flow before flowing through the flowmeters and the circulation pump, neither of which be operated under high temperature. The cooling duty of the main cooler is therefore much larger than that of the auxiliary cooler. The cooling

power required in the STL is listed in Table 41. All these parameters are estimated based on the calculated information from Table 41 and the parameters of the recuperator provided by the vendor.

Table 41. Primary parameters of heaters and coolers

	Items	Parameters
Main heater	Heating duty	7.42 kW
	Inlet temperature	60°C
	Outlet temperature	100°C
	Length requirement	72'' (1828.8 mm)
	Outside diameter requirement	<=12'' (304.8 mm)
Auxiliary heater	Heating duty	1.90 kW
	Inlet temperature	393.8°C
	Outlet temperature	418.8°C
	Length requirement	50'' (1270.0 mm)
	Outside diameter requirement	<=9'' (228.6 mm)
Main cooler	Cooling duty	17.45 kW
	Inlet temperature	203.9°C
	Outlet temperature	60°C
Auxiliary cooler	Cooling duty	6.96 kW
	Inlet temperature	589.4°C
	Outlet temperature	500°C

The circulation pump suitable for the high-pressure high-flow-rate application is extremely difficult to find on the commercial market. Fortunately, Parker Autoclave Engineers' 1-1/2 HP 316 stainless steel centrifugal Magnepump provides excellent performance in such an application, and the reliability has been proved in the test facility of the Knolls Atomic Power Laboratory, Schenectady, NY (D. Milone, et al. 2009). Therefore, this pump is used for circulating the s-CO_2 in the STL. Figure 124shows the product with high horsepower model. The pump is around 24'' long, therefore it was installed at one side of the MEP as shown in the Figure 124.

Figure 124. The MagneDrive Centrifugal MagnePump for liquid CO2 application (courtesy of Parker Autoclave Engineers)

In order to determine the required pumping power in the STL, it is necessary to estimate the overall pressure drop in the loop. There are in total four heat exchangers installed in the loop, the test PCHE, the recuperator, and the main and auxiliary coolers. These components are primary pressure drop contributors as well as the pressure drop in the piping system. Regarding the pressure drop in the test PCHE, the core region pressure drop, as calculated and shown in the Table 41, will be 37.08 kPa. However, it can be observed that a large pressure drop exists at the header, as mentioned before. Therefore, the pressure drop at headers of estimated 10% of the core region is taken into account. The pressure drop of the recuperator, as roughly estimated by the vendor, will be 33.1 kPa at each side. The main and auxiliary cooler, which are essentially the two tube-in-tube heat exchangers, will present approximately 25 and 9.97 kPa, respectively. The pressure drop of the piping system will be estimated to be around 10 kPa total. Then we have the overall pressure drop in the loop systems to be 152.0 kPa. The corresponding water head will be 15.5 m (50.8’), with volumetric flow rate of 6.36 LPM (1.68 GPM). Checking the head-vs.-flow-rate chart in Figure 125, we can determine that the 1-1/2 HP model of MagnePump is suitable to our application.

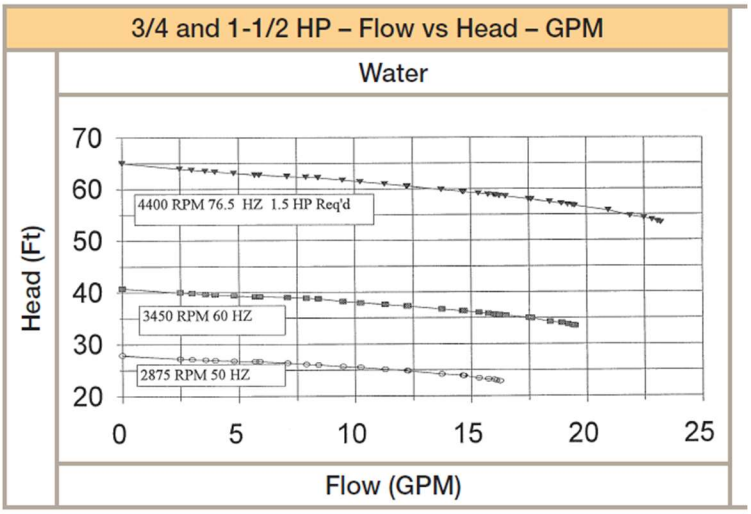

Figure 125.The head-vs.-flow-rate chart for the MagnePump (courtesy of Parker Autoclave Engineers)

Figure 126 shows the layout of the whole experimental facility, i.e. STL, in the existing HTHF laboratory. The distance of the system from the wall is carefully determined such that there is sufficient room for regular inspection, maintenance and operation. In the figure 90, the flow paths of helium and s-CO_2 are marked with red and blue arrows, respectively. MEP was constructed with green strut channels, consisting of major components of STL. Besides, the IHX test PCHE was installed between the existing piping system of HTHF and MPE to couple these two systems. The space available in the laboratory is sufficient to accommodate insulation on the piping system.

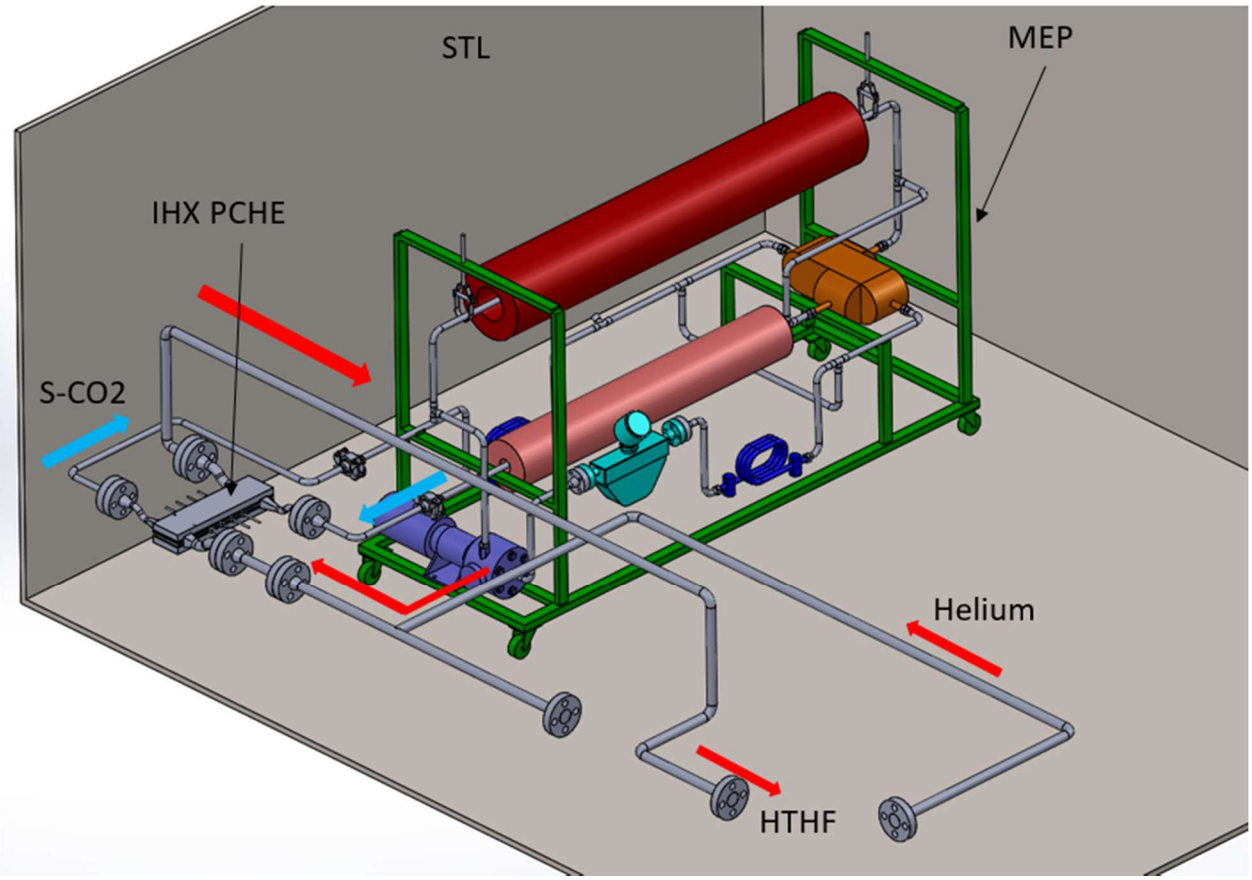

Figure 126. Isometric of the entire system of STL and HTHF

2.1.3 Scaling analysis of the test PCHE

As mentioned above, the operating conditions of existing OSU HTHF cannot provide the level of power needed for the PCHE. Therefore, the prototype design must be scaled down to generate a test PCHE design that can be practically tested in experiments. The primary task in scaling analysis is to maintain the Reynolds and Prandtl number identical to the prototypic PCHE. The major requirement is to reduce the operating pressure below 3 MPa and reduce temperatures as low as possible at helium side in order to satisfy the conditions of HTHF. Accordingly the s-CO_2 pressure is reduced to 16 MPa since an unchanged pressure differential of 13 MPa is preferred in the test PCHE to simulate the mechanical conditions in the prototype. The inlet and outlet temperatures on the s-CO_2 side are also preferred to drop by the same amount in accordance with the temperature reduction at helium side to maintain the heat exchanger effectiveness. Table 42 summarizes the operating conditions of both the prototypic and test PCHE design for an effectiveness of 95%.

Table 42. Summary of the operating conditions of both optimized and test PCHE design

Fluid	Item	Optimized PCHE	Test PCHE
Helium Side	System Pressure/ MPa	7	3
	Inlet Temperature/ °C	800	745
	Outlet Temperature/ °C	504.4	449.4
s-CO_2 Side	System Pressure/ MPa	20	16
	Inlet Temperature/ °C	488.8	433.8
	Outlet Temperature/ °C	665.1	610.1

The Reynolds number is defined as

$$\mathrm{Re} = \frac{\rho u D_h}{\mu} = \frac{\dot{m} D_h}{\mu A_c} \tag{2.1.6}$$

where ρ, u, D_h, μ, $\dot{m}$, A_c are fluid or gas density, flow velocity, hydraulic diameter of the channel, dynamic viscosity, mass flow rate and free flow area, respectively. If the Reynolds numbers for the prototypic and scaled-down design are remained the same, i.e. the ratio of Reynolds number is unity, then we can obtain

$$r_{\mathrm{Re}} = \frac{\mathrm{Re}_1}{\mathrm{Re}_2} = \left(\frac{\dot{m}_1 D_{h,1}}{\mu_1 A_{c,1}} \right) \Bigg/ \left(\frac{\dot{m}_2 D_{h,2}}{\mu_2 A_{c,2}} \right) = 1 \tag{2.1.7}$$

which is equivalent with

$$\frac{\mu_1}{\mu_2} = \frac{\dot{m}_1 D_{h,1} A_{c,1}}{\dot{m}_2 D_{h,2} A_{c,2}} \tag{2.1.8}$$

where subscripts 1 and 2 denotes the prototypic and scaled-down design, respectively. It is obvious that the left side of the equation, i.e. the ratio of thermo-physical properties, only depends on the pressure and temperature. Besides, an extra equation concerning the temperature rise of each side is introduced

$$\dot{q}_i = c_{p,i} N_i \dot{m}_i \Delta T_i, i = 1, 2 \tag{2.1.9}$$

where $\dot{q}$, c_p, N and ΔT are heat transfer rate, specific heat, total number of channels and temperature difference between inlet and outlet temperatures, respectively. Substituting the ratio of mass flow rates into Eq. (2.1.8), with the assumption of the same temperature difference, we can obtain

$$\frac{N_2 D_{h,2}}{N_1 D_{h,1}} = \frac{\mu_1 c_{p,1}}{\mu_2 c_{p,2}} \cdot \frac{\dot{q}_2}{\dot{q}_1} \tag{2.1.10}$$

It is observed that the right side of the equation above is constant when the temperatures, system pressure and heat load are specified. Therefore, the only parameters needed to be determined are the number of channels and the hydraulic diameter. Regarding the geometric parameters of the heat exchanger surface, the shape of the channels in the test PCHE must be the same as the one in the prototypic optimized PCHE, which is also known as geometric scaling law. To be specific, for zigzag channels the following equation must be satisfied

$$\frac{D_{h,2}}{D_{h,1}} = \frac{p_{l,2}}{p_{l,1}} = \frac{t_{p,2}}{t_{p,1}} = \frac{p_{x,2}}{p_{x,1}} \tag{2.1.11}$$

where p_l, t_p and p_x are longitudinal pitch, plate thickness and lateral pitch, respectively. The similar requirement can also be concluded through the mathematical analysis shown above for S-shaped fin channels. In addition, for heat exchanger scaling, the heat transfer area ratio must also be remained unity since the heat transfer performance is related to not only the heat transfer rate, which is governed by Nusselt number, but also the heat transfer area, which affects the overall heat transfer coefficient. Note that the Nusselt number is based on Reynolds and Prandtl number. In that case, additional equation is required

$$\left(\frac{A_{s,\mathrm{He}}}{A_{s,\mathrm{sCO_2}}}\right)_1 \Bigg/ \left(\frac{A_{s,\mathrm{He}}}{A_{s,\mathrm{sCO_2}}}\right)_2 = 1 \tag{2.1.12}$$

where A_s is the total heat transfer area. This equation can be modified to the following one

$$\left(\frac{A_{s,1}}{A_{s,2}}\right)_{\mathrm{He}} = \left(\frac{A_{s,1}}{A_{s,2}}\right)_{\mathrm{sCO_2}} \tag{2.1.13}$$

Using the definition of the heat transfer area

$$A_s = NP_L L \tag{2.1.14}$$

where P_L and L are wetted perimeter and total channel travel length, respectively, and combined with the geometric scaling law, which indicates that the ratio of any geometric parameters are equal to the ratio of the hydraulic diameter, we can obtain

$$\left(\frac{D_{h,1}N_1}{D_{h,2}N_2}\right)_{\mathrm{He}} = \left(\frac{D_{h,1}N_1}{D_{h,2}N_2}\right)_{\mathrm{sCO_2}} \tag{2.1.15}$$

Note that L is constant. This indicates that in order to maintain the heat transfer area ratio the same, it is necessary to make identical for the ratio of the product of the hydraulic diameter and the number of channels for each side. This also means it is not necessary to maintain the ratio of the hydraulic diameter for each side the same. As is known from the geometric scaling law, the ratio of the hydraulic diameter is equal to the ratio of the lateral pitch. Substituting that condition into equation. (2.1.15), we can obtain

$$\left(\frac{p_{x,\mathrm{He}}N_{\mathrm{He}}}{p_{x,\mathrm{sCO_2}}N_{\mathrm{sCO_2}}}\right)_1 = \left(\frac{p_{x,\mathrm{He}}N_{\mathrm{He}}}{p_{x,\mathrm{sCO_2}}N_{\mathrm{sCO_2}}}\right)_2 \tag{2.1.16}$$

Since the left side of the equation approximately equals unity, which implies the actual occupied widths of channels on each side are the same, it can be conclude that the additional geometric condition for test PCHE is to make sure the occupied widths on each side are the same.

Table 43 has shown the thermo-physical properties of helium and s-CO_2 at selected temperatures. It is concluded that the property ratio is negligible. Furthermore, the hydraulic diameter of the test PCHE is assumed to be the same as the one of the prototype. This is mainly because any attempts to increase or decrease the channel size will result in difficulties in satisfying the additional geometric condition. Therefore, Eq. (2.1.15) can be further simplified to the following form

$$\frac{N_2}{N_1} = \frac{\dot{q}_2}{\dot{q}_1} \tag{2.1.17}$$

Table 43. Thermo-physical properties of helium and s-CO2 at both prototypic and test conditions

Helium			
Temperature and Pressure	Thermo-physical properties	Units	Values
7MPa, 652 C	Viscosity	μPa·s	43.766
	Specific heat	kJ/kg-K	5.1895
	Pr	n/a	0.658
3MPa, 597 C	Viscosity	μPa·s	41.873
	Specific heat	kJ/kg-K	5.1914

	Pr	n/a	0.661
	Ratio	n/a	1.045
s-CO2			
20MPa, 577 C	Viscosity	μPa·s	38.237
	Specific heat	kJ/kg-K	1.2455
	Pr	n/a	0.7397
16MPa, 522 C	Viscosity	μPa·s	36.131
	Specific heat	kJ/kg-K	1.2236
	Pr	n/a	0.7397
	Ratio	n/a	1.077

It is then concluded that with the assumption of no change in channel size the scaling-down process simply becomes the problem of how to determine the proper number of channels in the test PCHE design, which depends on the selection of the experimental heat load. However, because of the additional geometric condition, the selection of the proper heat load is no longer random. Moreover, the heat load should not be too large because the high pressure pump usually runs at a relatively small volumetric flow rate, which sets the upper limit of the heat load for the test PCHE. Based on the above three scaling conditions, a preliminary design for the test PCHE has been completed. The detailed information is summarized in Table 44.

Table 44. The summary of the specification of the test and prototypic PCHE design

Category		Number	Item	Units	Test	Prototype
INPUT DATA	Primary side	1	Mass flow rate	kg/s	0.0125	428
		2	Pressure	MPa	3	7
		3	Inlet temperature	°C	745	800
	Secondary side	4	Mass flow rate	kg/s	0.0885	2991
		5	Pressure	MPa	16	20
		6	Inlet temperature	°C	433.8	488.8
THERMO-HYDRAULIC DATA	Primary side	7	Outlet temperature	°C	449.7	504.4
		8	Reynolds number	n/a	2484	2372
		9	Pressure drop	kPa	31.51	14.66
		10	Heat transfer coefficient	kW/m2-°C	2.64	2.70
		11	Heat transfer area	m2	2.35×10-1	80.76
	Secondary side	12	Outlet temperature	°C	610.8	665.1
		13	Reynolds number	n/a	28576	19828
		14	Pressure drop	kPa	48.80	48.20

		15	Heat transfer coefficient	kW/m2-°C	3.10	3.08
		16	Heat transfer area	m2	2.88×10-1	97.13
GEOMETRIC DATA	General	17	Heat exchanger core volume	m3	6.27×10-4	0.166
		18	Heat exchanger mass	kg	5.24×10-3	1.39
		19	Frontal area	m2	1.36×10-3	36
		20	Number of plates per block	n/a	16	312
		21	Heat exchanger physical length	m	0.46	0.46
	Primary side	22	Channel diameter	mm	2.92	2.92
		23	Hydraulic diameter	mm	1.78	1.78
		24	Channel angle	°	19.29	19.29
		25	Longitudinal pitch	mm	34.41	34.41
		26	Transverse pitch	mm	4.18	4.18
		27	Plate thickness	mm	2.33	2.33
		28	Number of channels per plates	n/a	8	141
		29	Flow area	m2	2.14×10-4	7.35
	Secondary side	30	Hydraulic diameter	mm	1.13	1.13
		31	Fin angle	°	52	52
		32	Longitudinal pitch	mm	7.57	7.57
		33	Transverse pitch	mm	3.43	3.43
		34	Plate thickness	mm	1.5	1.5
		35	Number of channels per plates	n/a	10	173
		36	Flow area	m2	1.32×10-4	4.46
AUXILIARY DATA		37	Heat exchanger capacity	kW	19.2	6.57×103
		38	Effectiveness	%	94.90	95.00

2.1.4 Design of the test PCHE

The plate (or shim) design of the test PCHE that is tested in the STL is based on the scaled-down test design. The thermal design is determined according to the scaling analysis of the prototypic optimized design. The PCHE channel geometries of both zigzag and S-shaped fins are identical with those in the prototypic design, therefore the number of channels are critical in the plate design. There are several factors considered in the design. First, the number of zigzag and S-shaped fin channels on each plate needs to be

designed to have the same overlapping width, due to the heat transfer area required to be overlapped as much as possible to obtain desired heat transfer performances. Additionally, the number of channels per plate needs to be sufficient to eliminate the maldistribution of fluids. Also, the number of plates is required to be large enough to reduce the effect of heat loss of the test PCHE. Furthermore, the total number of channels is related to the mass flow rate of the test PCHE, which is important in designing the s-CO_2 facility. The mass flow rate on the s-CO_2 side should be small enough so that there can be a pump commercially available for such a high pressure system. The pump to be installed in the STL should be magnetically sealed gear pump to reduce the potential leakage of s-CO_2 in the facility. In the current design, both of zigzag and S-shaped fin channels have 8 plates with a total of 16 plates stacked up to form the entire PCHE core. On each of zigzag plates there are 12 channels with a total width of 51.41 mm while on each of the S-shaped fin plates there are 14 channels with a total width of 51.04 mm. This indicates that in terms of the overlapping width the adopted number of channels per plate satisfies the design requirement. The overlapped heat transfer area of one pair of plates is shown in Figure 127.

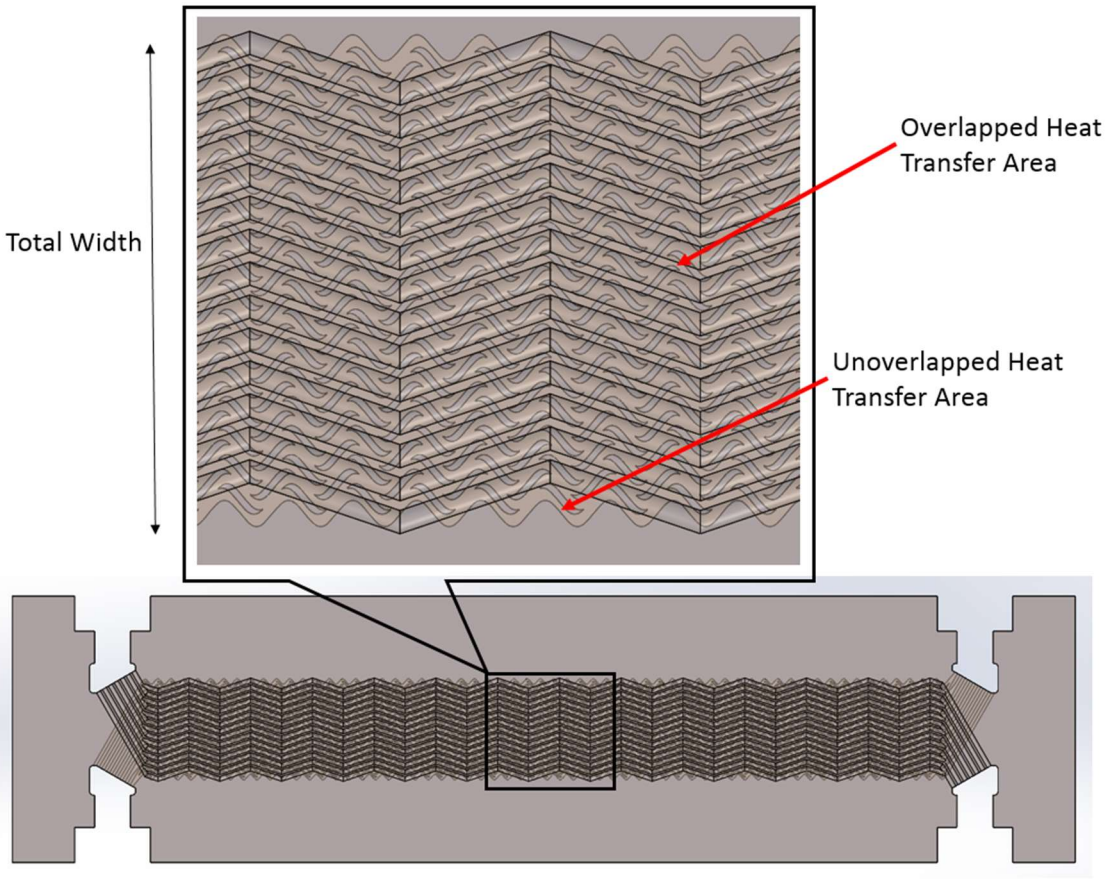

Figure 127. The overlapped heat transfer area in one pair of the plates

As to the size of the heat exchanger, the physical length needs to be large enough to reduce the pressure drop percentage in the distributing channels to the total pressure drop. The pressure drop in the PCHE consists of the core pressure drop and the pressure drop at distributors (manifolding channels). The pressure drop at the distributors needs to be small enough to reduce the errors in estimating the core pressure drop in flow channels from the pressure drop measurement across the PCHE. In addition to maintaining a relative large physical length, the channel diameter of the manifolding channels are required to be small. The lateral pitch of manifolding channels is required to be large enough so that the part of channel ridges at the inlet and outlet plenums is able to withstand high pressure and maintain mechanical integrity. However, this requires to merge each two flow channels into one manifolding channel. Merging and increasing the mass flow rate at manifolding channels can increase pressure drop four times if channel diameter and friction factor are unchanged. Therefore, the profile diameter is required to be carefully determined. This is then related to the geometry of the cross-sectional profile. The manifolding channels on both plates are shown in Figure 128.

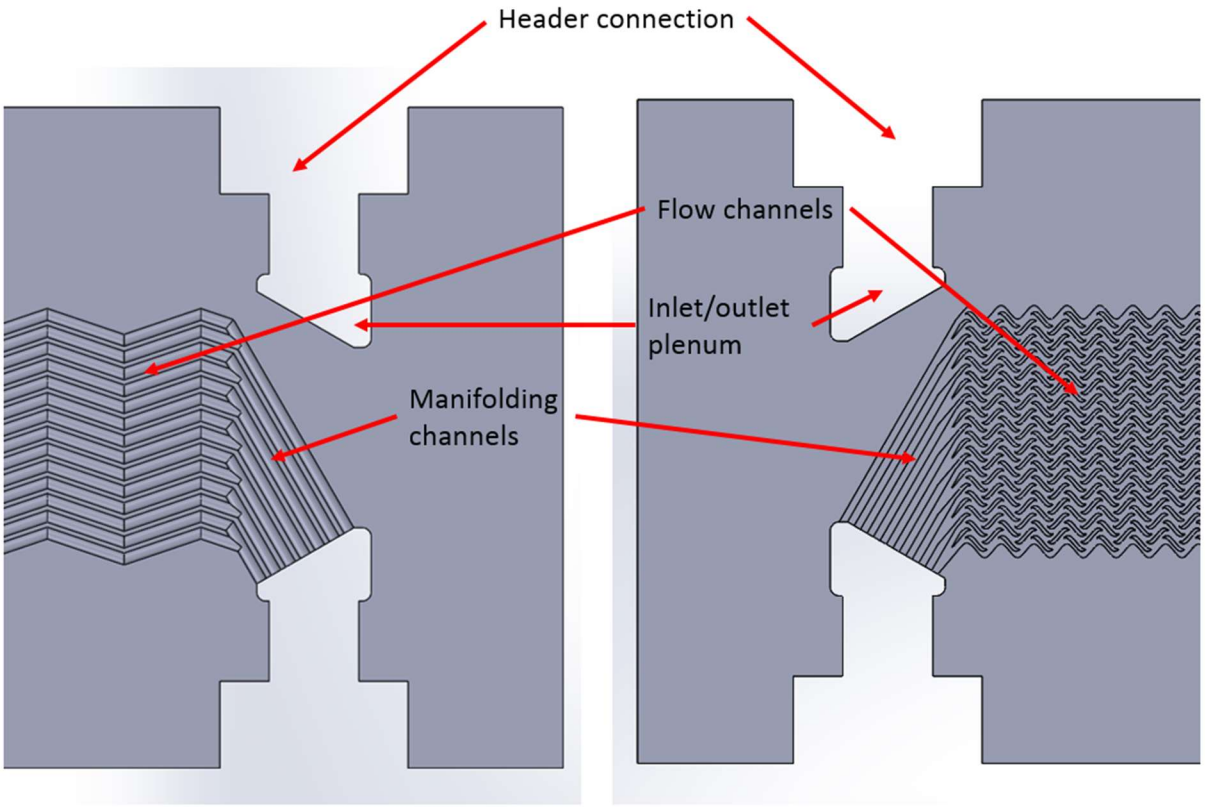

Figure 128. Manifolding channels and inlet/outlet plenums on the zigzag plate (left) and S-shaped fin plate (right)

For convenience to estimate the core pressure drop, the geometry of manifolding channels is assumed to be a circular profile in its cross-section and straight in flow direction. The existing correlations for channels with a circular segment in the cross-section are used for the estimation. The circular segment profile are shown in Figure 129. To mitigate the potential maldistribution imposed on them, the configurations of manifolding channels should be centrosymmetric. Therefore, the length of the manifolding channels in the calculation is assumed to be the total length of traveling path of fluid, which includes the one at inlet and outlet plenums. The estimated pressure drop and percentage accounting for the core pressure drop are less than 5%, which is acceptable.

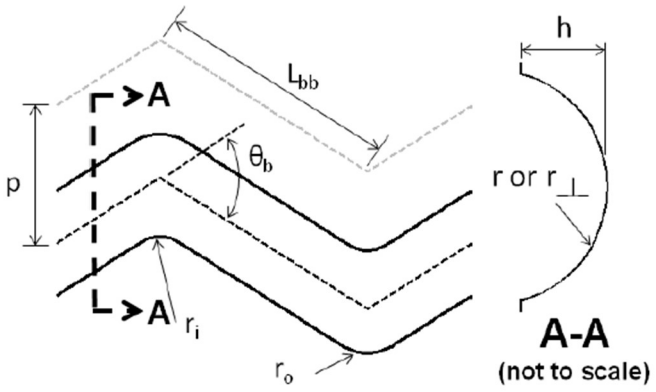

Figure 129. Circular segment profile in straight or zigzag channels

Regarding the design of the plenums, there are two designs with manifolds connecting either from sides or top of the test PCHE. The plenums are designed to be rectangular so that they fit the rectangular plate shape and make sufficient area to connect the manifolding channels. The adopted design is determined to be the one connecting manifolds at two sides because of the space-saving configuration. Headers are designed to be square-shaped connection at one end and standard flange at the other, as shown in Figure 130. The square-shaped end is connected to the test PCHE by brazing. Accordingly, there may be square part cut on the plate. The configuration of plates connecting the header is also shown in Figure 130. Also, the design of etched plates is displayed in Figure 131. The assembly of the test PCHE is shown in Figure 132.

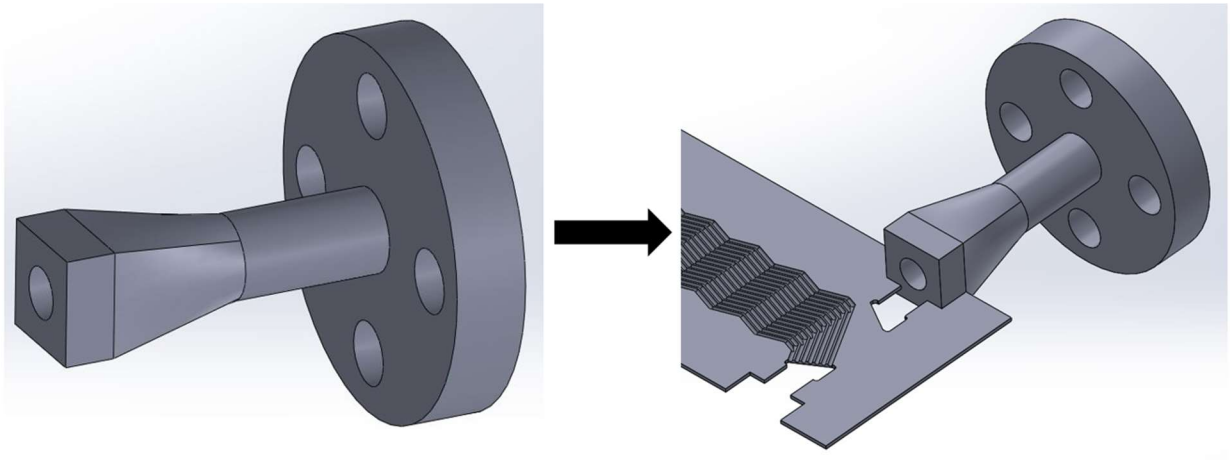

Figure 130. Design of the header and the illustration of the plate connecting the header

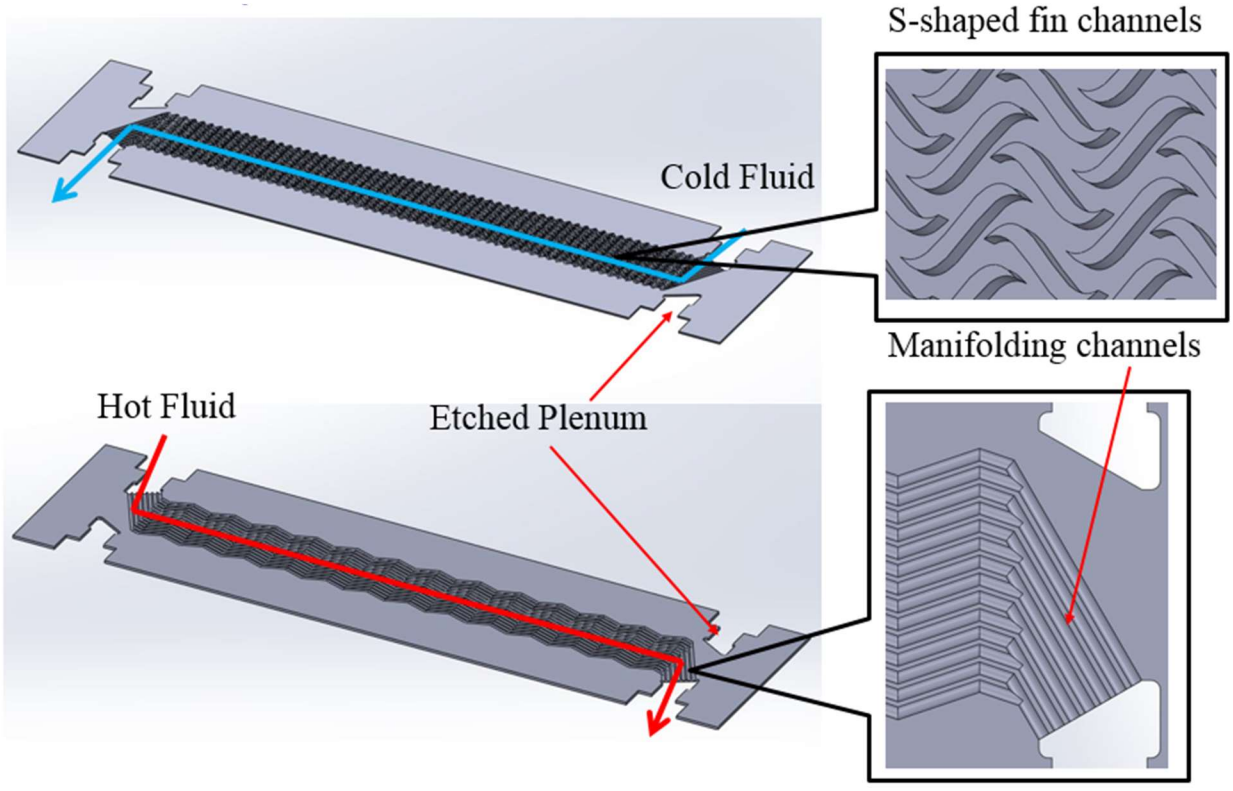

Figure 131. Etched plates with flow channels, manifolding channels and plenums

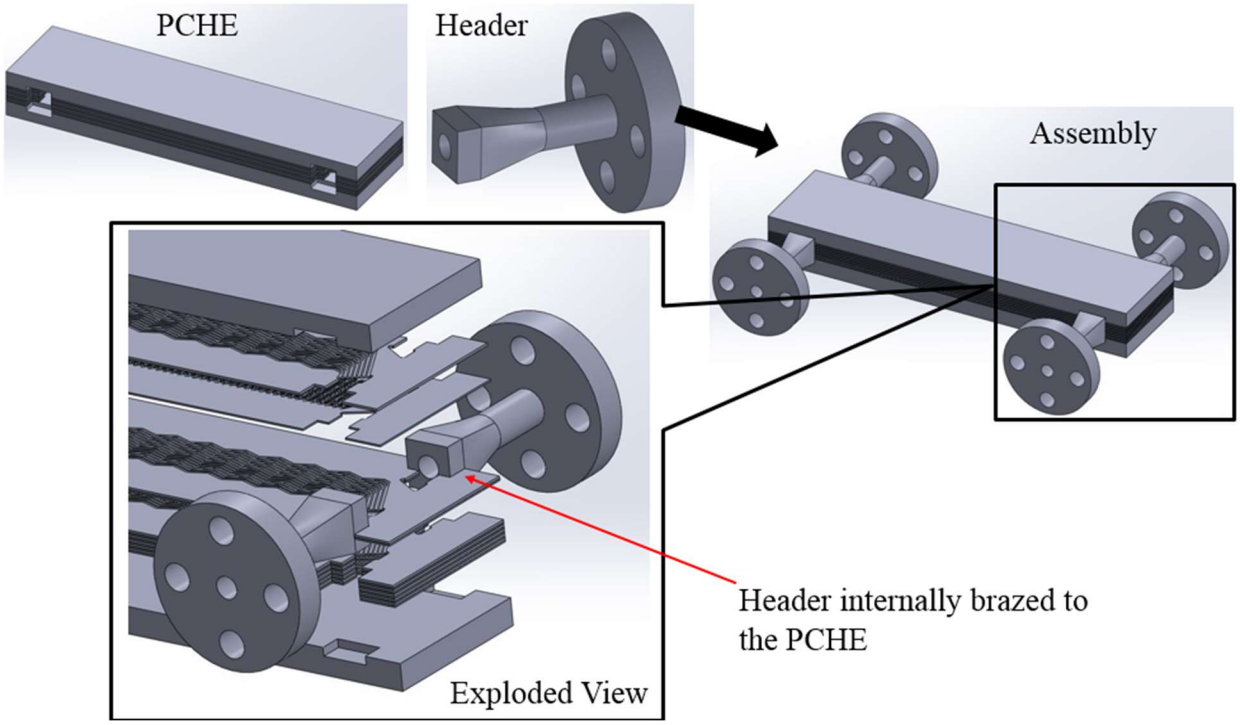

Figure 132. Assembly of the test PCHE and headers

Update of the design of the test PCHE

The original design of the test PCHE was based on the results of the scaling analysis as shown in section 2.1.3, and the features of the existing HTHF. However, in practice, some of the features are difficult to be realized. For example, the design limit of the operating system pressure in the HTHF is up to 3 MPa. In reality, when running experiments it is hard to operate the facility at that pressure. Moreover, the temperature-pressure rating of flanges to be used in the helium-to-s-CO_2 coupled facility indicates that it is nearly impossible to run experiments at 3 MPa for helium side because of the high temperature and potential leakage through flanges of class 2500 at 3 MPa (as shown in Table 45). Another aspect to be considered is the total heat transfer power rating of the test PCHE, which is related to the mass flow rate on both helium and s-CO_2 sides. Since in actual situations the HTHF can only handle helium flow rate up to 60 kg/hr, it is necessary to reduce the mass flow rate accordingly such that in the future experiments the helium mass flow rate can be provided by the existing gas booster in the HTHF. Additionally, the mass flow rate is also constrained by the design of the s-CO_2 test loop. The availability of the commercial supercritical fluid pumps or compressors requires as low mass flow rate on s-CO_2 side as possible. This results in the modification of the total number of channels in the test PCHE and the number of channels per plate. Furthermore, in order to obtain as large overlapped heat transfer areas between the zigzag and S-shaped fin channels as possible, the number of channels per plate on both side needs to be carefully adjusted.

Thus, the final design is characterized by 9 zigzag channels and 10 S-shaped fin channels per plate with in total 6 plates on each side, as shown in Figure 133. The details are listed in Table 45.

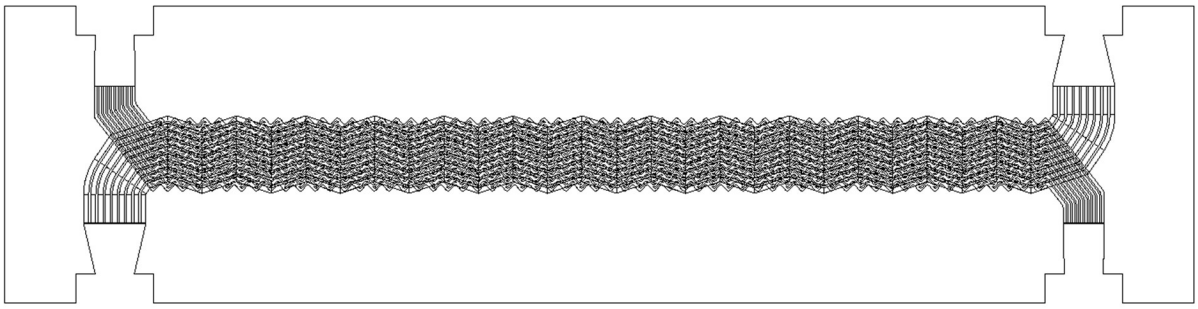

Figure 133. The design of the test PCHE with 9 zigzag channels and 10 S-shaped fin channels

Table 45. Specifications of the modified design of the test PCHE

Category		Number	Item	Units	Test
INPUT DATA	Primary side	1	Mass flow rate	kg/s	0.0092
		2	Pressure	MPa	2
		3	Inlet temperature	°C	730
	Secondary side	4	Mass flow rate	kg/s	0.064
		5	Pressure	MPa	15
		6	Inlet temperature	°C	418.8
THERMO-HYDRAULIC DATA	Primary side	7	Outlet temperature	°C	435.5
		8	Reynolds number	n/a	2330
		9	Pressure drop	kPa	45.79
	Secondary side	10	Outlet temperature	°C	599.4
		11	Reynolds number	n/a	20483
		12	Pressure drop	kPa	53.08
	Overall	13	Number of plates per block	n/a	12
GEOMETRIC DATA	Primary side	14	Channel diameter	mm	2.92
		15	Hydraulic diameter	mm	1.78
		16	Channel angle	°	19.29
		17	Longitudinal pitch	mm	34.41
		18	Transverse pitch	mm	4.18
		19	Plate thickness	mm	2.33
		20	Number of channels per plates	n/a	9
	Secondary side	21	Hydraulic diameter	mm	1.13
		22	Fin angle	°	52
		23	Longitudinal pitch	mm	7.57

		24	Transverse pitch	mm	3.43
		25	Plate thickness	mm	1.5
		26	Number of channels per plates	n/a	10
AUXILIARY DATA		27	Heat exchanger capacity	kW	14.07
		28	Effectiveness	%	94.65

Pressure drop estimation at manifolding channels

The pressure drop at the manifolding channels is extremely important, since from the past experimental experience most of the pressure drop across the PCHE is actually at the manifolding channels. Therefore it is necessary to estimate the pressure drop and modify the design accordingly. Usually, the manifolding channels are designed to be merged channels. The reason for that design is that it can reduce the number of channels required in the manifolding areas, thus the spacing of these manifolding channels are large enough to withstand mechanical loadings. The problem of this design is that for zigzag channels, if channels merge, the mass flow rate in manifolding channels is increased unless the channel hydraulic diameter of manifolding channels is increased as well, which leads to transitional flow observed in the manifolding channels. Certainly this may cause increase in the pressure drop. In addition, the increased mass flow rate will lead to rapidly increased pressure drop according to the equation below:

$$\Delta p = 4f \frac{L}{D_h} \cdot \frac{\dot{m}^2}{2\rho} \tag{2.1.18}$$

For a preliminary estimation, it is convenient to assume that the Fanning friction factor as well as thermos-physical properties are constant. Then the pressure drop at manifolding channels and the core region can be compared through the equation below:

$$\frac{\Delta p_m}{\Delta p_c} = \frac{L_m}{L_c} \cdot \frac{D_{h,c}}{D_{h,m}} \cdot \frac{\dot{m}_m^2}{\dot{m}_c^2} \tag{2.1.19}$$

This indicates that the increased mass flow rate has a great impact on the pressure drop at manifolding channels. Typically, the flow path at manifolding channels is around one-tenth of the total core region. Therefore, if two channels' flows merge at manifolding channels, it may result in approximately 20% of pressure drop ratio if we assume their hydraulic diameter is increased by two times. Similarly, if three channels' flows merge, this may result in approximately 45% of pressure drop ratio. This estimation does not include the consideration of the increased Fanning factor due to potential transitional flow, the additional form loss at manifolding channels and the actual geometry. Accordingly,

we can conclude that merging flows at manifolding channels yields large pressure drop and is strongly not suggested.

Figure 134 shows the modified design of manifolding channels. This design is characterized by no merge of flows and directly connecting the core region channels and the plenum. From the design, it is possible to calculate the flow path length, and then we can calculate the pressure drop ratio. The averaged pressure drop ratio is reduced to around 7% and 14% in total, which is far less than the one estimated under the merged flow. Although it is still a coarse estimation without considering the factors mentioned before that could further increase the pressure drop, it partially justifies the design with direct manifolding channels instead of the ones with flow-merging.

For zigzag channels, the manifolding channels are purposely designed to be similar to zigzag channels in the core region. The angles of manifolding channels are identical with those in the core region, and at some of the areas the sharp angles are smoothed out to reduce local form loss. For S-shaped fin channels, the manifolding channels are designed to be compatible with S-shaped fin patterns. Therefore, they look like much ‘thinner’ than zigzag manifolding channels.

It should be noted that the pressure drop estimated above only considers the pressure drop at manifolding channels. When we consider the pressure drop at the plenum and headers, the total amount of pressure drop might be very considerable even the pressure drop reduction approaches are applied. Hence, direct pressure-measuring lines are considered to be utilized in the modified design of the test PCHE.

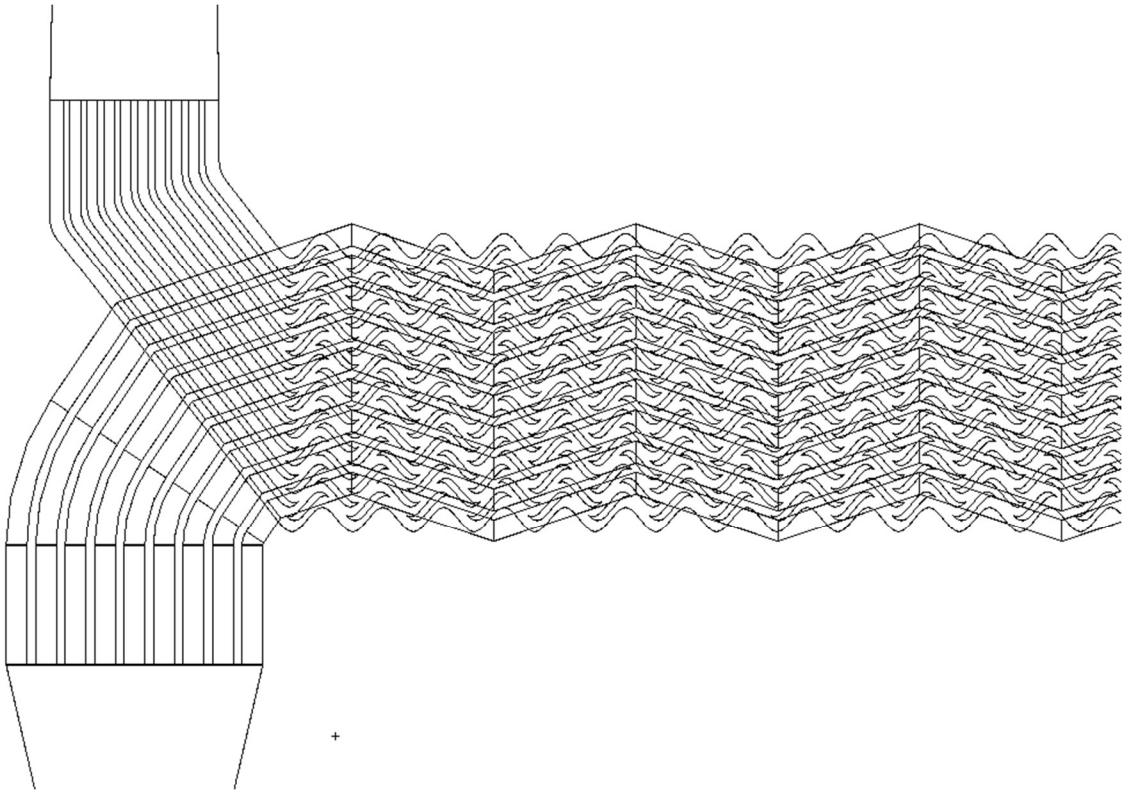

(a)

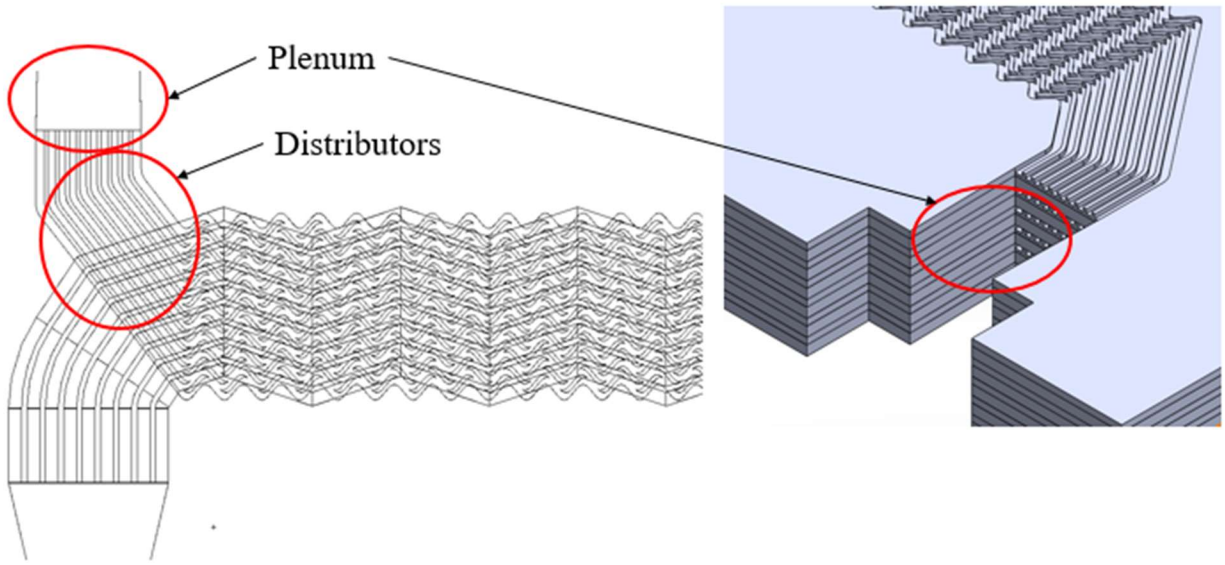

(b)

Figure 134. (a) The detailed design of the test PCHE manifolding and (b) the corresponding pressure drop

Direct pressure-measuring lines

From the estimation of pressure drop shown above, the pressure drop at manifolding channels and headers may yield extremely large uncertainties when measuring the pressure drop at the core region. In the past experience, this actually leads to large uncertainties in estimating the pressure drop and friction factor in the HTHF. As shown in Figure 135, it was stated that the pressure drop across the heat exchanger in the design of previous experimental PCHEs (straight channel PCHEs) tested in the HTHF involves multiple contributors. Therefore, there is a strong motivation to apply pressure-measuring line etched on plates in the current design to directly measure the pressure differential across the core region for reduction of uncertainties in the pressure drop data.

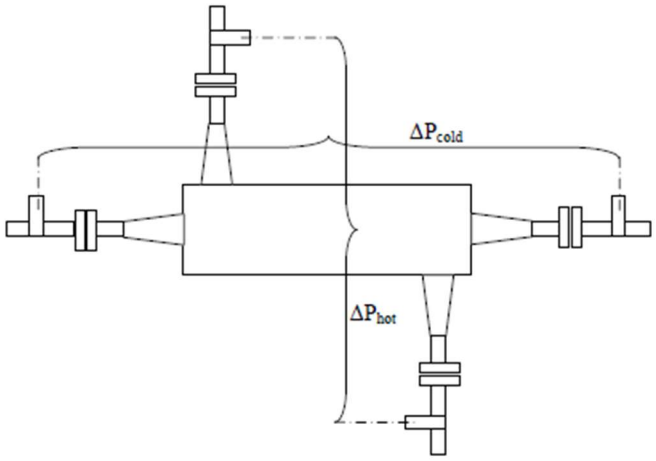

Figure 135. Schematic of the pressure drop measured in the straight channel PCHEs tested in the HTHF (Mylavarapu, 2011)

Figure 136 shows the concept of pressure-measuring line etched on plates. These lines will lead a measuring channel from a pressure transducer to the channel close to the PCHE side. Multiple measuring lines will be etched on the plate such that the pressure differential at various locations can be measured. However, this approach can only measure the pressure at the side channel instead of the center channel. Additionally, the pressure measured through measuring lines on one particular plate is not necessarily the same as the one measured on other plates, if the maldistribution of flow occurs. Thus, at least measurement of pressure differential on two plates is required.

Regarding the fittings of the pressure-measuring lines, there are two proposed options as shown in Figure 137. The first proposal is to weld the tube fitting directly on the side of PCHE, with the tube aligned with the measuring line. This design is easy to be realized. However, it may damage the diffusion bond and rip plates apart at the location where the

tube fitting is installed by welding. The other proposal is to use brazing to braze the fitting into the PCHE. Since brazing is isothermal, it won't compromise the safety and leak-tightness of the fitting. One of the concerns is the penetration depth associated with the brazing. One of the ideas provided by the diffusion bonding vendor is that it is possible to braze the tube into a boss and then stick it into the heat exchanger using brazing. That approach could save the process of machining of plates at pressure tap locations after diffusion bonding. A schematic is provided as shown in Figure 138.

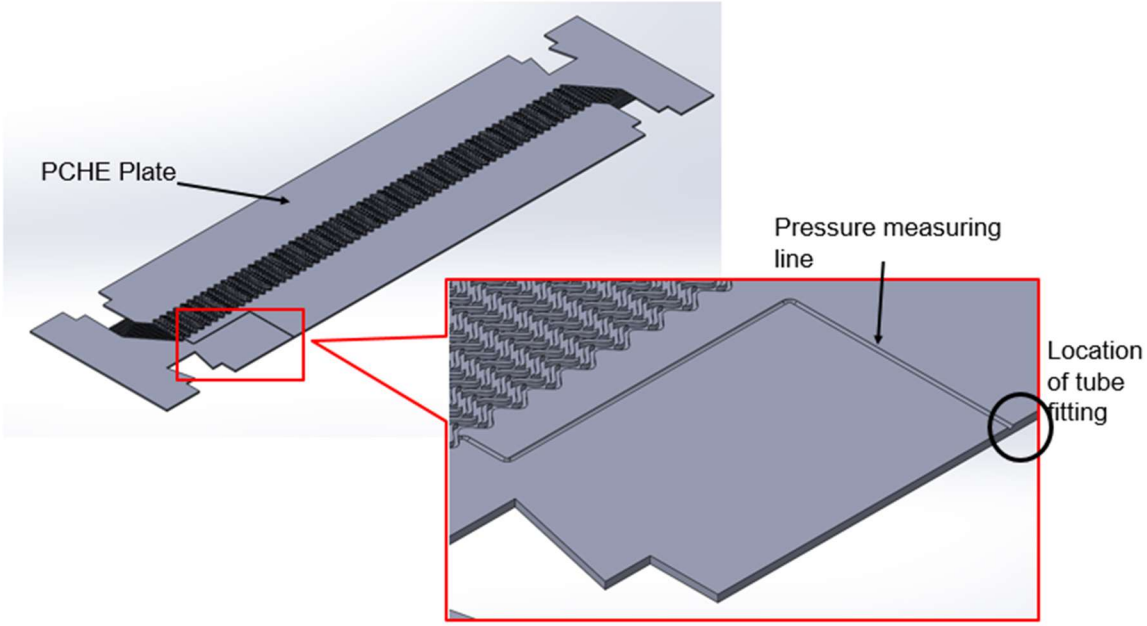

Figure 136. The concept of pressure-measuring lines

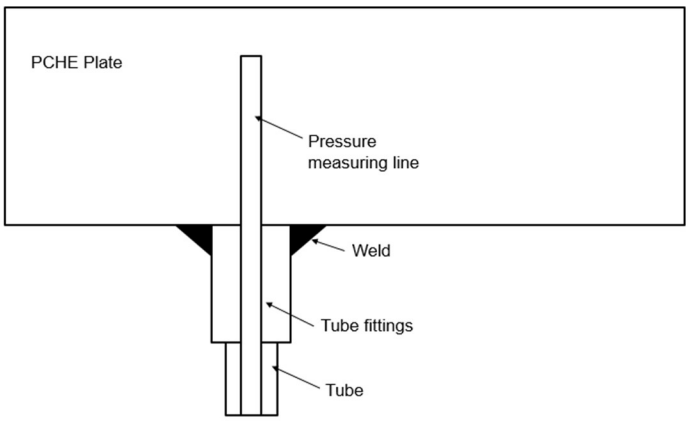

(a)

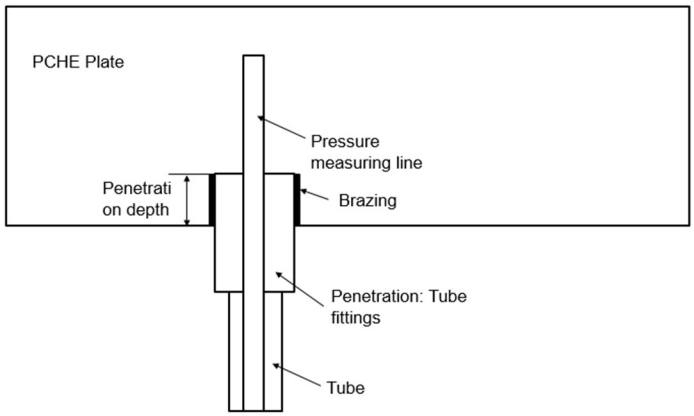

(b)

Figure 137. Two proposed design of pressure-measuring lines' fitting

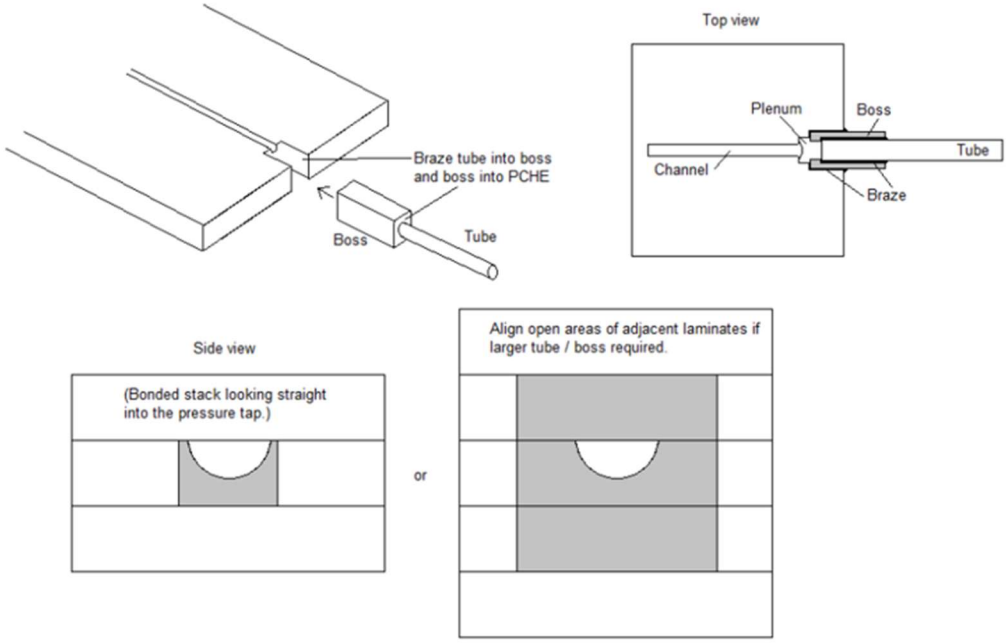

Figure 138. The proposed design of the pressure tap (Courtesy of Refrac Systems)

Design adjustment according to fabrication constraints

The design of the test PCHE was eventually sent to Refrac Systems, a vendor of diffusion-bonding and fabrication, for further discussion about the mechanical and fabricating constraints. Refrac Systems has been extensively involved in diffusion-bonding for three PCHE-type heat exchangers with the OSU in the past five years and has accumulated valuable experiences regarding the optimization of PCHE plates' design. The original design did not take into account the practical fabricating constraints from the vendor. For

example, it was proposed from Refrac Systems to keep the effective bonding area under 40 inch^2 so that the bonding stress in the stacked-up plates' block can reach up to 1500 psi, which is the minimum force that is anticipated to facilitate a bond strong enough to withstand the working pressure of the helium and s-CO_2 above 600 °C. In addition, the plates' dimension was advised to be no larger than 14''×5'' for the existing diffusion-bonding tool. This was the primary constraint as feedback received from the vendor. Originally it was assumed that the capability of diffusion-bonding large plates existed as indicated in literatures. But for small PCHE fabrications, the practice of diffusion-bonding size for mass-fabrication does not apply. This lead to a huge adjustment for the test PCHE design as well as the experimental facility design.

Fortunately, in the previous design optimization, we selected two designs, with the thermal effectiveness of 90% and 95%, respectively. The 95%-effectiveness design had a core length of approximately 17.83'' (452.8 mm), which was way beyond the recommended plate size. However, the 90%-effectiveness design had a core length of 13.1'' (333.1 mm), which was barely fit into the existing tooling. After communication with Refrac Systems, they could finally provide a tooling system capable of accommodating plates with size up to 19.5''×6'', which indicated that it was possible to design plates that were able to be diffusion-bonded in the available conditions. The next step for the design adjustment was to recalculate and determine important design and operating parameters for both the test PCHE and the experimental facility.

Subsequent adjustments in design indicate that the PCHE core can be further reduced to 12.8'' (325.2 mm). Then we can obtain the new adjusted design using the same scaling analysis and considering the same channel configuration on both S-shaped fin and zigzag channel plates, i.e. 9 zigzag channels and 10 S-shaped fin channels per plate, respectively, with 6 plates for each surface geometry. The calculated thermal effectiveness for the test PCHE is around 89.31%, slightly smaller than the prototypic design. The thermal duty is 13.28 kW along with the overall heat transfer coefficient of 1.36 kW/m^2-K. The required mass flow rate at both side does not change a lot. In fact, if mass flow rates remain the same, a better HX effectiveness can be achieved, which is 230 kg/h for the s-CO_2 flow and 33.1 kg/h for the helium flow. More detail information of the newly-adjusted test PCHE design is shown in the following table.

Table 46. Specifications of the newly-adjusted design of the test PCHE

Category		Number	Item	Units	Test
INPUT DATA	Primary side	1	Mass flow rate	kg/s	0.0092
		2	Pressure	MPa	2
		3	Inlet temperature	°C	730

	Secondary side	4	Mass flow rate	kg/s	0.064
		5	Pressure	MPa	15
		6	Inlet temperature	°C	418.8
THERMO-HYDRAULIC DATA	Primary side	7	Outlet temperature	°C	452.1
		8	Reynolds number	n/a	2,314
		9	Pressure drop	kPa	32.11
	Secondary side	10	Outlet temperature	°C	589.4
		11	Reynolds number	n/a	20,572
		12	Pressure drop	kPa	37.08
	Overall	13	Number of plates per block	n/a	12
GEOMETRIC DATA	Primary side	14	Channel diameter	mm	2.750
		15	Hydraulic diameter	mm	1.680
		16	Channel angle	°	18.65
		17	Longitudinal pitch	mm	36.10
		18	Transverse pitch	mm	3.884
		19	Plate thickness	mm	2.362
		20	Number of channels per plates	n/a	9
	Secondary side	21	Hydraulic diameter	mm	1.13
		22	Fin angle	°	52
		23	Longitudinal pitch	mm	7.57
		24	Transverse pitch	mm	3.43
		25	Plate thickness	mm	1.600
		26	Number of channels per plates	n/a	10
AUXILIARY DATA		27	Heat exchanger capacity	kW	13.28
		28	Effectiveness	%	89.31

After we determine the thermal design of the adjusted test PCHE core, it is necessary to look for commercially available alloy 617 plates to determine plates' dimensions. By searching, we found two raw plates in stock appropriate for our designs, which are 0.093'' and 0.063'' (2.362 mm and 1.600 mm) in thickness, respectively, and both are 48'' (1219.2 mm) in width and 120'' (3048.0 mm) in length. In order to cut as many plates to etch as possible on one raw large plate, the size needs to be carefully determined such that at least 6 plates can be procured by cutting the raw plate of each particular thickness. Additionally, it is ideal to have 2 extra etched plates so that they can be used for the measurement of etched channels' geometry or other inspections for quality control and research purposes. Furthermore, the side margin thickness for the core region cannot be too small since the recess for accommodating headers should be sufficient to remain mechanically strong at brazed locations, as shown in Figure 139.

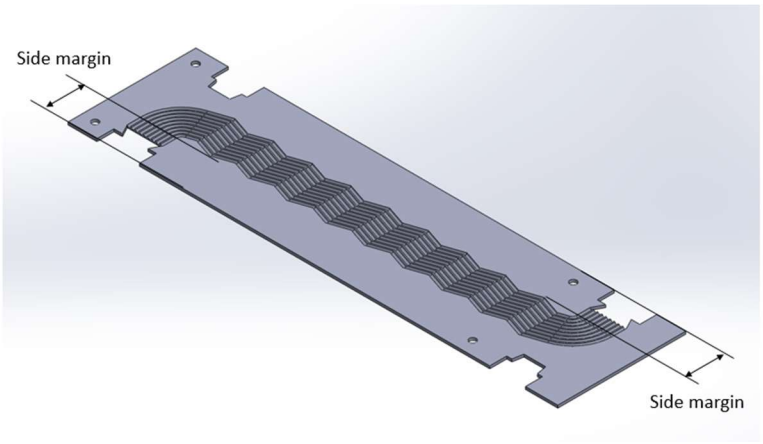

Figure 139. The side margin of plate (also applicable to S-shaped fin plate)

Besides, some mechanical consideration should be taken into account according to ASME BPVC code (ASME BPVC VIII-1). Figure 140 shows that it is possible to evaluate the edge width in a simplified model of rectangular vessel with stayed plates, and the requirements can be expressed by the following equations

$$S_m \leq SE \tag{2.1.20}$$

$$S_m + S_b^N \leq 1.5SE \tag{2.1.21}$$

$$S_m + S_b^Q \leq 1.5SE \tag{2.1.22}$$

where S and E are the maximum allowable stress intensity and joint factor, respectively. It is recommended (Pierres, et al. 2011) that E is 0.7 for diffusion-bonded block. The design criteria indicate that (1) the membrane stress at the edge S_m shall not exceed the design stress, (2) the total stress S_t, which is the sum of the membrane stress S_m and the bending stress S_b^N at the location of N (the middle of the short side) or S_b^Q at the location of Q (the corner) shall not exceed 1.5 times of the design stress. These stress values can be computed through following equations:

$$S_m = \frac{Ph}{2t} \tag{2.1.23}$$

$$S_b^N = \left(\frac{Pc}{24I}\right)\left(2h^2 - 3H^2\right), S_b^Q = \frac{Ph^2}{12I} \tag{2.1.24}$$

where

$$I = \frac{t^3}{12} \text{and} c = \frac{t}{2} \tag{2.1.25}$$

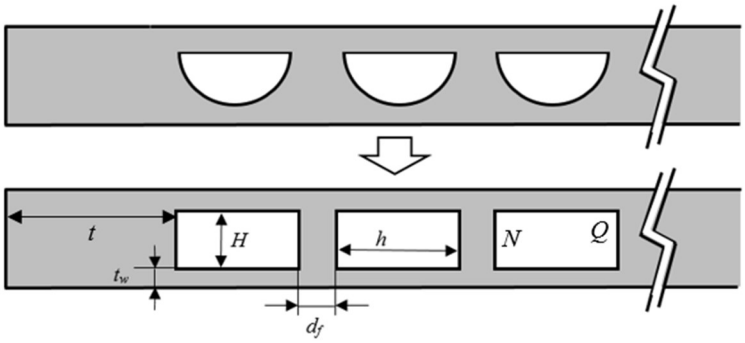

Figure 140. The schematic of the simplified rectangular vessel model with stayed plates

P denotes the design pressure in the vessel, which is 15 MPa for s-CO_2 environment and 2 MPa for helium. Other parameters related to the geometry of plates can be found in Figure 140. Therefore, the sufficient side margin can be determined as a reference for the size of the entire plate to etch. The final calculation results show that 18''×4.7'' (457.2 mm×119.4 mm) for an individual plate is preferred. The measured surface area in the 3-D models indicate 56.7 inch^2 for S-shaped fin plate and 59.7 in.^{2} for zigzag channel plate, respectively. This means that the surface area is very close to what is recommended for previous mentioned tooling systems. As informed by the vendor, it was confirmed that the surface area is sufficiently small to generate strong stress bond during the diffusion-bonding process in the new tooling systems. Therefore, the size of the plate is finalized.

Since it was planned to etch additional several pressure-measuring lines on the plate, generally all of the plates can be categorized into three groups for each design of plate. Figure 141 and Figure 142 show the categories and details of etched patterns on the plate. The 3rd-type plate is used to measure pressure through connecting the pressure tap installed on the heat exchanger and transducers installed outside of the heat exchanger. Therefore, the pressure-measuring lines should be etched on that particular plate. The 2nd-type plates are designed in such way as shown in the figures because the pressure taps are generally thicker and larger than the thickness of any of plates, which indicates that pressure taps may occupy several plates' thickness. Therefore, a couple of

pressure taps' recess needs to be etched on the plate. The 1st-type plates are the rest of regular plates that are not involved in pressure-measuring tasks.

There are 8 pressure taps installed on the test PCHE, 4 for each side, which can measure the differential pressure of 3 sections and one gauge or absolute pressure. The reason for that configuration is that the first and the last section of the differential pressure might be affected by inlet and outlet additional form loss. Because of the sudden change of flow channel geometry at the inlet and outlet of the core regions, it is expected to have extra pressure drop if the flow is not fully developed. The amount of form loss in pressure drop can be determined experimentally using such design, and the effect of the change of the channel's geometry can then be quantified. It is noted that the pressure measured through these lines are the one in the outmost channel, which might be different from the middle channels. The pressure lines' angle connecting the flowing channel is intentionally 90° such that no flows will enter these line to alter the actual flow field at those spots.

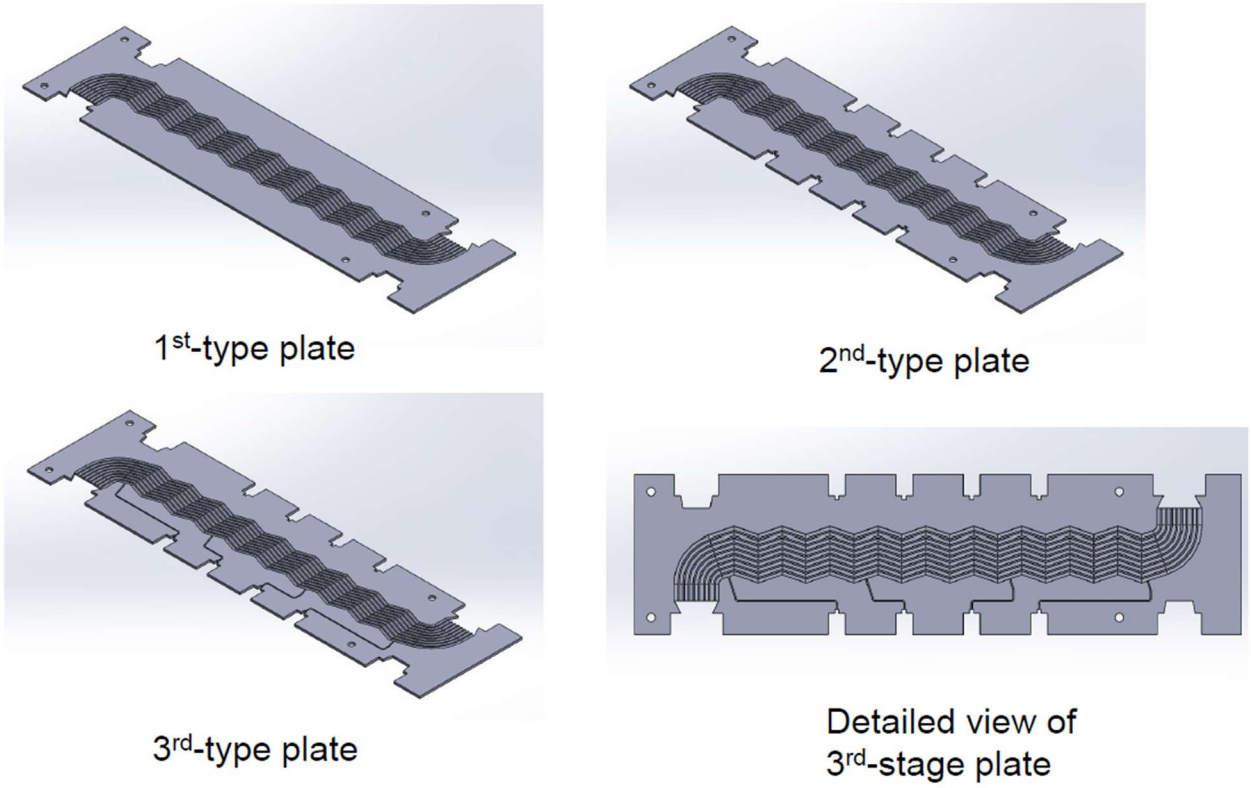

Figure 141. Detailed views of three categories of zigzag channel plates

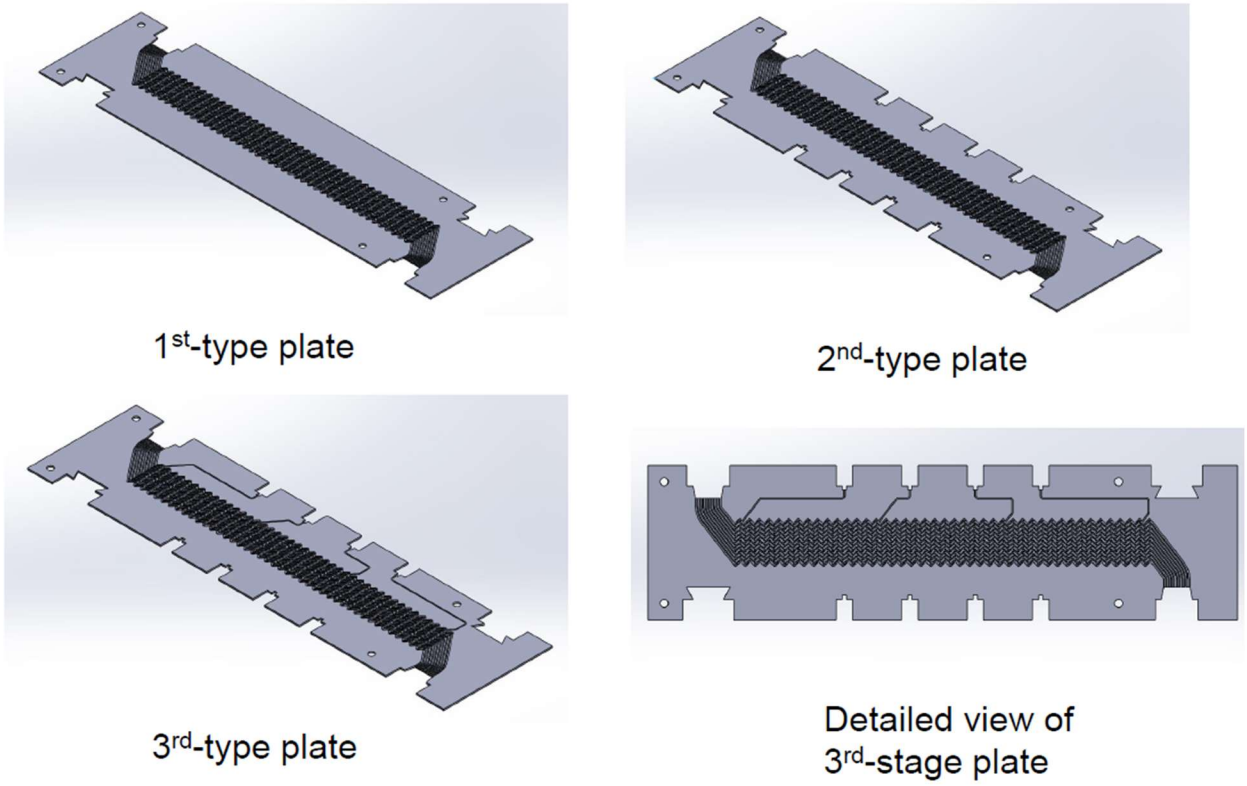

Figure 142. Detailed views of three categories of S-shaped fin channel plates

The header design was also adjusted as requested by Refrac Systems. It was proposed to make the flanges that may be welded on headers at the same elevation of the bottom of the test PCHE, as shown in Figure 143. The bent part was designed to be two 45° elbows welded with pipes. Figure 144 shows the final adjusted header designs. The square-to-circle transition part in the figure was carefully designed according to ASME BPVC code to make sure that it can withstand the system pressure.

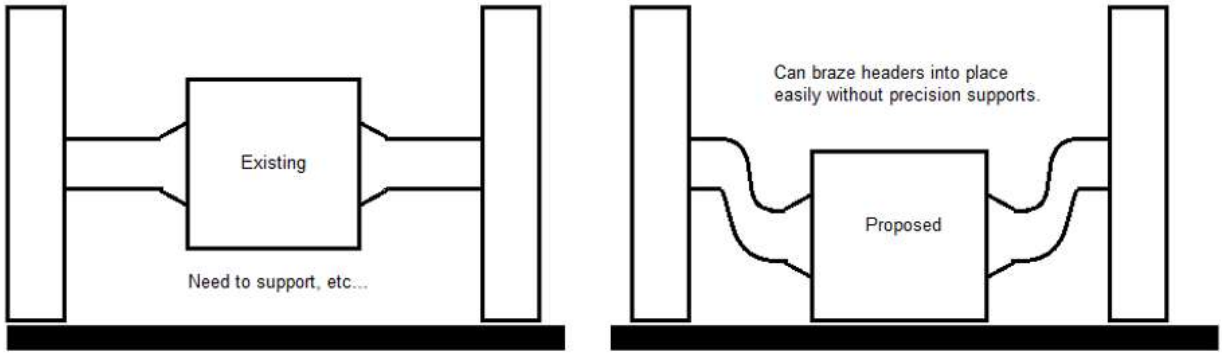

Figure 143. Proposed configuration of headers (Courtesy of Refrac Systems)

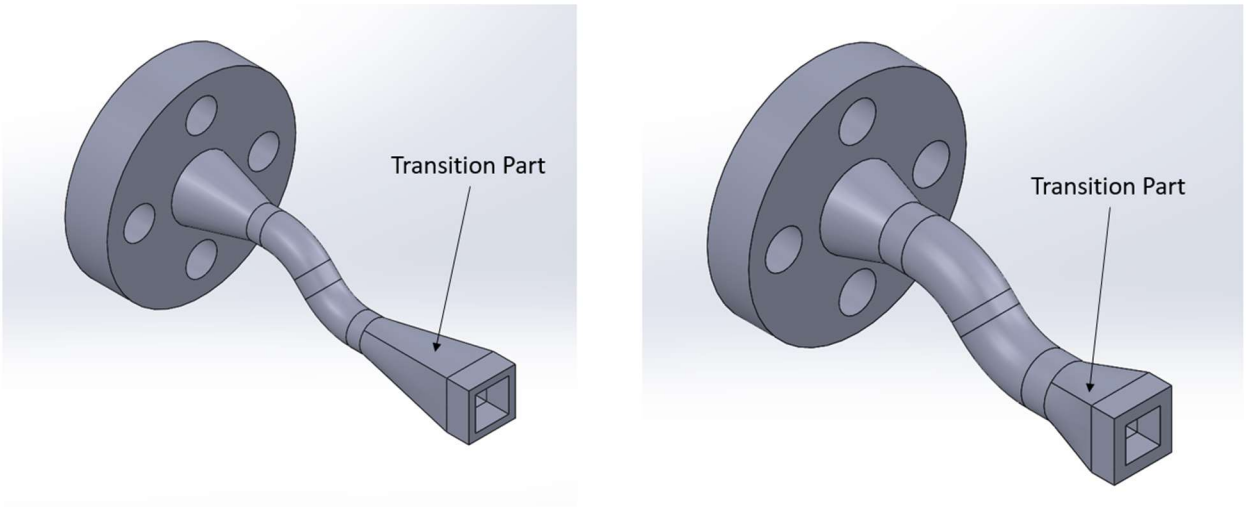

Figure 144. The header at s-CO2 side with NPS ½'' (left) and the header at helium side with NPS 1'' (right)

The design procedure for the transition part, which is shown in Figure 144 is actually the same as the one used for pressure-containing rectangular vessels. Although the transition part's square surface can be inserted into the heat exchanger, it is still valid to assume that the pressure differential between the inside and outside surface is identical with the system pressure for conservative evaluation. First is to determine the inside height of the square end. Since the fluid can be distributed through the transition part to the inlet plenum of the heat exchanger, it is legitimate to make the inside height identical with the thickness of the stacked-up core plates, which is 23.774 mm for 12 plates in total. According to the ASME BPVC code (ASME BPVC VIII-1), the non-circular cross-section of a pressure vessel must be designed in such way that the membrane stress at either long or short side of the vessel shall not be greater than the design stress, and the total stress, which is the sum of the membrane stress and the bending stress at either long or short side, shall not be greater than 1.5 times of the design stress, as expressed by:

$$S_m \leq SE \tag{2.1.26}$$

$$S_m + S_b^S \leq 1.5SE \tag{2.1.27}$$

$$S_m + S_b^L \leq 1.5SE \tag{2.1.28}$$

The membrane stress is, for long and short side, respectively,

$$S_m^S = \frac{PH}{2t_2} \tag{2.1.29}$$

$$S_m^L = \frac{Ph}{2t_1} \tag{2.1.30}$$

and the bending stress is, for long and short side, respectively,

$$\begin{aligned}
\left(S_b^L\right)_M &= \frac{Ph^2c}{12I_2}\left[-1.5 + \left(\frac{1+\alpha^2 k}{1+k}\right)\right];\\
\left(S_b^L\right)_Q &= \frac{Ph^2c}{12I_1}\left(\frac{1+\alpha^2 k}{1+k}\right);\\
\left(S_b^S\right)_N &= \frac{Pc}{12I_1}\left[-1.5H^2 + h^2\left(\frac{1+\alpha^2 k}{1+k}\right)\right];\\
\left(S_b^S\right)_Q &= \frac{Ph^2c}{12I_1}\left(\frac{1+\alpha^2 k}{1+k}\right).
\end{aligned} \tag{2.1.31}$$

where I is the moment of inertia of strip of thickness, as expressed by

$$I = bt^3/12 \tag{2.1.32}$$

and α, k and c are H/h, (I_2/I_1) α and $t/2$, respectively. The parameters can be also referenced to Figure 145. Note that b = 1.0 for vessels without reinforcement. The maximum allowable stresses, as found in ASME codes, for 800H at 730°C and 316H at 600°C are 26.20 MPa and 67.56 MPa, respectively. Using the aforementioned formulation, we can obtain a critical thickness for the square end's shell which ensure that the shell is thick enough mechanically. It is safe to only consider the total stress at location Q because the condition is the strictest. For s-CO_2 at 15 MPa, the critical shell thickness is 7.407 mm, whereas for helium at 2 MPa, the critical shell thickness is 4.107 mm. Therefore, we can determine the shell thicknesses based on the calculation, which are 7.938 mm (5/16'') for s-CO_2 side and 4.763 mm (3/16'') for helium side.

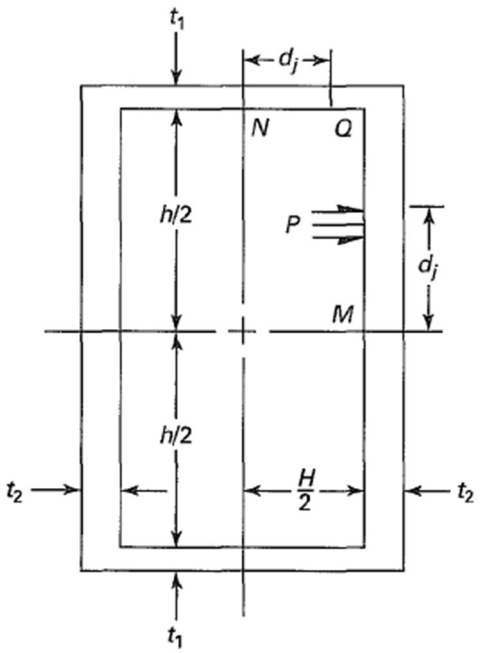

Figure 145. The schematic of rectangular vessel for calculating the transition shell thickness

The angle of the transition is also determined based on the BPVC VIII-1 code's requirement, which states that the angle shall not be greater 30°

2.1.5 Final design and construction of the STL and test PCHE

In the finalized design of the STL, There are four systems, which are 1) primary system; 2) gas supply system; 3) pumping system and 4) IHX test section. Also there is an instrumentation bay used in the entire experimental facility. The description is as follows:

Primary System

The primary system consists of the heating and cooling section, the recuperation section and associated pipes. The heating and cooling system is primarily constructed on a mobile skid that is made of strut channels. It is also called the mobile experimental platform (MEP). The mobility of the skid can provide capability of transferring the facility between remote sites. Additionally, the skid can solve the problem of thermal expansion of the piping system. The heating and cooling system consists of two heating sections and two cooling sections. The recuperation section is actually a recuperator PCHE. The two heating sections are installed at the upstream of the cold side of the recuperator PCHE and the test PCHE, respectively. They primarily provide capability of temperature control of inlet temperature for both PCHEs. The two cooling sections are installed at the downstream of the hot side of the recuperator PCHE and the test PCHE. The cooling section after the s-CO2 flow exiting the hot side of the recuperator, which is noted as the

primary cooler, is mainly served to reduce the operating temperatures for most of components including the centrifugal pump and the Coriolis flow meter, etc. The other cooling section, noted as the auxiliary cooler, which is installed after the s-CO2 exiting the test PCHE and before entering the hot side of the recuperator, is mainly served to reduce the temperatures for the pipe fittings that are used in the facility. The pipe fittings are supplied by Swagelok or similar vendors, and the temperature and pressure ratings indicate the maximum allowable temperature approximately 538 ºC. Therefore, the cooling section must assure s-CO2 flow temperature below 500 ºC at the outlet in order to allow minimum 38 ºC safety margin. As to the recuperator PCHE, it is designed and manufactured by a domestic vendor, VPE (Vacuum Process Engineering). The recuperator is served to recuperate 24.83 kW in the facility, which significantly reduces the required heating and cooling capacity. The recuperator PCHE is made of stainless steel 316/316H, with the core length of 206.2 mm, core width of 79.4 mm and core height of 97.2 mm. The entire matrix weighs 15.33 kg including headers and nozzles. The operating conditions are listed in Table 47. The CAD model is shown in Figure 146.

Table 47 Detail information of the recuperator PCHE

Design Data	Units	Hot Side (Straight Channels)		Cold Side (Zigzag Channels)	
Duty	kW	24.83			
		In	Out	In	Out
Working Fluid	n/a	Carbon Dioxide		Carbon Dioxide	
Flow Rate	kg/s	0.064		0.064	
Temperature	ºC	500	181	100	394
Inlet Pressure	bara	150		150	
Pressure drop	bar	0.132		0.094	
Construction Material	n/a	SS 316/316H		SS 316/316H	

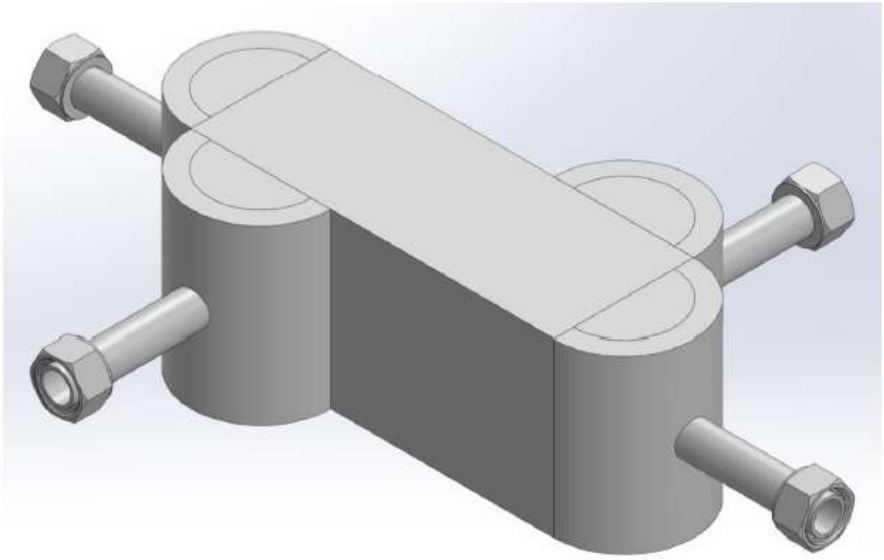

Figure 146. CAD model of the recuperator PCHE (Courtesy of VPE)

The primary cooler is a tube-in-tube coil heat exchanger manufactured by Exergy. The nominal cooling capacity is approximately 15.56 kW, and the thermal effectiveness is 72.7%. The pressure drop for the s-CO_2 flow is around 4.94 kPa. The cooling medium is chill water directly provided by the laboratory utility. More details are listed in Table 48.

Table 48. Detail information of the tube-in-tube coil heat exchanger

Design Data	Units	Hot Side		Cold Side	
Duty	kW	15.56			
		In	Out	In	Out
Working Fluid	n/a	Carbon Dioxide		Water	
Flow Rate	kg/s	0.064		0.182	
Temperature	ºC	181	60	14.5	34.9
Inlet Pressure	bara	150		1	
Pressure drop	bar	0.113		0.049	

The heater installed at the upstream of the cold side of the recuperator PCHE is noted as the primary heater. This is a radiant-type ceramic fiber heater. It is made out of ceramic fiber insulation material embedded with heating elements. The reason to choose radiant heaters is because it will not add additional pressure boundaries to the facility. The system pressure is extremely high, therefore any attempts to avoid adding connections or fittings is encouraged. The ceramic fiber units are wrapped around the heated section, i.e., the

pipe. The heating elements heat up the pipe surface by thermal radiation. The s-CO_2 flow is heated up by thermal conduction and convection. The ceramic fiber heaters are provided by Watlow, and the standard products do not fit the originally designed piping system. Therefore, the pipe used for the heating section is designed to be NPS 2". The base required heating power is 7.42 kW to heat up s-CO_2 flow from 60 to 100 ºC. The heat loss is not estimated yet. However, additional 20% margin is added to the base heating power to address the potential heat loss. Watlow standard stock products provide around 10 kW for this application. In total three modules (or six semi-cylinders) of ceramic fiber heaters are used. The extra insulation blanket was be used for the heat loss prevention. The outer diameter of the heating assembly is around 7 in. large. The length including the vestibules is approximately 7 ft. Those ceramic fiber modules are installed on the second level of the skid. More details are listed in Table 49.

Table 49 Detail information of the high-temperature ceramic fiber heaters from Watlow

Items	Units	Values
Vestibule end diameter	In. (mm)	2 (51)
Semi-cylinder module length	In. (mm)	27-1/2 (699)
Vestibule inner diameter	In. (mm)	3-1/2 (89)
Vestibule outer diameter	In. (mm)	7-1/2 (191)
Volts	V	240
Power	W	1800
Surface loading	W/in.^{2} (W/cm^2)	13.6 (2.1)

The heater installed at the upstream of the test PCHE is noted as the auxiliary heater. The required heating capacity is relatively small, only about 1.5 kW. In order to avoid adding additional pipe connections or fittings, tape heaters are used, which can be installed only by wrapping them around the heating section of the pipe. The allowed length of the heating section is around 6 ft., therefore the standard tape heating products are commercially available for the power density in this case. High-temperature heating tapes from Omega Engineering are used in this application.

The auxiliary cooler is a single pipe-in-pipe heat exchanger customized in design and fabrication. The schematic of the design is shown in Figure 147. The s-CO2 flows in the NPS 1" pipe and the chill water as the cooling fluid flows in the annular region between the NPS 1" and 2" pipe. The required cooling power is approximately 7 kW. As mentioned previously, the major function of this cooler is to reduce the s-CO2 flow temperature to below 500 ºC to avoid leak-tightness issues of the piping connection. The required cooling length is only 1 ft. long as the temperature difference between two sides are extremely large, therefore the thermal effectiveness is about 17.1%. This heat exchanger was

fabricated by a selected vendor. The two ends of the annular duct is sealed by two welded pipe caps drilled with holes at the center. The inner pipe was installed through the holes by welding. Since the annular flow does not experience high pressure, the welding can be completed by a local vendor.

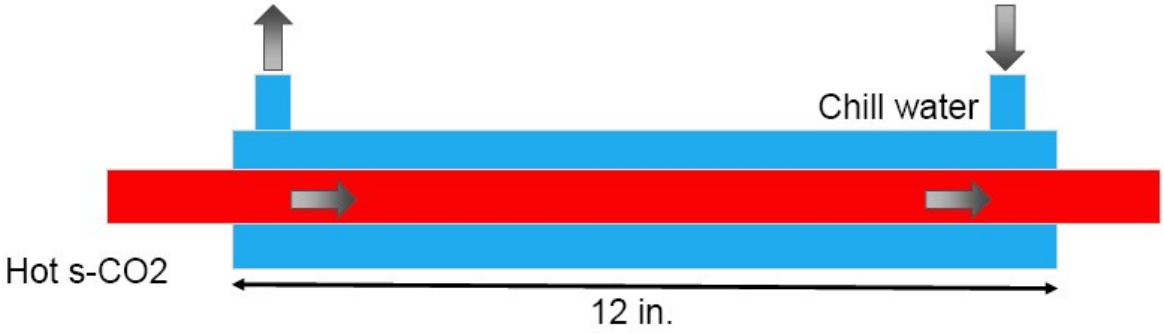

Figure 147. Schematic of customized cooling section

The fabrication and welding of the auxiliary cooling, heating section as well as the primary heating section was originally planned to be provided by American Tank & Fabrication Co. (AT&F). One of the major fabrication is the auxiliary cooling section. The design is updated to have 18” long cooling section. Therefore, the outside water jacket shell is 18” long, with caps welded at each end, and two tube compression-to-weld fittings placed close two ends as the chill water inlet and outlet. The other pipe section only requires to weld pieces of pipes and fittings together. Since the temperature and pressure condition is very extreme, reliable welds must be provided through the entire facility. It is worth noticing that the pipe section for the auxiliary cooling and heating is made of SS 316H for higher mechanical strength. The CAD model is shown in Figure 148.

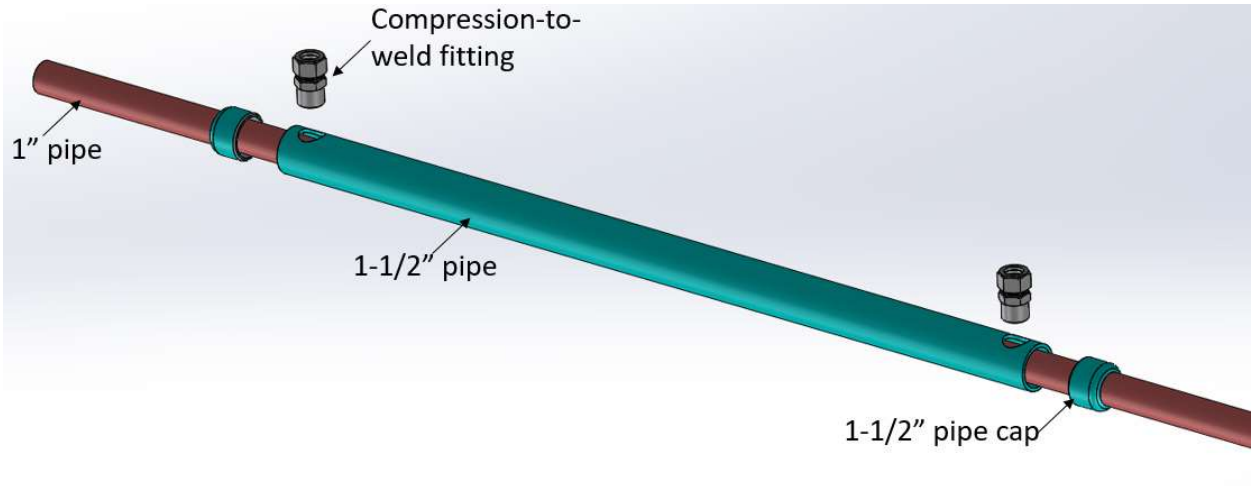

Figure 148. The exploded view of the auxiliary cooling section

As to the piping, there are four ports in the primary system, as shown in Figure 149. Two ports are for the s-CO_2 fluid from and to the IHX test section. These two ports can also be connected to form a closed loop for testing components and equipment under s-CO_2 conditions. In the previous design, the ports connection may use Grayloc connectors, which are very easy to assemble and disassemble compared with the conventional flanges. However, for the combination of high pressure and high temperature, (the maximum pressure and temperature is 2200 psi @ 600 °C), the proper model of Grayloc connectors become prohibitive since it requires high-mechanical-strength sealing rings and hubs. The pressure-temperature rating was made according to the ASME B31.3 Process Piping. #2500 1" ASME flanges are used instead. The other two ports are for the flow from and to the pumping system, which is primarily consisted of the circulation centrifugal Megnepump manufactured by Parker Autoclave. These two ports are connected to the pumping system through NPT connection, and in this case they can be either elbow or tee NPT fittings, depending on whether a thermocouple was installed.

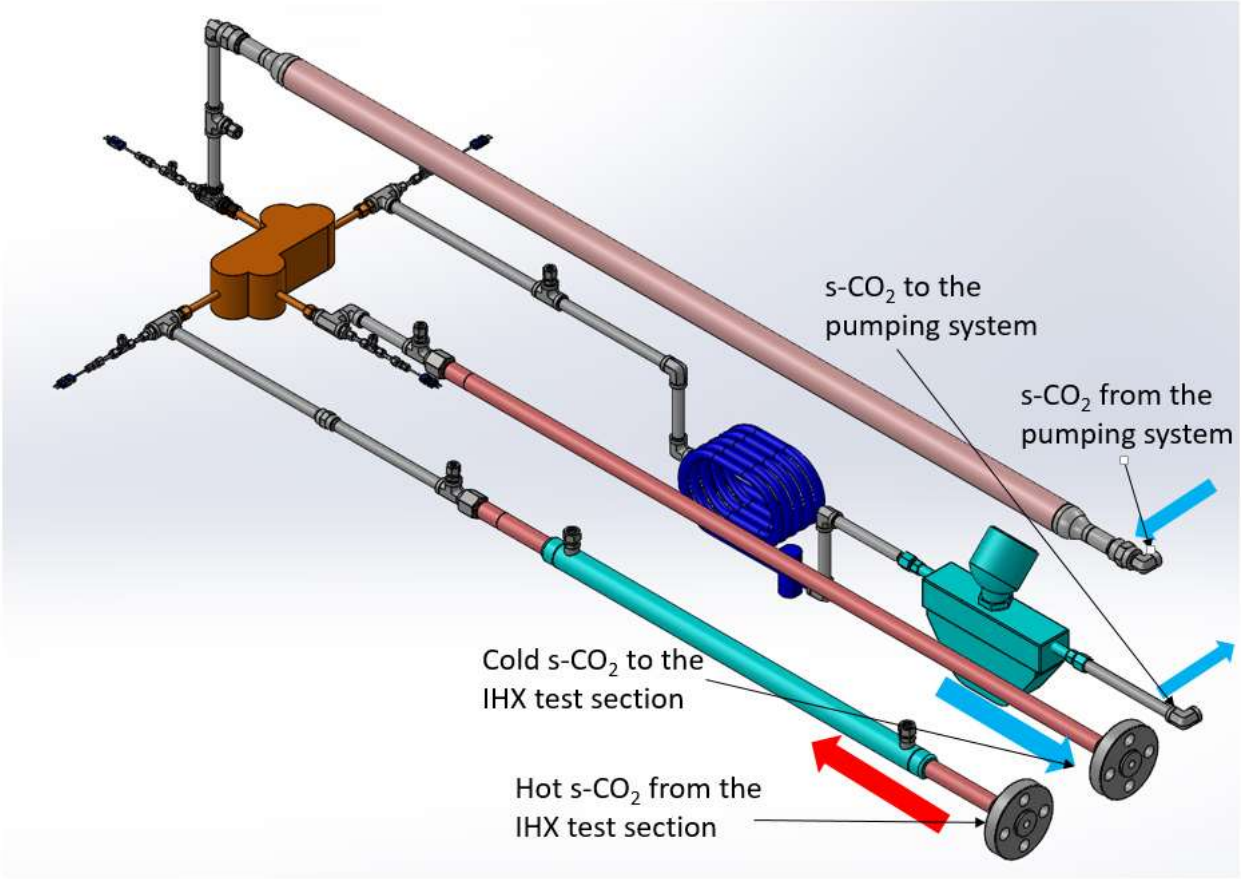

Figure 149. Four ports of the primary system in STL

As mentioned, there are two cooling sections and heating sections in the primary system. The connections between different piping sections are made through NPT connections.

The NPT fittings can be provided by both Swagelok and Hy-lok products. These fittings are rated beyond 2200 psi at the temperature of 537 °C, which is the maximum permissible temperature. Therefore, for the pipe sections that are operated over 537 °C, flanges were installed instead of the NPT fittings. In fact, at the outlet of the auxiliary cooling section, (downstream of the pipe section with 1-1/2” pipe jacket with chill water flowing through), the temperature must be smaller than 500 C such that 37 temperature margin can be achieved. The available NPT pipe fittings include pipe adapters, tees, regular elbows, street elbows, couplings and joint ball unions. Most of them are installed for NPS ½”. Given the competitive price, all of the pipe fittings are provided by Hy-lok. Below is the list of purchased fittings.

Table 50. List of purchased pipe and tube fittings (not complete to date)

Pipe fittings				
Number	Description	Quantity	Vendor	Order No.
1	1/2" Female NPT Tees, 316	5	Hy-Lok	H-STA-8N/S316
2	1/2" Female NPT Elbows, 316	6	Hy-Lok	H-SLA-8N/S316
3	1/2" Street Elbow, 316	6	Hy-Lok	H-SLC-8N/S316
4	1/2" x 6” Hex Long Nipples, 316	4	Hy-Lok	H-SNL-8N L 153/S316
5	1" x 1/2" Hex Reducing Coupling, 316	2	Hy-Lok	H-SSR16-8N/S316
6	1/2" Union Ball Joints, 316	2	Hy-Lok	H-SUR-8N/S316
7	1/2" Male NPT Pipe Plug, 316	4	Hy-Lok	H-SPB-8N
Tube fittings				
Number	Description	Quantity	Vendor	Order No.
1	1/2" On-off High-Pressure Ball Valve, 15 MPa, s-CO2	8	Hy-Lok	HB1H-4T-S316
2	1/2" to NPT 1/2" Straight Male Connector	5	Hy-Lok	CMC-8-8N
3	1/2" to NPT 1" Straight Weld Connector	3	Hy-Lok	CWC-8-8P
4	1/2" to NPT 1/2" Straight Female Connector	4	Hy-Lok	CFC-8-8N
5	1/2" Tees Unions	1	Hy-Lok	CTA-8
6	1/2" Cross Unions	1	Hy-Lok	CXA-8
7	1/4" to NPT 1/2" Straight Male Connector	4	Hy-Lok	CMC-4-8N
8	1/4" to NPT 1/4" Straight Male Connector	8	Hy-Lok	CMC-4-4N
9	1/4" Straight Unions	16	Hy-Lok	CUA-4

10	1/4" On-off High-Pressure Ball Valve, 15 MPa, s-CO2	17	Hy-Lok	HB1H-4T-S316
11	1/4" On-off High-Pressure Ball Valve, 2MPa, helium	9	Hy-Lok	BVH-4T-SL-S316
12	1/4" Tee Unions	8	Hy-Lok	CTA-4
13	1/4" Cross Unions	4	Hy-Lok	CXA-4

All of the pipe nipples between different components, heating and cooling sections and the recuperator are threaded at both ends to be connected with pipe fittings through NPT connections. Because of the extreme combination of the temperature and pressure of the application, the thread quality must be guaranteed no matter what sealants or sealing compounds are used. Initially, threaded pipe nipples and pipe sections were purchased from McMaster-Carr. However, it was found that there were generally thread defects that could be visually inspected by raw eyes (show in Figure 150). Compared with the threaded pipe nipples provided by Hy-lok, it is believed that the poor quality threads may affect the effectiveness of NPT sealing, though it is claimed that the threaded nipples can be used for high or extreme pressure with air, steam and water. During the initial try with female connectors, it was also found the general engagement of these threads were only 1 to 3 turns, far less the proper practice. There was a lot of resistance during the screw-in. After consulting with the vendor, these threaded pipe nipples were returned, and they were replaced with those from another vendor.

Figure 150. Defective threads on pipe nipples (left) and high-quality threads on the pipe nipple from Hy-lok (right)

The NPT fittings are generally tapered thread seals by means of an interference fit between the male and female threads. This means that NPT fittings should never bottom out in the port. The fitting should screw in only partway before jamming. If an NPT fitting screws all the way into a female port without binding, the threads are either mis-tapped

or worn out. After final tightening using the "Turns Past Finger Tight" method, 3 to 6 full threads should be engaged.

However, it is possible that a fitting cannot screw in far enough for a secure connection. This is because manufacturers often make the male threads slightly oversized and female threads a little tight to avoid undersized threads that bottom out without sealing. Too-tight fits are easily remedied by repeatedly hand-tightening the fitting into the port, turning just a little farther each time. This burnishes the threads and allows more thread engagement. It is recommended not to overtighten or force the fitting, as this can crack the female part. The idea is to polish or burnish the threads, not to change the thread size. The proper thread engagement is listed from the table below.

Table 51. Proper Practice of NPT Fitting Assembly

NPT Size	Turns Past Finger-Tight	Approximate Torque
1/8 NPT	1.5 to 3	12 ft-lb
1/4 NPT	1.5 to 3	25 ft-lb
3/8 NPT	1.5 to 3	40 ft-lb
1/2 NPT	1.5 to 3	54 ft-lb
3/4 NPT	1.5 to 3	78 ft-lb
1" NPT	1 to 2.5	112 ft-lb

Note that softer materials require fewer turns past finger-tight. The wide range allows for "clocking" fittings in the desired direction when necessary. Torque values in the table are given for reference only.

Once the desired thread engagement is achieved, the fittings need to be disassembled one last time. It is strongly recommended to clean any grit off the threads and apply a thread sealant. Because NPT fittings seal at the threads instead of at a flare or at the hex, thread sealant is the only type of gasket used. A liquid/paste sealant, or sealing compound as well as tape can be applied. Sealing tape can be decomposed at supercritical fluid environment, and fragments can break loose and cause problems in sensitive systems.

One of the sealants recommended from vendors for heavy duty use of stainless steel NPT fittings is Mill-Rose thread sealing tape, which is composed of 90% of PTFE (Teflon) and 10% nickel. It is claimed to be applicable to wide range of temperature and be capable of providing effective sealing for high pressure. It is believed to be effective at low-temperature legs of the primary system. For high-temperature application which can reach 2200 psi and 500 C, there are some products available from McMaster-Carr to meet the harsh requirement, such as Mil. Spec. Joint Sealants (1959A31) and High-Temperature Pipe Thread Sealants (1965k1). But the common issue about them is that

after exposed to heat for sufficient amount of time, the sealant becomes hardened, which indicates the disassembly of the connection may be extremely difficult and could damage the fittings. The compatibility with supercritical carbon dioxide environment is also not very clear.

All of the components are supported by the skid that is constructed from strut channels. Eight casters are used to equally distribute the entire weight of the facility. The total weight is estimated to be 1450 lb. (659 kg). Therefore, casters with individual maximum capacity of 350 lb. can sufficiently support the skid. The base support is made out of back-to-back strut channels to increase the strength. All connections between strut channels are made from 90º angles that can assure the integrity of the structure. There are three levels in the skid: on the first level, there are three piping sections connecting with the recuperator. These piping sections require relatively small amount of insulation. On the second level, the primary heating section with ceramic fiber heaters are installed. They require relatively large amount of insulation materials. On the third level, pressure transmitters and auxiliary instrumentation are installed. The 3D modeling of the skid is shown in Figure 145.

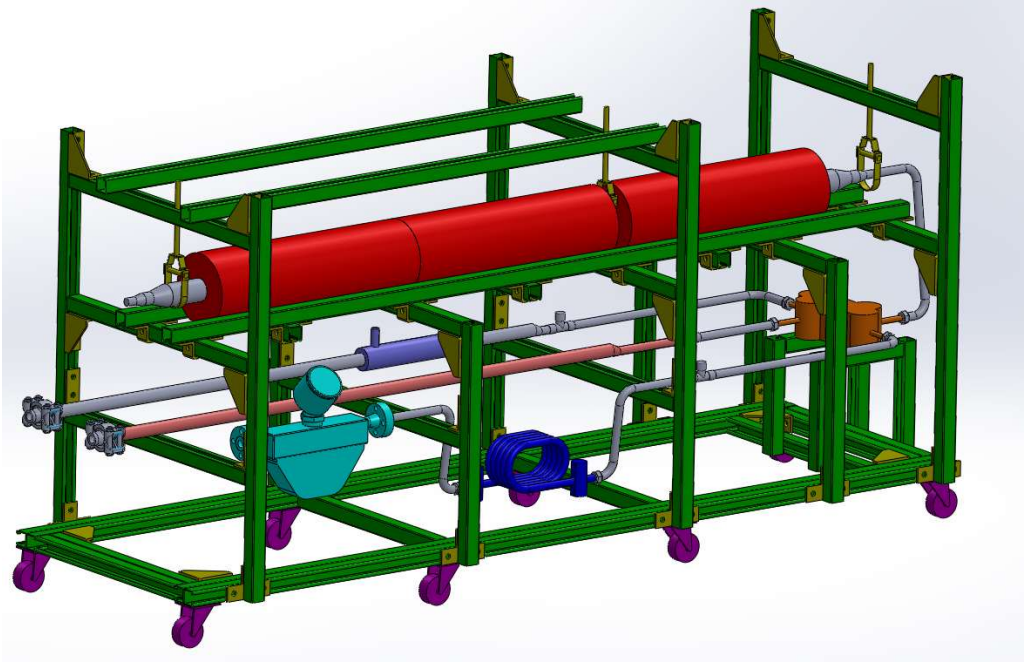

Figure 151. CAD model of the skid of STL

Gas Supply System

The gas supply system consists of an s-CO_2 reservoir, a liquid CO_2 pump with constant pressure control, two gas cylinders and tubing system. The s-CO_2 reservoir is designed to maintain the constant pressure in the loop and provide extra volume to buffer the CO_2

flow fluctuation. The reservoir is made of NPS 4” SCH 80 SS 316 pipe with a butt-weld neck and a blind flat face #1500 flange as well as a pipe cap. The pipe is 18” long, and therefore the reservoir can provide extra volume of 3.40 liter to the loop, which accounts for the original inventory volume of more than 30%. There are 7 outlets welded on the reservoir. 4 are welded on the top of the blind flange, of which two are connected to the liquid CO_2 pump, and other two are reserved for future use. 2 are welded on the opposite side of the reservoir body. One is for a safety relief valve, and the other is for a pressure gauge. The last one is welded at the bottom of the reservoir, which connects the pumping system and the primary system. Most of them are compression tube fittings except two are reserved for pipe couplings.

The pressure gauge can be procured from McMaster-Carr, with MNPT ½” connection and ±1% accuracy (3852k875). Another model available is from Swagelok pressure gauge. The safety relief valve needs to provide a quick-action release of CO_2 fluid to prevent over-pressurization in the test loop. Generally the safety valve is the last safety defense for vessels and pressure systems. The valve pops up when the pressure exceeds the set value to a fully open position until the system is depressurized to a certain level. A relief valve is generally open proportional to the pressure level of the system. They can be used for liquid system to limit the pressure. Though in this application, carbon dioxide at the nominal condition is at liquid phase in the s-CO_2 reservoir, there is no need for proportionally release the inventory because once released the s-CO_2 will instantly vaporize and depressurize similar to the steam system. Therefore, a safety valve is more appropriate for this case. The set value is determined to be 16.5 MPa as the maximum system pressure, which is 10% band beyond the nominal pressure. In reality, the system may be operated at low pressure occasions to accumulate experience in handling s-CO_2 and prevent any accidental errors to damage the facility. It will only be operated to the full nominal pressure at a few occasions. Available models of products are RV2 series safety relief valve from Hy-lok. It can be adjusted externally to set up the set value in the range of 2250-3000 psi, (16.5 MPa = 2340 psi) and Viton seat is rated as “excellent” compatible with carbon dioxide as seals. Another one is Kunkle 266 series from NASVI, which require the setting pressure set in the factory. The later one is much more expensive than the former one.

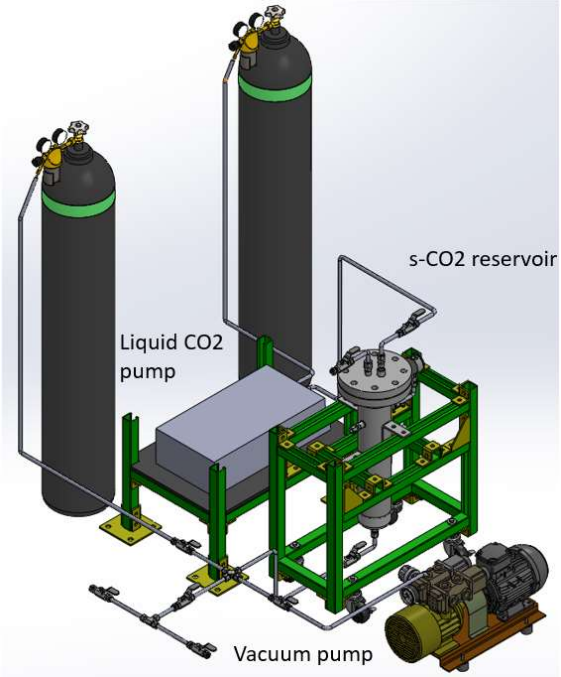

Figure 152. The layout of the gas supply system

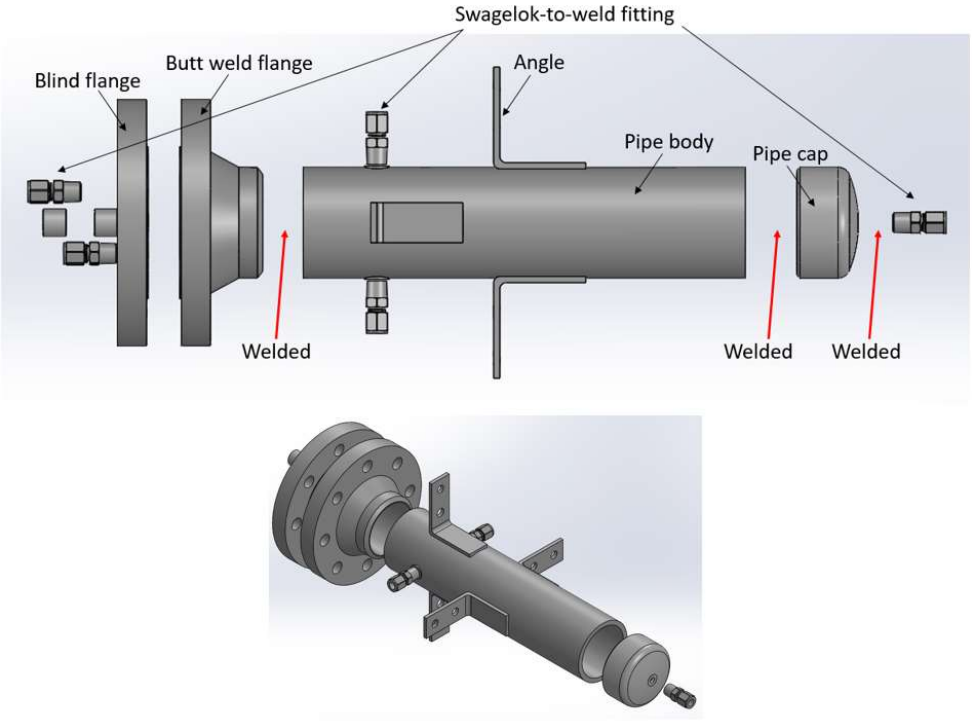

Figure 153. The exploded view of the s-CO_2 reservoir

The liquid CO_2 pump is available from Chrom Tech Inc. The one that satisfies the requirement of accurate control of the system is the model SFC-24, which is a positive

displacement pump that provides reliable pumping of liquid CO_2. The pressure setting is user-selectable, and the pump flow rate can be auto-adjusted to maintain the pressure. It also provides pressure monitoring, with pressure control accuracy of ±2% of full scale pressure. It can be used under pressure up to 10,000 psi, and the maximum flow rate is around 24 mL/min. It can be easily maintained. However, it is also very expensive compared with most of the components used in the STL. Hence it is not purchased for current stage of experiments and testing.

Regulators are used to connect the CO_2 gas cylinders to the gas supply system. Main parameters concerning regulators are the inlet and outlet pressure. Generally the upper limit of the outlet pressure (or the delivery pressure) is approximately 1,000 psi (around 70 bar) based on the inlet pressure and outflow that is controlled manually. Therefore, the possible achieved pressure level to the STL can be approximately 7 MPa by naturally discharge from the gas cylinder. Since the liquid CO_2 pump was not purchased, there was lack of effective control of the system pressure. One of the feasible solutions is to pressurize the loop by heating up the entire inventory. For carbon dioxide at high pressure, especially close the supercritical point, the ideal gas law is no longer applicable. Assuming the density is unchanged during the variation of temperatures to the carbon dioxide, the temperatures corresponding to the pressure level from 7 to 15 MPa are then available through NIST webbook. The information is listed below.

Table 52. Temperature variation of carbon dioxide corresponding to different pressure levels

Status	Pressure (MPa)	Temperature (C)	Density (kg/m^3)
Liquid	7	23	773
Liquid	8	25	777
Liquid	9	28	768
Liquid	10	30	772
Supercritical	11	32	774
Supercritical	12	34.5	772
Supercritical	13	36	774
Supercritical	14	39	771
Supercritical	15	41	773

Therefore, the temperature rise can effectively pressurize the system. With the safety relief valve installed, the over-pressurization by heating the inventory up can be prevented. As mentioned above, the CO_2 reservoir can dampen the pressure or flow fluctuation once the circulation pump starts up after the initial fill of the system. The pressure level that is achieved through this approach may not be accurately controlled,

but it is economically inexpensive and equally easy to realize as the control mechanism provide by the liquid CO_2 pump.

Pumping System

The pumping system consists of the centrifugal MegnePump, the filter, exhaust valve and support base. The pump can be operated at 60 °C other than room temperature to avoid severely unstable thermo-dynamic properties of the supercritical fluid close to the pseudo-critical point. One filter is installed right before the fluid entering the pump to prevent any impurities, debris or fragments sucked into the pump. An exhaust valve is installed at the downstream of the circulation pump for the release of the inventory after experiments and maintenance to the components. The pipe sections are used to connect the ports from the primary system. One of them is determined in dimension after all pipes and equipment are properly installed and be fabricated to fit into the facility to accommodate all the clearance gaps in the piping system.

These three systems can be slightly modified by adding a pipe section with two flanges to close the loop for experimentally testing the recuperator PCHE or other PCHE-type heat exchangers in the future. The figure below demonstrates the layout of the STL test rig.

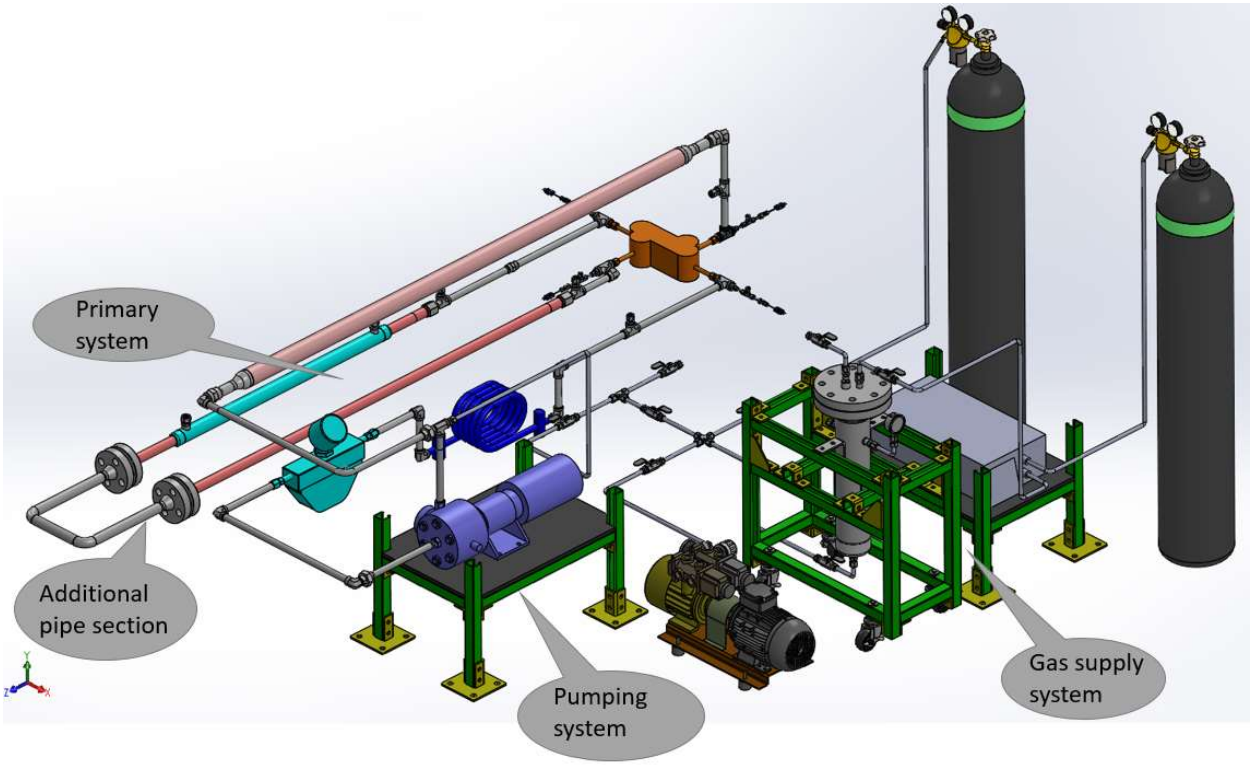

Figure 154. STL test rig for testing the recuperator

IHX Test Section

The IHX test section is mainly consisted of the IHX test PCHE and associated pipes. The IHX is custom designed with zigzag shims for helium side and S-shaped fin shims for s-CO_2 side. The shim is particularly designed to fit into the etching, diffusion-bonding and fabricating requirement in VPE, which is responsible for the final testing and shipping of the heat exchanger. The IHX test PCHE is connected with the primary system through flanges and pipe section. There are two U-type sections that can absorb the thermal expansion of the piping system in the facility. The IHX test PCHE is also characterized by in total 8 pressure taps installed on the core of the heat exchanger, which are capable of measuring multiple pressure differentials for each side. The core is constructed with Inconel 617. The nozzles are constructed with Incoloy 800H. For the helium side, two #1500 ¾" flanges are installed as the terminal of nozzles, while for the s-CO_2 side, two #2500 ¾" flanges are installed. The detailed technical parameters are listed in Table 53. The CAD modeling of the IHX test PCHE is shown in Figure 155. The layout of the entire facility for testing the IHX PCHE is shown in Figure 156.

Table 53. IHX PCHE specification

Design Data	Units	Hot Side (Zigzag Channels)		Cold Side (S-fin Channels)	
Duty	kW	13.28			
		In	Out	In	Out
Working Fluid	n/a	Helium		Carbon Dioxide	
Flow Rate	kg/s	0.0092		0.064	
Temperature	ºC	730	435.5	418.8	599.4
Inlet Pressure	bara	20		150	
Pressure drop	bar	0.321		0.371	
Core Material	n/a	Inconel 617		Inconel 617	
Header and Nozzle Material	n/a	Incoloy 800H		Incoloy 800H	

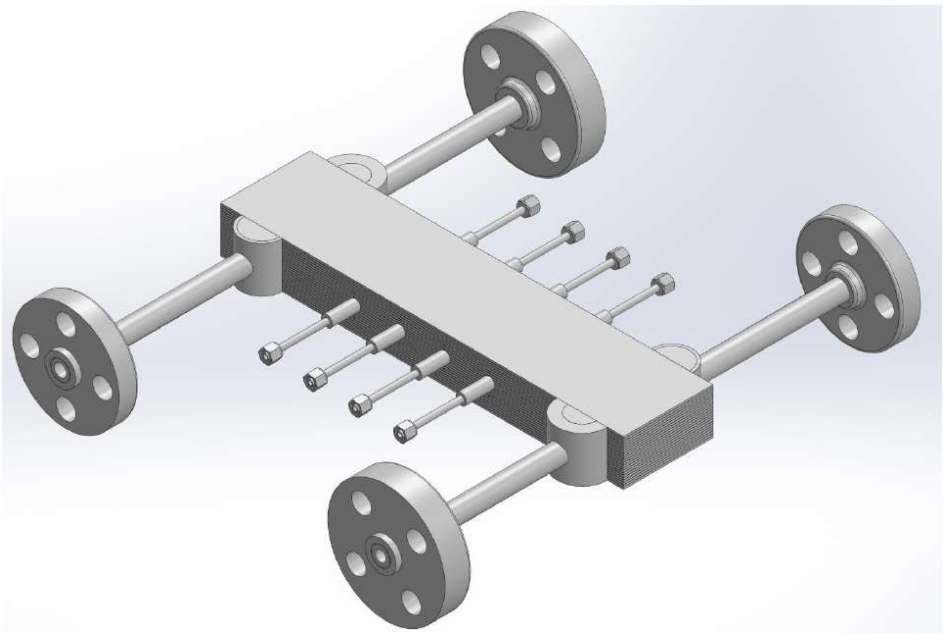

Figure 155. CAD modeling of the IHX test PCHE

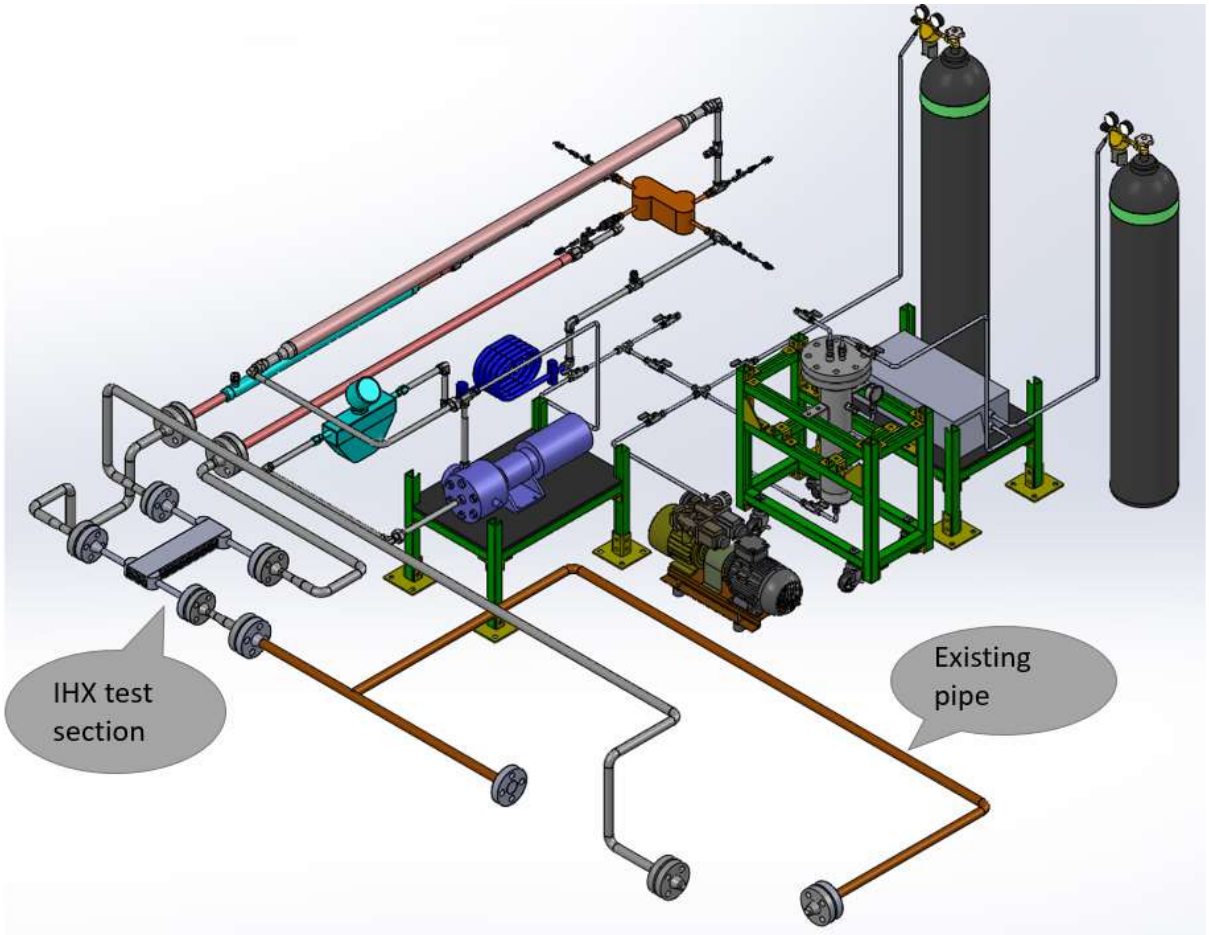

Figure 156. The layout of the entire facility

In addition to the recuperator testing, the IHX PCHE test is performed on the IHX test section and the three other systems. Two working fluids was used in experimental tests, helium and carbon dioxide. The helium flow was provided by the HTHF, which can supply helium gas up to 60 kg/h and temperature up to 800 ºC. The carbon dioxide flow was be under supercritical pressure, and be supplied by the STL. The s-CO_2 flow can be provided up to 300 kg/h and temperature up to 500 ºC. The maximum allowed outlet temperature of s-CO_2 in the test PCHE is 630 ºC. Most of the experimental conditions were in the range of 400 to 600 ºC with the system pressure in the range of 8 MPa to 15 MPa.

Instrumentation Bay

The temperature measurement is very important in the primary system because of the need to monitor the temperatures at the multiple sections of heating, cooling and heat recuperation. The recuperator PCHE, which is designed and fabricated by VPE, is used both for recuperating the heat necessary to operate the IHX test PCHE, and experimental test to validate the CFD simulation. Therefore, the pressure and temperature measurement on the recuperator PCHE is even more important. The instrumentation set up for the recuperator PCHE can also be used for the measurement of future other heat exchangers or recuperators installed on the primary system. Therefore, the design of the pressure tap and thermocouple assembly should be versatile and flexible in use. In the current design, the pressure tap and thermocouple can measure the same location in the flow field or at different locations away with a pre-set distance. The thermocouple sheath, which is essentially ⅛” tube, is placed at the center of another tube of ¼” diameter. The pressure is measured through annulus. The only drawback of the device is that the pressure measure through the stagnation point at the end of the ¼” tube is the sum of the static pressure and dynamic pressure. The dynamic pressure requires good knowledge of flow velocity, which can be calculated with uncertainties. The terminal end can be inserted to the recuperator plenum to measure the temperature and pressure of the flow mixture. It can also be inserted to any location in the nozzle, as shown in Figure 158. The size of the thermocouple sheath is determined with several factors taken into account, such as the block area by the thermocouple at the center and the flow-induced vibration to the small tube hanging in the nozzle. Another potential problem is that the occupation of the thermocouple and pressure tap in the nozzle can affect the flow field and thus affect the heat transfer to the thermocouple. The degree of the effect is not clear, but can be possibly estimated according to the thermowell calculation guide in ASME codes.

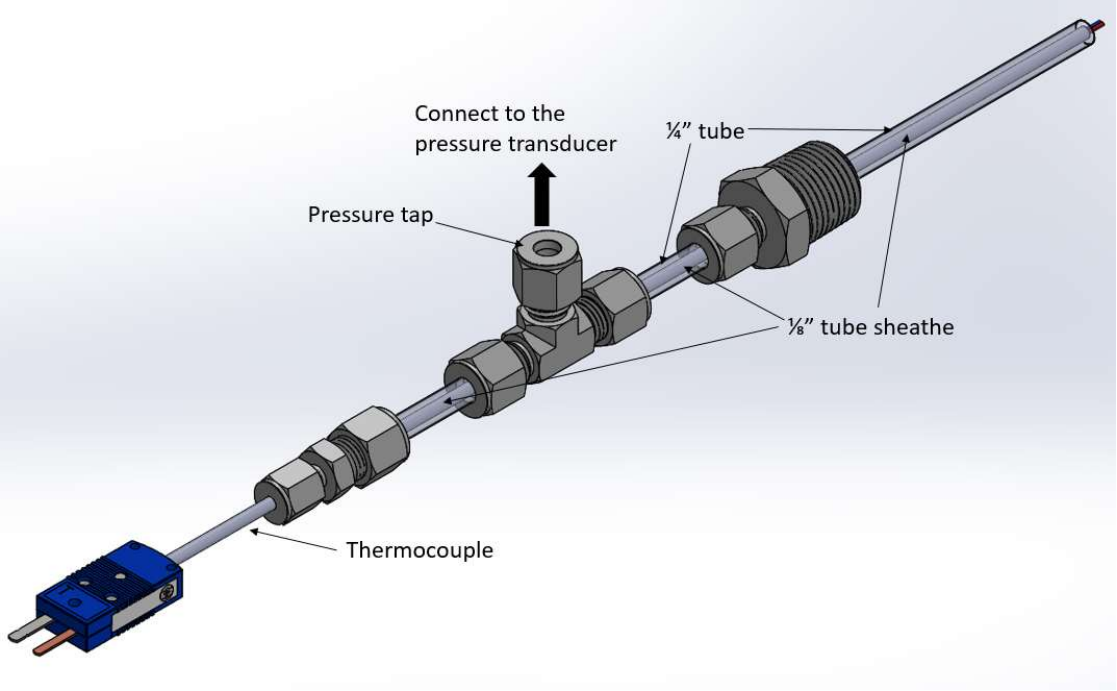

Figure 157. Thermocouple and pressure tap assembly

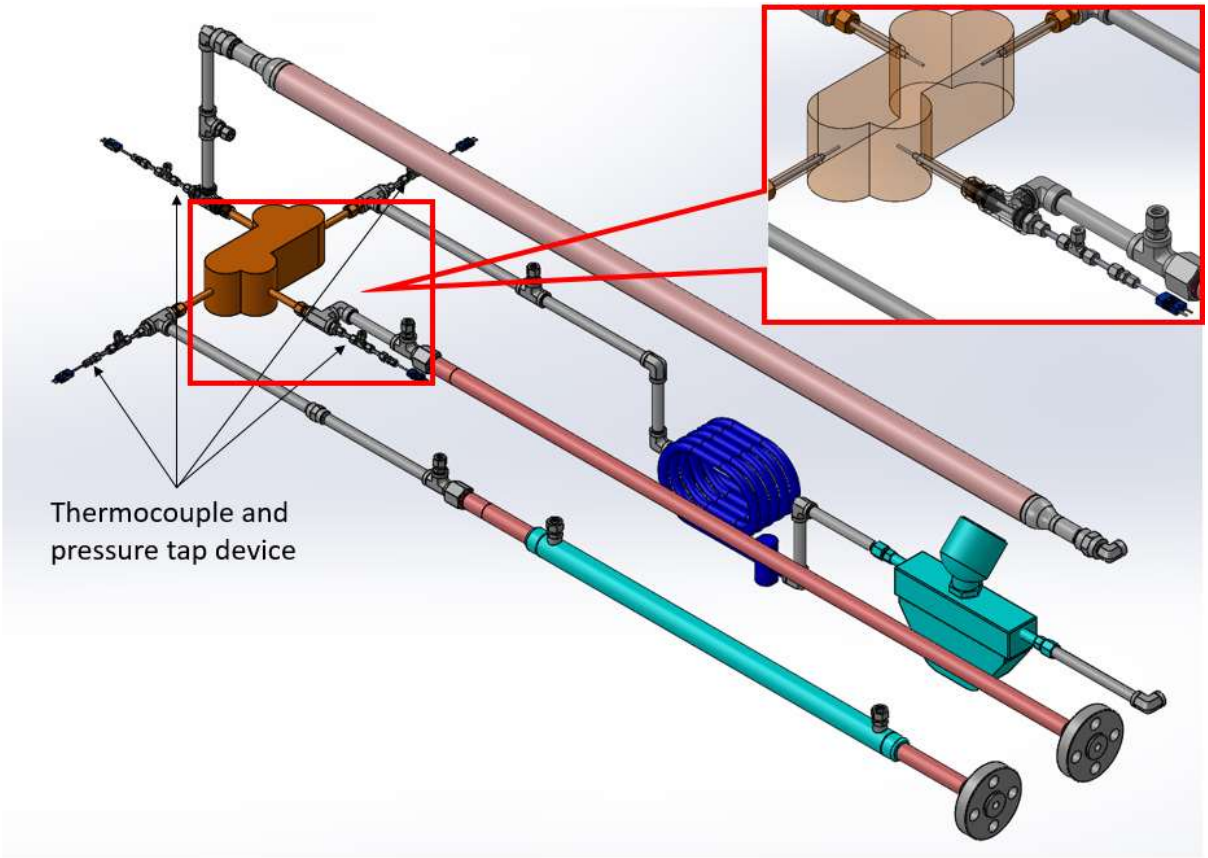

Figure 158. The installation of the thermocouple and pressure tap assembly

In addition to the temperature measurement capabilities, the pressure measurement capabilities are also developed, including the pressure differential at the heat exchanger manifolds as well as inside the heat exchanger. The pressure differential between manifolds of both the IHX test PCHE and the recuperator PCHE provides an effective way to collect the pressure drop data. However, from previous experience in operating PCHE-type recuperators in HTHF, the pressure drop in the manifolds or headers was considerably large, creating huge uncertainty in the pressure drop of the primary section of the flow channels on the etched metal plates. Therefore, additional pressure differential measurement across the PCHE heat exchanger core is developed. The configuration of the pressure-measuring line is related to the pressure taps installment (Figure 159). Three sections of pressure drop are measured, each theoretically accounting for 1/3 of the total pressure drop across the core, as shown in Figure 160. A system of pressure-measuring line is developed to easily switch the section of pressure differential measurement, as shown in Figure 161. The accurate measurement of the pressure drop is very useful to the analysis of the local pressure drop distribution, which can be used to improve the design of the manifolds and headers.

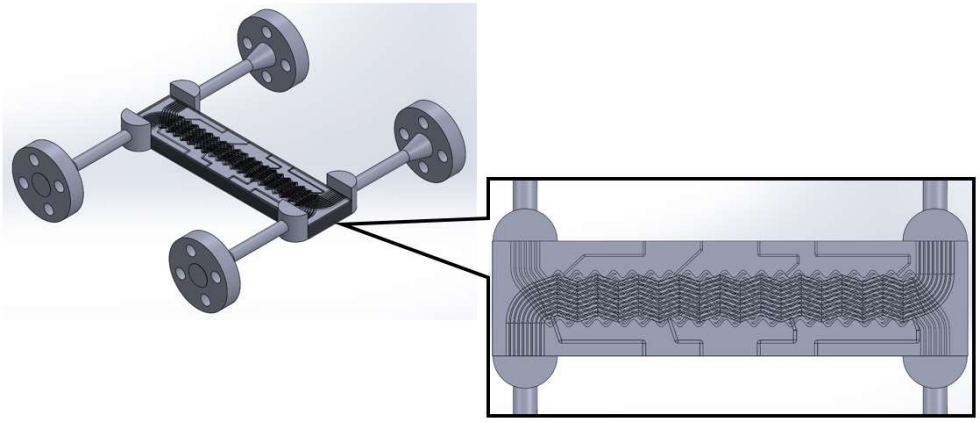

Figure 159. The configuration of pressure-measuring lines in the heat exchanger core

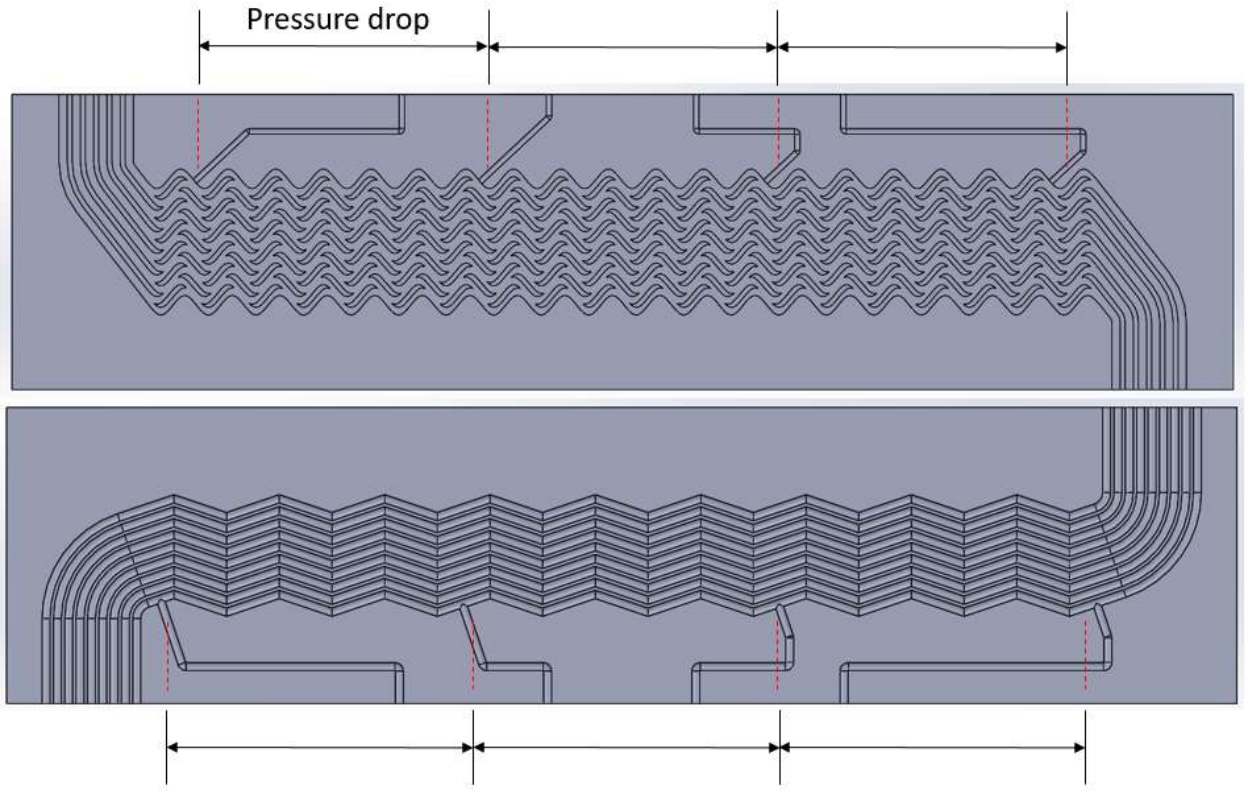

Figure 160. Pressure drop measurement on each etched metal shim

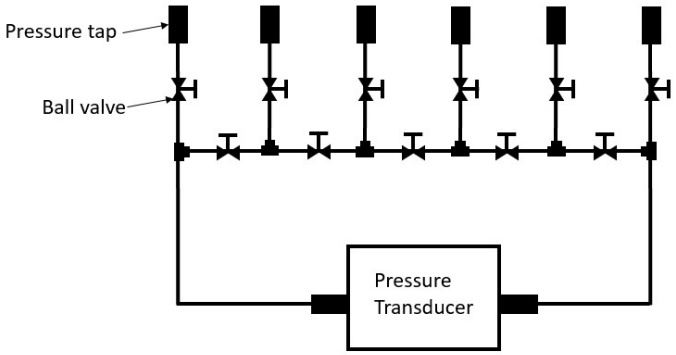

Figure 161. The diagram of the pressure measurement system

Besides the temperature and pressure differential measurement, a strain measurement can also be included in the experimental capabilities of STL. The thermal stress of the PCHE-type heat exchangers at high temperatures is very important to the structural integrity. During the experimental tests, both the recuperator PCHE and IHX test PCHE experience high temperatures in the range of 180 C to 730 C. Little experimental data is available for the thermal strain measurement of PCHE heat exchangers. Preliminary investigation on the thermal stress can be performed on the recuperator PCHE. In total

six strain gauges are installed at different locations on the heat exchanger, as shown in Figure 162 (only four are shown). The measurement can collect critical thermal strain information at locations close to the headers where a large temperature difference between the cold and hot side of the heat exchanger can be observed. The data can also be compared with numerical simulation results.

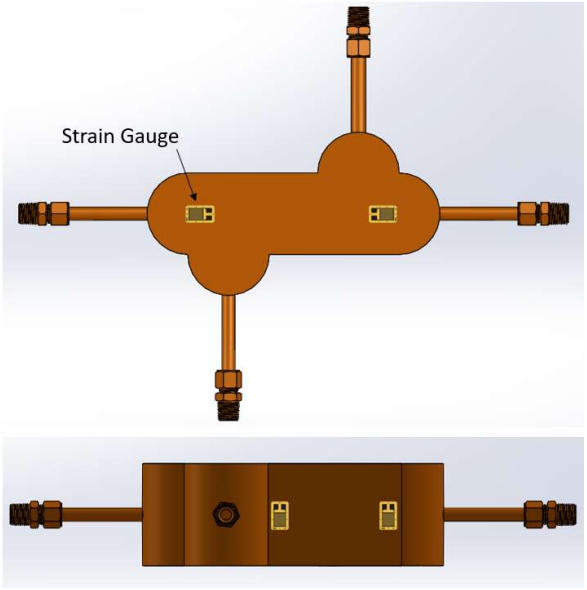

Figure 162. The strain gauges' installment on the recuperator PCHE

2.3 Construction of Airfoil and Zig-zag test recuperators in UW

2.3.1 Channel design and recuperator sizing

The University of Wisconsin Madison created two test PCHE recuperators for the experimentally validation of recuperative performance. Sizing of the PCHE recuperators was based on previous experience in performance testing of an industry partner's recuperator design. The two recuperators currently built are an NACA0010 airfoil channel counter flow recuperator and a 80 zig-zag channel counter flow recuperator. Both feature etched microchannels with hydraulic diameters of 1.62 mm and 1.16 mm respectively. Etched channels from each recuperator are shown in Figure 163 and Figure 164.

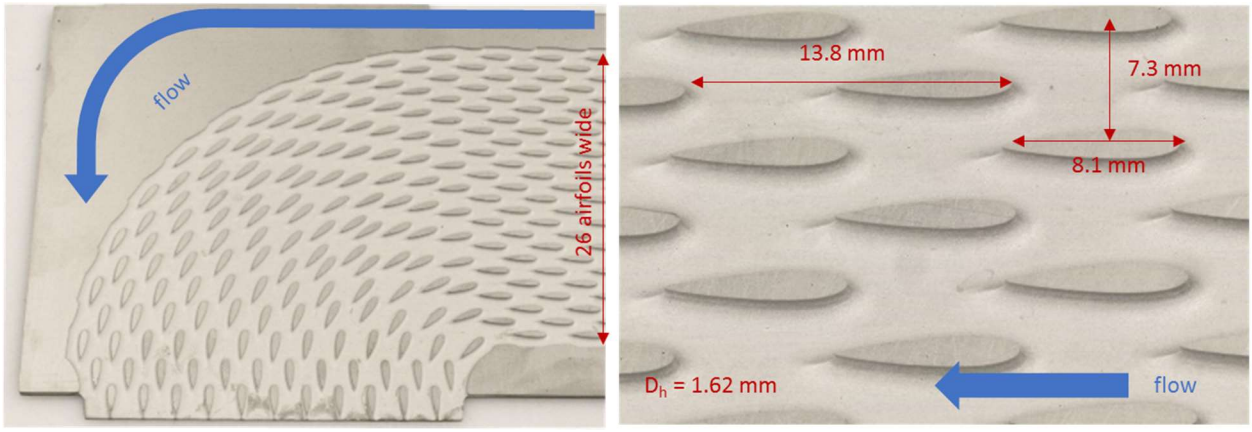

Figure 163: Airfoil channels; (left) exit to header, (right) detail of etched airfoil array (1 mm deep channel)

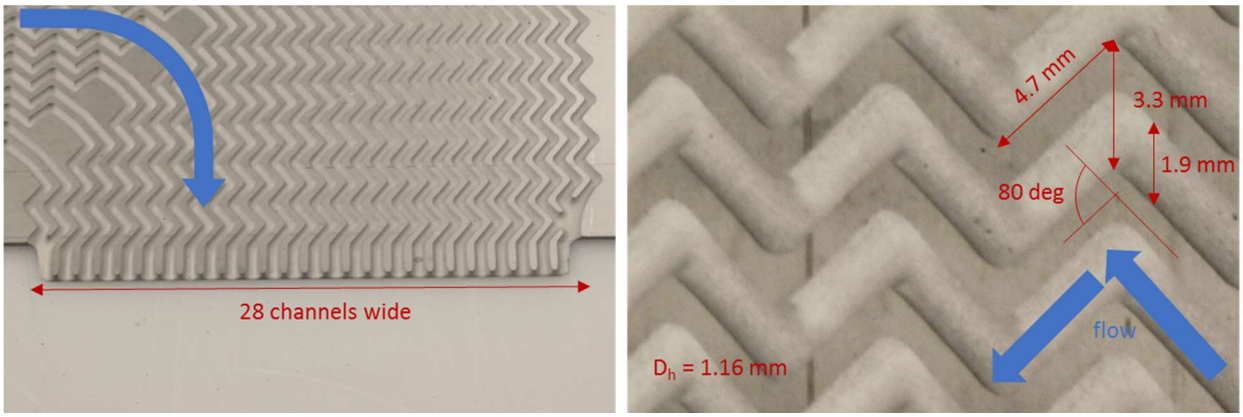

Figure 164: 80 deg Zig-Zag channels; (left) exit to header, (right) detail of etched airfoil array (1 mm deep channel)

The size of the recuperators was chosen to closely match that of a previously tested industry partner's recuperator. The performance of the industry partner's recuperator was found for a range of flow rates from Re 1490 to Re 16600 as shown in Table 54. UW Madison's airfoil and zig-zag recuperators were sized to have similar surface area and cross section as the industry partner's and are expected to achieve similar performance. A comparison of the construction of the airfoil, zig-zag, and industry partner's recuperator is given in Table 55.

Table 54: Tested performance of Industry Partner's recuperator

	Lowest flow	Highest flow
Re [-]	1492	16581
Effectiveness [%]	93.1	82.56
UA [-]	61.6	219.3

Table 55: Comparison of test recuperator construction

	Airfoils, 8.1mm NACA0010	Zig-Zag, 80 deg	Industry Partner
	note 26 airfoils wide	note 28 channels wide	
volume per plate [mm^3/mm]	70.75797101	40.13768178	235.8304
surface area per plate [mm^2/mm]	176.1339674	158.5279538	724.9892
surface/volume [mm^2/mm^3]	2.489245591	3.949604132	3.074197389
hot side plates [-]	4	6	1
length [mm]	773.87196	577.85	758.1392
total volume [L]	0.219030439	0.139161356	0.178792271
total surface area [m^2]	0.545220554	0.549632269	0.549642732
total cross sectional area [mm^2]	283.031884	240.8260907	235.8304
cold side plates [-]	5	7	2
length [mm]	773.87196	577.85	758.1392
total volume [L]	0.273788049	0.162354916	0.357584542
total surface area [m^2]	0.681525693	0.641237647	1.099285464
total cross sectional area [mm^2]	353.7898551	280.9637725	471.6608

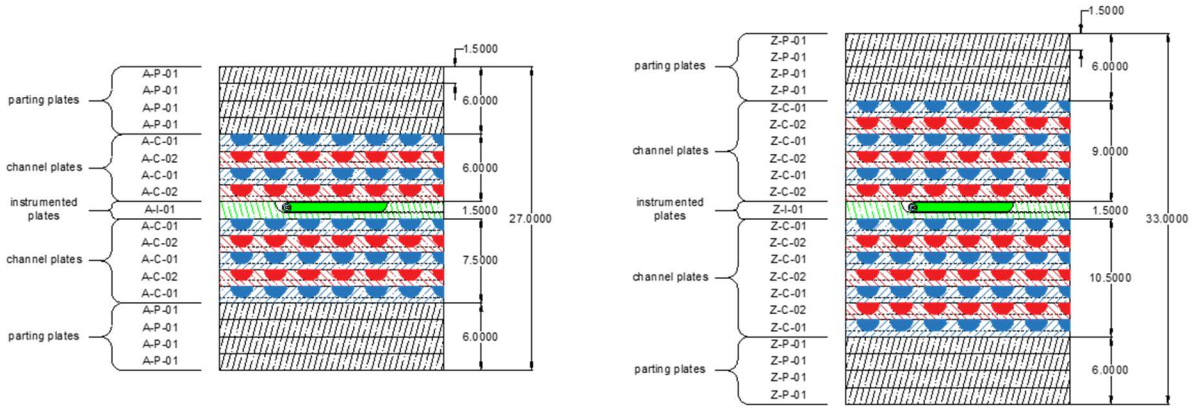

Figure 165: Plate stacking order in the airfoil recuperator (left) and 80 deg zig-zag recuperator (right). Hot channels are red, cold channels blue, and instrumented plate green.

Each recuperator is made of a number of stacked counter flow channels, top and bottom solid channel-less plates, and a central instrumentation plate. Plates are 1.5 mm thick 316 Stainless Steel and are chemically etched to a depth of 1 mm. The stacking of the airfoil and zig-zag plates is shown in Figure 165. In flow channels the resulting profile is

semicircular as etching proceeds from one direction. Channeled plates are stacked alternatively in counter flow with the outmost plates being the cold side. Solid un-etched plates bonded to the top and bottom of the stack. Bonded 4 thick they form 6 mm of solid wall within the recuperator. The 6 mm is needed as a weld region so headers can be attached without damaging the fragile internal micro-channels.

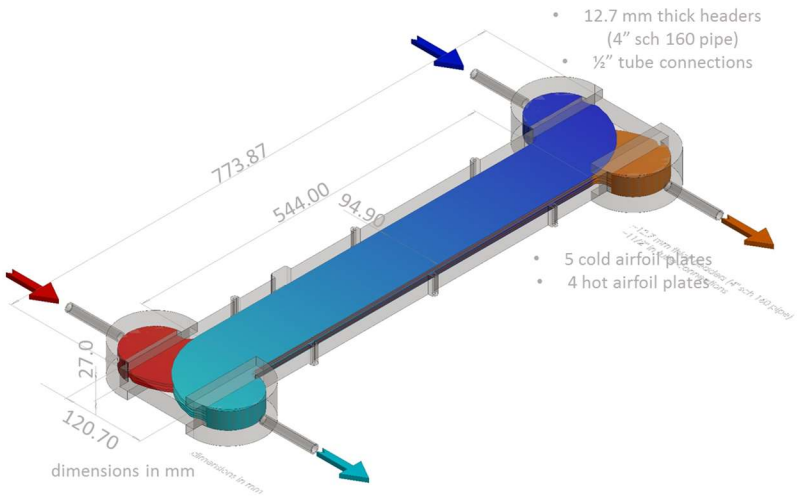

Figure 166: Overview of Airfoil PCHE with headers and channels

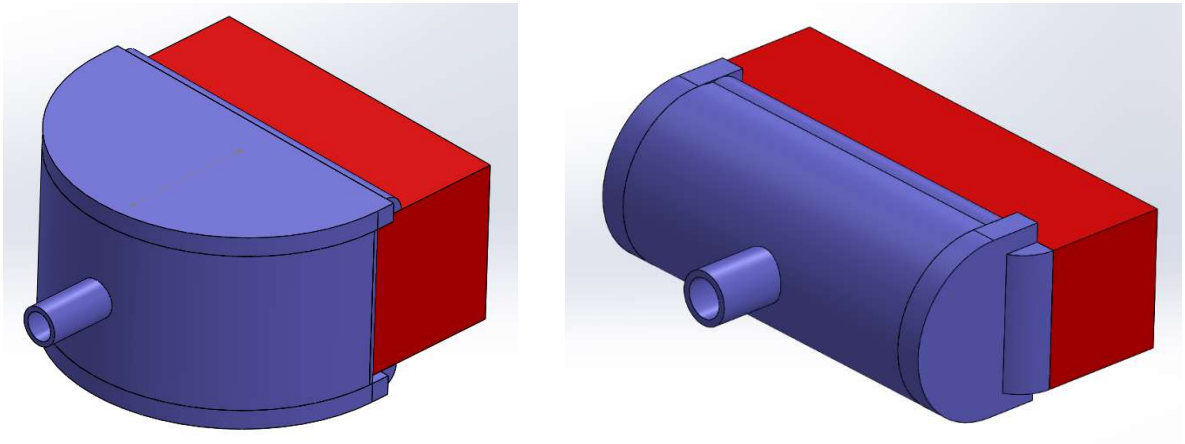

Figure 167: Header designs for Airfoil (left) and Zig-zag (right) PHCEs. Header is colored blue while a subsection of the PCHE block is colored red.

Inlets and outlets to the hot and cold channels are brought together in a manifold and linked to plumbing through four separate headers. Headers are place on the sides of the recuperator as show in the diagram of the airfoil recuperator in Figure 166. Different

header designs were used for the Airfoil and Zig-zag PHCEs as the design was adapted after welding of the Airfoil headers.

2.3.2 Header Design

Headers design was different between the Airfoil and Zig-zag blocks. Headers on the Airfoil PCHE were made out of 12.7 mm thick plate and 4" sch 160 NPS pipe while headers on the Zig-zag were made with 6.125 mm thick 1-1/4" sch 160 NPS pipe. The orientation of the pipe sections of the header was rotated 90 degrees between the Airfoil and Zig-zag as seen in Figure 167. The design change was made to reduce the number of welding passes needed to attach the headers.

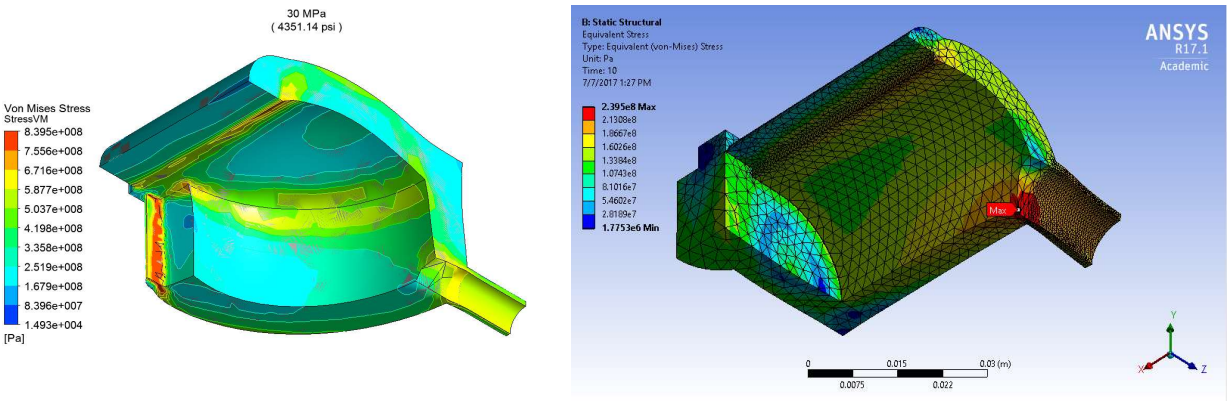

Figure 168: Most extreme stress results from FEA modeling of the Airfoil PCHE header (left), and the Zig-zag PCHE header (right)

As the recuperators are designed to operate within the conditions of the s-CO2 Brayton cycle, the headers were designed to meet around 20 MPa of pressure at temperatures of up to 650C. FEA modeling was performed at header temperatures of 200C, 500C, and 650C with ranges in pressure of 0-30 MPa for the Airfoil header and 0-60 MPa for the Zig-zag header.

Airfoil headers stress concentrations occur at the side weld bead and at the instrumentation port at the top and bottom plates as shown in Figure 168. These stresses built up rather quickly, giving lower pressure ratings of 29.6 MPa at 200 C and 11.3 MPa at 650 C. Design of the Zig-zag headers was changed to reduce stress concentrations. These occur primarily along the top weld bead and the center of the arced 1-1/4 sch 160 pipe section as shown in Figure 168. Stress doesn't build up as rapidly in the Zig-zag headers, resulting in higher pressure ratings of 60 MPa at 200 C, 56.4 MPa at 500 C, and 14.4 MPa at 650 C.

2.4 Description of s-CO_2 test facility

Experimental systems created at the University of Wisconsin-Madison (UW) consisted of an s-CO_2 loop that was modified for recuperator testing, along with a recuperator experiment bay that was specifically built for the purpose. The s-CO_2 loop serves as a base for any CO_2 flow requiring experiment. The loop is based around a 50 hp Hydropac™ reciprocating dual-piston compressor. Control of flow in the loop is achieved with manually controlled needle-valves. The s-CO_2 loop provides a continuous CO_2 circuit whose flow can be tapped for any variety of CO_2 experiments. Added to the s-CO_2 loop is a recuperator experiment bay that provides plumbing and instrumentation for testing of two pass counter-flow recuperators. Manual needle-valve control exists between the main s-CO_2 loop and recuperator bay to allow variable mass flows up to 0.04 kg/s within the recuperator. The experimental bay contains a 6 kW heater which is used to drive power to the recuperator.

The s-CO_2 loop and recuperator experiment bay were specifically designed to allow versatility in the recuperator being tested, so that a variety of recuperators and heat-exchangers can be tested with minimal re-plumbing and setup between experiments.

2.4.1 The s-CO_2 loop

The s-CO2 loop incorporates all pumping, chilling, heating, and control of the system. It is diagrammed in Figure 169 with major components, plumbing, instrumentation, and control valves shown. The system is plumbed primarily with 1/2” 316 stainless steel tubing, except going to and from the compressor where 3/4” tube is used. CO2 flow through the

pipes in the direction indicated by ⇒. Control and data handling is managed by a National Instruments (NI) CompactRIO (cRIO) controller and associated modules.

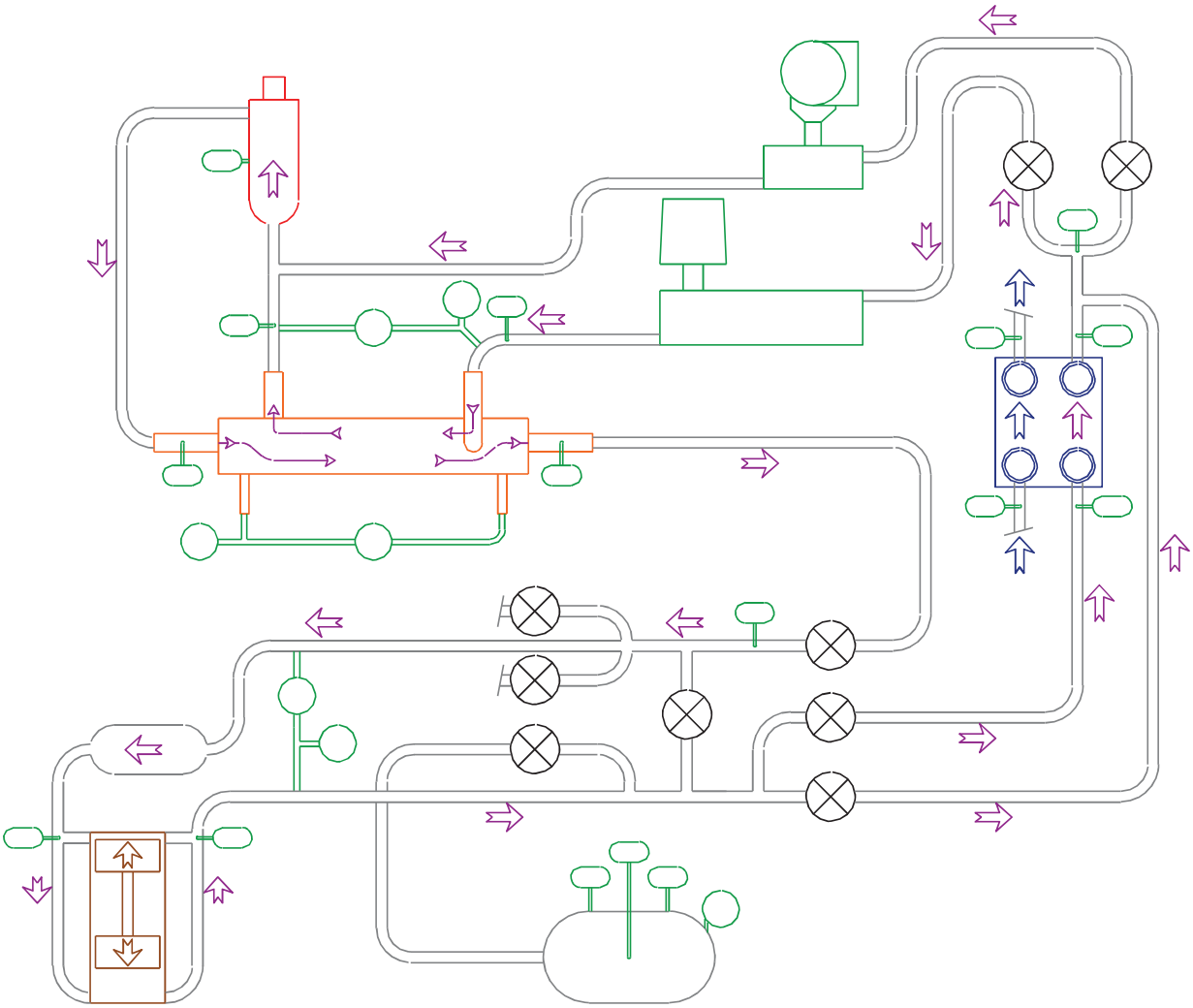

Figure 169: UW Madison s-CO_2 loop diagram

Diagram of the s-CO_2 loop facility at the UW. Flow, indicated by ⇒, is driven by the reciprocating compressor in the bottom-left of the diagram. The compressor empties CO_2 into a large reservoir at the bottom of the diagram. Manually controlled needle and ball valves, marked as ⊗, are used to control flow in the CO_2 loop. The recuperator in the center-left of the diagram is driven by an annular resistance heater at the top-left. Cooling of the CO_2 flow is provided ahead of the recuperator by a water-cooled brazed-plate chiller in the center-right of the diagram. Temperature, pressure, and flow instrumentation exist throughout the loop and within the recuperator.

Flow was split between two loops, the recuperator loop and a bypass loop. The recuperator loop is shown in Figure 169, where flow moved from the compressor outlet through both passes of the recuperator and was throttled down to return to the compressor inlet. The bypass loop skipped the recuperator with compressor output being allowed to pass through the bypass valve directly back to the compressor inlet. The inclusion of the bypass loop allowed for control of mass flow through the recuperator and was useful during low flow experiments. In this way the compressor could be run at or

near full power. Most CO_2 was pumped through the bypass loop to create a consistent source of pressure drop and drive flow through the recuperator. At low mass flows the recuperator system tapped this pressure drop to maintain consistent control of mass flow. When higher mass flow through the recuperator was desired, the bypass loop was shutoff and all flow was directed though the recuperator. Flow then being regulated by adjusting compressor power.

Heating and cooling of CO_2 is needed to drive recuperator systems. A 5 kW water-cooled brazed-plate heat exchanger made by GEA FlatPlate was used as a CO_2 chiller. Building chilled water at 18◦C was used on the water side of the chiller and CO_2 cooling was controlled by selectively passing some CO2 flow through the chiller and the rest around the chiller. The chiller was placed before the recuperator so that the cold side of the recuperator can be properly cooled. Pressure within the brazed-plate chiller was limited to 450 psi and thus was the original limit on pressure in the system. Later experiments replaced the brazed-plate chiller with a PCHE heatexchanger so that system pressures in excess of 2200 psi could be achieved. Heating was provided by a 6 kW Watlow cartridge heater powered by variable voltage AC current. The cartridge heater was mounted within a 1” schedule 40 pipe surrounded by a 2” schedule 40 pipe. The heater was positioned on the hot side of the recuperator. With CO_2 flowing between the two concentric pipes, a 54” long heated region of annular flow was created. With a large area of heat transfer this heater arrangement could heat up to 6 kW for mass flows in excess of 0.019 kg/s. At lower mass flows convective heat transfer to the CO2 limited the amount of power that could be put into the heater.

2.4.2 Recuperator experimental bay

The recuperator experiment bay consisted of the recuperator and its instrumentation. Plumbing around the recuperator experiment bay contained break points so that minimal re-plumbing was required when swapping recuperators. Located in a separate mount extending off the side of the CO_2 loop rig, the recuperator could be easily replaced and re-plumbed. Plumbing consisted of 1/2” 316 stainless steel tubing with 1/4” tubing used for pressure transducer connections. A schematic of the recuperator and its plumbing is shown in Figure 170. In this figure the position of thermocouples and the linking of pressure transducers is illustrated.

Control of mass flow through the recuperator was achieved with needle valves upstream of the experimental bay. The flow through the 1st and 2nd recuperator passes was balanced by controlling flow through the 1^{st} recuperator pass and having the option for some CO_2 flow to bypass the 1st pass and directly go to the heater and 2nd pass. In practice this balancing option was not utilized and only flow through the 2^{nd} pass was

used in pressure drop experiments. Equal flow through the 1st and 2nd passes (no bypass) was used for recuperator testing.

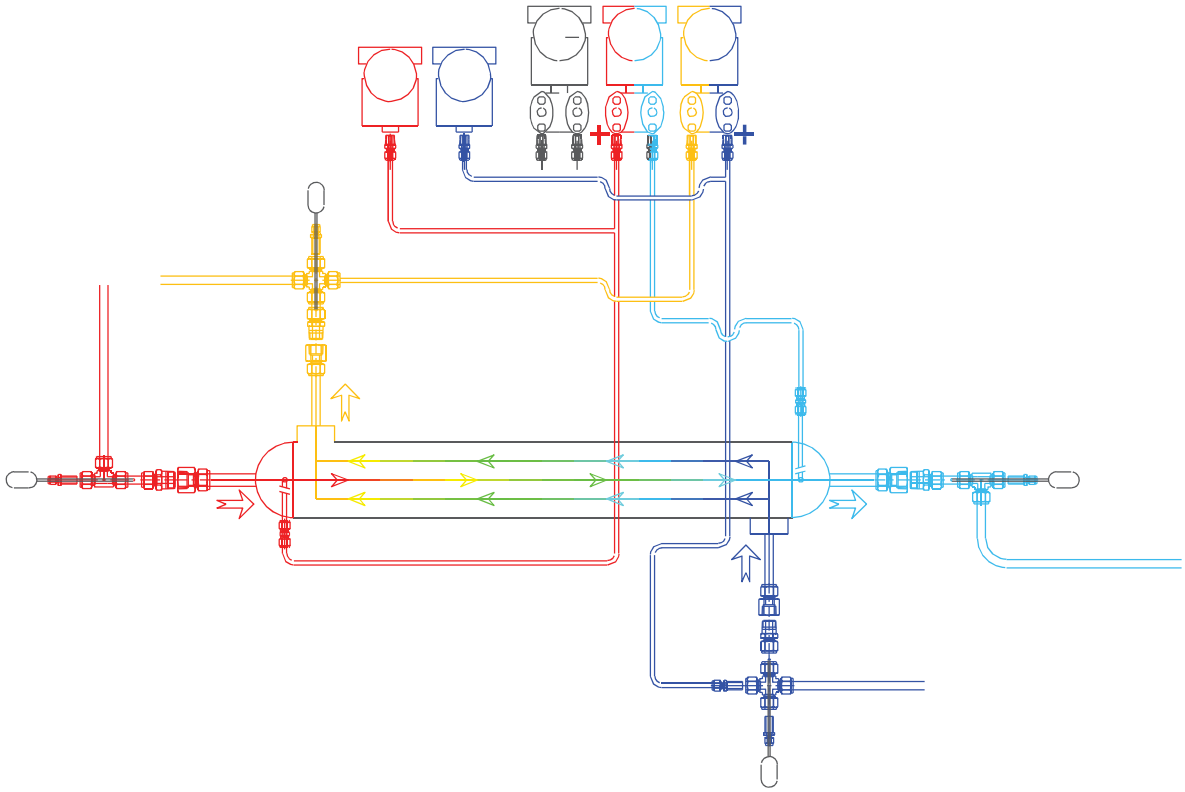

Figure 170: Recuperator experiment bay diagram

Diagram of the recuperator experimental bay within the s-CO_2 loop. Flow enters the 1st pass (cold side) of the recuperator from the inlet line in the bottom-right of the diagram, passes through the recuperator via two channel, and leaves in a heated state through the outlet line in the top-left of the diagram. After being heated, flow enters the 2nd pass (hot side) of the recuperator from the inlet line on the left, passes through the recuperator through a singular central channel, and leaves in a cooled state through an outlet line. Thermocouples are embedded within the headers of the four inlets and outlets. Differential pressure transducers DP5 and DP6 measure pressure drops across headers of the 1st pass (cold side) and 2nd pass (hot side) respectively. Absolute pressure transducers P9 and P10 measure pressure within the headers of the 1st pass (cold side) inlet and the 2nd pass (hot side) inlet.

There is considerable room for expansion in the recuperator experiment bay. Besides the four dedicated pressure transducers, 32 thermocouple reading slots, 4 DC trace heating slots, and 3 AC trace heating slots are available for use. This allows for flexibility in future recuperator experiments. Instruments within the recuperator experiment bay are read and

logged by a separate NI process than those within the CO_2 loop in order to simplify programming changes between recuperator experiments.

2.4.3 Instrumentation

Thermocouple instrumentation was placed throughout the CO_2 loop and the recuperator experiment bay. Large 0.125” thermocouples were used to measure flow temperature. Small precision 0.032” diameter thermocouples were used for embedded measurement of internal recuperator temperatures. These embedded thermocouples are inserted into holes in the recuperator along with a conductive nickel & oil thermal paste to improve reading accuracy. Other thermocouples are directly spot welded to components to get rough wall temperatures. Table 56 gives a list of all thermocouples, their size, and location within the facility. Location of all but the embedded thermocouples are shown in Figure 169.

Table 56: List of Thermocouple Instruments in UW sCO_2 loop

Label	Thermocouple Type	Location
TC1 TC2	0.125” sheathed Omega® K-type	Compressor inlet Compressor outlet
TC3	spot-welded Omega® K-type	Surge Tank wall 1
TC4	0.125” sheathed Omega® K-type	Surge Tank interior
TC5	spot-welded Omega® K-type	Surge Tank wall 2
TC6 TC7 TC8 TC9 TC10	0.125” sheathed Omega® K-type	Chiller CO_2 inlet Chiller CO_2 outlet Cooled CO_2 1^{st} pass (cold side) inlet 1^{st} pass (cold side) outlet
TC11	spot-welded Omega® K-type	Heater wall
TC12 TC13	0.125” sheathed Omega® K-type	2^{nd} pass (hot side) inlet 2^{nd} pass (hot side) outlet
TC14 TC15	... ...	Throttle expansion chiller water inlet
TC16	... ...	chiler water outlet

TC17-24	0.032" sheathed Omega® K-type	Embedded, recuperator interchannel wall
TC25-32	... ...	Embedded, recuperator exterior wall

Coriolis meters were placed between the CO_2 loop and recuperator experiment bay. The units used were a Siemens Sitrans F 2100 and an Endress-Hauser Cubemass meter. Both are 6 mm ID Coriolis meters with a measurement range of 0-3600 kg/s and are setup to operate in the gas phase. While capable of reading and indicating mass flow and density simultaneously, the Sitrans F 2100 meter could only transmit data for one reading at a time. On the other hand the Cubemass meter could transmit both mass flow and density and was thus placed on the 2nd pass line so that density readings could be used in pressure drop tests. The Sitrans meter was placed on the 1st pass line since only mass flow readings were necessary for recuperator tests. Meter characteristics and location are summarized in Table 57. The placement of the Coriolis meters are shown in the loop diagram in Figure 169: UW Madison s-CO_2 loop diagram.

Table 57: List of Instruments in UW sCO_2 loop

Label	Instrument Make	Instrument Range	Location
Flow1 Density2 Flow3 Density4	Sitrans F 2100 Sitrans F 2101 CubeMass CubeMass	0-3600 [kg/s] 0-2000 [kg/m^3] 0-3600 [kg/s] 0-2000 [kg/m^3]	1st pass line 1st pass line 2nd pass line (bypass) 2nd pass line (bypass)
DP5	Sitrans P, differential	0-5 [bar]	across 1st recuperator pass (cold side)
DP6	Sitrans P, differential	0-5 [bar]	across 2nd recuperator
DP7	Sitrans P, differential	0-30 [bar]	across Compressor
P8	Rosemount	0-150 [bar]	Compressor outlet
P9	Sitrans P, absolute	0-400 [bar]	1st recuperator pass (cold side) inlet
P10	Sitrans P, absolute	0-400 [bar]	2nd recuperator pass (hot side) inlet

Pressure transducers were used to measure absolute pressure and pressure drop throughout the system. Most units were Siemens Sitrans P pressure traducers capable of indication and transmission of pressure readings. One unit was a Rosemount pressure transducer only capable of reading transmission. All pressure transducers were mounted

on a level rack to eliminate hydraulic differences between the meters. The make, maximum range, and location of all pressure transducers is given in Table 57 while their positions are diagrammed in both Figure 169 and Figure 170.

2.4.4 Experimental pressure drop measurements

Pressure drop experiments were performed with the Airfoil PCHE and friction factor data was obtained for Reynolds ranging from Re 295 – 61480. Pressure drop experiments were performed at room temperature and steady state so as to keep CO_2 properties uniform through the heat exchanger. Pressure data taken in 5 min sets at 2 Hz was the used to calculate the friction factor and Reynolds number of the flow within the airfoil channels.

The Darcy friction factor of the central channel, f, is calculated from experimental density and pressure drop measurements. The total pressure drop, ΔP, is related to the Darcy friction factor, f, as follows,

$$\Delta P = f \frac{L}{D_h} \frac{1}{2} \rho \mathrm{v}^2 \tag{2.4.1}$$

where ρ, v, and ΔP are directly measured across the channels of the Airfoil heatexchanger. Since pressure and temperature do not vary greatly across the channels it is reasonable to assume that ρ is constant along the length of the channels and equal to that measured at the inlet by the Coriolis meter. Along with measuring the density, the Coriolis meter measures mass flow, which when combined with the known cross sectional area of the channels, A_c^*, leads to an accurate measurement of velocity, i.e. $v = \dot{m} / \rho A_c^*$. The cross-sectional of all channels is A_c^* = 283.0 mm^2. A differential pressure transducer accurately measures the ΔP from header-to-header across the channel.

The Reynolds number of the flow through the channels was also determined. The general form of the Reynolds equation can be reduced to a form utilizing the known experimental mass flow, ṁ, as follows,

$$Re = \frac{\rho \mathrm{v} D_h}{\mu} = \frac{\dot{m} D_h}{A_C \mu} \tag{2.4.2}$$

where the hydraulic diameter, D_h, of the central channel is 1.620 mm. Viscosity, μ, is determined using a viscosity correlation provided by Fenghour et. al. (1998). When calculating Reynolds of the channels, μ is taken as the viscosity of CO_2 at the state

defined by the average temperature within the channels and the density measured at the inlet by the Coriolis meter.

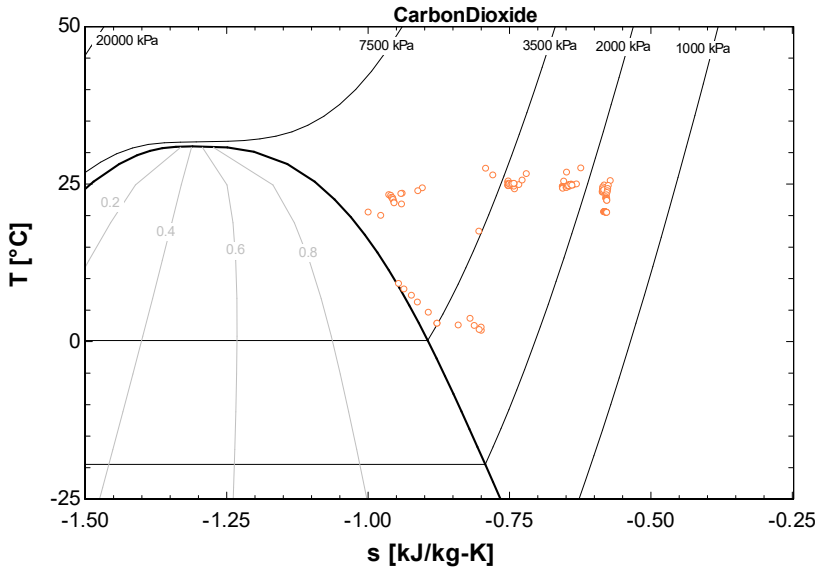

Figure 171: points of operation during pressure drop testing of the Airfoil recuperator.

In order to get a full range of Reynolds numbers, tests had to be run at a variety of pressures. High Reynolds tests used pressures nearer the critical pressure, ranging from 3.5-4.5 MPa, and corresponding densities of 70-150 kg/m^3. These are the points close to the vapor dome in Figure 171: points of operation during pressure drop testing of the Airfoil recuperator.. Low Reynolds tests had to be performed at lower pressures and densities as velocity in the system could only be throttled down if the operation point was away from the vapor dome, or else expansion in throttle valves would cause a two phase condition to occur in the Airfoil recuperator. The low Reynolds points were made at pressures ranging from 1.7-3.0 MPa and ρ of 34-48 kg/m^3.

The resulting Darcy friction factor data is shown in Figure 172. Instrument measurement error was propagated through all calculation of Re and f. High error in f at low Re resulted from using an oversized, and less accurate, 0-500 kPa differential pressure transducer. Ultimately it was decided not to retake the lower Reynolds data with a more accurate pressure transducer at the data is both far too low in Re to be practically applicable, and most likely in the transition region and therefore unrepeatable between tests.

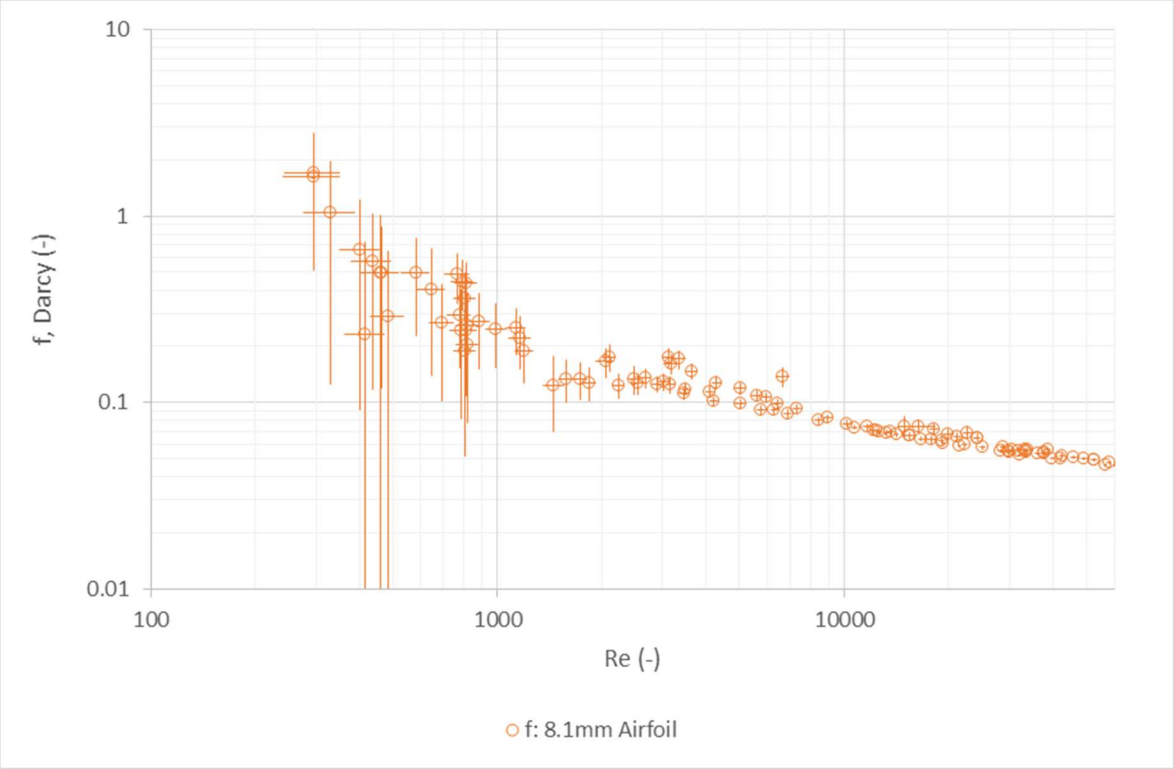

Figure 172: Darcy friction factor of Airfoil Recuperator channels

2.4.5 Experimental heat transfer measurements

Heat transfer experiments were performed with the Airfoil PCHE and Colburn heat transfer coefficients (j) were obtained for Reynolds ranging from Re 1000 – 7816. Heat transfer experiments were performed with equal mass flow on both the hot and cold sides of the recuperator. Measurements were made at steady state so as to keep CO_2 properties uniform through the heat exchanger. Data was taken in 10 min sets at 2 Hz and was used in calculating the Colburn factor and Reynolds number of the flow within the airfoil channels.

The method of determining the heat transfer coefficient was the gross-UA method. It is a simple method of determining j that does not account for spatial variations in the heat transfer coefficient caused by CO_2 property variation. It is referred to as a gross method because it only accounts for external measurement of s-CO_2 conditions and ignores the effect of locally varying s-CO_2 properties along the length of the heating and cooling channels.

The total heat transfer rate is the first quantity determined from the experimental data. Heat is added to the cold 1st pass of the recuperator and removed from the hot 2nd pass. The heat transfer rate is found through the enthalpy change in either flow. Enthalpy at the

inlets and outlets of the recuperator channels is determined using the Span-Wagner equation of state for CO_2 [5]. Temperature and pressure are used to find the state of s-CO_2 since they are both directly measured in the inlet and outlet headers of each recuperator channel. From experimentally measured variables, heat flow into each channel is simply,

$$\dot{q}_C = \dot{m}_C\left[i\left(T = T_{C,out}, P = P_{C,out}\right) - i\left(T = T_{C,in}, P = P_{C,in}\right)\right] \quad (2.4.3)$$

$$\dot{q}_H = \dot{m}_H\left[i\left(T = T_{H,out}, P = P_{H,out}\right) - i\left(T = T_{H,in}, P = P_{H,in}\right)\right] \quad (2.4.4)$$

In a well-insulated recuperator $\dot{q}_C$ and $\dot{q}_H$ are identically since all heat flows from one side of the recuperator to the other and are not lost elsewhere. Such insulation was achieved in the recuperator as $\dot{q}_C$ and $\dot{q}_H$ never differed in magnitude by more than 1-4%.

The capacitance flows,$\dot{C}$ for both the cold (1st pass) and hot (2nd pass) are determined from the recuperator power $\dot{q}$ and each channel's inlet and outlet temperature.

$$\dot{C}_C = \frac{\dot{q}}{T_{C,out} - T_{C,in}} \; ; \; \dot{C}_H = \frac{\dot{q}}{T_{H,in} - T_{H,out}} \quad (2.4.5)$$

the balance of these capacitance flow is best expressed through the capacitance ratio,

$$C_r = \frac{\dot{C}_{min}}{\dot{C}_{max}} \quad (2.4.6)$$

The Prandtl number used in evaluating j is taken at properties average between the inlet and outlet of both streams.

$$Pr_C = \frac{0.5\left(\mu_{C,in} + \mu_{C,out}\right) * 0.5\left(c_{p,C,in} + c_{p,C,out}\right)}{0.5\left(k_{C,in} + k_{C,out}\right)} \quad (2.4.7)$$

$$Pr_H = \frac{0.5\left(\mu_{H,in} + \mu_{H,out}\right) * 0.5\left(c_{p,H,in} + c_{p,H,out}\right)}{0.5\left(k_{H,in} + k_{H,out}\right)} \quad (2.4.8)$$

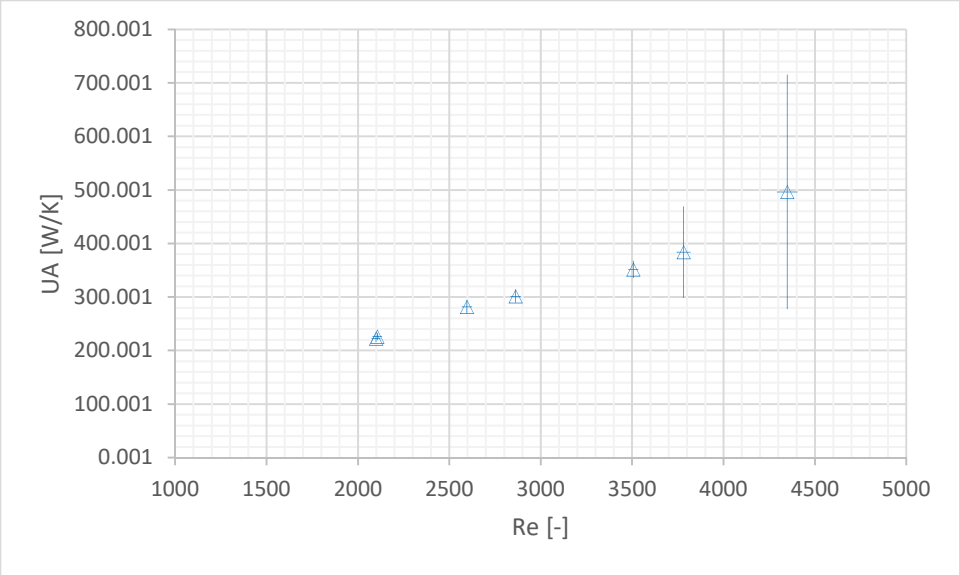

Figure 173: UA vs. Reynolds for Airfoil Recuperator

where c_p is found using the Span-Wagner equation of state [5] while k is determined in the manner described by Vesovic et. al. [6]. Viscosity μ is found using a correlation presented by Fenghour et. al. [4].

Performance of the recuperator using the effectiveness-NTU method (ε-NTU). When evaluated over the entire recuperator, the UA of the recuperator is found. Effectiveness of the recuperator ranged from ε = 0.87 to 0.94 with an average UA ≈ 323 W/K. A plot of UA vs. Reynolds number is shown in Figure 173. UA and effectiveness are calculated as follows:

$$\varepsilon = \frac{\dot{q}}{\dot{C}_{min}(T_{H,in}-T_{C,in})}; \quad Ntu = \begin{cases} \frac{ln\left(\frac{1-\varepsilon C_r}{1-\varepsilon}\right)}{1-C_r}, & C_r < 1 \\ \frac{\varepsilon}{1-\varepsilon}, & C_r = 1 \end{cases}; \; UA = Ntu * \dot{C}_{min} \tag{2.4.9}$$

The conventional form of the Colburn heat transfer coefficient equation can be rewritten in terms of UA, the cross section of flow in the channel A_c, and total surface area of the channel A_s.

$$j = \frac{hPr^{2/3}A_c}{\dot{C}} = UA\frac{A_c}{A_s}\frac{Pr^{2/3}}{\dot{C}} \tag{2.4.10}$$

Colburn heat transfer coefficients were the same for both the hot and cold side of the Airfoil recuperator as both channels were designed to have the same effective surface area. Colburn j results over Reynolds numbers tested in the Airfoil recuperator are shown in . Large errors at higher Re stemmed from errors in measurement at the cold side inlet.

As the recuperator's cold side was at room temperature the Airfoil recuperator would pinch at high mass flows. Further testing will put two recuperators in series so that pinching can be kept to a low temperature recuperator while experimental measurements can be made on the high temperature recuperator.

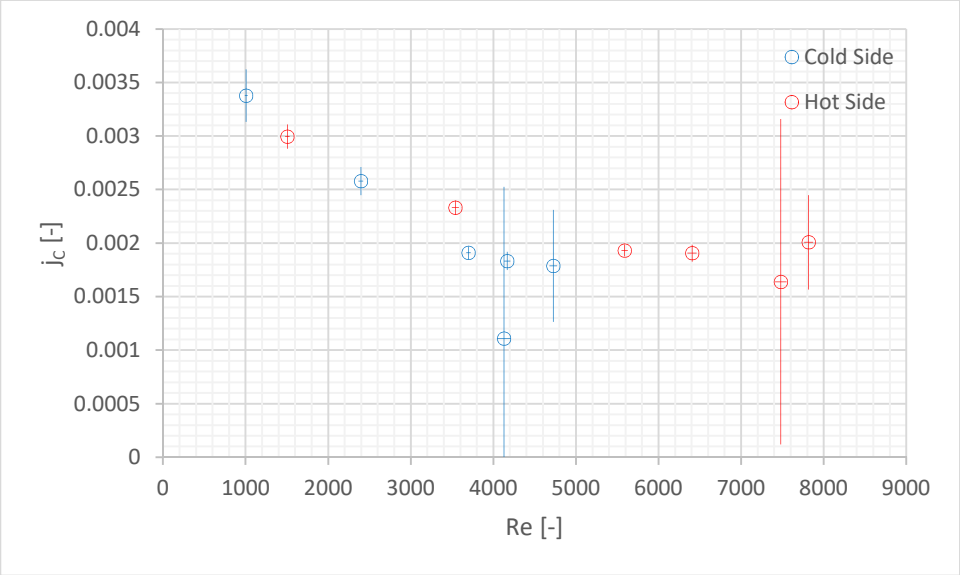

Figure 174: Colburn j heat transfer vs. Reynolds for the Airfoil Recuperator

2.5 Measurement of Thermal Gradients and Strain in PCHEs

The airfoil and zig-zag recuperator built at UW Madison for heat transfer performance analysis are also designed for measurement of thermal strain. Fiber optic temperature probes are built into the central instrumentation channel shown in Figure 175, allowing temperature readings to be made along the length of the recuperator at 0.6125 mm intervals. Eight fiber probes are laid side-by-side as shown in Figure 175. In this way a planar map of temperatures can be made within the recuperator.

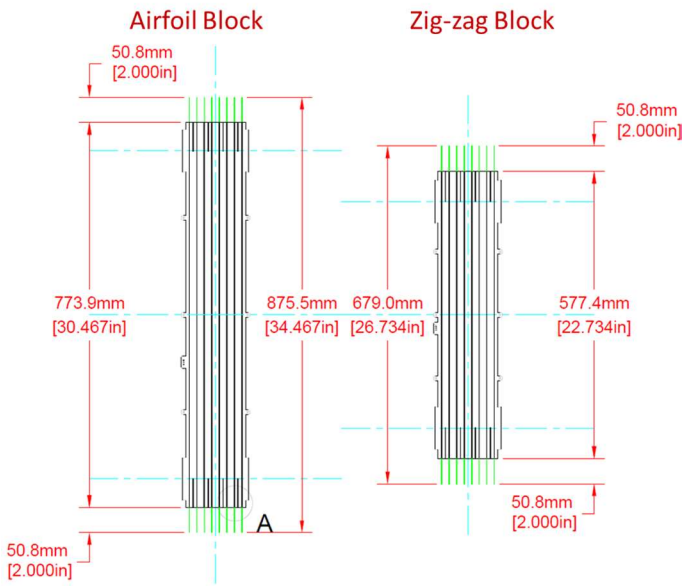

Figure 175: Fiber optic instrumentation layout in the airfoil and zig-zag recuperators. Fibers are highlighted in green.

The fibers read an internal temperature of the PCHE block in real-time, enabling thermal stresses in the block to be determined. By recording thermal transients during cycling tests experimental thermal stress histories can be recorded. These can be compared directly to FEA models of the system to verify our FEA BPVC certification methods.

An in house code, FiberMap, for obtaining and interpret fiber data was created. Data acquisition consists of a couple of purpose built LabView codes that interface with the Luna ODiSI fiber sensor system to create .csv databases of experimental data. A set of mat lab scripts within FiberMap are then used to read and assemble the .csv database, convert fiber data to temperature readings, and create final 2D maps of temperature in the recuperator over time. An example of a temperature map made at a low temperature run is shown in Figure 176.

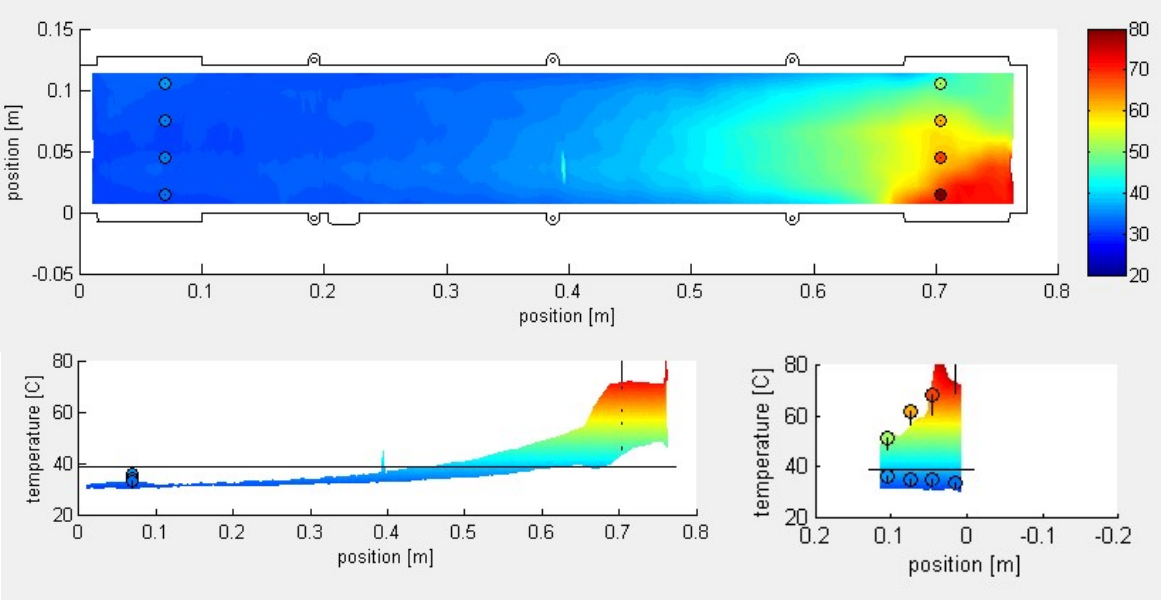

Figure 176: Temperature distribution in Airfoil recuperator during a high mass flow test (Re 7500 in hot-stream, Re 4130 in cold-stream). As seen from above (top), in side profile (bottom left), and end profile (bottom right)

Thermal stress concentrations have been identified in the Airfoil recuperator during high flow low efficiency tests. An example of steady state temperature distribution is shown in Figure 176. The temperature gradient of this distribution is shown in Figure 177.

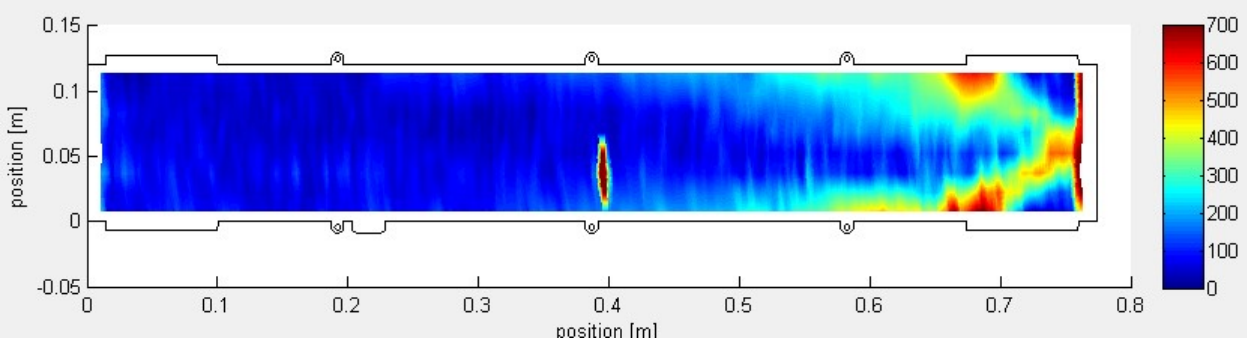

Figure 177: Temperature gradient in Airfoil recuperator during a high mass flow test (Re 7500 in hot-stream, Re 4130 in cold-stream). Units are K/m. Fiber reading noise creates some non-physical gradient readings (located at x = 0.4 and x = 0.78).

As mass flow is increased in the recuperator to bulk of heat transfer shifts toward the hot side and the corresponding inlets. At the hot side of the recuperator flow entering from the hot-stream channel inlet enters at a right angle, completing a 90 degree turn into the counterflow portion of the recuperator. Simultaneously cooler flow in the cold-stream channels are leaving the counterflow portion of the recuperator and completing a mirroring 90 degree turn out of the recuperator.

Thermal stress concentrations are clearly visible at the entrance of the hot-stream and exit of the cold-stream (as seen at x = 0.68 in Figure 177). These occur because local cross-flow conditions exist within the inlet and outlet of the recuperator.

2.6 Sodium heated sCO2 facility

2.6.1 Sodium heated sCO_2 facility

The University of Wisconsin Madison has begun to design and built a sodium heated sCO_2 facility. The facility consists of a new sCO_2 loop based around a high pressure triplex pump and a set of PHCE heat exchangers to interface with an existing sodium loop. A heater uprate in the existing sodium loop is planned to provide sufficient power for the sCO_2 experiments. A diagram of the system is shown in Figure 178. On the CO_2 side the system consists of the triplex pump, an expansion volume, a recuperator, a sodium-sCO2 heat exchanger and a chiller. The sodium side consists of an electromagnetic pump, expansion reservoir, and a 5 kW cartridge heater as show in Figure 179.

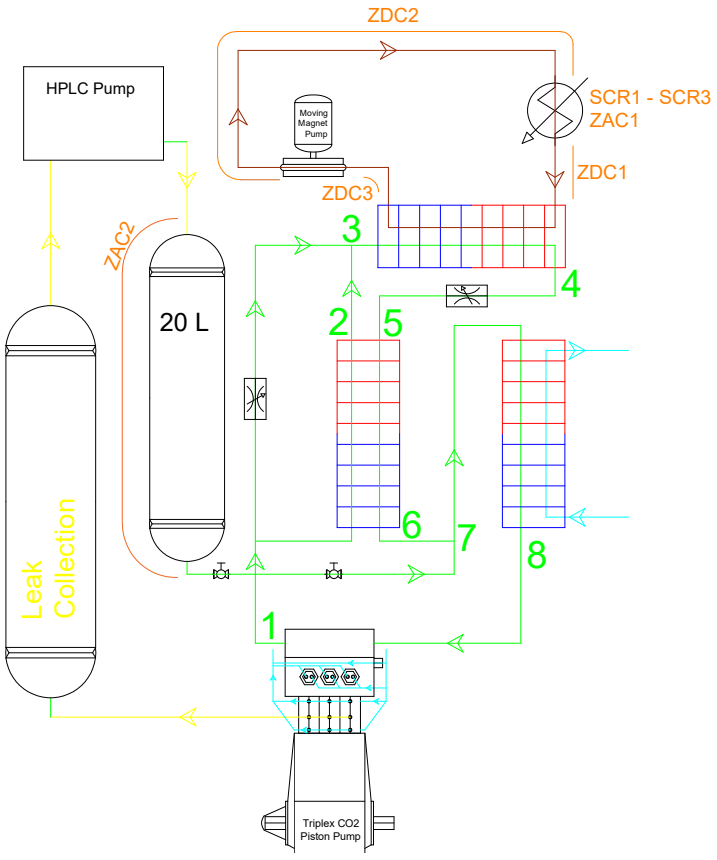

Figure 178: Sodium-sCO_2 Facility Diagram

The triplex pump is specifically designed for sCO_2 applications and features high pressure cooled seals. Driven by a 30 kW variable speed motor, the triplex pump operates at 30 MPa with flow rates up to 0.9 kg/s. The pistons are sealed using CO_2 bled off of the main system and expanded into a catch reservoir (seen on the left in Figure 178). CO_2 from the catch reservoir is then compressed back up to system pressure using an HPLC pump. Cooling water is used to cool the piston bores and the pump manifold.

Heatexchangers used in the system will be a mix of existing and new PCHEs. The sCO_2-sCO_2 recuperator (pictured center in Figure 178) will be the existing airfoil recuperator. The chiller is a re-purposed heatexchanger that was tested for an industry partner. The sodium to sCO_2 heat exchanger has to be purpose built. It will be made of alloy 800H so that it can operate at temperatures of up to 750 C. The sodium heat exchanger will feature the larger hydraulic diameter ShimRex^{tm} channels of our industry partner CompRex LLC. These channels have more flexibility in hydraulic diameter and cross-sectional area, enabling the sodium and sCO_2 sides to be more easily balanced.

The sodium facility will be upgrade with additional heating to bring its power up to 10 kW. The existing facility is shown in Figure 179. The sodium loop is constructed of 316 stainless steel and being at low pressure can be brought up to 700 C. It features a moving magnet EM pump that can achieve 40 GPM of flow along with 20 psi of head. Oxide control is maintained with a 0.82 L cold trap. Mass flow is measured using an electro-magnetic flow meter. The sodium-sCO_2 heatexchanger will be plumbed between two taps that currently serve a Diagnostic loop.

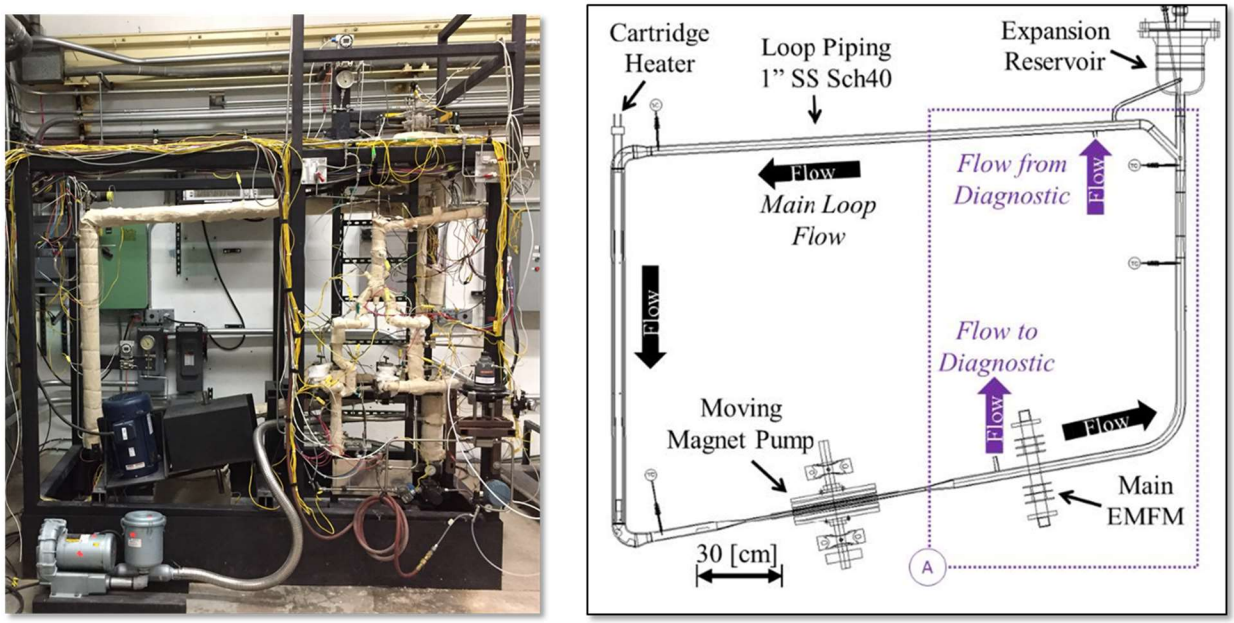

Figure 179: Sodium loop facility at University of Wisconsin Madison

3. Diffusion Bonding Techniques Study and Post-Test Inspection

3.1 Diffusion bonding parameters

3.1.1 Literature survey

Generally, the diffusion bonding process includes several parameters such as pressure, temperature and time. The Heatric developed specific bonding procedures and qualification for ASME certification. It is shown that the pressure imposed on the stack of metal plates is critical to the grain growth at bond interfaces. Appropriate amount of pressure leads to the interface deformation, thus allowing its breakdown and promoting the grain growth. The grain growth rate is related to the temperature and time. The new grains may grow rapidly at first, but gradually slow down, as the analytical model indicates, which is shown below:

$$d^n - d_0^n = k \exp\left(-\frac{Q}{RT}\right) t \tag{3.1.1}$$

Insufficient amount of time can possibly result in incomplete bonds at interfaces, as demonstrated by INL. Besides, the grain-growth process is sensitive to temperature changes. However, it is unclear that whether a higher temperature could significantly promote the grain growth once a sufficient temperature “threshold” is reached. Too high temperature may induce excessive grain growth. The common operating temperatures for alloy 617 are 1120 C or 1150 C. It should be noted that the melting point is in the range of 1332-1380 C.

The diffusion bonding parameters for another alloy H230 demonstrated by computational models shows the similar trend. The model assumes that the surface preparation creates a series of long parallel ridges, which inevitably leads to voids when two binding surfaces are bonded. The input of temperature and pressure to the model yield the output of the required time to close the voids and eventual bonding area percentage. Below shows the relationship between the bonding parameters and area bonded for Ni-plated H230. It generally indicates that the large percentage of bonded area requires longer hours of the process at the same pressure, which is similar to what is found to INL tests on alloy 617 diffusion bonding.

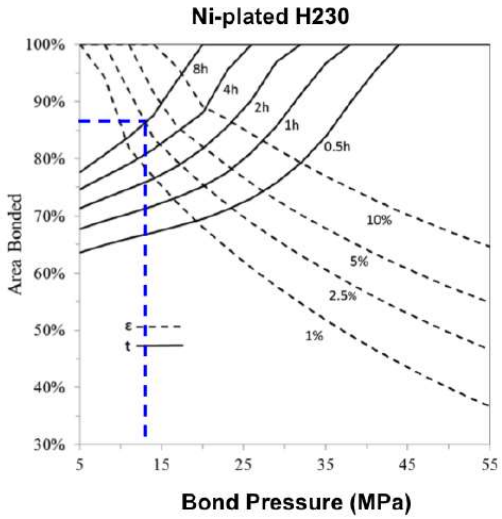

Figure 180. Area bonded as a function of pressure during the diffusion bonding process for Ni-Plated H230

Moreover, another two important bonding parameters are the atmosphere during the diffusion-bonding and the presence of Ni-interlayer. Regarding the atmosphere, the bonding is normally carried out in a vacuum environment such that the excessive formation of metal oxides or nitrides at bonding interfaces could be prevented. The impurity control is also important. As to the use of Ni-interlayer, it becomes an extremely important factor in the joint tests demonstrated in INL. In fact, the grain growth across the bond line generally did not happen with the absence of Ni-interlayers no matter what other bonding parameters changed, as shown in Figure 181. This interesting finding indicates that Ni-interlayers play an important role in diffusion bonding, but meanwhile deteriorate the mechanical strength at the bonding interfaces. Therefore, it is critical to know the exact amount of Ni-interlayers used in diffusion bonding process.

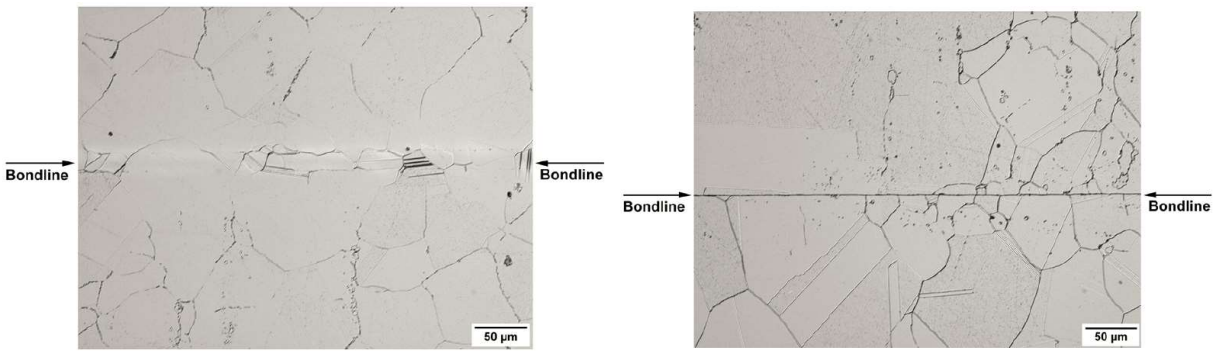

Figure 181. Inspection on the bond line with (left) and without Ni-interlayer (right) at the diffusion bonding conditions of 1120C, 15 MPa and a 3 hour hold time. Inspections were carried out in INL.

Other essential parameters relevant to the diffusion bonding include the surface preparation of alloys prior to the diffusion bonding and Post Bonding Heat Treatment (PBHT), etc. According to the Heatric experience, the surface preparation needs to remove any dirt and grease as well as reduce the thickness of oxide layers to ensure acceptable surface finish. However, this procedure is the least controllable and the effect has to be evaluated for individual diffusion bonding process. Concerning the PBHT, it is used to achieve the desired microstructure and properties for some alloys. This process involves controllable parameters such as temperature, time and cooling rate, which might be specifically established for different materials. These two diffusion-bonding parameters particularly mentioned in the diffusion bonding procedure specification (DBPS) need more studies on selected materials of interest.

3.1.2 Etching defects in the diffusion bonding process

As the manufacturing step preceding diffusion bonding in the creation of Printed Circuit Heat Exchangers, chemical etching of desired channel geometries greatly affects the quality of the diffusion bond. Mask Leak Intrusion is an etching defect that directly affects the quality of the bonded PCHE by introducing crack initiation sites at the diffusion bond interface. Although large Mask Leak Intrusion defects can be detected on etched plates prior to bonding, the ability to detect small defects on increasingly larger etching jobs is not guaranteed.

Mask Leak Intrusion was noticed during the etching of plates for UW Madison's Zig-Zag Test Recuperator. The defect occurs along a mask edge when the etching solution is able to penetrate the mask-metal interface and effectively peel back the mask and expand the area being etched as shown in Figure 182. This leads to shallow but wide pans at the top and bottom of etched features which when diffusion bonded manifest themselves as large cracks located at the diffusion bond. Mask Leak Intrusion defects were found through manual inspection of PCHE plates prior to bonding. All plates that were found to contain internal Mask Leak Intrusion defects had to be thrown out and replace with new etched plates. Plates that only exhibited the defect at the periphery were kept as the defects could be fixed with TIG torch. Eternal Mask Leak Intrusion defects at the corners of the UW Madison Zig-Zag Recuperator are shown in Figure 183.

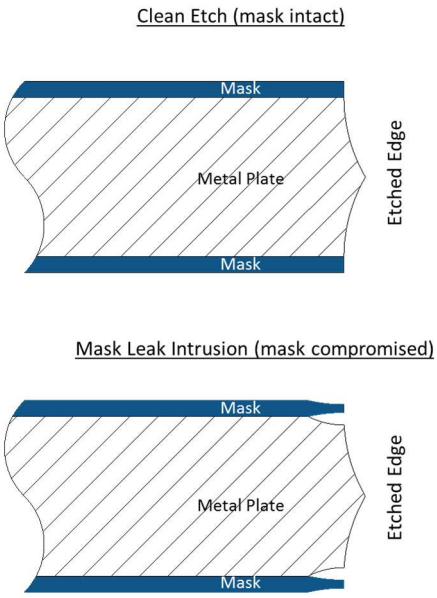

Figure 182: Diagram of Mask Leak Intrusion along the edge of an etched feature

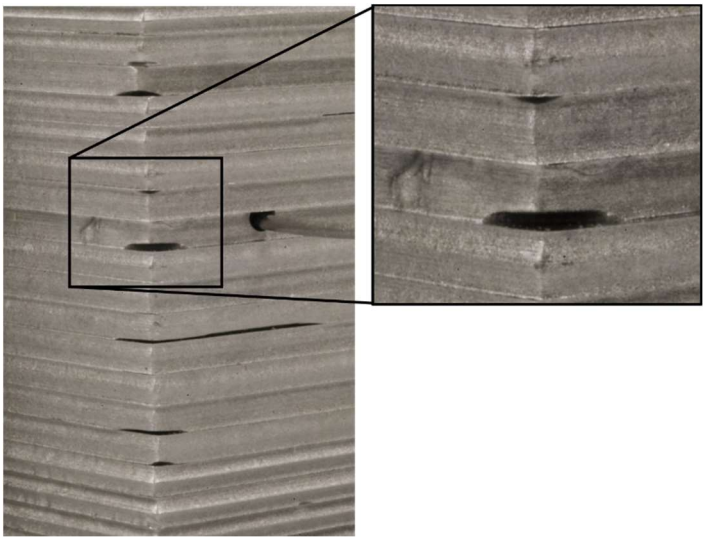

Figure 183: Mask Leak Intrusion defects within corners of UW Madison's diffusion bonded Zig-Zag Recuperator

Perfect etch quality might be difficult to guarantee at the industrial scale as a commercial PCHE would consist of hundreds of etched plates each with multiple square meters of etched channels. At the lab scale etch defects were detectable as each etched plate and the finished PCHE were inspected manually. At the industrial scale automated post-etch inspection would have to be implemented to ensure quality and any defective etched plates will have to be discarded. Detecting and eliminating defective etched plates will drive up the cost of larger PCHEs. This is because etching gets more costly the larger

the area per plate to be etched becomes and more plates will have to be thrown out as the probability of plate ruining etch defects will also scale with plate size. To better understand the industrial scale up of the PCHE an investigation must be made into the probability of etch defect occurrence and how it can be reduced.

3.2 SLA Printed Pressurizations Tests

3.2.1 SLA Printed Pressurizations Tests

Pressurization tests were done on Stereolithographically (SLA) printed air-foil channel specimens. The brittle nature of the SLA plastic allowed for a weakened section that could easily be broken and the transparency of SLA printed parts made observation of failure possible. SLA printed parts are substantially less expensive and quicker to produce than diffusion bonded specimens and thus were favored for initial experiments. The SLA pressurization tests allowed for a quick evaluation of the air-foil design's strength without the need to diffusion bond a specimen.

The test sections produced were made of the Accura60® plastic resin. In the SLA process, a solid part is formed by selectively curing a resin bath by way of two intersecting lasers. In this fashion the part is built up layer by layer. After removal from the printing bath the part is cleaned and flushed with ethanol, dislodging any uncured resin and clearing the interior air-foil channels. To aid the printing of air-foil test sections, pump aided flushing of the interior channel was done for 15min to consistently clear all resins trapped in the microchannels. A freshly printed part, its flushing step, and the final product are shown in Figure 184. After cleaning and flushing the parts are cured in a UV chamber to achieve their ultimate strength. This results in cured Accura60® parts with reported tensile strength of 58-68 MPa.

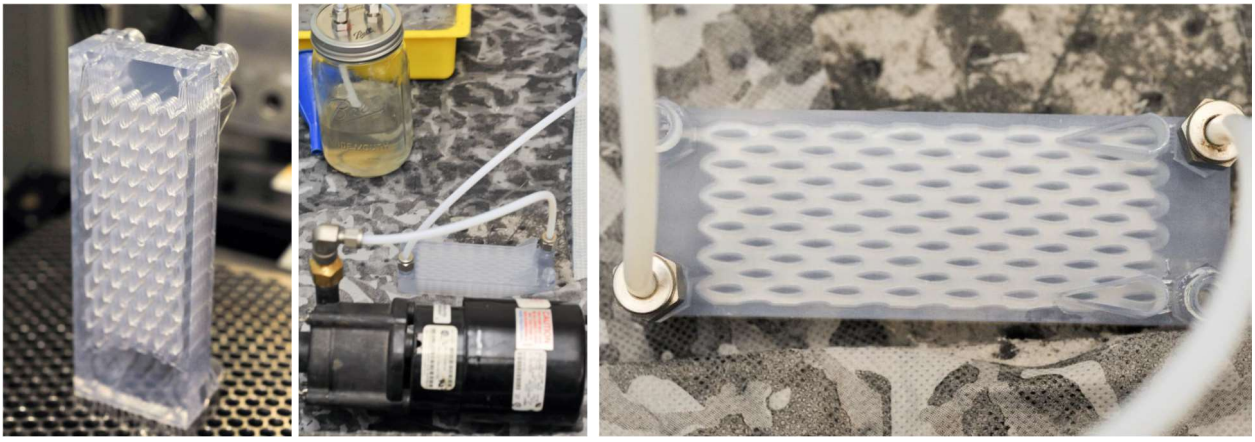

Figure 184:(left) SLA part coming off of printer, (center) flushing uncured resin out of microchannels, (right) final SLA printed air-foil channel test section

A full SLA test section included 11 stacked airfoil channels. Each channel was 12 airfoils wide (43.8mm) and 15 airfoils long (103.5mm) with channel depth of 1mm and an inter-channel thickness of 0.5mm separating each channel layer. Simple inlet and outlet channels were incorporated at the corners of the channel so that alternating channels could be linked together, allowing differential pressurization of the channels. These inlets and outlets also enabled the flushing of the channels prior to the ultimate curing of the SLA parts. The inlets and outlets were channeled out of the SLA block an ended in ¼" Swagelok^{tm} fittings so that the section could be hooked up to fluid lines.

Dissection of one test section revealed the quality of the SLA printed channels, see Figure 185. The SLA process was able to resolve microchannel features down to .0002in. The airfoil shape and filleting can be seen in the cutaway in Figure 185. Printing lines can be seen on the airfoil fillets. These lines are the result of the SLA printing process, as each layer of the part is cured in a plane directly above the previous printing plane and as such there are discontinuous jumps in along the vertical axis. These discontinuities would eventually be problematic in the pressurization failure of the test sections.

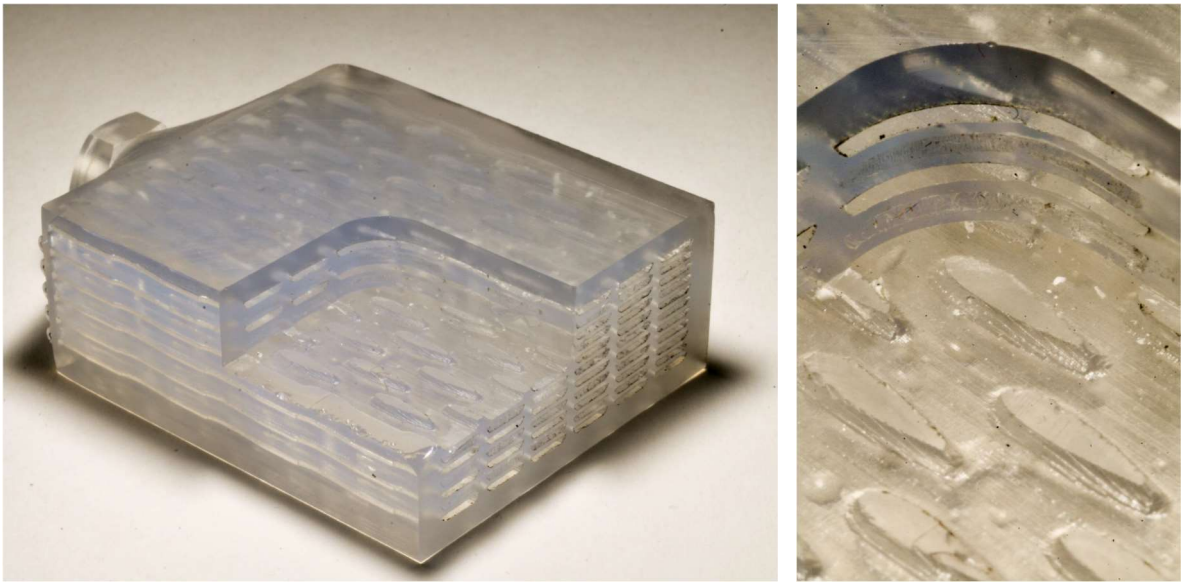

Figure 185: (left) dissected SLA test section (right) close-up of cutaway showing airfoil-channel features

Mechanical modeling of the pressurization of the SLA part predicted interior failure at the airfoil tail when channel pressure reached 262kPa (38psi). The prediction was based off of stress concentrations modeled in ANSYS Mechanical and Accura60's reported ultimate tensile strength of 58-68MPa. Given general conservativeness in the reporting of ultimate tensile strength, the actual strength could be up to 3 times greater than that reported by

the manufacturer of Accura60. Considering a conservative reporting factor of 3, failure should occur at pressures in the range of 262-786kPa (38-114psi).

Pressurization tests were carried out in a pressure test stand, shown in Figure 186. The test stand consisted of pressurization, data recording, camera, and safety equipment. Pressurization equipment consisted of a hydraulic screw for the incremental pressurization of water, a pressure transducer for pressure readings, a line linking the screw and transducer to the test section, and the sealed test section. Signal from the pressure transducer was sent to a LabView^{tm} controller and computer interface which logged pressure data and pressurization rate. Camera equipment was mounted above the test section to monitor failure and attempt to capture the propagation of failure cracks. To aid optical clarity the test section was mounted on top of a light box and the pressurizing water was tinted blue. To keep the operator, cameras, and data logging equipment safe, the pressurization section was housed inside of a Plexiglas box.

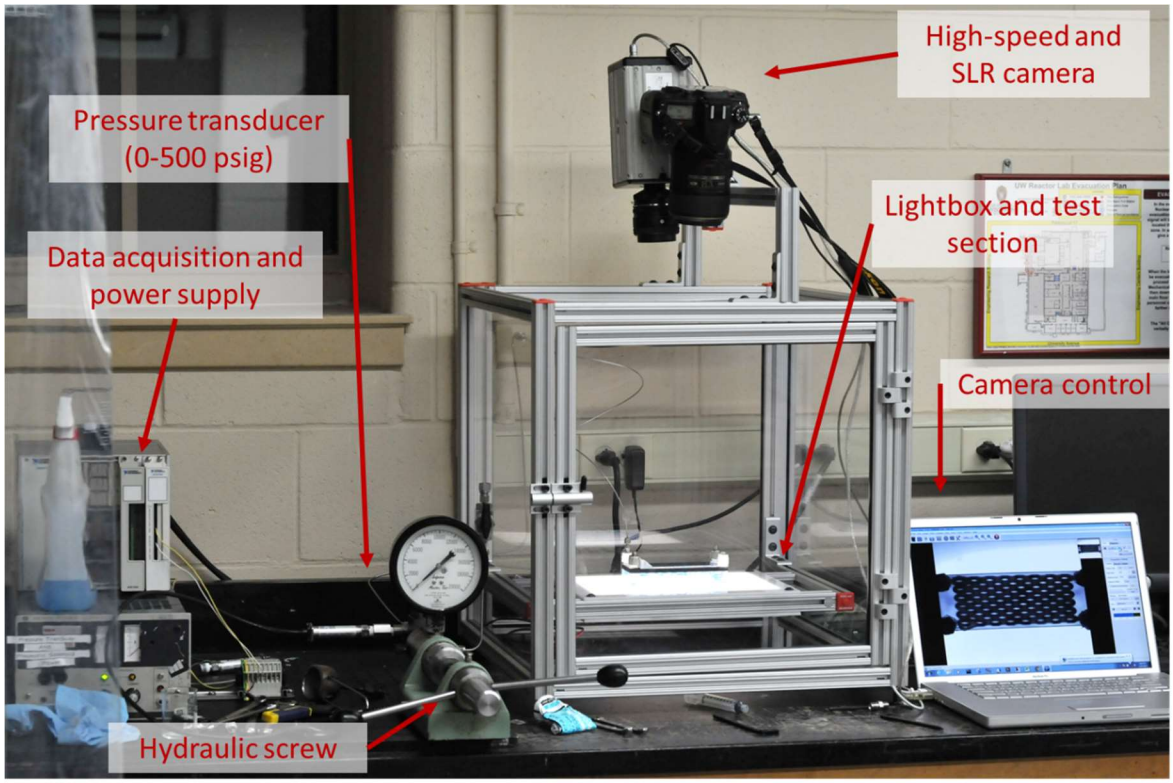

Figure 186: Pressure test system with test section on top of light box inside of Plexiglas containment

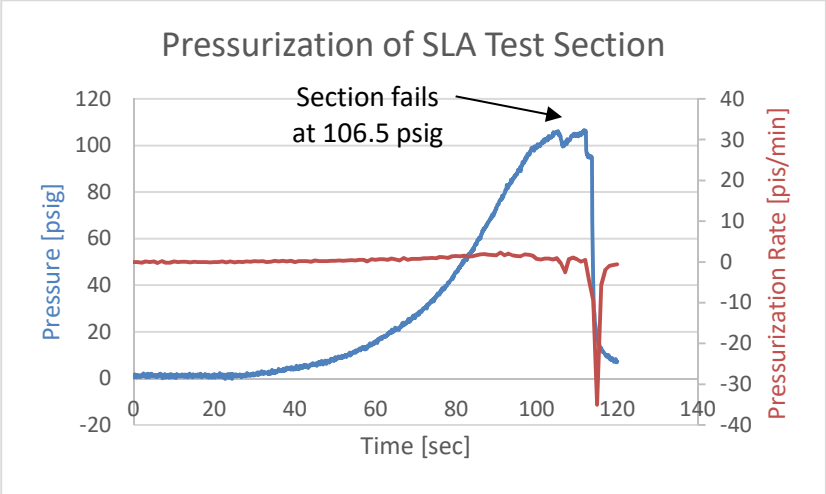

Figure 187: Pressure trace during an SLA test section failure experiment

Pressure data was logged as the test section was pressurized by the hydraulic screw. Traces shown in Figure 188 could be used to determine the failure pressure of the section. In the Figure 188 the pressure trace in psig is shown in blue and the pressurization rate in psig per minute is shown in orange. Throughout the test the hydraulic screw was turned at a constant rate to ensure a steady pressurization rate. Failure was detected by noting the onset of sudden pressurization rate dips, as these indicate the formation of a crack and release of hydraulic fluid. The section was found to fail at 106.5psig, compared to the predicted failure pressure of 38-114psig.though failing in the predicted pressure range, failure was not in the predicted location. Failure was predicted to be in the interior of the section and across the airfoil interface. To the contrary failure of the SLA section occurred at an exterior airfoil and occurred perpendicular to the airfoil interface as shown in Figure 187. This failure occurred because of stress concentrations in minute printing features. The SLA printing process created small discontinuities between successive printing layers which can be seen in the right side of Figure 185. These features created a stress concentration that failed prior to the stress concentration at the airfoil.

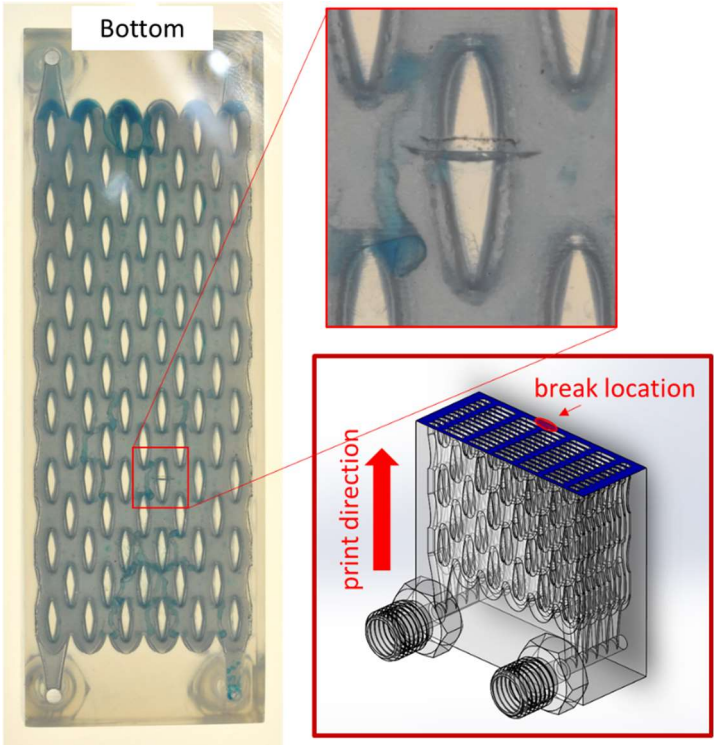

Figure 188: Crack failure in SLA test section occurred on exterior airfoil along printing features

Further pressure tests of SLA printed sections has been stopped as the SLA sections didn't fail in the predicted way and instead failed along minute SLA printing features. This inherit undesired weakness in the SLA printed structure does not work with further pressurization evaluation of the air-foil channel. SLA printed parts could still be used for other applications such as flow visualization and pressure drop experimentation.

3.3 Post-test PCHE Destructive Analysis

3.3.1 Development of Post-Test Inspection Specimen and Procedures

The original goal of the post-test destructive test of the diffusion-bonded matrix integrity is to study the mechanical strength of diffusion bonds after operations of the heat exchanger matrix at elevated temperatures, deformation of the cross-section of pressure-containing boundaries and potential corrosion situation for selected materials and working fluids. The major challenge to achieve that goal is that the fabrication of the diffusion-bonded PCHE is extremely expensive, especially for the construction material of Ni-base alloy. Due to its high up-front cost, the custom-designed PCHE needs to be thermal-hydraulically tested for an extended period of time in order to collect as much data as possible. Before having a new PCHE to be tested, the current designed PCHE will not be used for post-test inspection. An alternative candidate for that purpose is the PCHE recuperator operated in helium flow environment for more than 1000 hours. The

construction material is Inconel 617, diffusion-bonded with Ni-interlayers. It is one of two 617 PCHE recuperators used in the OSU HTHF (high-temperature helium facility), and operated at higher temperature condition. The operating temperatures and pressure for the 617 PCHE recupeator varied during experiments, and the helium flow's impurity was not recorded. This makes it very difficult to develop a correlation between operating parameters and the resulting information such as deformation, creep and corrosion at diffusion bonds. However, the post-test inspection could provide important qualitative information and guidance in future post-test mechanical analysis.

The proposed procedure of the post-test inspection on the 617 PCHE recuperator (higher-temperature one) can be summarized as the following four aspects:

-- SEM material characterization for both the general diffusion bonds and the ones at the pressure-containing boundaries, namely, the flow channels;

-- Preparation of tensile test specimens machined from the diffusion-bonded block, and tensile tests at three temperatures: room temperature, 550 C and 750 C;

-- Characterization of the pressure-containing channels' deformation, especially at the diffusion bonds, i.e., the corner tips of semi-circular channels;

-- The quantification of the corrosion effect on the diffusion bonds.

Standard metallographic procedures can be used to prepare cross-sections of the base materials and diffusion bonds for microstructural characterization. A combination of electron microscopy characterization methods can be performed, including the scanning electron microscopy (SEM) to observe second phase particles along diffusion-bonding interfaces, and the orientation imaging microscopy (OIM) to characterize the grain structure. These methods have been widely used for material microstructure characterization. Figure 189 shows the SEM inspection results of alloy 617 from OSU and INL, respectively. The results can be compared with the pre-test inspection results. It can also be used for quantify the corrosion effect through the included energy-dispersive spectroscopy (EDS) results.

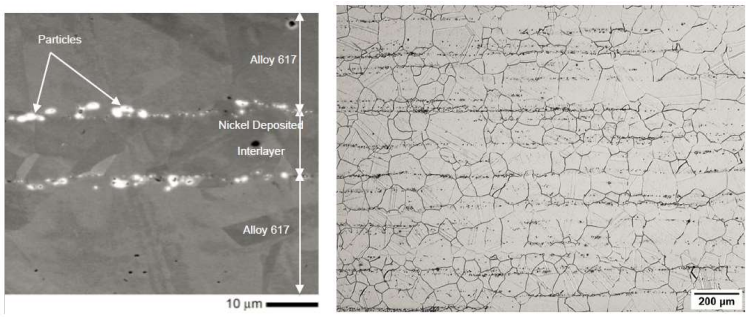

Figure 189. Representative SEM image of diffusion bond with Ni-interlayer at OSU (left) and the microstructure of material 617 at INL (right) (Mylavarapu, 2011)

The tensile test specimens can be machined out from the diffusion-bonded matrix. The PCHE was welded with four headers (as shown in Figure 190), which might damage the bonds close to the manifolds from the previous experience. Therefore, the specimens can be machined out away from the headers. Six tensile test specimens with flat shoulders can be prepared for tensile test at different temperatures.

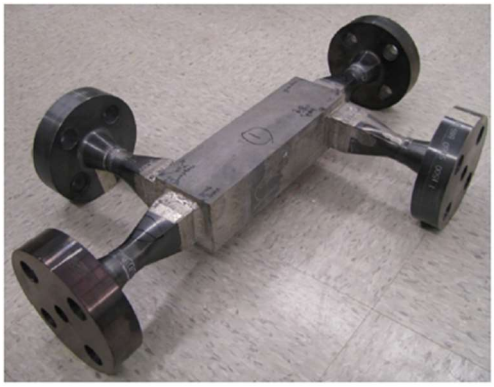

Figure 190. Post-test inspection candidate PCHE

3.3.2 Bursting Test per ASME Standards

The research work consists of a burst/proof test of a PCHE, post-test inspection and mechanical tensile test. The objective of the post-test destructive analysis is to establish the maximum allowable working pressure of PCHEs by a burst/proof pressure test in compliance with ASME standards. Such destructive test was carried out before in industry. Kobe Steel (Japan) tested a few diffusion-bonded compact heat exchangers that are essentially PCHEs (Miwa et al., 2013). In an example of the burst test, a sample made of SS 316L was tested with maximum withstanding pressure up to 450 MPa. With a conservative safety factor of 4 used, the design pressure, or more precisely speaking, the maximum allowable working pressure was determined to be 100 MPa.

According to ASME BPVC, Section VIII, Division 1, UG-98, “The maximum allowable working pressure for a vessel is the maximum pressure permissible at the top of the vessel in its normal operating position at the designated coincident temperature specified for that pressure.” Hence, the maximum allowable working pressure (or MAWP) is a function of temperature. For the MAWP at temperatures different from the temperature in the test, a formula is available in UG-101:

$$P_0 = P_t \frac{S}{S_2} \tag{3.3.1}$$

where P_0, P_t, S and S_2 are MAWP at the design temperature, MAWP at test temperature, maximum allowable stress (MAS) value at the design temperature, as given in the referenced tables in UG-23, (but not to exceed S_2), and maximum allowable stress value for the materials used in the test at test temperatures, respectively.

The MAWP at room temperature can be determined through bursting test. The bursting test at room temperature is applied to vessels or vessel parts under internal pressure when constructed of any material permitted to be used. As stated in ASME standards, “the maximum allowable working pressure of any component part proof tested by this method shall be established by a hydrostatic test to failure by rupture of a full-size sample of such pressure part.” Also, “the hydrostatic pressure at which rupture occurs shall be determined. Alternatively, the test may be stopped at any pressure before rupture that can satisfy the requirements for the desired maximum allowable working pressure.” This means that either the burst or proof pressure can be used as the final MAWP. Two formulas are available:

$$P = \frac{B}{4} \times \frac{S_\mu E}{S_{\mu,avg}} \text{ or } P = \frac{B}{4} \times \frac{S_\mu E}{S_{\mu r}} \tag{3.3.2}$$

where B, E, S_μ, $S_{\mu,avg}$ and $S_{\mu r}$ are the bursting test pressure or the hydrostatic test pressrure at which the test was stopped, efficiency of welded joint, which is assumed to be 0.7 for a PCHE made of Inconel 617, specified minimum tensile strength at room temperature, average actual tensile strength of test specimens at room temperature, and maximum tensile strength of range of specification at room temperature, respectively. If it is assumed that the actually tensile strength is close to the product of the minimum tensile strength and the welded joint factor, the determined MAWP at room temperature is approximately the burst/proof pressure with a safety factor of 4 considered. In this method, one can quickly estimate the proof pressure for the test.

The Inconel 617 PCHE that was tested is shown in Figure 190. The specification is listed in literature with details. The design pressure and temperature is 3 MPa at 800 °C, respectively. The estimated proof test pressure can be computed as below

$$B_p \approx 4P_t = 4P_0 \frac{S_2}{S} = 4 \times (1.5P_d) \frac{S_2}{S} \tag{3.3.3}$$

where P_d is the design pressure. Here we consider a factor 1.5 to determine the MAWP. From the ASME BPVC Section III Part D, we can know the MAS for Inconel 617, of which at some typical temperatures are listed in Table 58. Therefore, the proof pressure is around:

$$B_p \approx 4 \times 1.5 \times 3\,\text{MPa} \times \frac{161\,\text{MPa}}{31.3\,\text{MPa}} = 92.6\,\text{MPa} \tag{3.3.4}$$

which means that if the proof test of the PCHE passes the hydrostatic pressure greater than 92.6 MPa, it can ensure that the design pressure of 3 MPa at 800 °C is strictly proved safe, and the stress analysis used in the design of the PCHE is applicable. Therefore, in the process of bursting test, a hydrostatic pressure around 100 MPa should be considered.

Table 58. Maximum allowable stress of Inconel 617 (N06617) in ASME BPVC

Temperature (°C)	-30 ~ 40	250	400	550	700	800
MAS (MPa)	161	161	150	144	81	31.3

ASME also states the procedure to apply pressure to the test sample. It is stated in detailed that “the hydrostatic pressure in the vessel or vessel part shall be increased gradually until approximately one-half the anticipated working pressure is reached. Thereafter, the test pressure shall be increased in steps of approximately one-tenth or less of the anticipated maximum allowable working pressure until the pressure required by the test procedure is reached. The pressure shall be held stationary at the end of each increment for a sufficient time to allow the observations required by the test procedure to be made, and shall be released to zero to permit determination of any permanent strain after any pressure increment that indicates an increase in strain or displacement over the previous equal pressure increment.” In this case, the proof test pressure can set the hydrostatic pressure at 100 MPa, and a pressure increment of 20 MPa can be applied to reach 200 MPa, and then an increment of 40 MPa can be applied to reach to the testing facility’s maximum capacity (around 400~450 MPa)..

3.3.3 Testing Procedure

There were in total two tests with the assumption that the “Z”-side channels may experience less strength than straight-side channels, as shown in Figure 191. This is based on the fact that hot fluid flows through “Z”-side channels with almost 200 °C temperature difference. Since we only want to burst the PCHE in the second test, the first test would be carried out on the straight-side channels, and a proof pressure of 100 MPa (1000 bar) was set with the dwell time from 30 to 60 seconds. The second test would be carried out on the “Z”-side channels, and the application of pressure would be ramping to 100 MPa, with 20 MPa increment to 200 MPa, and 40 MPa increment to maximum capacity or rupture afterwards. The dwell time for each increment would be 10 seconds.

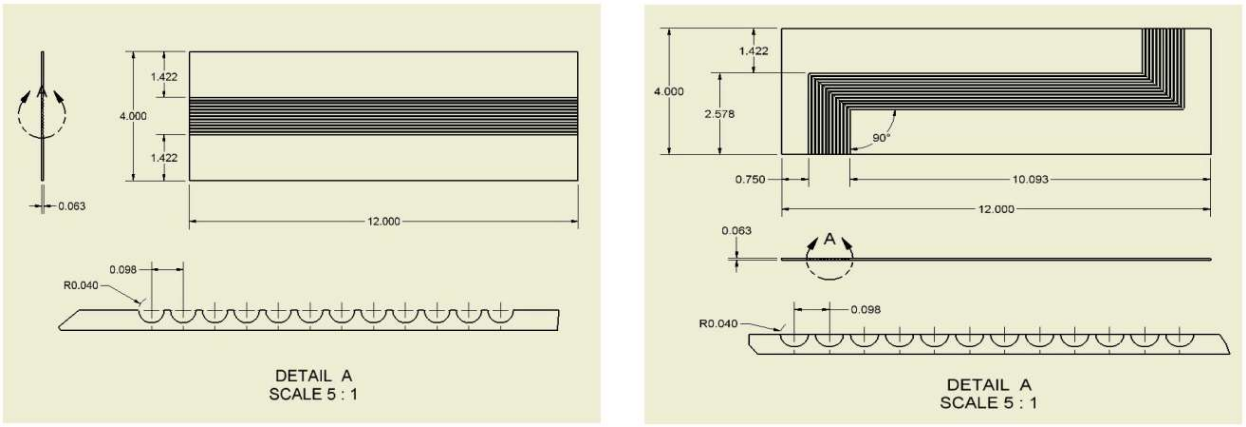

Figure 191. Straight-side channels (left) and “Z”-side channels (right)

3.2.4 Results and Discussion

The test results are listed in Table 59. In the first test, the sample passed the test sequence of 1000 bar (14,504 psi) for 60 seconds. No sign of damage or failure post-test was observed. In the second test, the sample was not able to reach the beginning dwell pressure of 1000 bar (14,504 psi) of the incremental test. The sample failed at the body of the sample with a pressure of 783 bar (11,357 psi). The measured pressure over time for each test is shown in Figure 192.

Table 59. Summary of the bursting tests

Test No.	Sample	Max. Pressure (bar)	Results
1	PCHE, 617, Straight side	1028.83	Passed
2	PCHE, 617, “Z” side	783.42	Leakage/Burst

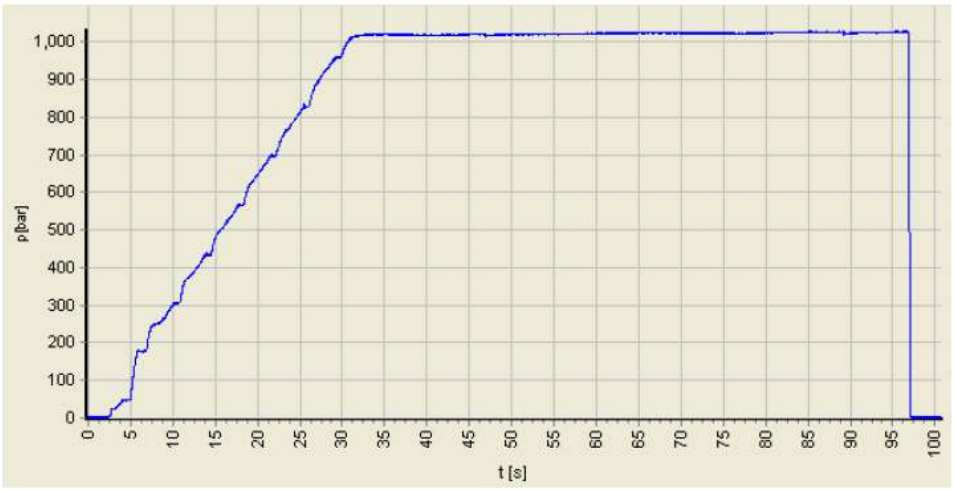

(a)

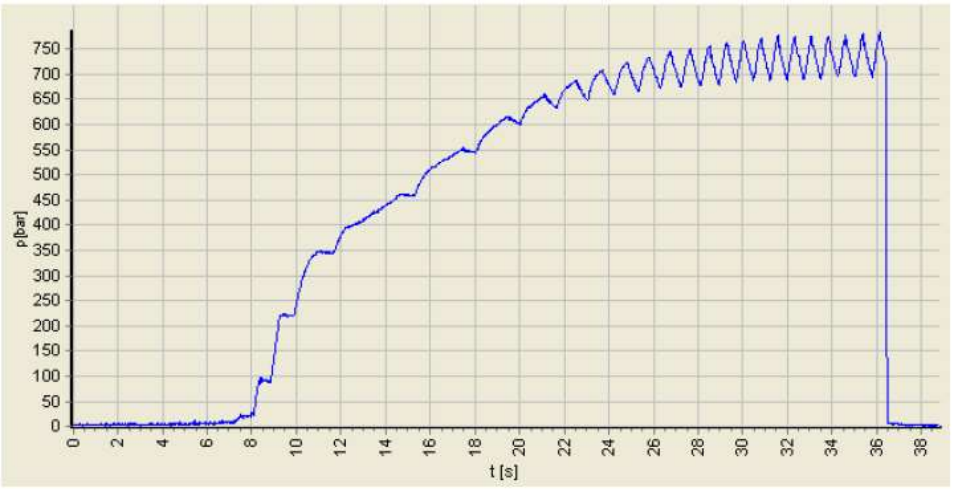

(b)

Figure 192. Pressure measurement versus time. (a) Test 1, passed; (b) Test 2, failed

The second test indicated that there was a potential leakage in the PCHE as the pressure was maintained around 725 bar but failed to reach pre-set pressure of 1000 bar. The snapshot of the recording shows that the leakage location is at somewhere close to two headers where significant amount of welded joints were applied. From the video (shown in Figure 193), it could be observed that the leakage occurred at three to four points that were aligned at one level. This indicated that the diffusion bond was damaged and the joint between two plates were ripped open. Since the pressure was somehow maintained during the test, the sudden rupture of diffusion bonds is highly unlikely.

Figure 193. The leakage of the PCHE during the second test

The possible reason to cause such leakage may be the thermal stress during welding. Welding can generate extreme localized high temperature, and it can cause undesired thermal stress concentration, making diffusion bonds susceptible to failure. It was observed in the previous experience, and brazing was suggested afterwards to avoid localized thermal stress. However, the permanent damage may not be repaired and remained in the PCHE.

Since the straight channel passed the proof test, it could be concluded that the stress analysis design is effective and proven correct. Although the final MAWP needs data of tensile strength tests of specimens procured from the PCHE, it is estimated that the MAWP can be at least greater than 4.5 MPa at 800 °C.

3.4 Summary

Studies of diffusion bonding parameters reveal the importance of several factors including bonding time, bonding atmosphere conditions, use of Ni-interlayers and PBHT, etc. The post-test destructive inspection involved a burst test of a decommissioned PCHE made of Inconel 617 to establish MAWP. The testing procedures were in compliance with ASME standards. There were two tests, each on different side of the PCHE. 1000 bar was reached and dwelled for 60 seconds on the straight-side channels, which were proven to withstand the hydrostatic pressure, whereas the “Z”-side channel failed with leakage indicating permanent damage due to the extreme thermal stress caused by the welding process ripping the diffusion bond open. It is currently estimated that MAWP for the PCHE is 4.5 MPa at 800 °C and 25 MPa at room temperature.

LIST OF REFERENCES

American Society of Mechanical Engineers, ASME Boiler & Pressure Vessel Code: an International Code, New York (2015).

Carlson, M.D., “Measurement and Analysis of the Thermal and Hydraulic Performance of Several Printed Circuit Heat Exchanger Channel Geometries,” M.S. Thesis, University of Wisconsin – Madison (2012).

Chen, M. “Design, Fabrication, Testing, and Modeling of a High-Temperature Printed Circuit Heat Exchanger,” M.S. Thesis, The Ohio State University (2012).

Deb, K. “A Fast and Elitism multi-objective: NSGA-II,” IEEE transaction on Evolutionary Computation, 6, 182-197, (2002).

Deb, K., Multi-Objective using Evolutionary Algorithm, Chapters 2 & 5, John Wiley & Sons, London, UK (2001).

Dostal, V., “A Supercritical Carbon Dioxide Cycle for Next Generation Nuclear Reactors,” Ph.D. Dissertation, Massachusetts Institute of Technology (2004).

Dostal, V., Driscoll, M. J., and Hejzlar, P., “A Supercritical Carbon Dioxide Cycle for Next Generation Nuclear Reactors,” Advanced Nuclear Power Technology Program, Massachusetts Institute of Technology, Cambridge, MA (2004).

Fenghour, A., Wakeham, W. A., and Vesovic, V., “The Viscosity of Carbon Dioxide,” J. Phys. Chem. Ref. Data, vol. 27, no. 1, (1998).

Gezelius, K., “Design of Compact Intermediate Heat Exchanger for Gas Cooled Fast Reactor,” M.S. Thesis, Massachusetts Institute of Technology (2004).

Gibbs, J.P., Hejzlar, P., and Driscoll, M.J., “Applicability of Supercritical CO2 Power Conversion Systems to GEN IV Reactors,” Topical Report, No. MIT-GFR-037, Massachusetts Institute of Technology (2006).

Hejzlar, P., Dostal, V., Driscoll, Dumza, M.J. P., Poullennec, G., and Alpy, N., “Assessment of Gas Cooled Fast Reactor with Indirect Supercritical CO2 Cycle”, Nuclear Engineering and Technology, 38(2), pp. 109-118 (2006).

Hesselgreaves, J.E., Compact Heat Exchangers -- Selection, Design and Operation, Elsevier Science, Oxford, UK (2001).

Hilbert, R., Janiga, G., Baron, R., and Thevnin, D., “Multi-objective Shape Optimization of a Heat Exchanger Using Parallel Genetic Algorithms,” International Journal of Heat and Mass Transfer, 49, pp. 2567-2577 (2006).

Ishizuka, T., Kato, Y., Muto, Y., Nikitin, K., Ngo, T.L., and H. Hashimoto, “Thermal-Hydraulic Characteristics of a Printed Circuit Heat Exchanger in a Supercritical CO2 Loop,” The 11th International Topical Meeting on Nuclear Reactor Thermal-Hydraulics (NURETH-11), Avignon, France, October 2-6, 2005.

Kim, D.E., Kim, M.H., Cha, J.E., and Kim, S.O, “Numerical Investigation on Thermal-Hydraulic Performance of New Printed Circuit Heat Exchanger Model”, Nuclear Engineering and Design, 238, pp. 3269-3276 (2008a).

Kim, E.S., Oh, C.H., and Sherman, S. “Simplified Optimum Sizing and Cost Analysis for Compact Heat Exchanger in VHTR,” Nuclear Engineering and Design, 238, pp. 2635-3647 (2008b).

Kim, I.H., and No, H.C., “Thermal hydraulic performance analysis of a printed circuit heat exchanger using a helium-water test loop and numerical simulations,” Applied Thermal Engineering, 31, pp. 4064-4073 (2011).

Kim, I.H., and No, H.C., “Thermal–hydraulic physical models for a Printed Circuit Heat Exchanger covering He, He–CO2 mixture, and water fluids using experimental data and CFD,” Experimental Thermal and Fluid Science, 48, pp. 213-221 (2013).

Kim, I.H., and No, H.C., “Physical model development and optimal design of PCHE for intermediate heat exchangers in HTGRs,” Nuclear Engineering and Design, 243, pp. 243-250 (2012).

Kim, I.H., No, H.C., Lee, J.I., and Jeon, B.G., “Thermal Hydraulic Performance Analysis of the Printed Circuit Heat Exchanger using a Helium Test Facility and CFD Simulations,” Nuclear Engineering and Design, 239, pp. 2399-2408 (2009).

Kruizenga, A., “Heat Transfer and Pressure Drop Measurements in Prototypic Heat Exchangers for the Supercritical Carbon Dioxide Brayton Power Cycles,” University of Wisconsin Madison, (2010).

Le Pierres, R., Southall, D., and Osborne, S., “Impact of Mechanical Design Issues on Printed Circuit Heat Exchangers,” in Proceedings of SCO2 Power Cycle Symposium Boulder, CO, 2011.

Lee, S.M., Kim, K.Y., and Kim, S.W., “Multi-objective Optimization of a Double-faced Type Printed Circuit Heat Exchanger,” Applied Thermal Engineering, 60, pp. 44-50, (2013).

Lee, Y., and Lee, J.I., “Structural Assessment of Intermediate Printed Circuit Heat Exchanger for Sodium-Cooled Fast Reactor with Supercritical CO2 Cycle”, Annals of Nuclear Energy, 73, pp. 84-95 (2014).

Moisseytev, A., Sienicki, J.J., Cho, D. H., and Thomas, M. R., "Comparison of Heat Exchanger Modeling with Data from CO2-to-CO2 Printed Circuit Heat Exchanger Performance Tests," in Proceedings of ICAPP ‘10, San Diego, CA, USA, 2010.

Mylavarapu, S. K., “Design, Fabrication, Performance Testing, and Modeling of Diffusion Bonded Compact Heat Exchangers in a High-Temperature Helium Test Facility,” Dissertation, The Ohio State University (2011).

Mylavarapu, S., Sun, X., Glosup, R., Christensen, R., and Patterson, M., “Thermal Hydraulic Performance Testing of Printed Circuit Heat Exchangers in a High-Temperature Helium Test Facility,” Applied Thermal Engineering, 65, (1-2), 605, (2014).

Najafi, H., Najafi, B., and Hoseinpoori, P., “Energy and Cost Optimization of a Plate and Fin Heat Exchanger Using Genetic Algorithm,” Applied Thermal Engineering, 31, pp. 1839-1847 (2011).

Ngo, T.L., Kato, Y., Nikitin, K., and Ishizuka, T., “Heat Transfer and Pressure Drop Correlations of Microchannel Heat Exchanger with S-shaped and Zigzag Fins for Carbon Dioxide Cycles,” Experimental Thermal and Fluid Science, 32, pp. 560-570 (2007).

Nitikin, K., Kato, Y., and Ngo, L., “Printed Circuit Heat Exchanger Thermal-Hydraulic Performance in Supercritical CO2 Loop,” International Journal of Refrigeration, 29, pp. 807-814 (2006).

Oh, C.H., Kim, E.S., and Patterson, M., “Design Option of Heat Exchanger for the Next Generation Nuclear Plant”, Journal of Engineering for Gas Turbine and Power, 132, 032903 (2010).

Pra, F., Tochon, P., Mauget, C., Fokkens, J., and Willemsen, S., “Promising Designs of Compact Heat Exchangers for Modular HTRs using the Brayton Cycle,” Nuclear Engineering and Design, 238, pp. 3160-3173 (2008).

Sanaye, S. and Hajabdollahi, H., “Thermal-economic Multi-objective Optimization of Plate Fin Heat Exchanger using Genetic Algorithm,” Applied Energy, 87, pp. 1893-1902 (2010).

Shah, R.K., and Sekulić, D.P., Fundamentals of Heat Exchanger Design, John Wiley & Sons, Inc. Hoboken, New Jersey (2003).

Sohal. M. S., Ebner, M.A., Sabharwall, P., Sharpe, P. “Engineering database of liquid salt thermophysical and thermalchemical properties,” Idaho National Laboratories, INL/EXT-10-18297 (2010).

Southall, D., Le Pierres, R. and Dewson, S. J., "Design Considerations for Compact Heat Exchangers," in Proceedings of ICAPP '08, Anaheim, CA, USA, (2008).

Span, R., and Wagner, W., “A New Equation of State for Carbon Dioxide Covering the Fluid Region from the Triple-Point Temperature to 1100 K at Pressures up to 800 MPa,” J. Phys. Chem. Ref. Data, vol. 25, no. 6, (1996).

Tsuzuki, N., Kato, Y., and Ishizuka, T., “High Performance Printed Circuit Heat Exchanger,” Applied Thermal Engineering, 27, pp. 1702-1707 (2007).

Tsuzuki, N., Kato, Y., Nikitin, K., and Ishizuka, T., “Advanced Microchannel Heat Exchanger with S-shaped Fins,” Journal of Nuclear Science and Technology, 46, pp. 403-412 (2009).

Vesovic, V., “The Transport Properties of Carbon Dioxide,” *J. Phys. Chem. Ref. Data*, vol. 19, no. 3, (1990).

Xie, G.N., Sunden, B., and Wang, Q.W., “Optimization of Compact Heat Exchangers by a Genetic Algorithm,” Applied Thermal Engineering, 28, pp. 895-906 (2008).

Yoon, S.H., No, H.C., and Kang, G.B., “Assessment of Straight, Zigzag, S-shape, and Airfoil PCHEs for Intermediate Heat Exchangers of HTGRs and SFRs,” Nuclear Engineering and Design, 270, pp. 334-343 (2014).

Yoder, G. L., “Examination of liquid fluoride salt heat transfer,” Proceedings of ICAAP, paper 14332, Charlotte, US (2014)